

https://dspace.org/

Functionalized Immunomodulatory Biopolymeric Nanosystem For The Targated Deliveryof Anti-Tuberculosis Bioactives

Khoza, Leon Joseph Khoza

2025

University of the Witwatersrand, Johannesburg

https://hdl.handle.net/10539/48447

Khoza, Leon Joseph Khoza. (2025). Functionalized Immunomodulatory Biopolymeric Nanosystem For The Targated Deliveryof Anti-Tuberculosis Bioactives [PhD thesis, University of the Witwatersrand, Johannesburg]. WIReDSpace. https://hdl.handle.net/10539/48447

Downloaded from a DSpace repository. https://dspace.org/

FUNCTIONALIZED IMMUNOMODULATORY BIOPOLYMERIC NANOSYSTEM FOR THE TARGETED DELIVERY OF ANTI-TUBERCULOSIS BIOACTIVES

LEON JOSEPH KHOZA

A thesis submitted to the Faculty of Health Sciences, University of the Witwatersrand, Johannesburg, in fulfilment of the requirements for the degree of

Doctor of Philosophy



Supervisors

Professor Yahya Essop Choonara

Professor Pradeep Kumar

Associate Professor Admire Dube

Department of Pharmacy and Pharmacology, Faculty of Health Sciences, University of the Witwatersrand, Johannesburg, South Africa

School of Pharmacy, Faculty of Natural Sciences, University of the Western Cape, Cape Town, South Africa

Johannesburg

2025

DECLARATION

I, Leon Joseph Khoza, declare that this thesis is my own work. It has been submitted for the Doctor of Philosophy degree in the Faculty of Health Sciences at the University of the Witwatersrand, Johannesburg. It has not been submitted before for any degree or examination at this or any other university.

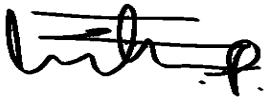

Signed on the 07th of May 2025

RESEARCH OUTPUTS

Publications Articles:

1. Insights into innovative therapeutics for drug-resistant tuberculosis: Host-directed therapy and autophagy-inducing modified nanoparticles. Leon J. Khoza, Pradeep Kumar, Admire Dube, Patrick H. Demane, Yahya E. Choonara., 2022. *International Journal of Pharmaceutics, 622,121893;https://doi.org/10.1016/j.ijpharm.2022.121893*

Appendix A1

Submitted for Publication:

1. Enhancing TB Therapy with Precision: Immunomodulatory Nanoparticles Co-Delivering Rifampicin and Vitamin D3 for Macrophage-Targeted Treatment. Khoza, Leon; Kumar, Pradeep; Dube, Admire; Gordhan, Bhavna; Kana, Bavesh; Choonara, Yahya. *ACS Applied Bio Materials* (Revisions Requested).

Podium Presentations:

1. Functionalized Immunomodulatory biopolymeric nanosystem for the targeted delivery of anti-TB bioactives. Leon J. Khoza, Pradeep Kumar, Admire Dube and Yahya E. Choonara. *Annual Young Scientists Conference 2023***.** University of Venda, Thohoyandou, South Africa, June 12 – 13, 2023.

Appendix A2

Poster Presentations:

1. Functionalized Immunomodulatory biopolymeric nanosystem for the targeted delivery of anti-TB bioactives. Leon J. Khoza, Pradeep Kumar, Admire Dube and Yahya E. Choonara. *STHS Biennial Research Day*. University of the Witwatersrand, Johannesburg, South Africa, September 5, 2023.

Appendix A3

Research Awards:

1. Erasmus+ International Scholarship; National and Kapodistrian University of Athens, 2024.
2. National Research Foundation (NRF) Postgraduate (Doctoral) Scholarship, 2021-2024.
3. University of the Witwatersrand PhD Postgraduate Merit Award (PMA), 2021-2023.

PATENT FILED

A patent for this research was filed under the Republic of South Africa Patent Act, 1978, titled **“Nanoparticles for Antimicrobial Therapy**”. The inventors are Leon J. Khoza, Pradeep Kumar, and Yahya E. Choonara. Patent Application No: 2024/07866

Status: "The specification has been drafted, and the patent application has been filed (Under Review).

Appendix B

ABSTRACT

Tuberculosis (TB) continues to be the leading cause of death from a single infectious disease globally, with over 6.2 million new cases and nearly 2 million deaths annually. Pulmonary TB, which affects the lungs, accounts for approximately 83% of cases and is particularly concerning due to its high contagiousness. Despite the availability of treatment options, including first-line drugs requiring a six-month regimen and second and third-line drugs for drug-resistant TB, current therapies face significant limitations. These include prolonged treatment duration, high pill burden, poor patient compliance, and the emergence of multidrug-resistant (MDR) TB strains. The cost of treating MDR-TB is prohibitively high, and the side effects are more severe, especially in patients with co-infections, exacerbating drug-drug interactions. TB's ability to hijack the host immune system during infection necessitates novel therapeutic strategies to target TB bacteria and modulate the host immune response. This study aimed to develop a biocompatible, multifunctional drug delivery system using 1,3-β-glucan-functionalized chitosan-polycaprolactone nanoparticles (1,3-β-Glu-CS-PCL-VITD3/RIF) for co-delivering Rifampicin (RIF) and Vitamin D3 (VITD3) to alveolar macrophages, where TB bacteria reside. The nanoparticles exhibited spherical shapes with average particle sizes of 182.90 ± 1.15 nm (Glu-CS-PCL-VITD3) and 122.63 ± 5.11 nm (Glu-CS-PCL-RIF) and zeta potentials of +24.8 ± 0.73 mV and +19.5 ± 0.21 mV, respectively. They demonstrated sufficient entrapment efficiency (54% for VITD3 and 62% for RIF) and pH-responsive, sustained drug release over 48 hours (86% for VITD3 and 96% for RIF at pH 6.4). Cytocompatibility studies with RAW 264.7 cells confirmed 100% cell viability. ROS generation was significantly enhanced by Glu-CS-PCL-RIF (1.5- to 1.8-fold) and Glu-CS-PCL-VITD3 (1.7-fold higher than non-functionalized nanoparticles). Glu-CS-PCL-VITD3 also significantly stimulated TNF-α secretion (1.8-fold increase), while CS-PCL nanoparticles showed increased IL-4 levels (48.58 ± 10.16 pg/mL), indicating a balanced M1/M2 response. Minimum Inhibitory Concentration (MIC) studies revealed that Glu-CS-PCL-RIF exhibited superior bactericidal activity against drug-susceptible laboratory (H37Rv) strain and clinically resistant isolates (MDR11) of *M. tuberculosis* (Mtb), with a remarkably low MIC of 0.00149 µg/mL on day 7, two times lower than standard RIF. The combination of Glu-CS-PCL-RIF and Glu-CS-PCL-VITD3 demonstrated significant potency against MDR11, with the nanoparticles containing 0.745 µg/mL of RIF, four times lower than standard treatment. Intracellular killing of H37Rv TB in THP-1 macrophages demonstrated that CS-PCL-RIF achieved higher bactericidal activity with significantly lower Mtb CFU counts (4.05E+02 and 3.27E+03 CFU/mL) despite containing approximately 15 times less RIF than the standard 50 µg/mL RIF treatment. CS-PCL-VITD3 exhibited a highly significant reduction in CFUs compared to the untreated group and CS-PCL, indicating that VITD3 potentiates bactericidal mechanisms within macrophages. The Glu-CS-PCL-VITD3 exhibited higher bactericidal activity than non-functionalized nanoparticles, demonstrated by Mtb CFU counts of 1.08E+04 compared to 7.85E+04 for CS-PCL-VITD3. This enhanced activity is attributed to the successful functionalisation with 1,3-β-glucan. In conclusion, this study developed multifunctional 1,3-β-glucan-functionalized nanoparticles with immunomodulatory capabilities (host-directed therapy) and potent antibacterial activity. This nanosystem offers a promising approach for targeted anti-TB treatment, with significant potential for further development and clinical application.

ACKNOWLEDGEMENTS

First and foremost, I express my heartfelt gratitude to the Almighty for bestowing upon me the strength and courage that have propelled me to this significant milestone in my academic journey.

I sincerely appreciate my dedicated supervisors, Prof. Yahya. E Choonara, Prof. Pradeep Kumar, and Prof. Admire Dube, whose unwavering guidance and support have been instrumental throughout my PhD journey. Working with them has been an absolute honour, and I am eternally grateful for their mentorship.

A special acknowledgement goes to the remarkable Wits Advanced Drug Delivery Platform (WADDP) Research Unit colleagues and friends. Their support during challenging times was invaluable, and I extend my gratitude to the entire team. I also want to thank the technical staff in the Department of Pharmacy and Pharmacology for their assistance with chemicals and supplies, which significantly contributed to the success of this study.

I am indebted to Dr Bhavna Gordhan and Professor Bhavesh Kana at the National Health Laboratory Institute (NHLS) for their indispensable resources and vital role in completing this study. Their support has been crucial, and I sincerely appreciate their contribution.

Furthermore, I extend my thanks to everyone who played a role in completing this project. Your collective efforts have not gone unnoticed, and I am grateful for the collaborative spirit that fuelled the success of this endeavour.

I want to express my gratitude to the National Research Foundation (NRF) of South Africa and the University of the Witwatersrand (Postgraduate Financial Aid and Scholarships Administration) for their financial assistance, which significantly facilitated the progression of my research.

Last but certainly not least, I thank my family and friends; their unwavering love and support have been a source of strength throughout this long and challenging yet ultimately rewarding academic pursuit. May the Almighty bless them abundantly for their enduring encouragement and companionship.

DEDICATION

In profound sincerity, I dedicate this work to the memory of my late mother, Mrs. Nokuthula "Ntombazanyana" Mlambo-Khoza. Her unwavering support and boundless love have been the guiding light that led me to where I stand today. This journey would not have been possible without her, and I carry her spirit with me in every achievement.

I also dedicate this work to the memory of my late father, Mr. Mhlahleki Joseph Khoza. His strength and wisdom continue to inspire me, and his presence, though physically absent, is felt on every page of this endeavour.

Lastly, but by no means least, I extend this dedication to my brothers, Mr. Aucran “Nqobizitha” Khoza and Iven “Khanya” Khoza. Their support, often silent yet immensely impactful, has been a pillar of strength during moments I may not even be aware of. This work is a tribute to the unity and resilience of the Khoza Family. It reflects the love, encouragement, and collective spirit that binds us together, even across the realms of time and space.

TABLE OF CONTENTS

DECLARATION	i
RESEARCH OUTPUTS	ii
PATENT FILED	iii
ABSTRACT	iv
ACKNOWLEDGEMENTS	v
DEDICATION	vi
TABLE OF CONTENTS	vii
APPENDICES	xix
LIST OF FIGURES	xx
LIST OF TABLES	xxvi
LIST OF EQUATIONS	xxvii
LIST OF ABBREVIATIONS	xxviii

CHAPTER 1

INTRODUCTION AND BACKGROUND

1.1.	Background of the Study	1
1.2.	Rational and Motivation for the Study	4
1.3.	Aim and Objectives	8
1.4.	Novelty of the Study	8
1.5.	Overview of the Thesis	9

CHAPTER 2

INSIGHT INTO INNOVATIVE THERAPEUTICS FOR DRUG-RESISTANT TUBERCULOSIS: HOST-DIRECTED THERAPY AND AUTOPHAGY-INDUCING MODIFIED NANOPARTICLES

2.1. Introduction 17

2.2. Recognition and uptake of Mtb by macrophages 21

2.3. Mtb defence mechanisms against the host immune response (Autophagy) 23

2.3.1. Disruption of phagolysosome maturation and acidification 23

2.3.1.1. Inhibition of Phagolysosome Maturation and Fusion 23

2.3.1.2. Inhibition of Phagolysosome Acidification 24

2.3.2. Disruption of reactive oxygen species production 25

2.3.3. Disruption of apoptosis and Mtb antigen presentation 26

2.4. Autophagy induction as host-directed TB therapy 27

2.4.1. Vitamin D3 and autophagy induction 28

2.4.2. Trehalose and Autophagy induction 30

2.4.3. L-arginine and Autophagy induction 31

2.5. Nanoparticle-based approaches for HDT-TB 33

2.5.1. Polymeric-based HDT-TB drug delivery systems 36

2.5.2. Solid Lipid Nanoparticles-based HDT-TB Drug Delivery System 40

2.5.3. Vesicular-based HDT-TB drug delivery systems: Liposomes and Niosomes 42

2.6. Delivery of NPs to the targeted host 44

2.7. Conclusion and Future Research Perspective 46

2.8. Acknowledgments 47
2.9. References 48

CHAPTER 3

SYNTHESIS AND CHARACTERISATION OF 1,3-B-GLUCAN-MODIFIED NANOPARTICLES ENCAPSULATING RIFAMPICIN AND VITAMIN D3 FOR POTENTIAL DELIVERY IN TUBERCULOSIS THERAPY

3.1.	Introduction		63
3.2.	Materials and Methods		65
	3.2.1.	Materials	65
	3.2.2.	Synthesis/formulation of functionalised and non-functionalised Nanoparticles	65
	3.2.3.	Analysis of hydrodynamic particle size distribution, zeta potential, and polydispersity index (PDI)	66
	3.2.4.	Evaluation of Drug Entrapment Efficiency and Loading Capacity of the Nanoparticles	66
	3.2.5.	Quantification of β-1,3-Glucan content on β-1,3-Glucan Functionalised Nanoparticles	67
	3.2.6.	Morphological analysis	67
	3.2.7.	Evaluation of Functional Transformation and Chemical Transitions of Nanoparticles Using Fourier transform infrared spectroscopy (FTIR)	68
	3.2.8.	Analysis of the crystallographic structure of the nanoparticles	68
	3.2.9.	Evaluation of the thermal behaviour/properties of the optimised Nanoparticle samples	68
	3.2.10.	*In vitro* release of VITD3 and RIF in formulated Nanoparticles	69

3.2.11. *In vitro* cytotoxicity assay of formulated nanoparticles optimised Nanoparticle samples 69

3.3. Results and Discussion 70

3.3.1. Particle size distribution, zeta potential, PDI, stability, morphology, and drug entrapment efficiency 70

3.3.2. Evaluation of Functional Transformation of Nanoparticles Before and After Drug Encapsulation and Functionalization 75

3.3.3. Analysis of the crystallographic structure of the nanoparticles 78

3.3.4. Evaluation of the thermal behaviour and storage stability of the optimised Nanoparticles 79

3.3.5. *In vitro* release of VITD3 and RIF in formulated nanoparticles 83

3.3.6. *In vitro* Cytotoxicity Assay and Metabolic Activity of Formulated Nanoparticles in RAW 264.7 Cell Line 88

3.4. Concluding Remarks 90

3.5. References 91

CHAPTER 4

PRO-INFLAMMATORY VS ANTI-INFLAMMATORY RAW 264.7 MACROPHAGE CELLS RESPONSES: INSIGHTS FROM INTRACELLULAR ROS AND CYTOKINE QUANTIFICATION POST-NANOPARTICLE TREATMENT

4.1. Introduction 99

4.2. Materials and Methods 100

4.2.1. Materials 100

4.2.2. Quantification of ROS and Pro-inflammatory Cytokines in RAW 264.7 Cells 101

4.2.2.1. Intracellular ROS (Superoxide and Hydroxy radicals) Quantification 101

4.2.2.2. TNF-α Quantification using ELISA Kit 101

4.2.2.3. IFN-γ Quantification using ELISA Kit 102

4.2.3. Quantification of Anti-inflammatory Cytokines in RAW 264.7 Cells 102

4.2.3.1. IL-4 Quantification using ELISA Kit 102

4.2.3.2. IL-10 Quantification using ELISA Kit 103

4.2.4. Morphological Analysis of RAW 264.7 Macrophages: Untreated vs Treated Groups 103

4.2.5. Statistical analysis 103

4.3. Results 103

4.3.1. Intracellular ROS Quantification 103

4.3.2. Quantification of TNF-α secretion 105

4.3.3. Quantification of IFN-γ secretion 106

4.3.4. IL-4 Quantification in RAW 264.7 Cells 108

4.3.5. Quantification of IL-10 secretion 110

4.3.6. Morphological Analysis of RAW 264.7 Macrophages: Untreated vs Treated Groups 111

4.4. Discussion 111

4.5. Concluding Remarks 117

4.6. References 118

CHAPTER 5

ASSESSMENT OF ANTI-TUBERCULAR EFFICACY OF FORMULATED NANOPARTICLES AGAINST MYCOBACTERIUM TUBERCULOSIS STRAINS AND INTRACELLULAR KILLING IN ACTIVATED THP-1 MACROPHAGES

5.1.	Introduction		122
5.2.	Methods and Materials		124
	5.2.1.	Materials	124
	5.2.2.	Evaluation of Formulated Nanoparticles Against *M.tuberculosis* using the Broth Microdilution Method	124
	5.2.3.	Intracellular killing of Susceptible Mtb, H37Rv in THP-1 activated Macrophages	125
5.3.	Results and Discussion		126
	5.3.1.	MIC Evaluation of Formulated Nanoparticles Against H37Rv and MDR11 Strains	126
	5.3.2.	Intracellular killing of Susceptible Mtb, H37Rv in THP-1 activated Macrophages	130
5.4.	Concluding Remarks		137
5.5.	References		138

CHAPTER 6

INTEGRATION OF NANOPARTICLES WITH A MODEL THERMOGEL: A DUAL-THERMORESPONSIVE NANOCOMPOSITE DELIVERY SYSTEM

6.1. Introduction 141

6.2. Materials and Methods 142

6.2.1. Materials 142

6.2.2. Preparation of pure and Pluronic nanocomposite Thermogel 143

6.2.3. Morphological analysis 143

6.2.4. Evaluation of Fourier transform infrared spectroscopy of the Nanocomposite 143

6.2.5. X-ray powder diffraction (XRPD) analysis 144

6.2.6. Evaluation of the thermal behaviour of the optimised samples 144

6.2.7. Gelation Temperature and Dynamic Viscosity Analysis of Thermogel Formulations 144

6.2.8. Porosity profile analysis of nanocomposite Thermogel 145

6.2.9. *In vitro* release of VITD3 and RIF from the nanocomposite Thermogel 145

6.2.10. *In vitro* cytotoxicity assay of the Nanocomposite Thermogel 145

6.3. Results and Discussion 146

6.3.1. Integrated Analysis of the Thermogel and nanocomposite: Spectroscopy, Diffraction, and Thermal properties 144

6.3.2. Assessment of the surface morphology and porosity of the Thermogel nanocomposite 149

6.3.3. Gelation temperature and dynamic viscosity analysis 151

6.3.4. pH-Dependent Release Profiles of VITD3 and RIF from 155

Glu-CS-PCL Nanoparticles Incorporated into Pluronic Thermogel: A Thermogel Nanocomposite Release Profile

6.3.5. MTT Assay: Cell Viability and Cytocompatibility of the Thermogel Nanocomposite 157

6.4. Concluding Remarks 158

6.5. References 159

CHAPTER 7

CONCLUSIONS, LIMITATIONS AND RECOMMENDATIONS

7.1. Conclusion 162

7.2. Limitations and Recommendations 165

APPENDICES

Appendix A:	Research Outputs	167
Appendix B:	Patent Application	170
Appendix C:	Similarity Report	171

LIST OF FIGURES

Figure 1.1:	Typical Schematic Representation of the Proposed β-Glucan Surface-Functionalized Multifunctional Biopolymeric Nanosystem Synthesis and Characterisation.	07
Figure 2.1:	Summarises macrophage polarisation to produce distinct functional phenotypes as a reaction to specific microenvironmental stimuli and signals.	22
Figure 2.2:	Normal process of autophagy where Mtb is digested and cleared. However, Mtb evades this response by blocking maturation (ii), phagolysosome fusion (iii), acidification of the phagosomes (iv) and antigen presentation (Reprinted from Carranza and Chavez-Galan, 2019 with permission).	27
Figure 2.3:	Induction of autophagy by Vitamin D_3 and its metabolites (Reprinted from Hewison, 2011 with permission).	29
Figure 2.4:	Different types of the most common nanostructures used as drug delivery systems (Reprinted from Dahanayake and Jayasundera, 2021 with permission).	34
Figure 2.5:	Results from Dube et al., 2014 show concentrations of (A) TNF-α, (B) IFN-γ and (C) IL-12p70 in ALM supernatants in different groups after 2 and 24 hours (Reprinted from Dube et al., 2014, with permission).	37
Figure 2.6:	Results from Dube et al., 2014 showing total ROS/RNS generated after six hours of incubation of ALM with free drug solution (RIF), CS-PLGA, and Glu-CS-PLGA nanoparticles (Reprinted from Dube et al., 2014, with permission).	38
Figure 2.7:	Different routes of nanoparticle administration targeting the host and granuloma (Reprinted from Baranyai et al., 2020, with permission).	45
Figure 3.1:	Particle Size Distribution and Zeta Potential of **(a)** CS-PCL-VITD3 and **(b)** Glu-CS-PCL-VITD3 Nanoparticles, Indicating Favorable Characteristics for Macrophage Internalization.	72
Figure 3.2:	Particle Size Distribution and Zeta Potential of **(a)** CS-PCL-RIF and **(b)** Glu-CS-PCL-RIF Nanoparticles,	72

Indicating Favourable Characteristics for Macrophage Internalization.

Figure 3.3: SEM and TEM images, respectively, showcasing the morphological characteristics of **(a)** unloaded CS-PCL nanoparticles, **(b)** drug-loaded CS-PCL nanoparticles, and **(c)** β-1,3-Glucan surface-functionalized CS-PCL nanoparticles. The images illustrate smooth, spherical, and well-segregated nanoparticles at varying magnifications. The observed particle sizes correspond closely with those obtained from DLS analyses, as presented in **Figure 3.1** and **3.2**, confirming the consistency in size distribution and morphology across different characterisation techniques. 73

Figure 3.4: Percentage degree of β-1,3-Glucan functionalisation of CS-PCL nanoparticles as a function of time (n = 3, mean ± SD). Statistical significance between 12 hours and other groups is indicated as *** (very significant, $p < 0.001$). 75

Figure 3.5: FTIR spectra analysis illustrating the molecular composition and transitions. **(a)** Comparison between excipient pristine polymers and the formulated CS-PCL nanoparticles, highlighting the characteristic peaks and indicative of polymer hybridisation. **(b)** Spectra of the formulated CS-PCL nanoparticles, excipient drugs, and the drug-loaded nanoparticles (CS-PCL-VITD3/RIF) demonstrating the incorporation of active ingredients and the resulting molecular interactions. The spectra reveal shifts and intensity changes that confirm the integration of the bioactive agents into the polymer matrix. 76

Figure 3.6: FTIR Spectra of Pristine β-1,3-Glucan (Glu), Functionalized (Glu-CS-PCL), and Non-Functionalized (CS-PCL) Nanoparticles: Demonstrating Molecular Composition and Transitions upon Surface Functionalization. 77

Figure 3.7: XRD Diffractograms of **(a)** Excipient Materials, **(b)** Formulated Nanoparticles with and without Drug Encapsulation, and **(c)** Pristine β-1,3-Glucan, Functionalized, and Non-Functionalized Nanoparticles: Illustrating the Crystallinity of Formulated Nanoparticles. 79

Figure 3.8: Thermogravimetric Analysis of Excipient Materials and Nanoparticles: Degradation Temperatures of Formulated Nanoparticles. 80

Figure 3.9: DSC Thermograms of **(a)** Formulated CS-PCL Nanoparticles and Excipient Polymers, **(b)** Formulated Nanoparticles with Excipient Drugs/Bioactives, and **(c)** β-1,3-Glucan and Glucan-Functionalized CS-PCL Nanoparticles. Illustrating the Good Miscibility of Pristine Drugs and Their Interaction with the Nanoparticle's Matrix. 82

Figure 3.10: Cumulative release of VITD3 from **(a)** CT-PCL-VITD3 and **(b)** Glu-CS-PCL-VITD3 nanoparticles over 48 hours at different pH levels (pH 4.6, 6.8, and 7.4) at 37°C, highlighting sustained and pH-dependent release profiles (n = 3, mean ± SD). 85

Figure 3.11: Cumulative release of RIF from **(a)** CT-PCL-RIF and **(b)** Glu-CS-PCL-RIF nanoparticles over 48 hours at different pH levels (pH 4.6, 6.8, and 7.4) at 37°C, highlighting sustained and pH-dependent release profiles (n = 3, mean ± SD). 87

Figure 3.12: MTT assay measurement of the viability of RAW 264.7 murine macrophage cells after 48-hour treatment with free RIF, VITD3, CS-PCL and VITD3/RIF CS-PCL nanoparticles at different concentrations (n = 3, mean ± SD). The horizontal line at 80% represents the threshold for non-toxic effects. 89

Figure 3.13: MTT assay measurement of RAW 264.7 cell viability after 48-hour treatment with pristine β-1,3-Glucan and β-1,3-Glucan functionalised nanoparticles at different concentrations (n = 3, mean ± SD). The horizontal line at 80% represents the threshold for non-toxic effects. 90

Figure 4.1: Relative Fluorescence Units (RFU) of Reactive Oxygen Species (ROS) generation in RAW 264.7 macrophage cells after 24-hour treatment with 36 µg/mL of RIF pristine drug solution and 145 µg/mL of different RIF nanoparticle solutions. Data is presented as mean ± SD. Statistical significance between groups is indicated as follows: n.s. (not significant, $p > 0.05$); and *** (very significant, $p < 0.001$). 104

Figure 4.2: Relative Fluorescence Units (RFU) of Reactive Oxygen Species (ROS) generation in RAW 264.7 cells after 24-hour treatment with 36 µg/mL of VITD3 pristine drug solution and 145 µg/mL of different VITD3 nanoparticle solutions, respectively. Data is presented as mean ± SD. 105

Statistical significance between groups is indicated as follows: n.s. (not significant, $p > 0.05$); and *** (very significant, $p < 0.001$).

Figure 4.3: Concentration of TNF-α in RAW 264.7 macrophage cells following 24-hour treatment with 145 µg/mL and 36 µg/mL of **(a)** VITD3 nanoparticles and VITD3 pristine drug solution, and **(b)** RIF nanoparticles and RIF pristine drug solution, respectively. Data is presented as mean ± SD. Statistical significance compared between groups is indicated as follows: **** (highly significant, $p < 0.01$) and *** (very significant, $p < 0.001$). 106

Figure 4.4: Concentration of IFN-gamma in RAW 264.7 cells following 24-hour treatment with 145 µg/mL and 36 µg/mL of **(a)** VITD3 nanoparticles and VITD3 pristine drug solution, and **(b)** RIF nanoparticles and RIF pristine drug solution, respectively. Data is presented as mean ± SD. Statistical significance between groups is indicated as n.s (non-significant, $p > 0.05$). 107

Figure 4.5: Concentration of IL-4 in RAW 264.7 cells following 24-hour treatment with 145 µg/mL and 36 µg/mL of **(a)** RIF nanoparticles and RIF pristine drug solution, and **(b)** VITD3 nanoparticles and VITD3 pristine drug solution, respectively. Data is presented as mean ± SD. Statistical significance compared to the control is indicated as ### (very significant, $p < 0.001$), # (significant, $p > 0.05$) and statistical significance between groups is shown as * (significant, $p < 0.05$). 109

Figure 4.6: Concentration of IL-10 in RAW 264.7 cells following 24-hour treatment with 145 µg/mL and 36 µg/mL of **(a)** VITD3 nanoparticles and VITD3 pristine drug solution, and **(b)** RIF nanoparticles and RIF pristine drug solution, respectively. Data is presented as mean ± SD. Statistical significance between groups is indicated as n.s (non-significant, $p > 0.05$). 110

Figure 4.7: Morphological Comparison of RAW 264.7 Macrophage Cell Line in Untreated and Treated Conditions. The untreated group displays a typical round, smooth, small morphology with a uniform appearance (characteristic of the M0 phenotype). The treated group exhibits an enlarged, elongated, irregular shape with pronounced cytoplasmic extensions, typical of the M1 phenotype. Some cells in the treated group are oval-shaped, 111

indicating partial differentiation towards the M2 phenotype at different magnifications.

Figure 5.1: Intracellular survival of *M. tuberculosis* H37Rv in macrophages. Activated THP1 cells were infected with H37Rv bacterial cells and treated with 7 different formulations. Rifampicin was included as the control. Survival was monitored by enumerating colony-forming units (CFU/ml) after 5 days of incubation. Data is presented as mean ± SD. Statistical significance compared to the control is indicated as ** (Highly significant, $p < 0.05$), * (significant, $p > 0.05$). 133

Figure 6.1: Spectroscopic and Crystallographic Analysis of the Hydrogel and Nanocomposite. **(a)** FTIR spectra of the hydrogel blend and the nanocomposite, showing similar absorption peaks at 2879, 1342, and 1096 cm^{-1} and **(b)** XRPD patterns of the nanocomposite, hydrogel and excipient materials, demonstrating semi-crystalline structures with major peaks at 19.07º and 23.31º, indicative of retained physical phases and degree of crystallinity similar of the starting materials. 147

Figure 6.2: Thermal Analysis of Hydrogel and Nanocomposite. **(a)** TGA curves showing the thermal stability of the hydrogel and nanocomposite and **(b)** DSC thermograms showing the melting peaks of the hydrogel and nanocomposite at 55.18°C and 55.14°C, respectively. 149

Figure 6.3: Surface Morphology and Isotherm Analysis of Hydrogel and Nanocomposite. SEM images showing the surface morphology of **(a)** pure hydrogel and **(b)** nanocomposite hydrogel; Isotherm linear plots of **(c)** pure hydrogel before incorporation with nanoparticles and **(d)** nanocomposite hydrogel, indicating changes in adsorption and Desorption due to nanoparticle incorporation. 151

Figure 6.4: Shows elastic modulus rheogram as a function of temperature and gelation temperature for **(a)** Pure Pluronic hydrogel and **(b)** nanocomposite hydrogel containing 10% of nanoparticles. 153

Figure 6.5: Test Tube Inversion and Rheological Analysis of Sol-Gel Transition: **(a)** Test tube inversion method showing the sol-gel transition of the pure hydrogel. **(b)** Test tube inversion method showing the sol-gel transition of the nanocomposite hydrogel. 154

(c) Elastic modulus rheogram as a function of temperature, depicting the gelation temperature for the nanocomposite hydrogel with 20% nanoparticles, illustrating an increase in gelation temperature from **Figure 6.5b** with the further addition of nanoparticles.

Figure 6.6: Cumulative release profiles of **(a)** VITD3 and **(b)** RIF from nanoparticles incorporated into a Pluronic hydrogel (nanocomposite) over 12 days at different pH levels (4.8, 6.8, and 7.4) at 37°C. The cumulative release of VITD3 was significantly higher at pH 4.8, reaching approximately 30% by day 12. At pH 6.8 and pH 7.4, the release was lower, reaching around 20% and just over 10%, respectively. The cumulative release of RIF was also highest at pH 4.8, reaching approximately 45% by day 12. The release at pH 6.8 was around 35%, and at pH 7.4, it was approximately 25%. The results are presented as mean ± SD (n = 3). 156

Figure 6.7: MTT assay measurement of RAW 264.7 cell viability and cytocompatibility after 48-hour treatment with different concentrations of the hydrogel and nanocomposites. The results are presented as mean ± SD (n = 3). 158

LIST OF TABLES

Table 2.1:	A summary of other potential HDT-TB drugs targeting autophagy and their mechanism of action.	32
Table 2.2:	A brief overview of distinct classes of nanostructures as drug delivery vehicles with desirable features employed to deliver host-directed therapeutics and their limitations.	35
Table 2.3:	Detailed results from Sharma et al., 2018 showing the total number of Mtb CFU recovered after dose- and time-dependent treatment with bare and encapsulated MIAP and INH in a Colony Forming Assay (Reprinted from Sharma et al., 2018, with permission).	39
Table 2.4:	Summary of anti-mycobacterial nanoparticle-based carriers that can be employed for HDT-TB.	43
Table 3.1:	DLS properties of CS-PCL unloaded, loaded, functionalised and non-functionalized nanoparticles, and the drug loading capacity and entrapment efficiency.	71
Table 3.2:	Stability profile of formulated nanoparticles as a function of time using DLS at room storage temperature.	83
Table 5.1:	Minimum Inhibitory Concentration of Nanoparticle Formulations Against Susceptible *Mycobacterium tuberculosis*, H37Rv.	127
Table 5.2:	Minimum Inhibitory Concentration of Nanoparticle Formulations Against Drug-Resistant *Mycobacterium tuberculosis* MDR11 Strain.	129
Table 5.3:	Concentration of nanoparticles and drug equivalent concentration used to treat H37Rv-infected THP-1 cells.	131
Table 5.4:	Intracellular Survival of M.tuberculosis H37Rv in THP-1 Macrophage-like cells Treated with various nanoparticle formulations.	134
Table 7.1:	General Comparative Summary of Reported TB Drug Delivery Systems and the Developed 1,3-β-Glu-CS-PCL Nanoparticles.	164

LIST OF EQUATIONS

Equation 3.1:	% EE	66
Equation 3.2:	% LC	67
Equation 3:3:	% Cell viability	12
Equation 6.1:	% Cell viability	70

LIST OF ABBREVIATIONS

1,25D	1,25-dihydroxy vitamin D3
AMs	Alveolar Macrophages
AICs	Autophagy-Inducing Compounds
ATGs	Autophagy-related genes
AuPd	Gold-palladium
A_q	Absorbance Drug
BET	Brunauer-Emmett-Telle
BPaL	Bedaquiline, Pretomanid and Linezolid
CFU	Colony Forming Unit
CMI	Cell-Mediated Immune
COVID19	Corona Virus Disease of 2019
CS	Chitosan
DCM	Dichloromethane
DDW	Double-distilled Water
DEFB4	Beta-defensin-4
DLS	Dynamic Light Scattering
DMEM	Dulbecco's Modified Eagle Medium
DSC	Differential Scanning Calorimeter
EE	Entrapment Efficacy
ELISA	Enzyme-Linked Immunosorbent Assay
EMB	Ethambutol
F68	Pluronic F68
F127	Pluronic F127
FTIR	Fourier Transform Infrared Spectroscopy
Glu	1,3-beta Glucan
H37Rv	Susceptible Mtb Strain
HDT	Host-directed Therapy
HIV	Human Immunodeficiency Virus
HRTEM	High-Resolution Transmission Electron Microscopy
IFN-γ	Interferon Gamma
IL-10	Interlukin-10
IL-4	Interlukin-4
INH	Isoniazid
LC	Loading capacity

M1	Classically Activated Macrophages
M2	Alternatively Activated Macrophages
mBar	Millibar
MDR	Multi-Drug Resistance
MDR-TB	Multi-Drug-Resistant Tuberculosis
MIC	Minimum Inhibitory Concentration
Mtb	Mycobacterium Tuberculosis
MTT	3-(4,5-dimethyl thiazole-2-yl)-2,5-diphenyl tetrazolium bromide
NPs	Nanoparticles
PAMPs	Pathogen-associated molecular patterns
PBS	Phosphate Buffered Saline
PCL	Polycaprolactone
PDI	Polydispersity Index
PRRs	Pattern Recognition Receptors
PVA	Polyvinyl alcohol
RAW 264.7	Mouse Monocyte Macrophage Cell Line
RFU	Relative Fluorescence Units
RIF	Rifampicin
RONS	Reactive Oxygen and Nitrogen Species
ROS	Reactive Oxygen Species
SEM	Scanning Electron Microscopy
STD	Standard Deviation
TB	Tuberculosis
TEM	Transmission Electron Microscopy
TGA	Thermogravimetric Analyzer
THP-1	Human leukaemia Monocytic Cell Line
TNF-α	Tumour Necrosis Factor-Alpha
VITD3	Vitamin D3
w/v	Weight by volume
WHO	World Health Organization
XDR	Extensively-Drug Resistant
XRPD	X-ray Powder Diffractometer
ZP	Zeta Potential

CHAPTER 1

INTRODUCTION AND BACKGROUND

1.1. Background of the Study

Tuberculosis (TB), caused by Mycobacterium tuberculosis (Mtb), is considered one of the deadliest infectious diseases throughout the world (Yunus Basha et al., 2019, Clemens et al., 2012). Tuberculosis infects approximately 33% of the world's population and causes about 1.7 million deaths yearly (Yunus Basha et al., 2019). The disease remains a significant health challenge across the globe and In South Africa, which is among the eight countries with the highest burden of TB, TB/HIV co-infection, and multi-drug-resistant TB (MDR-TB) (Organization, 2019, Organization, 2021). Approximately 280,000 people in South Africa were infected with TB, with over 25,000 TB-related deaths in 2022 (Foster et al., 2024, Organization, 2022). Across the African continent, the situation is similarly concerning, with 2.5 million people having contracted TB and accounting for a quarter of new TB cases reported in 2022 (Organization, 2022). Efforts to combat TB across the globe have been severely hampered by various factors, including the COVID-19 pandemic, which disrupted TB control programs and led to an increase in both TB cases and deaths (Organization, 2021, Khoza et al., 2022).

Mtb is primarily transmitted through the air, making it an airborne pathogen. When an infected person coughs, sneezes or speaks, tiny droplets containing the bacteria are released into the air and can be inhaled by others (Bussi and Gutierrez, 2019). Once inhaled, Mtb enters the respiratory system, where it is taken up by alveolar macrophages (AMs), the immune cells responsible for engulfing and destroying pathogens (Bussi and Gutierrez, 2019). Suppose the immune response is weakened to eliminate the initial infection; In that case, the Mtb bacilli replicate within the host (AMs), leading to disease infection progression (Guirado et al., 2013, Queval et al., 2017, Rajaram et al., 2014). The infected AM cells respond by producing pro-inflammatory cytokines and chemokines that attract other phagocytic cells (dendritic cells, neutrophils, and monocyte cells) and subsequently forming a granulomatous structure known as tubercle to contain Mtb (Ernst, 2012, Wani, 2013, Kumar, 2016).

However, Mtb has evolved mechanisms to survive and replicate within these cells, leading to the establishment of infection (Maphasa et al., 2020). If bacterial growth is not adequately controlled, the tubercle enlarges and spreads to the draining lymph nodes, causing lesions in the lymph node and lung parenchyma, which can result in the clinical manifestation of primary TB infection (Kumar, 2016, Wani, 2013). Within ten weeks, an effective cell-mediated immune

(CMI) response typically develops; however, if this response is insufficient, further lung damage occurs, and the infection may progress to disseminated TB through haematogenous spread, making the host infectious to others (Wani, 2013). HIV infection exacerbates this risk by reducing $CD4^+$ T cells, which are crucial for TB immunity, thereby increasing the likelihood of rapid progression and reactivation of latent TB infection (Kumari and Meena, 2014).

The treatment of TB follows the standard guidelines outlined by the World Health Organisation (WHO), which consists of the following combination of first-line anti-TB drugs (acronym RIPE): rifampicin (RIF), isoniazid (INH), pyrazinamide (PZA), and ethambutol (EMB) (Horsburgh et al., 2015, Nasiruddin et al., 2017, Costa et al., 2016). The recommended treatment plan involves the daily administration of all first-line drugs (RIPE) for the initial two months, which is followed by daily administration of INH and RIF for a further four months (WHO, 2020). However, this treatment plan often faces challenges, including poor patient compliance due to the lengthy 4-6-month multidrug therapy, severe side effects and increased pill burden from co-morbidities (Costa et al., 2016, Dartois, 2014). This often results in patient withdrawal before the course of treatment is completed, resulting in treatment failure and the subsequent development of drug-resistant strains, such as MDR-TB, which is resistant to both RIF and INH, and extensively drug-resistant (XDR) TB, which is MDR-TB that shows resistance to at least one second-line drug, such as amikacin, capreomycin, or kanamycin, and any fluoroquinolone (Organization, 2017, Koch et al., 2018, Dartois, 2014).

The development of TB-resistant strains is a global threat in the fight against TB. It is one of the significant contributors to the limitations of the current anti-TB treatment regime (Mishra et al., 2020, Koch et al., 2018). Besides developing resistant strains, the difficulty of managing TB comes from the fact that several anti-TB drugs fail to reach the lungs and penetrate the AMs when administered systematically (Andrade et al., 2013, Pandey and Khuller, 2005). Recently, new drugs such as delamanid and bedaquiline have been used increasingly in the treatment of MDR and XDR-TB; however, they are recommended to be only used under strict and specific conditions by WHO (Migliori et al., 2017). They are effective in shortening the treatment plan and significantly improving treatment outcomes; however, concerns remain regarding the potential for cardiotoxicity, which arises from drug-drug interactions (Migliori et al., 2017).

Another recently approved novel regimen by the U.S Food and Drug Administration (FDA) in 2019, consisting of bedaquiline, pretomanid, and linezolid (BPaL), has demonstrated high efficacy against drug-resistant TB, particularly in cases of non-responsive MDR and XDR-TB (Holger et al., 2024, Deb and Biswas, 2021). Clinical trials have demonstrated that the BPaL

regimen can achieve high cure rates; for example, the Nix-TB trial conducted in South Africa reported a cure rate of approximately 90% in patients with XDR-TB (Motta et al., 2024, Gomez et al., 2021). The treatment showed favourable outcomes in relatively short periods, typically lasting six months, shorter than many traditional XDR-TB (Motta et al., 2024). Despite its effectiveness, linezolid toxicities, such as myelosuppression, neuropathy, and gastrointestinal disturbances, are frequently reported (Bigelow et al., 2020). These toxicities often necessitate dose adjustments or even discontinuation of the treatment, which can compromise treatment success (Bigelow et al., 2020).

However, the cost of the individual drugs, bedaquiline, pretomanid, and linezolid, can be high, particularly bedaquiline and pretomanid, which are newer and patented drugs (Otto-Knapp et al., 2024). This higher cost imposes a significant barrier to access, especially in low and middle-income countries where the burden of drug-resistant TB is often the highest (Gomez et al., 2021). Efforts have been made to negotiate lower prices and increase access to these drugs, particularly in high-burden countries (Gomez et al., 2021). Global health organisations, such as the Global Drug Facility, have made the regimen more affordable through subsidies and agreements with pharmaceutical companies (Gomez et al., 2021). However, the cost remains a challenge that hinders access to patients who need this treatment

To mitigate the limitations and drawbacks associated with current TB treatment regimens, cost-effective strategies are being explored, particularly those focusing on repurposing existing medications and developing innovative therapeutic approaches. One such area of research is host-directed therapy (HDT), which aims to enhance the host's immune response to combat TB more effectively using repurposed drugs or biologics (Zhao et al., 2023, Khoza et al., 2022). Repurposing drugs that are already approved for other conditions presents a promising avenue through HDT to improve TB treatment outcomes while potentially reducing the costs and time associated with developing new TB-specific medications (Young et al., 2020). HDT works by enhancing specific immune responses that are typically suppressed or manipulated by the Mtb pathogen rather than directly attacking the bacteria; for instance, it can activate pathways that promote the destruction of infected cells or inhibit the pathogen's ability to evade the immune system (Khoza et al., 2022, Young et al., 2020).

This approach not only boosts the host's ability to combat the infection but also reduces the reliance on conventional antibiotics, which can be particularly beneficial in managing drug-resistant TB strains (Maphasa et al., 2020, Kilinc et al., 2021). Moreover, HDT can address the complex challenges of TB-HIV co-infection. In patients with both TB and HIV, HDT may reduce the risks associated with drug-drug interactions between anti-TB and antiretroviral

medications, leading to safer and more effective treatment options (Zumla et al., 2015). Combining HDT with standard anti-TB drug regimens may also shorten the duration of treatment, decrease the likelihood of developing further drug resistance, and improve overall treatment outcomes (Singh, 2024). Additionally, this combination strategy could reduce the chances of relapse, offering a more durable cure for TB patients (Zumla et al., 2015).

Along with HDT, integrating nanotechnology into TB treatment is also emerging as a transformative field. Nanotechnology-based drug delivery systems have the potential to enhance the bioavailability and targeted delivery of TB drugs, ensuring that higher concentrations of the medication reach the infected tissues while minimising systemic side effects (Maretti et al., 2017, Zazo et al., 2016, Dobrovolskaia et al., 2016, Andrade et al., 2013, Andrade et al., 2011, Kumar et al., 2023). This targeted approach not only improves the efficacy of the treatment but also allows for lower doses of drugs to be used, further reducing the risk of toxicity and the overall cost of therapy (Kumar et al., 2023). These fields (HDT and nanotechnology) represent a synergistic strategy that could revolutionise TB treatment. By leveraging existing drugs in novel ways and incorporating advanced delivery systems, these approaches aim to overcome the challenges of drug resistance, toxicity, and treatment duration, ultimately leading to more effective, affordable, and accessible TB therapies.

1.2. Rationale and Motivation for the Study

The clinical management of tuberculosis continues to pose a significant challenge to global public health due to a multitude of factors. Recently, it has become evident that many of the currently approved anti-TB therapeutics have diminished efficacy or have become ineffective in eradicating this persistent global burden (Singh et al., 2020, Khoza et al., 2022). As of the latest data from the WHO, in 2022, an estimated 10.6 million people fell ill with TB, and it accounts for over 1.5 million deaths yearly (Organization, 2021, Bagcchi, 2023). Unfortunately, TB remains a significant health challenge, with 1.3 million deaths reported in 2022, including 167,000 people with HIV (Bagcchi, 2023). The rise of drug-resistant strains further significantly contributes to the problem despite the availability and effectiveness of current anti-TB drugs (Shehzad et al., 2013, Dartois and Rubin, 2022).

The limitations of current anti-TB therapeutics are further exacerbated by the extended treatment duration, which comes with severe side effects, such as hepatotoxicity, ototoxicity, and nephrotoxicity (Shehzad et al., 2013, Ma et al., 2010). These adverse effects contribute to patient non-compliance, exacerbating the challenge of effective TB management. Co-

infection with HIV introduces additional complications due to drug-drug interactions, leading to overlapping severe side effects and further reducing patient adherence to treatment plans due to increased medication burden (Singh et al., 2020, Shehzad et al., 2013). Various pharmacokinetic factors, including gastrointestinal degradation, low drug solubility, reduced drug concentration, and low cellular permeability, hinder the bioavailability of current anti-TB therapeutics (Kumar et al., 2023, Abdelgawad et al., 2022). Co-infection, particularly TB-HIV, leads to intestinal malabsorption of anti-TB drugs, further reducing their bioavailability and effectiveness (Butov, 2020). Making altered bioavailability one of many significant limitations of current anti-TB drugs. Given these substantial limitations, an urgent need is to develop advanced drug delivery systems that can enhance TB pharmacotherapy. These systems should possess immunomodulatory and host-directed therapy capabilities while ensuring the targeted delivery of anti-TB bioactives to the host.

Nanoparticles present a promising solution due to their unique properties as drug carriers, including improved bioavailability, stability, targeted delivery, and reduced side effects (Joudeh and Linke, 2022, Chandrakala et al., 2022). Another significant advantage of nanoparticles is their ability to be finely tuned to enhance the response of host cells, thereby facilitating host-directed therapy. Nanoparticles can be engineered with precise control over their size, shape, surface charge, and functionalisation, allowing for a customised interaction with specific cell types, such as macrophages and dendritic cells, which play crucial roles in the immune response against TB (Khoza et al., 2022, Maphasa et al., 2020). By modulating these physical and chemical properties, nanoparticles can be designed to improve cellular uptake, ensure controlled release of encapsulated bioactives, and enhance intracellular trafficking to specific subcellular compartments where the therapeutic action is most effective (Mitchell et al., 2021). This level of customisation is particularly beneficial in HDT, as it allows for the modulation of the host's immune system to recognise better, respond to, and eliminate the Mtb pathogen without solely relying on direct antimicrobial activity (Khoza et al., 2022). Moreover, the surface of nanoparticles can be functionalised with ligands that target specific receptors on immune cells, such as dectin-1, enhancing their ability to stimulate a more robust and focused immune response (Dube et al., 2014). This targeted approach not only improves the efficacy of the treatment but also reduces off-target effects and minimises the risk of adverse reactions.

Thus, this present study seeks to address these limitations by fabricating a β-glucan surface-functionalized biopolymeric nanosystem encapsulating anti-TB bioactives such as RIF and Vitamin D3 (1α,25-dihydroxy vitamin D3). β-glucans have a potent immunomodulatory effect on innate and adaptive immune responses (Singh and Bhardwaj, 2023). They bind to dectin-

1 receptors expressed in innate immune response cells such as macrophages, neutrophils, and dendritic cells. This binding triggers an effective immune response, phagocytosis, and pro-inflammatory cytokine production, eliminating infectious agents (Dube et al., 2014, Singh and Bhardwaj, 2023). Functionalising a biopolymeric nanoparticle with β-glucan will enable active targeting and heightened immunomodulatory response of macrophages, improving the activity of anti-TB bioactives by directly transporting them to their target site (alveolar macrophages) while protecting them from premature elimination and enhancing their absorption across biological barriers.

RIF will be a primary anti-TB bioactive encapsulated within the nanosystem due to its potent sterilising effect and high bactericidal action against Mtb in both cellular and extracellular sites (Joshi et al., 2021). This allows for a shorter treatment regime with a high cure. Additionally, Vitamin D3 (VITD3) will be included to facilitate host-directed therapy, further enhancing the host's immune response to control TB progression without directly interacting with the pathogen, potentially preventing the development of drug-resistant TB (Paik et al., 2019). Calcitriol stimulates mycobacterial killing in macrophages by promoting the production of the antimicrobial peptide LL-37 and enhancing autophagy and phagolysosome fusion, thereby improving treatment effectiveness and potentially reducing the treatment duration (Chung et al., 2020, Paik et al., 2019).In conclusion, this functionalised biopolymeric nanosystem (as shown in **Figure 1.1**) is anticipated to play a significant role in TB treatment by providing unique capabilities such as immunomodulatory effects, host-directed therapy, and active targeting of host cells. These benefits will be evaluated through in vitro studies, aiming to offer a more effective and patient-compliant solution to the global TB crisis.

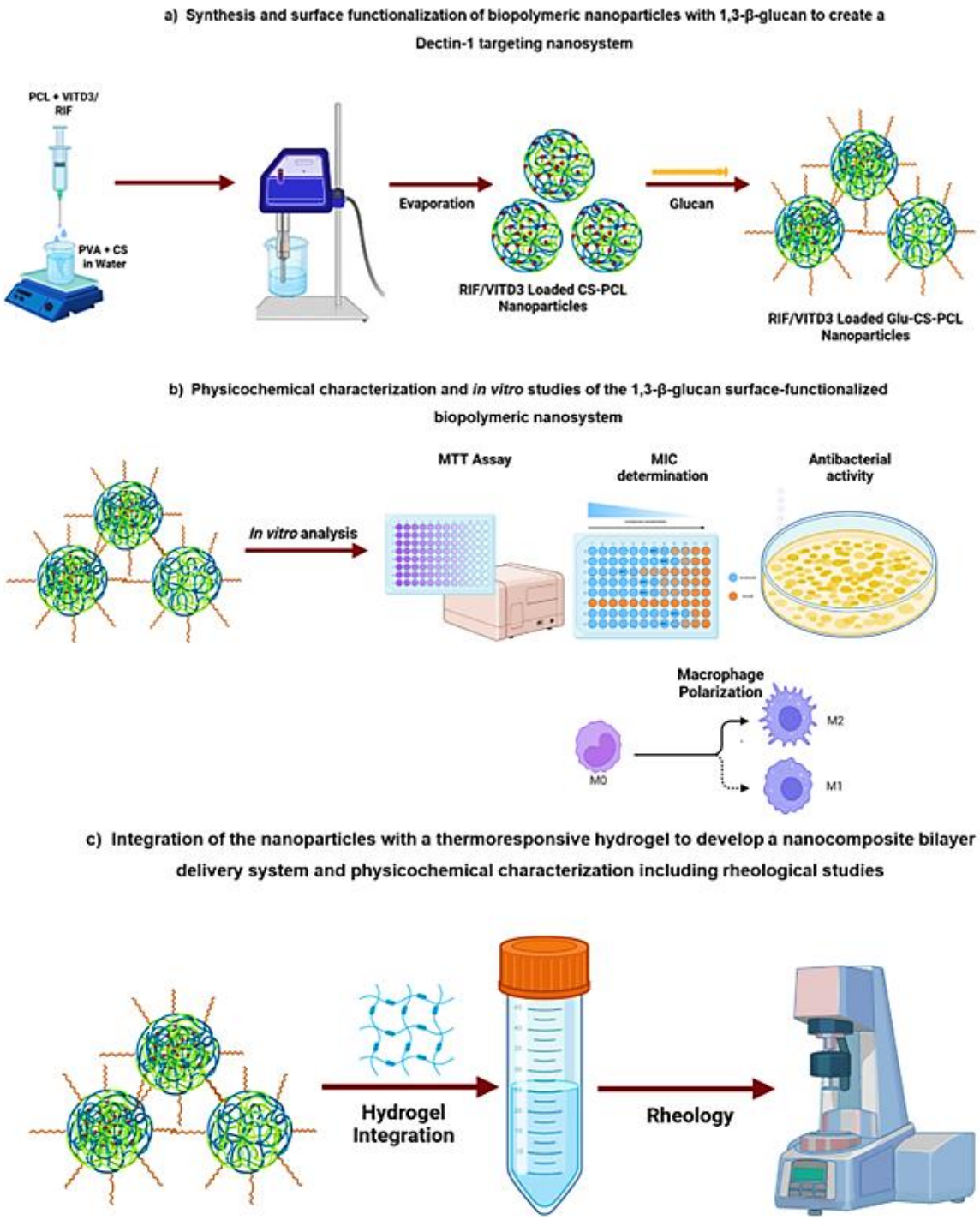

Figure 1.1: Typical Schematic Representation of the Proposed β-Glucan Surface-Functionalized Multifunctional Biopolymeric Nanosystem Synthesis and Characterisations. **a)** Fabrication of chitosan (CS)/polycaprolactone (PCL) nanoparticles encapsulating RIF or VITD3, functionalised with 1,3-β-glucan for Dectin-1 targeting. **b)** Physicochemical characterisation of the nanoparticles, in vitro assessments of cytotoxicity (MTT assay), minimum inhibitory concentration (MIC) against Mtb strains, and bacterial activity, along with evaluation of macrophage polarisation by cytokine production. **c)** Integrating the functionalized nanoparticles with a thermoresponsive hydrogel to develop a nanocomposite bilayer delivery system for controlled drug release. Created by the author using BioRender for academic use and non-publication purposes.

1.3. Aim and objectives

This study aimed to develop a multifunctional, Dectin-1-targeted, surface-functionalised biopolymeric nanosystem for the targeted delivery of anti-tuberculosis bioactives to infected macrophages, and to conduct comprehensive in vitro studies to evaluate its physicochemical properties, immunomodulatory potential, and antimycobacterial activity. To achieve the aim, the following set of objectives were carried out:

1) Fabricated biopolymeric nanoparticle system made of chitosan and polycaprolactone encapsulating RIF or VITD3 using a modified emulsion solvent evaporation method.
2) Functionalised the surface of biopolymeric nanoparticles with 1,3-β-glucan to create a Dectin-1 targeting nanosystem.
3) Characterised the functional transformation, physicochemical properties, size, morphology, and stability of the 1,3-β-glucan surface-functionalised biopolymeric nanoparticles.
4) Determined the loading capacity and encapsulation efficiency of bioactives within the functionalised biopolymeric nanoparticles, followed by an in vitro drug release study as a function of pH.
5) Assessed the *in vitro* cytotoxicity of 1,3-β-glucan surface-functionalised biopolymeric nanoparticles compared to non-functionalized nanoparticles.
6) Quantified the levels of reactive oxygen species (ROS) and pro-inflammatory cytokines (TNF-α, IFN-γ) as well as anti-inflammatory cytokines (IL-4, IL-10) using ELISA kits to ascertain the targeting and polarisation effect of 1,3-β-glucan surface-functionalized biopolymeric nanoparticles. Additionally, studied the morphological changes in macrophages upon treatment.
7) Evaluated the *in vitro* minimum inhibitory concentration (MIC) of 1,3-β-glucan surface-functionalised biopolymeric nanoparticles against Mtb-susceptible strain H37Rv and resistant strain MDR11.
8) Conducted *in vitro* antimycobacterial and cytotoxicity analyses of 1,3-β-glucan surface-functionalized biopolymeric nanoparticles on THP-1 macrophage-like cells infected with the H37Rv TB strain.
9) Integrated the nanoparticles with a thermoresponsive hydrogel to develop a nanocomposite bilayer delivery system.

1.4. Novelty of the study

The novelty of this study lies in integrating three distinct research disciplines, autophagy modulation, host-directed therapy, and nanotechnology, to address the challenges posed by Mycobacterium tuberculosis. While these fields have been explored individually, the unique combination of all three represents an innovative approach that has not been extensively investigated before.

1) The research designed 1,3-β-glucan nanoparticles encapsulating RIF and VITD3 as anti-tuberculosis and autophagy-inducing agents, respectively. These nanoparticles demonstrated excellent stability over a period of three months.

2) The study revealed that the nanoparticles, whether used in combination or individually, could induce macrophage polarisation towards the M1 phenotype, which is vital for microbial killing.

3) The study also showed that combined nanoparticles encapsulating RIF or VITD3 significantly killed Mtb in H37Rv-infected THP-1 activated cells. These nanoparticles exhibited a greater minimum inhibitory concentration even against the resistant Mtb strain MDR11 compared to standard treatments.

4) This study further developed a model dual carrier thermogel system that effectively encapsulates both RIF and VITD3 nanoparticles. This innovative approach serves a dual purpose by combining HDT and bactericidal actions. The dual functionality of the thermogel, along with its model status, provides a significant advancement in the design of nanocomposite delivery systems.

1.5. Overview of the Thesis

The thesis is structured into multiple chapters, each collated to provide a comprehensive understanding of the design and development of a functionalised biopolymeric immunomodulatory nanosystem for the delivery of antituberculosis bioactives.

Chapter 1: This chapter provides a brief introduction and background on the study, the rationale behind the research, the aims and objectives, and outlines the perceived novelty of the study.

Chapter 2: This chapter delves deeper into the rationale behind designing new TB therapeutics, exploring cutting-edge approaches to combat drug-resistant tuberculosis. It examines the challenges posed by drug-resistant TB strains and highlights the limitations of current multidrug therapies. The chapter emphasises the potential of Host-Directed Therapies (HDTs) and autophagy-inducing nanoparticles as innovative strategies to enhance treatment efficacy. By targeting the host's immune response and utilising advanced nanotechnology for precise drug delivery, these approaches aim to overcome drug resistance and improve patient outcomes. The chapter provides a comprehensive overview of these novel therapeutic strategies' mechanisms, benefits, and prospects in the fight against TB.

Chapter 3: This chapter describes the preliminary synthesis and characterisation of 1,3-β-glucan-modified nanoparticles encapsulating rifampicin and vitamin D3 for potential delivery in tuberculosis therapy. It investigates the physicochemical properties of the formulated nanoparticles and their morphology. The stability of the formulated nanoparticles over time and the extent of functionalisation are also assessed. Additionally, the release profile of the nanosystem at different pH levels that simulate physiological environments is examined. The chapter further evaluates the cytotoxicity and biocompatibility of the nanosystem with RAW 264.7 cell lines.

Chapter 4: This chapter evaluates the potential of the synthesised nanoparticles as immunomodulatory agents capable of inducing macrophage polarisation toward the M1 or M2 phenotype. It explores the pro-inflammatory versus anti-inflammatory responses of RAW 264.7 macrophage cells by quantifying intracellular ROS and cytokine levels post-nanoparticle treatment. The potential of the nanosystem to enhance the host's response during the initial stages of infection is also discussed. Additionally, the chapter includes a morphological analysis of the treated cells to assess their physical changes.

Chapter 5: This chapter details the *in vitro* studies of the designed nanoparticles, aiming to determine the minimum inhibitory concentration (MIC) of these nanosystems using two

different Mycobacterium tuberculosis (Mtb) strains: the susceptible H37Rv and the resistant MDR11 strains. The chapter further explores the antitubercular activity of the designed nanoparticles using infected THP-1 macrophage cells with the H37Rv Mtb strain to determine their efficacy.

Chapter 6: This chapter outlines the development of a model dual carrier thermogel system that encapsulates both RIF and VITD3 nanoparticles by incorporating them into a thermogel. This system serves a dual purpose by combining host-directed therapy with bactericidal actions. The thermogel nanocomposite was further characterised based on its physicochemical properties, rheological properties, morphology, and gelation abilities. Additionally, the cytotoxicity of this dual drug delivery system is examined, highlighting its potential as a safe and effective carrier for therapeutic agents.

Chapter 7: This chapter summarises the overall findings of the research study and provides proactive recommendations for further potential pre-clinical investigations on the formulated nanosystems.

1.6. References

Abdelgawad, N., Chirehwa, M., Schutz, C., Barr, D., Ward, A., Janssen, S., et al. Denti, P. 2022. Pharmacokinetics of antitubercular drugs in patients hospitalized with HIV-associated tuberculosis: a population modeling analysis. *Wellcome open research,* 7**,** 72.

Andrade, F., Rafael, D., Videira, M., Ferreira, D., Sosnik, A. & Sarmento, B. 2013. Nanotechnology and pulmonary delivery to overcome resistance in infectious diseases. *Advanced Drug Delivery Reviews,* 65**,** 1816-1827.

Andrade, F., Videira, M., Ferreira, D. & Sarmento, B. 2011. Micelle-based systems for pulmonary drug delivery and targeting. *Drug Delivery Letters,* 1**,** 171-185.

Bagcchi, S. 2023. WHO's Global Tuberculosis Report 2022. *Lancet Microbe,* 4**,** e20.

Bigelow, K. M., Tasneen, R., Chang, Y. S., Dooley, K. E. & Nuermberger, E. L. 2020. Preserved Efficacy and Reduced Toxicity with Intermittent Linezolid Dosing in Combination with Bedaquiline and Pretomanid in a Murine Tuberculosis Model. *Antimicrobial Agents and Chemotherapy,* 64**,** e01178-20.

Bussi, C. & Gutierrez, M. G. 2019. Mycobacterium tuberculosis infection of host cells in space and time. *FEMS microbiology reviews,* 43**,** 341-361.

Butov, D. O. 2020. Malabsorption syndromes in patients with tuberculosis as a cause of ineffective treatment: how to diagnose and overcome? *Infusion & Chemotherapy***,** 24-25.

Chandrakala, V., Aruna, V. & Angajala, G. 2022. Review on metal nanoparticles as nanocarriers: current challenges and perspectives in drug delivery systems. *Emergent Materials,* 5**,** 1593-1615.

Chung, C., Silwal, P., Kim, I., Modlin, R. L. & Jo, E. K. 2020. Vitamin D-Cathelicidin Axis: at the Crossroads between Protective Immunity and Pathological Inflammation during Infection. *Immune network,* 20**,** e12.

Clemens, D. L., Lee, B. Y., Xue, M., Thomas, C. R., Meng, H., Ferris, D., et al. Horwitz, M. A. 2012. Targeted intracellular delivery of antituberculosis drugs to Mycobacterium tuberculosis-infected macrophages via functionalized mesoporous silica nanoparticles. *Antimicrob Agents Chemother,* 56**,** 2535-45.

Costa, A., Pinheiro, M., Magalhaes, J., Ribeiro, R., Seabra, V., Reis, S. & Sarmento, B. 2016. The formulation of nanomedicines for treating tuberculosis. *Adv Drug Deliv Rev,* 102**,** 102-15.

Dartois, V. 2014. The path of anti-tuberculosis drugs: from blood to lesions to mycobacterial cells. *Nat Rev Microbiol,* 12**,** 159-67.

Dartois, V. A. & Rubin, E. J. 2022. Anti-tuberculosis treatment strategies and drug development: challenges and priorities. *Nat Rev Microbiol,* 20**,** 685-701.

Deb, U. & Biswas, S. 2021. Pretomanid: The latest USFDA-approved anti-tuberculosis drug. *Indian J Tuberc,* 68**,** 287-291.

Dobrovolskaia, M. A., Shurin, M. & Shvedova, A. A. 2016. Current understanding of interactions between nanoparticles and the immune system. *Toxicology and Applied Pharmacology,* 299**,** 78-89.

Dube, A., Reynolds, J. L., Law, W. C., Maponga, C. C., Prasad, P. N. & Morse, G. D. 2014. Multimodal nanoparticles that provide immunomodulation and intracellular drug delivery for infectious diseases. *Nanomedicine : nanotechnology, biology, and medicine,* 10**,** 831-8.

Ernst, J. D. 2012. The immunological life cycle of tuberculosis. *Nature Reviews Immunology,* 12**,** 581-591.

Foster, I., Biewer, A., Vanqa, N., Makanda, G., Tisile, P., Hayward, S. E., et al. Nathavitharana, R. R. 2024. "This is an illness. No one is supposed to be treated badly": community-based stigma assessments in South Africa to inform tuberculosis stigma intervention design. *BMC Glob Public Health,* 2**,** 41.

Gomez, G. B., Siapka, M., Conradie, F., Ndjeka, N., Garfin, A. M. C., Lomtadze, N., et al. Vassall, A. 2021. Cost-effectiveness of bedaquiline, pretomanid and linezolid for treatment of extensively drug-resistant tuberculosis in South Africa, Georgia and the Philippines. *BMJ Open,* 11**,** e051521.

Guirado, E., Schlesinger, L. S. & Kaplan, G. 2013. Macrophages in tuberculosis: friend or foe. *Seminars in Immunopathology,* 35**,** 563-583.

Holger, D. J., Althubyani, A., Morrisette, T., Rebold, N. & Tailor, M. 2024. Updates in pulmonary drug-resistant tuberculosis pharmacotherapy: A focus on BPaL and BPaLM. *Pharmacotherapy,* 44**,** 268-282.

Horsburgh, C. R., Barry, C. E. & Lange, C. 2015. Treatment of Tuberculosis. *New England Journal of Medicine,* 373**,** 2149-2160.

Joshi, S., Yadav, D. & Yadav, R. 2021. Fluoroquinolones: a review on anti-tubercular activity. *Monatshefte für Chemie - Chemical Monthly,* 152**,** 881-894.

Joudeh, N. & Linke, D. 2022. Nanoparticle classification, physicochemical properties, characterization, and applications: a comprehensive review for biologists. *Journal of Nanobiotechnology,* 20**,** 262.

Khoza, L. J., Kumar, P., Dube, A., Demana, P. H. & Choonara, Y. E. 2022. Insights into innovative therapeutics for drug-resistant tuberculosis: Host-directed therapy and autophagy inducing modified nanoparticles. *International journal of pharmaceutics,* 622**,** 121893.

Kilinc, G., Saris, A., Ottenhoff, T. H. M. & Haks, M. C. 2021. Host-directed therapy to combat mycobacterial infections. *Immunol Rev,* 301**,** 62-83.

Koch, A., Cox, H. & Mizrahi, V. 2018. Drug-resistant tuberculosis: challenges and opportunities for diagnosis and treatment. *Curr Opin Pharmacol,* 42**,** 7-15.

Kumar, M., Virmani, T., Kumar, G., Deshmukh, R., Sharma, A., Duarte, S., et al. Fonte, P. 2023. Nanocarriers in Tuberculosis Treatment: Challenges and Delivery Strategies. *Pharmaceuticals (Basel, Switzerland),* 16.

Kumar, P. 2016. Adult pulmonary tuberculosis as a pathological manifestation of hyperactive antimycobacterial immune response. *Clinical and Translational Medicine,* 5**,** 38.

Kumari, P. & Meena, L. S. 2014. Factors Affecting Susceptibility to Mycobacterium tuberculosis: a Close View of Immunological Defence Mechanism. *Applied Biochemistry and Biotechnology,* 174**,** 2663-2673.

Ma, Z., Lienhardt, C., Mcilleron, H., Nunn, A. J. & Wang, X. 2010. Global tuberculosis drug development pipeline: the need and the reality. *Lancet,* 375**,** 2100-9.

Maphasa, R. E., Meyer, M. & Dube, A. 2020. The Macrophage Response to Mycobacterium tuberculosis and Opportunities for Autophagy Inducing Nanomedicines for Tuberculosis Therapy. *Front Cell Infect Microbiol,* 10**,** 618414.

Maretti, E., Costantino, L., Rustichelli, C., Leo, E., Croce, M. A., Buttini, F., et al. Iannuccelli, V. 2017. Surface engineering of Solid Lipid Nanoparticle assemblies by methyl α-d-mannopyranoside for the active targeting to macrophages in anti-tuberculosis inhalation therapy. *International journal of pharmaceutics,* 528**,** 440-451.

Migliori, G. B., Pontali, E., Sotgiu, G., Centis, R., D'ambrosio, L., Tiberi, S., et al. Esposito, S. 2017. Combined Use of Delamanid and Bedaquiline to Treat Multidrug-Resistant and Extensively Drug-Resistant Tuberculosis: A Systematic Review. *International Journal of Molecular Sciences,* 18**,** 341.

Mishra, R., Krishan, S., Siddiqui, A. N., Kapur, P., Khayyam, K. U. & Sharma, M. 2020. Potential role of adjuvant drugs on efficacy of first line oral antitubercular therapy: Drug repurposing. *Tuberculosis,* 120**,** 101902.

Mitchell, M. J., Billingsley, M. M., Haley, R. M., Wechsler, M. E., Peppas, N. A. & Langer, R. 2021. Engineering precision nanoparticles for drug delivery. *Nat Rev Drug Discov,* 20**,** 101-124.

Motta, I., Boeree, M., Chesov, D., Dheda, K., Gunther, G., Horsburgh, C. R., Jr., et al. Infectious, D. 2024. Recent advances in the treatment of tuberculosis. *Clin Microbiol Infect,* 30**,** 1107-1114.

Nasiruddin, M., Neyaz, M. K. & Das, S. 2017. Nanotechnology-Based Approach in Tuberculosis Treatment. *Tuberc Res Treat,* 2017**,** 4920209.

Organization, W. H. 2017. Global tuberculosis report 2017.

Organization, W. H. 2019. *Global tuberculosis report 2019,* Geneva, World Health Organization.

Organization, W. H. 2021. Global tuberculosis report 2021.

Organization, W. H. 2022. Global tuberculosis report 2021.

Otto-Knapp, R., Edwards, S., Kuchukhidze, G., Kroger, S., Hacker, B., Bivol, S. & Yedilbayev, A. 2024. Availability of drugs for the treatment of multidrug-resistant/rifampicin-resistant tuberculosis in the World Health Organization European Region, October 2023. *Euro surveillance : bulletin Europeen sur les maladies transmissibles = European communicable disease bulletin,* 29.

Paik, S., Kim, J. K., Chung, C. & Jo, E. K. 2019. Autophagy: A new strategy for host-directed therapy of tuberculosis. *Virulence,* 10**,** 448-459.

Pandey, R. & Khuller, G. K. 2005. Antitubercular inhaled therapy: opportunities, progress and challenges. *Journal of Antimicrobial Chemotherapy,* 55**,** 430-435.

Queval, C. J., Brosch, R. & Simeone, R. 2017. The Macrophage: A Disputed Fortress in the Battle against Mycobacterium tuberculosis. *Frontiers in Microbiology,* 8.

Rajaram, M. V. S., Ni, B., Dodd, C. E. & Schlesinger, L. S. 2014. Macrophage immunoregulatory pathways in tuberculosis. *Seminars in Immunology,* 26**,** 471-485.

Shehzad, A., Rehman, G., Ul-Islam, M., Khattak, W. A. & Lee, Y. S. 2013. Challenges in the development of drugs for the treatment of tuberculosis. *Braz J Infect Dis,* 17**,** 74-81.

Singh, R., Dwivedi, S. P., Gaharwar, U. S., Meena, R., Rajamani, P. & Prasad, T. 2020. Recent updates on drug resistance in Mycobacterium tuberculosis. *Journal of applied microbiology,* 128**,** 1547-1567.

Singh, R. P. & Bhardwaj, A. 2023. beta-glucans: a potential source for maintaining gut microbiota and the immune system. *Front Nutr,* 10**,** 1143682.

Singh, V. 2024. Tuberculosis treatment-shortening. *Drug Discov Today,* 29**,** 103955.

Wani, R. L. S. 2013. Tuberculosis 2: Pathophysiology and microbiology of pulmonary tuberculosis. *South Sudan Medical Journal,* 6**,** 10-12.

Who 2020. Global Tuberculosis Report. 2020.

Young, C., Walzl, G. & Du Plessis, N. 2020. Therapeutic host-directed strategies to improve outcome in tuberculosis. *Mucosal Immunol,* 13**,** 190-204.

Yunus Basha, R., T.S, S. K. & Doble, M. 2019. Dual delivery of tuberculosis drugs via cyclodextrin conjugated curdlan nanoparticles to infected macrophages. *Carbohydrate Polymers,* 218**,** 53-62.

Zazo, H., Colino, C. I. & Lanao, J. M. 2016. Current applications of nanoparticles in infectious diseases. *Journal of Controlled Release,* 224**,** 86-102.

Zhao, L., Fan, K., Sun, X., Li, W., Qin, F., Shi, L., et al. Zheng, C. 2023. Host-directed therapy against mycobacterium tuberculosis infections with diabetes mellitus. *Front Immunol,* 14**,** 1305325.

Zumla, A., Chakaya, J., Hoelscher, M., Ntoumi, F., Rustomjee, R., Vilaplana, C., et al. Maeurer, M. 2015. Towards host-directed therapies for tuberculosis. *Nature Reviews Drug Discovery,* 14**,** 511-512.

CHAPTER 2

INSIGHT INTO INNOVATIVE THERAPEUTICS FOR DRUG-RESISTANT TUBERCULOSIS: HOST-DIRECTED THERAPY AND AUTOPHAGY-INDUCING MODIFIED NANOPARTICLES

International Journal of Pharmaceutics 622 (2022) 121893

Contents lists available at ScienceDirect

International Journal of Pharmaceutics

journal homepage: www.elsevier.com/locate/ijpharm

Insights into innovative therapeutics for drug-resistant tuberculosis: Host-directed therapy and autophagy inducing modified nanoparticles

Leon J. Khoza [a], Pradeep Kumar [a], Admire Dube [b], Patrick H. Demana [c], Yahya E. Choonara [a,*]

[a] Wits Advanced Drug Delivery Platform Research Unit, Department of Pharmacy and Pharmacology, School of Therapeutic Science, Faculty of Health Sciences, University of Witwatersrand, Johannesburg, Parktown 2193, South Africa
[b] School of Pharmacy, Faculty of Natural Sciences, University of the Western Cape, Cape Town, South Africa
[c] Division of Pharmaceutical Sciences, School of Pharmacy, Sefako Makgatho Health Sciences University, Pretoria 0208, South Africa

ARTICLE INFO

Keywords:
Mycobacterium tuberculosis
Innate immunity
Autophagy induction
Host-directed therapy
Nanoparticles
Alveolar macrophages

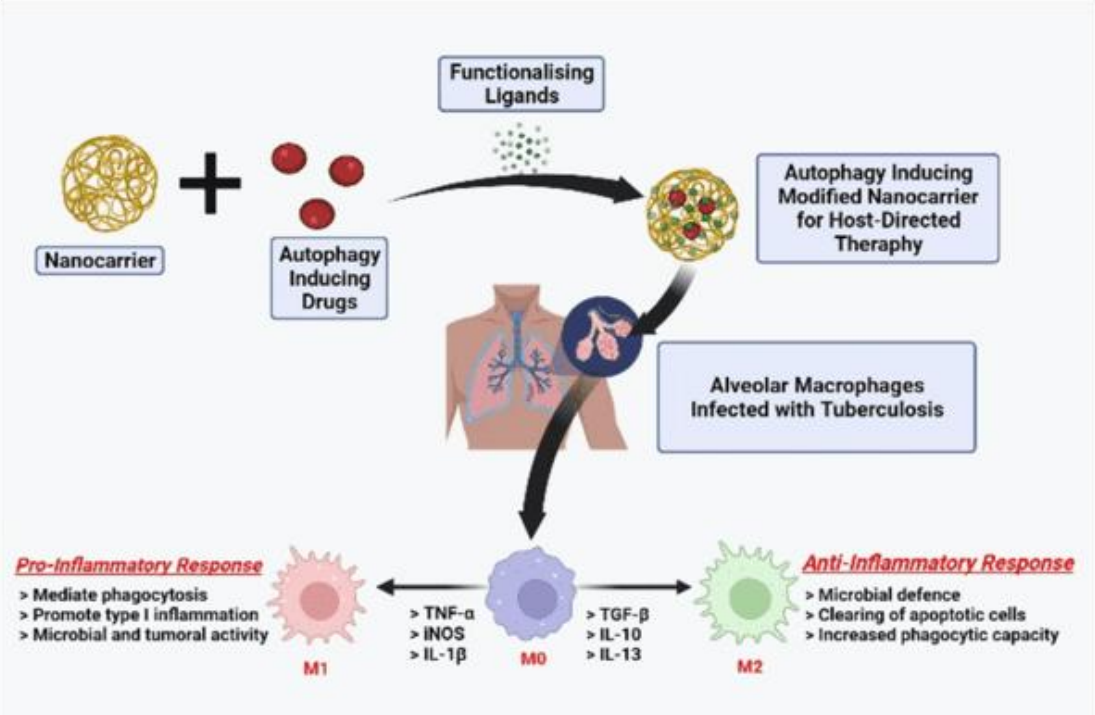

2.1. Introduction

Tuberculosis (TB) remains one of the deadliest communicable diseases caused by *Mycobacterium tuberculosis* (Mtb) since its discovery in the 1880s (Cambau and Drancourt, 2014, Singh et al., 2020). Over 1 billion mortalities have been recorded to date due to TB, and it was the leading cause of death from a single infectious agent before the COVID-19 pandemic, with an estimated 10.4 million new cases and an average of 1.7 million deaths yearly (Gagneux, 2018, Barberis et al., 2017, Scriba et al., 2020, Allue-Guardia et al., 2021, Organization, 2021). Further, about 25% of the world's population is latently ill or infected, providing a substantial pool for future cases of active TB (Gagneux, 2018). The World Health Organisation (WHO) reported that in 2019, an average of 10 million new cases were recorded, with 1.2 million cases being children and an estimated total of 1.4 million mortalities (Organization, 2019). Eight countries known for high TB burden accounted for 67% of the total cases logged in 2019. India was the leading country, followed by Indonesia, China, the Philippines, Pakistan, Nigeria, Bangladesh, and South Africa (Organization, 2019).

However, between 2020 and 2021, services aimed at eradicating TB were severely disrupted, and case recordings were significantly hindered by the COVID-19 pandemic (Crowther and Qualls, 2020, Pai et al., 2022, Organization, 2021). In 2020, WHO estimated that over 10 million individuals contracted TB, but only 5.8 million cases were diagnosed and recorded, a decline of 18% from 2019 (Pai et al., 2022, Organization, 2021). The decline spread across 16 countries, with Asian countries witnessing far more significant reductions in case of reporting due to substantial COVID-19 outbreaks and healthcare service interruptions (Organization, 2021). As a result, there was an increase in TB mortality, with about 1.5 million deaths globally, the first increase in TB deaths since 2005 (Organization, 2021). Other adverse COVID-19-related drawbacks included a 15% drop in the number of people treated for drug-resistant TB and a 21% drop in people receiving TB infection prevention treatment (Organization, 2021, Pai et al., 2022).

TB mainly affects the lungs (pulmonary TB); however, it can spread to other neighbouring organs, which is known as extrapulmonary TB (EPTB) (Sunnetcioglu et al., 2015). EPTB results from the hematogenous spread of Mtb, with about 10% of all TB cases having pulmonary and EPTB (Narita and Spitters, 2017). Different factors contribute to high susceptibility to TB infection. These include compromised immune systems and defects in immune cells (macrophages and monocytes) due to various diseases or conditions such as human immunodeficiency virus (HIV), kidney disease, diabetes, substance abuse, and cancer (Kumari and Meena, 2014, Alavi-Naini et al., 2012). Other essential factors include

malnutrition and smoking (tobacco). Various studies have demonstrated that more current smokers developed TB and successively died within the follow-up period than non-smokers (Alavi-Naini et al., 2012).

The treatment of TB follows the standard guidelines outlined by the WHO, consisting of the multidrug therapy of first-line anti-TB drugs (acronym RIPE): rifampicin (RIF), isoniazid (INH), pyrazinamide (PZA), and ethambutol (EMB) (Organization, 2017). The recommended treatment plan comprises daily administration of all the first-line drugs (RIPE) in the first two months, followed by the day-to-day administration of INH and RIF for four months (Organization, 2020). However, this treatment plan is often met with numerous challenges, such as poor patient compliance due to lengthy multidrug therapy (4-6 months), increased pill burden and drug-drug interaction from co-morbidities, which often leads to overlapping severe side effects (Dartois, 2014, Costa et al., 2016). This often leads to patient withdrawal before the course of treatment is completed, leading to treatment failure and subsequent development of drug-resistant TB (Dartois, 2014). The development of drug-resistant TB is a global threat in the fight against TB, and It is one of the significant contributors to the current anti-TB treatment regime failure (Mishra et al., 2020, Koch et al., 2018). MDR-TB is defined as TB that is resistant to RIF and INH, whilst extensively drug-resistant (XDR-TB) is defined as MDR-TB that is resistant to at least one of the injectable second-line drugs (amikacin, kanamycin and capreomycin) and any fluoroquinolone(Organization, 2017, Koch et al., 2018).

Besides the development of drug-resistant TB, the difficulty of managing TB is that several anti-TB drugs fail to effectively reach the lungs and penetrate the alveolar macrophages (AMs) where the pathogen is hosted (Andrade et al., 2013, Pandey and Khuller, 2005). As a result, this enables the Mtb pathogen to remain viable within the host AMs for a more extended period following its adaptation to survive and evade the destructive environment of the host (Pieters, 2008). Treatment of drug-resistant TB makes use of the 2nd line anti-TB therapeutics with an extended treatment period (18-24 months) and with even more toxic severe side effects such as hepatotoxicity (liver damage), ototoxicity (loss of hearing and balance) and nephrotoxicity (kidney damage) (Shehzad et al., 2013, Ma et al., 2010, Niemi et al., 2003).

In the last 40 years, only three anti-TB drugs with novel mechanisms of action have been approved to treat MDR-/XDR-TB: delamanid**,** bedaquiline, and pretomanid, respectively (Baranyai et al., 2020). Bedaquiline and delamanid have demonstrated an effective improved treatment outcome rate at the end of treatment and a shorter treatment period for drug-resistant TB. Nonetheless, there are concerns about the possibility of cardiotoxicity caused by drug-drug interactions (Baranyai et al., 2020, Conradie et al., 2017, Olugbosi et al., 2020). The

Food and Drug Administration (FDA) recently approved a novel oral regimen containing bedaquiline, pretomanid, and linezolid (BPaL) for the treatment of XDR-TB and MDR-TB after undergoing intensive clinical trials (NIX-TB trial) (Baranyai et al., 2020). This novel regime therapy has shown highly favourable effective outcomes against drug-resistant TB; however, linezolid toxicity was frequently observed (Bigelow et al., 2020, Baranyai et al., 2020). Studies conducted in South Africa demonstrated the favourable outcome of the BPaL regime after treatment therapy (six months) in many patients with MDR and XDR-TB, with some related toxic effects to the treatment observed (Conradie et al., 2017, Olugbosi et al., 2020, Conradie et al., 2020). Despite the positive results or outcomes demonstrated by the BPaL treatment regimen, WHO guidelines on drug-resistant TB treatment recommend that it be used only if all other options are ineffective (Organization, 2019).

To overcome these limitations and challenges posed by drug-resistant TB, new research fields are emerging, such as Host Directed Therapeutics (HDTs), autophagy manipulation and Nanotechnology. HDT aims to increase the success of TB treatment by providing immunomodulation to the host response to infection by interfering with the host's mechanisms required by an Mtb pathogen for progressive persistence and replication (Kaufmann et al., 2018, Young et al., 2020, Gina et al., 2019). HDT differs from the conventional treatment plan. It stimulates the immune response by enhancing host defence mechanisms against Mtb by targeting pathways perturbed by the Mtb pathogen without interacting with the pathogen itself (Kaufmann et al., 2018, Kilinc et al., 2021, Gina et al., 2019). HDT can also be used to treat MDR/XDR TB, which is resistant to commonly used antibiotics. Because Mtb bacillus is not subjected to direct selection pressure, host-targeting drugs are less likely to generate drug resistance (Kilinc et al., 2021). The combinations of HDT with conventional anti-TB regimens may reduce the duration of the treatment period, attain better treatment outcomes, lessen the chances of relapse and permit dose lowering of standard antibiotics, thus reducing toxicity without impacting efficacy (Zumla et al., 2015a, Kilinc et al., 2021). Furthermore, HDT may reduce risks associated with drug-drug interactions in patients with co-morbidities, such as antiretroviral drug interaction in TB-HIV patients (Zumla et al., 2015a, Kolloli and Subbian, 2017).

Autophagy is a cellular process responsible for the lysosomal degradation of intracellular components, including invading pathogens such as Mtb (Goletti et al., 2013). The significant antimicrobial role of Autophagy against Mtb was first reported by Gutierrez et al. and Nakagawa et al. in 2004, respectively (Deretic, 2014). Mtb host cells (AMs) have mechanisms that induce autophagy to eliminate and decrease the bacterial loads within the infected host cell (Bento et al., 2015). Manipulation of autophagy activation in the infected host cell using

various autophagy-inducing compounds (AICs) has gained significant momentum as an alternate new treatment approach for treating TB (Maphasa et al., 2020). Treatment of drug-resistant TB with or without conventional TB antibiotics is one of the envisaged advantages of autophagy activation/manipulation (Paik et al., 2019, Maphasa et al., 2020). In addition, manipulation of autophagy activation further aids in controlling inflammation, contributing to a more efficient innate and adaptive immune response against Mtb bacilli (Bento et al., 2015, Goletti et al., 2013). Various novel innovations in anti-TB therapeutics have been envisaged based on manipulating autophagy activation, such as surface functionalised or modified nanoparticles (NPs) encapsulating conventional anti-TB therapeutics and other AICs capable of host-directed therapies. Some show significant success in clinical trials, increasing their possible implementation in the healthcare system (Bento et al., 2015). Given that HDT and autophagy manipulation are relatively new advances in the treatment of TB, there is minimal data published regarding the delivery of AICs or HDT adjuncts to the host and their treatment outcome and duration in the treatment of TB when combined with conventional treatment regimens (Maphasa et al., 2020). This dramatically enables a significant need to directly deliver HDT adjunct/AICs to their intended target sites to prevent undesired effects in other cells or organs (Paik et al., 2019).

NPs have provided significant advances as drug delivery systems in lung and respiratory infectious diseases for targeted drug delivery directly to their target sites (Andrade et al., 2013). They are designed to increase conventional drugs' efficacy by enhancing the absorption, stability, solubility, uptake by cells, and drug payload on targeted cells using minimum dosage whilst reducing immunotoxicology (Maretti et al., 2017, Zazo et al., 2016, Dobrovolskaia et al., 2016, Andrade et al., 2013, Andrade et al., 2011). Due to their highly desirable features, the nanoparticle can improve the efficacy of AICs or HDT adjuncts by directly transporting them to their target site (AMs) while protecting AICs from premature elimination, enhancing their absorption past biological barriers (Maphasa et al., 2020). Furthermore, some of the materials used in the fabrication of nanoparticles have an immunomodulatory effect on the host, and they can be further functionalised with AICs (Bekale et al., 2018). This review will summarise macrophages' role in Mtb uptake and response to early infection as a first-line defence innate immune response against invading pathogens. This review will also briefly examine the immunovasive and immunosuppressive processes that allow Mtb to survive in the host's hostile environment. In addition, the use of AICs to treat the host and nanoparticles for targeted distribution of AICs in the host will be discussed.

2.2. Recognition and uptake of Mtb by macrophages

Macrophages are an essential component of the innate immune system. They play a crucial role in eliminating intracellular Mtb and initiating the innate and adaptive immune response through various bactericidal mechanisms (Liu et al., 2017, Hmama et al., 2015, Queval et al., 2017, Mortaz et al., 2015). However, AMs also serve as the primary host or reservoir for Mtb in initial and latency infection stages (Liu et al., 2017, Cadena et al., 2016). Mtb gains entry to macrophages via inhalation of tiny droplets from an infected individual, where it quickly reaches the lungs' alveolar spaces (Queval et al., 2017). The bacillus is then recognised and phagocytised by AMs upon its entry into alveolar spaces (Guirado et al., 2013). The AMs and other innate immune cells (neutrophils, natural killers and dendritic cells) contain different types of pattern recognition receptors (PRRs); these include C-type lectin receptors (CLRs), Toll-like receptors (TLRs) and Nod-like receptors (NLRs) (Liu et al., 2017). Upon Mtb infection, PRRs are stimulated by pathogen-associated molecular patterns (PAMPs) such as carbohydrates, lipoproteins and glycolipids expressed on the surface of Mtb (Mortaz et al., 2015, Liu et al., 2017). The stimulation of PRRs triggers various innate immune responses, including macrophage polarisation, phagocytosis, inflammation activation, autophagy (phagosome maturation, acidification and phagosome-lysosome fusion), production of reactive oxygen and nitrogen species (RONS), programmed cell death (apoptosis), and antigen processing (Mortaz et al., 2015, Liu et al., 2017, Atri et al., 2018).

Macrophages are classified into two types: classically activated macrophages (M1) and alternatively activated macrophages (M2). The physiological environment governs the functional response and polarisation of AMs into M1 or M2 during different stages of acute bacterial infection (Yao et al., 2019, Murray, 2017, Atri et al., 2018). Macrophage polarisation (**Figure. 2.1)** is associated with both resolving inflammation, wherein the tissue heals after infection, and non-resolving inflammation, whereby the pathogen prolongs inflammation (Italiani et al., 2014). M1/M2 macrophages have different essential activities to eliminate pathogens, repair inflammation, and maintain homeostasis, and this polarisation can happen at any point during the inflammatory process (Italiani et al., 2014). However, research has revealed that the regulated biological polarisation process and its induction routes are complex interlacing network systems that remain unclear rather than a simple process. (Yao et al., 2019, Atri et al., 2018). To ensure a protective function during Mtb infection, macrophages are polarised toward the M1 phenotype, which has significant bactericidal activity during the early phases of infection (Atri et al., 2018).

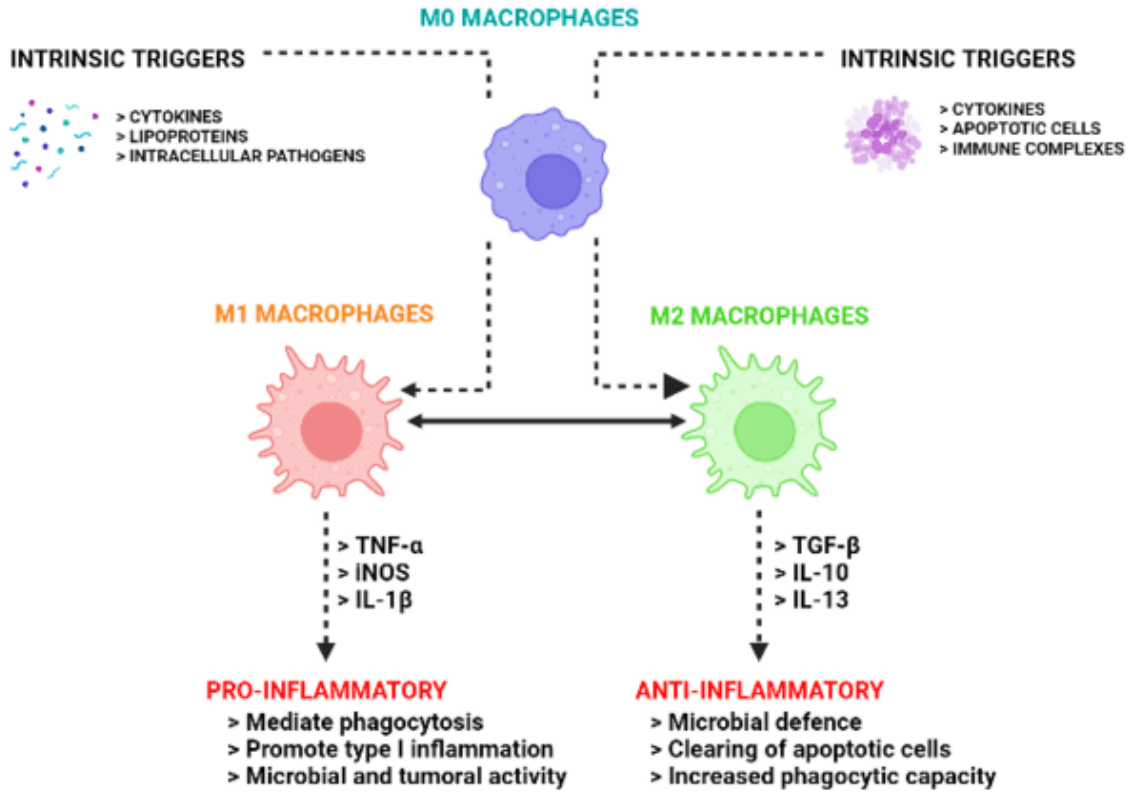

Figure 2.1: Summarises macrophage polarisation to produce distinct functional phenotypes as a reaction to specific microenvironmental stimuli and signals.

Briefly, M1 macrophages are activated by intracellular bacterial stimuli such as lipoproteins or tumour necrosis factor (TNF-α) and Interferon-gamma (IFN-γ) cytokines, as shown in **Figure 2.1** (Roszer, 2015). Activation of M1 macrophages results in the secretion of pro-inflammatory cytokines, chemokines, and nitric oxide (NO) production (**Figure 2.1**); this activates the Th1 response, facilitates complement-mediated phagocytosis, promotes type I inflammation, and assists in bacterial killing (Liu et al., 2017, Yao et al., 2019, Roszer, 2015). As a result, M1 macrophages are often found in an inflammatory milieu dominated by TLRs, TNF-α and IFN-γ signalling (Atri et al., 2018). M2 macrophages, in contrast to classically activated M1 macrophages, exhibit modulator activity, negatively regulate pro-inflammatory cytokines and increase the synthesis of anti-inflammatory mediators. (Jaguin et al., 2013, Atri et al., 2018). Various interleukin cytokines activate M2 macrophages (IL-3, IL-10, and IL-13), tumour growth factor-beta (TGF-β) and macrophage colony-stimulating factor (MCSF) (Roszer, 2015, Liu et al., 2017). Activation of M2 macrophages results in anti-inflammatory cytokines, increased phagocytic capacity, microbial defence, clearing of apoptotic cells and tissue repair (Roszer, 2015, Tarique et al., 2015).

2.3. Mtb defence mechanisms against the host immune response (Autophagy)

Autophagy is a homeostatic and inducible process in which cytoplasmic components, such as organelles and intracellular pathogens, are collected in autophagosomes and delivered to the lysosome for degradation in macrophages (**Figure 2.2**) (Gutierrez et al., 2004). Through autophagy, macrophages have demonstrated an effective antimicrobial response against Mtb infection. However, Mtb has adopted supreme strategies to evade, disrupt and manipulate the antimicrobial mechanisms of macrophages (Queval et al., 2017, Upadhyay et al., 2018, Chai et al., 2020). Mtb gains control of the host by disrupting autophagy, which includes the following vital steps: phagosome maturation, acidification and phagosome-lysosome fusion, and further by disrupting the production of reactive oxygen species (ROS), apoptosis and antigen presentation (Queval et al., 2017, Hmama et al., 2015). Disruption of these vital mechanisms alters the macrophages' ability to recognise and neutralise Mtb infection effectively and subsequently enables the survival and advanced replication of the Mtb within the host (Hmama et al., 2015).

2.3.1. Disruption of phagolysosome maturation and acidification

Once phagocytosed by AMs, Mtb is enclosed within phagosomes, the organelles responsible for routine clearance of pathogens (Chai et al., 2020). The phagosomes rapidly undergo a maturation process, a vital cellular process where phagosomes interact and fuse with lysosomes and endosomes, resulting in the exchange of endocytic solute materials and membrane components between them (Sturgill-Koszycki et al., 1994, Hmama et al., 2015). The maturation process is subsequently followed by the production of RONS intermediates, resulting in microbicidal and degrading characteristics being acquired by the phagolysosomes (Queval et al., 2017, Sturgill-Koszycki et al., 1994, Hmama et al., 2015).

2.3.1.1. Inhibition of Phagolysosome Maturation and Fusion

The maturation process of phagosomes from early to late stages is primarily regulated by Rab GTPase proteins (Queval et al., 2017, Prashar et al., 2017). Rab GTPase proteins also contribute to the endosomal organelle identity and further facilitate many fusion events during the maturation process (Prashar et al., 2017). Studies have shown that Mtb actively inhibits the accumulation of Rab GTPase proteins by secreting bacterial macromolecules such as ATP1/2, secretory acid phosphatase (SapM), tyrosine phosphatase (PtpA), early secretory antigen target-6 (ESAT-6) and culture filtrate protein, resulting in decreased intracellular pH

and subsequently suppressing the phagosome maturation (Zhai et al., 2019, Maphasa et al., 2020, Chai et al., 2018). Cytokine IFN-α has also been found to inhibit phagosome maturation by inducing the production of IL-10 in a signal transducer and activator of transcription-1 dependent manner (Ma et al., 2014). The induced release of IL-10 reduces the excess IL-1β resulting in the suppression of caspase1-dependent IL-1β maturation of pleural fluid mononuclear cells (Ma et al., 2014, Maphasa et al., 2020).

Mtb further inhibits the formation of lysosomes by enhancing the expression of the coronin-1 protein (Zhai et al., 2019, Schuller et al., 2001). Coronin-1 is a tryptophan aspartate-rich coat protein recruited to phagosomes containing active bacilli but rapidly released from phagosomes containing inactive Mtb (Maphasa et al., 2020, Schuller et al., 2001). Coronin-1 activates calcium-calcineurin signal on the phagosome surface, blocking the fusion of lysosomes and Mtb phagosomes (Queval et al., 2017, Hmama et al., 2015). Mtb further secretes protein kinase G (PKnG), which aids in the inhibition of lysosome maturation by downregulating adrenoleukodystrophy (ALD) and GlpK and upregulating the expression of Ag85A and Ag85C, resulting in enhanced Mtb infectivity, metabolism, growth rate and drug resistance (Walburger et al., 2004, Zhai et al., 2019, Maphasa et al., 2020). PKng further inhibits the fusion of the lysosomes with phagosomes by enhancing a transduction signal in the host cell (Zhai et al., 2019, Maphasa et al., 2020). The phagolysosome fusion is also inhibited via the calmodulin-dependent production of phosphatidylinositol-3-phosphate (PI3P), lower biosynthesis and trafficking of the toxin lipoarabinomannan (LAM) following Mtb infection (Vergne et al., 2003, Maphasa et al., 2020, Queval et al., 2017).

2.3.1.2. Inhibition of Phagolysosome Acidification

Phagosome acidification is essential for intracellular bacterial clearance. The RONS production and optimal activity of lysosome digestive enzymes require an acidic intracellular environment (Queval et al., 2017, Sun-Wada et al., 2009); hence, inhibition of phagosome acidification is crucial for the survival of Mtb within macrophages. The phagosome pH is hastily dropped by the high activity of a vesicular proton-pump ATPase (H+ V-ATPase) from neutral to pH~4.5 as the maturation process progresses (Russell et al., 2009, Hmama et al., 2015). The H+ V-ATPase pump is a protein complex that controls phagosome acidification by transporting protons across membranes (Hmama et al., 2015). However, Mtb inhibits the assembly of the H+ V-ATPase complex and its subsequent fusion with the phagosome membrane to stabilise the phagosome pH between 6.2 and 6.5 (Queval et al., 2017, Sturgill-

Koszycki et al., 1994); thus enabling Mtb to persist and progress within an intracellular environment.

2.3.2. Disruption of reactive oxygen species production

Reactive oxygen species (ROS) are essential signalling molecules involved in many cellular processes, including the clearance of intracellular pathogens in macrophages (Lammas et al., 1997). The activation of phagocytosis, a first-line innate defence mechanism, induces ROS generation; the phagocytic process is triggered by the detection of PAMPs by particular receptors present on the surface of phagocytic cells such as TLRs, Fc-gamma receptors (FcγR), β-glucan receptor or complement receptors (Pauwels et al., 2017, Liu et al., 2017). TLR signalling is activated during phagocytosis, resulting in the recruitment of the microtubule-associated 1A/1B-light chain-3 autophagy protein (LC3) to the phagosome, which speeds phagosome maturation and improves microbial elimination and antigen presentation (Pauwels et al., 2017, Yang et al., 2012). The recruitment of the autophagy protein LC3 to phagosomes distinguishes a type of phagocytosis known as 'LC3-associated phagocytosis' (LAP) (Mehta et al., 2014); LAP is required for effective control of IFN production and clearance of dead cells (Martinez et al., 2011). TLR and FcγR signalling also cause the phagocyte NADPH oxidase 2 (NOX2) to assemble in the phagosome membrane, resulting in the generation of ROS, including superoxide by the transfer of electrons from cytosolic NADPH to oxygen in the phagosome lumen (Bedard and Krause, 2007, Maphasa et al., 2020).

ROS produced during this process are extremely powerful and may actively kill intracellular microorganisms, including Mtb pathogens (Bedard and Krause, 2007, Yang et al., 2012); furthermore, NOX2-derived ROS generation is essential for driving the LAP process (Martinez et al., 2015). However, Mtb has gained the ability to deactivate NOX2-derived ROS via the secretion of various molecules such as Mtb nucleoside diphosphate kinase (Ndk) and Eis protein (Sun et al., 2013, Shin et al., 2010). Ndk binds to and deactivates Rac1 GTPase, a vital recruiter of NOX2 in the phagosomes, hence impairing the mediated production of ROS (Sun et al., 2013). Impaired ROS-mediated production alters LAP-associated proteins further, resulting in a deficiency in the effective engulfment and digesting of apoptotic cells (Martinez et al., 2016). The Eis protein by Mtb further improves its intracellular survival by reducing macrophage inflammatory responses, apoptosis, and autophagy by blocking ROS generation (Shin et al., 2010). In addition, the Eis protein has been found in the cytoplasm of infected macrophages and sera taken from individuals with pulmonary TB, thus signifying that Eis is produced during Mtb infection in humans (Dahl et al., 2001, Samuel et al., 2007).

2.3.3. Disruption of apoptosis and Mtb antigen presentation

Apoptosis is a regulated cell death process vital for removing damaged cells in multicellular organisms (Green, 2011). Damaged cells are confined within a membrane-bound structure known as apoptotic bodies, which expresses phosphatidyl serine signals, leading to the recognition and removal of these cells by phagocytic cells (Behar et al., 2011). Hence, apoptosis is vital for the efficient removal of intracellular Mtb by eliminating the favourable intracellular niche for replicating and initiating effective antigen cross-presentation for the effective immune response against Mtb (Schaible et al., 2003, Hmama et al., 2015). Mtb has developed strategic mechanistic approaches to actively evade or disrupt macrophage apoptosis, thus enabling Mtb to survive within the host and spread to other neighbouring cells (Martin et al., 2014). Mtb contains apoptosis-inhibitory genes such as secA2, nuoG, Ndk and PtpA (Hmama et al., 2015). Some studies have demonstrated that infecting SecA2 and nuoG with knockout strains results in a proapoptotic phenotype (Hinchey et al., 2007, Velmurugan et al., 2007, Sun et al., 2013).

SecA2 serves as the primary transporter of superoxide dismutase (SodA) out of the bacterial cell, resulting in the deactivation of ROS activity by Mtb (Hinchey et al., 2007). Hence, inactivation of the secA2 by knockout strain results in impaired SodA secretion, leading to enhanced apoptosis associated with increased macrophage antigen presentation to CD8+ T cells (Hinchey et al., 2007). Similarly, the knockdown of the nuoG gene in Mtb reverses apoptosis inhibition and reduces Mtb virulence in mice (Velmurugan et al., 2007). Mtb PtpA further inhibits macrophage apoptosis by dephosphorylating the glycogen synthase kinases α (GSK3α), resulting in anti-apoptotic activity, promoting pathogen survival in early infection stages (Poirier et al., 2014). Apoptosis in macrophages not only helps to eliminate the favourable intracellular environment for Mtb pathogen replication, but it also aids Mtb antigen cross-presentation by delivering apoptotic blebs to non-infected dendritic cells (DCs), ensuring optimal antigen presentation to T cells, a process known as the detour pathway (Lee et al., 2009). Hence, apoptosis obstruction in macrophages subsequently results in obstruction of Mtb antigen presentation (Kilinc et al., 2021).

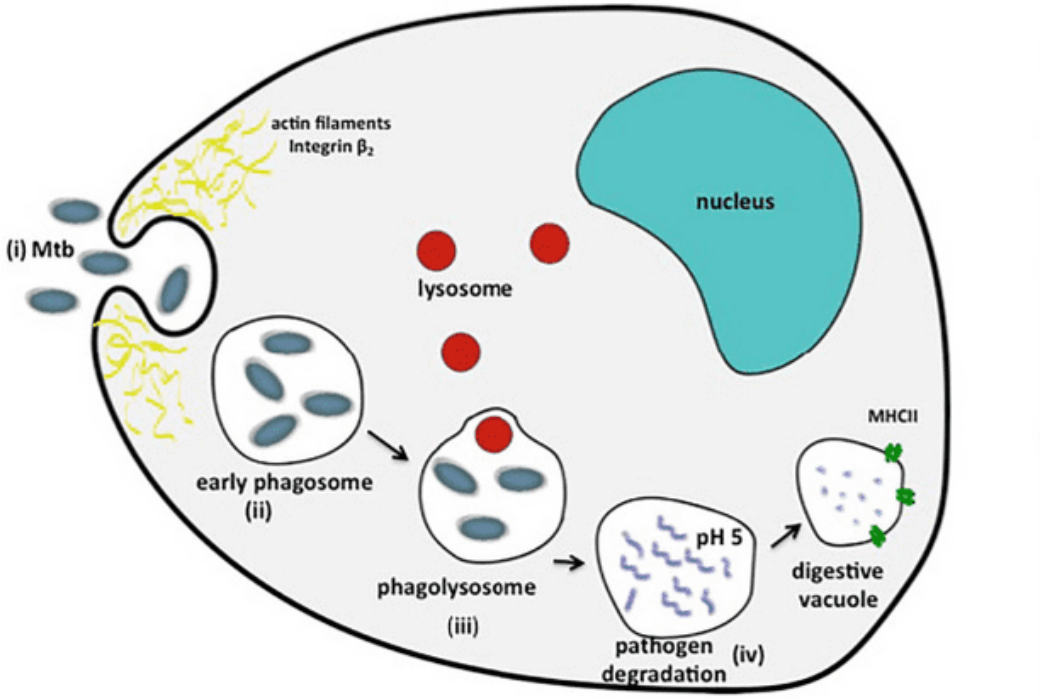

Figure 2.2: Normal process of autophagy where Mtb is digested and cleared. However, Mtb evades this response by blocking maturation (ii), phagolysosome fusion (iii), acidification of the phagosomes (iv) and antigen presentation (Reprinted from Carranza and Chavez-Galan, 2019 with permission).

2.4. Autophagy induction as host-directed TB therapy

Several HDT strategies focus on repurposing already approved medications, vitamins and cytokines with well-defined pharmacokinetics and safety profiles for other conditions, such as cardiovascular disease, metabolic disorders, and cancer (Gina et al., 2019, Periyasamy et al., 2020). As a result, the application of HDT in treating Mtb is a ground-breaking concept that offers new prospects needed to combat increasing Mtb infection (Zumla et al., 2015b). Most HDT techniques are used in conjunction with existing TB drugs and not as stand-alone treatments (Rao et al., 2019, Gina et al., 2019). HDT can be employed to restrict Mtb growth by modulating several host immune cell responses, such as increasing the production of ROS, antimicrobial peptide synthesis, and autophagy in infected cells (Kolloli and Subbian, 2017, Zumla et al., 2016). HDT drugs can also inhibit pro-inflammatory responses, thus reducing inflammation and tissue damage during the active stage of the disease (Kolloli and Subbian, 2017, Wallis and Hafner, 2015). In addition, HDT adjunct can modulate cell-mediated immune responses, such as antigen-specific T-cell responses and alteration of the granuloma integrity

and improve drug accessibility (Wallis and Hafner, 2015, Zumla et al., 2016, Young et al., 2020).

2.4.1. Vitamin D_3 and autophagy induction

One of the most investigated adjuncts for HDT-TB is vitamin D_3 due to the link between vitamin D_3 deficiency and TB susceptibility and its potential to stimulate autophagy and the production of antimicrobial peptides (Lee and Bhakta, 2021). Vitamin D_3 exert an immunomodulatory effect on the innate immune system by upregulating its response and inflammatory response, respectively, via its active form 1,25-dihydroxyvitamin D_3 (1,25D) pathway (Chun et al., 2011). Vitamin D_3 acquire its physiological properties by being first hydroxylated in the liver by vitamin D-25-hydroxylase enzyme (CYP2R1), to 25-hydroxyvitamin D (25D), which is then converted into the active form (1,25D) in the kidneys by 25-hydroxyvitamin D-1-hydroxylase (CYP27B1) (Periyasamy et al., 2020, Chun et al., 2011). Some studies have shown that CYP27B1 is expressed in kidneys and intestines and is also expressed in the innate immune cell, which enables macrophages to produce 1,25D from 25D (Periyasamy et al., 2020, Aranow, 2011). Increased expression of CYP27B1 in macrophages is triggered by recognising Mtb lipopolysaccharide (LPS) by TLRs in the macrophages (Periyasamy et al., 2020). 1,25D, then induces the production of RONS, antimicrobial peptides such as beta-defensin-4 (DEFB4) and cathelicidin antimicrobial peptide (CAMP/LL-37) in macrophages, thus enhancing bactericidal activity as seen in **Figure 2.3** (Sia et al., 2015, Salamon et al., 2014, Rivas-Santiago et al., 2013). In addition,1,25D enhances autophagosome initiation and fusion with the lysosome and inhibits Mtb growth by regulating the expression of autophagy-related proteins (ATGs) such as ATG5 and Beclin-1 (Campbell and Spector, 2011).

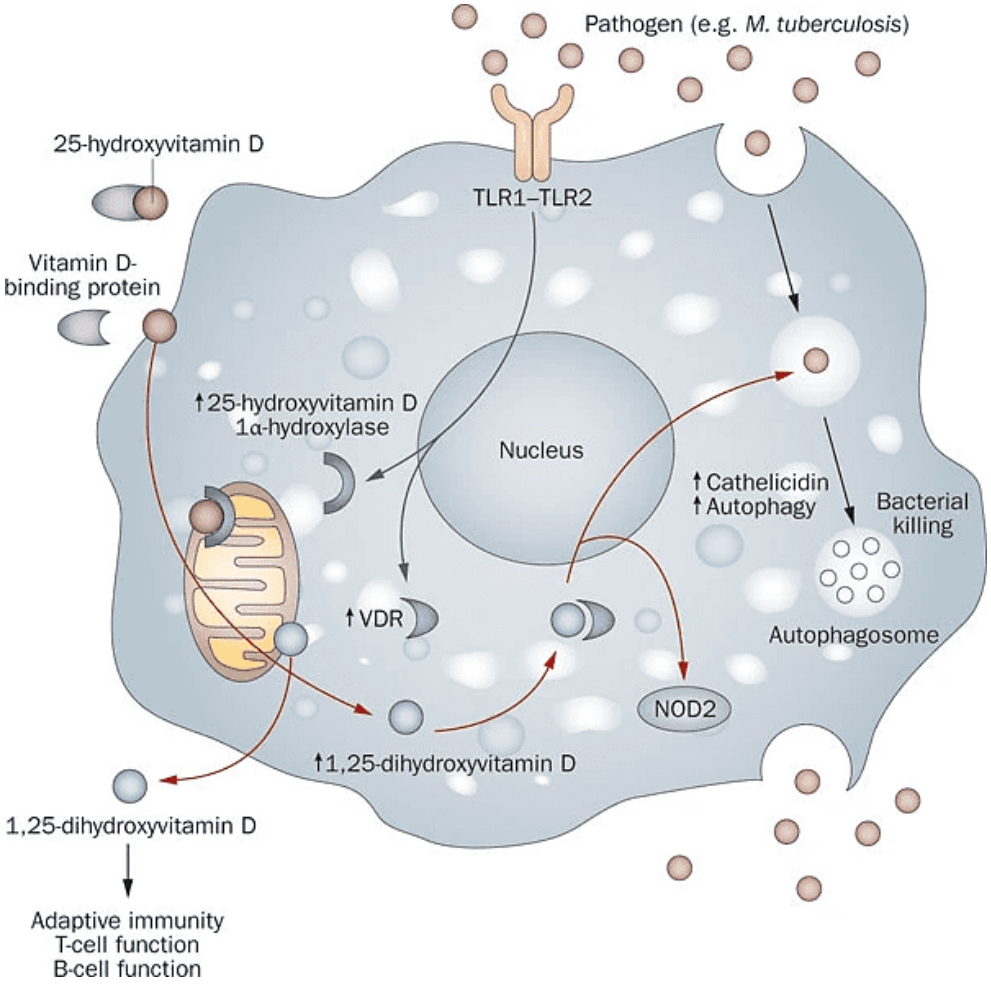

Figure 2.3: Induction of autophagy by Vitamin D_3 and its metabolites (Reprinted from Hewison, 2011 with permission).

In pulmonary TB, 1,25D also act as an anti-inflammatory agent by inhibiting pro-inflammatory chemokines and cytokines such as IL-23, IL-17, IL-12, and IP-10 while increasing the production of anti-inflammatory cytokines (IL-10, TGF-1, and IL-4) (Kolloli and Subbian, 2017). In vivo studies in TB patients found that combining a high dose of vitamin D_3 with standard anti-TB drugs suppressed antigen-stimulated pro-inflammatory cytokine production and accelerated inflammatory response resolution during treatment, thus improving the clinical and radiology outcomes (Coussens et al., 2012, Salahuddin et al., 2013). Another study demonstrated that a combination of traditional anti-TB therapeutics, vitamin D_3, and phenylbutyrate (PBA), a histone deacetylase inhibitor, stimulated CAMP gene expression and inhibited intracellular Mtb growth in human monocyte-derived macrophages (MDMs) (Mily et al., 2013, Mily et al., 2015). In addition, another clinical trial found that adding PBA and vitamin D_3 to standard chemotherapy lowers Mtb growth in MDMs and speeds up clinical recovery compared to a placebo group (Mily et al., 2015). These findings suggest that vitamin D_3 may

play a significant role in treating Mtb when paired with other adjuncts such as PBA (Mily et al., 2015). Despite extensive research, the role of vitamins in the treatment of tuberculosis remains uncertain. Nevertheless, in parts of the world where malnutrition and inherent vitamin shortages impair the immune system, it is tempting to make vitamin supplementation a regular treatment for TB-infected people (Lee and Bhakta, 2021). Therefore, more clinical trials are needed to establish Vitamin D_3's efficacy as HDT in treating drug-resistant TB.

2.4.2. Trehalose and Autophagy induction

Trehalose is a naturally occurring disaccharide composed of two D-glucose molecules connected by glycosidic linkage, with the α, α-1,1-trehalose form being the most common in living organisms (Adikesavalu et al., 2021, Vanaporn and Titball, 2020). Trehalose is a vital carbon source for many bacteria and can support bacterial development; therefore, it plays a crucial function in protecting bacteria from various stressors (Vanaporn and Titball, 2020). The bacterial capacity to utilise trehalose as a carbon source might thus explain the found correlations between virulence and bacterial proliferation (Vanaporn and Titball, 2020). However, using trehalose as a carbon source is only likely to benefit infections that thrive in carbon-limited environments, such as outside of host tissues or cells (Vanaporn and Titball, 2020). Trehalose is transformed into several glycolipids present on the cell walls of Mtb and other bacteria: Lipooligosacharide, sulfolipids, polyacyltrehaloses, trehalose 6,6 mycolate (TMM), and trehalose 6,6 dimycolate (TDM) are the essential glycolipids identified in Mtb (Kalscheuer and Koliwer-Brandl, 2014). Many of these trehalose-derived lipids have a role in Mtb pathogenicity and are anti-mycobacterial therapeutic targets (Ghazaei, 2018).

TDM is the most well-known trehalose-derived lipid on the Mtb cell surface. It shields bacterial cells from macrophage killing by inhibiting phagosome fusion with lysosomes and increasing Mtb cell wall Impermeability, resulting in drug resistance (Hunter et al., 2006, Vanaporn and Titball, 2020). On the other hand, Trehalose has been shown to successfully induce autophagy in different cell lines (HEK293T and U937, U1.1) against Mtb and non-Mtb strains, either alone or in combination with HIV-1 infection (Sharma et al., 2021). This is because Trehalose increases the mucolipin transient receptor potential (TRPML) channel agonist production and, therefore, increases the release of Ca^{2+} from the lysosomal lumen to promote autophagic flux (Dong et al., 2010). The generated Ca^{2+} stimulates calcineurin, a serine-threonine phosphatase that dephosphorylates Transcription factor EB (TFEB), resulting in TFEB nuclear translocation driven by trehalose and autophagy activation independent of mTOR in macrophages (Sharma et al., 2021).

A more recent study by Sharma et al., 2021 discovered that trehalose therapy significantly decreased bacterial load in H37Rv–-infected U937-derived macrophages and that excess trehalose did not interfere with or enhance bacterial growth (Sharma et al., 2021). The study further reported that trehalose also induced autophagy via mTOR inhibition and AMPK activation, resulting in a pseudo-starvation response by competitively blocking glutamate transporters (Sharma et al., 2021). Despite the numerous studies on trehalose and its bactericidal function, the specific mechanism of trehalose-mediated autophagy induction remains unknown; its role in virulence and autophagy induction is a topic that warrants more research.

2.4.3. L-arginine and Autophagy induction

L-arginine is a semi-essential amino acid that becomes necessary in certain illnesses and situations (Schon et al., 2003). Dietary consumption and citrulline renal production help keep plasma levels of L-arginine normal (Schon et al., 2003). L-arginine serves as a critical metabolite for many cellular processes in macrophages. It has been shown to improve innate immune function response, particularly when driving macrophage nitric oxide (NO) production (McKell et al., 2021). Inducible NO synthase (iNOS) catalyses the synthesis of NO from l-arginine in macrophages activated by TLRs and cytokine (IFN-γ and TNF-α) stimulation (Crowther and Qualls, 2020). The produced NO can kill Mtb bacteria with a molar potency greater than standard anti-TB drugs (Ralph et al., 2013a, Long et al., 1999). Several studies have found that NO concentration correlates with Mtb killing in mice and that mice with low NO concentrations fail to control Mtb infection. (Scanga et al., 2001, Garcia et al., 2000, MacMicking et al., 1997). NO and iNOS production has also been detected in human macrophages in vitro and the lungs of Mtb-infected patients, indicating that NO plays a role in human immune responses to Mtb infection (Crowther and Qualls, 2020). In a randomised clinical study of TB patients without HIV infection, arginine supplementation resulted in greater sputum conversion rates, quicker symptom improvement, and an increase in weight gain (Swanson et al., 2002, Schon et al., 2003); These benefits, however, were not observed in individuals with HIV in the same or another study. Another study published in 2013 by Ralph et al. found that decreased pulmonary NO bioavailability is linked to severe illness and delayed mycobacterial clearance. (Ralph et al., 2013b). However, the contribution of NO in the pathogenesis of human Mtb infection remains highly debated and controversial (Crowther and Qualls, 2020, Farazi et al., 2015). Nonsteroidal anti-inflammatory drugs (NSAID), tyrosine

kinase inhibitors, inflammatory modulators, antihyperglycemic medications, and other HDT adjuncts with great potential in Mtb therapy are summarised in **Table 2.1**.

Table 2.1: A summary of other potential HDT-TB drugs targeting autophagy and their mechanism of action.

Adjunct-HDT drug	Mechanism of action in mediating innate immune response/autophagy	References
Aspirin	Aspirin enhances vitamin D-mediated anti-mycobacterial effects.	(Tobin and Ramakrishnan, 2013)
Lipopolysaccharides	Activates autophagy and restores Mtb-inhibited immunological function.	(Fang et al., 2020)
PBA and Vitamin D_3	PBA interacts with vitamin D metabolites to increase the production of cathelicidin antimicrobial peptide, which augments Mtb proliferation. Simultaneously, it generates antibacterial and anti-inflammatory responses that benefit the host.	(Mily et al., 2015, Coussens et al., 2015)
Rapamycin	Induces autophagy via mTOR complex inhibition.	(Floto et al., 2007, Gutierrez et al., 2004)
Fluoxetine	Induces autophagy by increasing the secretion of TNF-α.	(Stanley et al., 2014)
Immunoxel	Increases interferon production and boosts the immune system by re-establishing humoral and cellular immunity and enhancing the host's capacity to fight infectious diseases.	(Efremenko et al., 2012)

Pravastatin	Mediate non-productive inflammation and tissue damage, enhance host bactericidal mechanisms by promoting the macrophage-mediated killing of Mtb and reduce bacterial growth.	(Banerjee and Bhattacharyya, 2014)
Metformin	It increases autophagic flux by enhancing autophagosome-lysosome fusion and increasing ROS generation.	(Efremenko et al., 2012)
Carbamazepine	Reduces MDR-TB burden in the lungs and spleen via depleting inositol triphosphate and activating AMPK.	(Schiebler et al., 2015)
Enbrel	Reduces lung pathology by Neutralizing TNF-α and disrupting granuloma.	(Bourigault et al., 2013)
Bazedoxifene	Enhances autophagosome formation via phosphorylation of mTOR signalling.	(Ouyang et al., 2020)

2. 5. Nanoparticle-based approaches for HDT-TB

The use of NPs as drug nanocarriers or drug delivery vehicles is an emerging approach in the fight against many illnesses. NPs are solid particles with sizes ranging from 10 to 1000 nm (Grotz et al., 2018). As opposed to free drugs, using NPs as new immunotherapeutic platforms is attractive for several reasons. To begin with, NPs can encapsulate a high amount of bioactive metabolites that can enhance the immune response against infection (Look et al., 2010). Secondly, they may be made out of materials that can release encapsulated drugs for several days to months at a time (Look et al., 2010, Baranyai et al., 2020). Thirdly, some NPs have innate antimycobacterial activity and serve as a vehicle for various anti-TB drugs, hence being instrumental in reducing the dosing frequency and related side effects (Nabi et al., 2020). Finally, NPs may be extensively modified to improve their bioactivity or distribution to specific cells and organs inside the body (Look et al., 2010). Other benefits include the ability to reduce administered dosages and, therefore, the associated adverse effects and dosing recurrence (Baranyai et al., 2020). NPs desired properties, such as drug-load capacity, cellular absorption, and biodistribution, are influenced by their physicochemical characteristics, such

as size, surface charge, hydrophobicity, and composition (Booysen et al., 2013). The material composition and size of the NPs, for example, may be used to adjust the rate of release of an encapsulated substance, and this characteristic has allowed the use of NPs in a variety of applications (Tinsley-Bown et al., 2000, Look et al., 2010).

Bioactive agents for host-directed therapy can also be integrated into NPs by chemical conjugation on the particle surface or by physical encapsulation inside the particle-matrix (Grotz et al., 2018, Nasiruddin et al., 2017). In most cases, the surface of the NP's material is modifiable using ligands, allowing the integrated therapeutics to be targeted to specific cells and organs (Gu et al., 2008, Mohamed and van der Walle, 2008). These ligands can also directly have pharmacologic effects by inducing immunological responses via cell-surface receptor-mediated signalling events, such as when NPs surface-associated PAMPs stimulate TLRs (Look et al., 2010). NPs are classified into several categories based on their composition, as shown in **Figure 2.4** and **Table 2.2.** Polymeric NPs, for example, are biocompatible and biodegradable materials made from natural or synthetic polymers (Nasiruddin et al., 2017). In comparison, solid lipid NPs (SLNPs) are considered a combination of polymeric NPs and liposomes (LPs) (Grotz et al., 2018). They have a solid lipid core supported by surrounding surfactants, giving them more stability and drug-loading capability than LPs on their own (Grotz et al., 2018, Abed and Couvreur, 2014). Based on their composition, other categories of NPs may include micelles, dendrimers, nanogels, inorganic NPs, and nanocapsules (Baranyai et al., 2020).

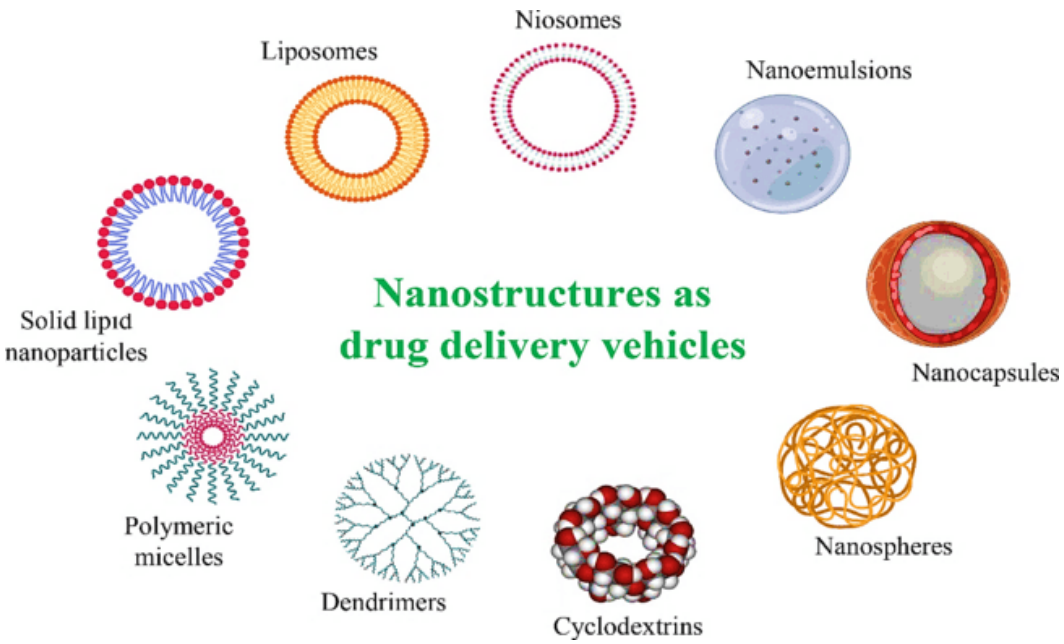

Figure 2.4: Different types of the most common nanostructures used as drug delivery systems (Reprinted from Dahanayake and Jayasundera, 2021 with permission).

Table 2.2: A brief overview of distinct classes of nanostructures as drug-delivery vehicles with desirable features employed to deliver host-directed therapeutics and their limitations.

Different classes of nanostructures	Features	Advantages	Limitations	References
Cyclodextrins (CDs) assisted NP drug delivery systems	CD molecules are amphiphilic, consisting of a macrocyclic ring of glucose subunits linked together by α-1,4 glycosidic bonds.	They are safe for oral ingestion since they can bypass gastrointestinal tract absorption and are rapidly removed from the body. They may be used with other NPs to improve hydrophobic drug loading and biological tissue permeability.	Some CDs' derivates, such as - α-CD and β-CD, are hazardous because they can recrystallise and accumulate in renal tissue, resulting in nephrotoxicity.	(Haimhoffer et al., 2019, Shelley and Babu, 2018, Muankaew and Loftsson, 2018)
Lipid-based nanoparticulate (LNPs) drug delivery systems	They are categorised into several classes based on their synthesis and physicochemical properties. Nanostructured lipid carriers (NLCs) exist as a solid lipid matrix at room and body temperatures	LNPs can integrate lipophilic and hydrophobic drugs with minimal acute and lifelong toxicity. They effectively deter drug leakage and degradation during storage.	They have excessive water content, which can create stability issues, and modification to some crystalline lipids can cause the leaking of the encapsulated drug.	(Khosa et al., 2018, Dhiman et al., 2021)

	like SNLPs but have different interior patterns.			
Polymeric micelles-based drug delivery systems	Polymeric micelles are composed of amphiphilic block copolymers that form nanosized micellar structures with a hydrophobic core and a hydrophilic shell, which provides stability to the micelle.	They can efficiently solubilise various low-soluble drugs while encapsulating them within the polymeric micelle core, protecting them against quick clearance from circulation.	Some polymeric micelles are easily degraded when exposed to oxygen, and they have adverse reactions, such as hypersensitive reactions, which may result in anaphylactic shock.	(Jhaveri and Torchilin, 2014, Galetti et al., 2019, Lu and Park, 2013)

2.5.1. Polymeric-based HDT-TB drug delivery systems

Polymeric NPs have triggered a vast research interest as a drug delivery system due to their exceptional properties, including passive deposition in the target site, modified release biocompatibility and physicochemical stability (Praphakar et al., 2017). Furthermore, the hydrophilic outer core and hydrophobic inner core of polymeric NPs allow for the entrapment of various drugs within it (Praphakar et al., 2017). Several natural polymer-carriers, including poly (lactic-co-glycolic acid) (PLGA), hyaluronic acid, alginate, carboxymethyl cellulose, and other biodegradable, have been used as nano-based drug delivery systems with high drug loading capacity, drug incorporation feasibility, and variable route of administration feasibility (Hussain et al., 2019). Polymeric-based drug delivery may be engineered for delayed, sustained, and controlled drug release from the matrix (Hussain et al., 2019).

Dube et al. developed a host-directed based polymeric 1,3, Beta-glucan functionalised chitosan PLGA polymeric nanosystem (Glu-CS-PLGA) that increased ROS/RNS, pro-inflammatory cytokine production, and RIF delivery within human alveolar like macrophages (ALM) (Dube et al., 2014). This system further increased ALM secretion of INF-γ (23-fold), IL-12p70 (2.9-fold) and TNF-α (16-fold) over 24 hours **(Figure 2.5)** and doubled ROS/RNS

production over 6 hours (**Figure 2.6)**, compared to controls; compared to the RIF solution, Glu-CS-PLGA NPs delivered 4-fold more RIF into ALM (Dube et al., 2014). Recent similar work by D'Souza et al. found that curdlan functionalised PLGA NPs intended for host-directed therapy increased and accelerated the release of pro-inflammatory cytokine TNF-α in macrophages, resulting in lower intracellular Mtb levels within the macrophages (D'Souza et al., 2022). The study also revealed that curdlan has a high affinity for Dectin-1 receptors (D'Souza et al., 2022), giving an advantage in delivering anti-TB therapeutics and AICs directly to macrophages, enhancing drug payload on targeted cells while decreasing immunotoxicity. Furthermore, the study demonstrated that the produced nanosystem was non-toxic, necessitating future research as a host-directed treatment therapy for Mtb intracellular elimination (D'Souza et al., 2022).

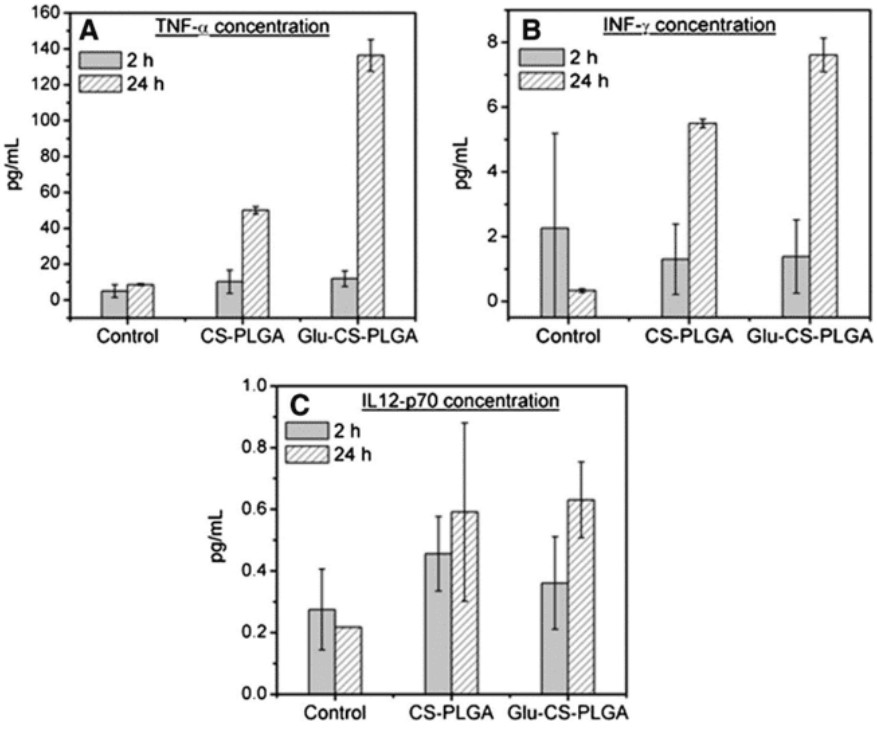

Figure 2.5: Results from Dube et al., 2014 show concentrations of (A) TNF-α, (B) IFN-γ and (C) IL-12p70 in ALM supernatants in different groups after 2 and 24 hours. (Reprinted from Dube et al., 2014, with permission).

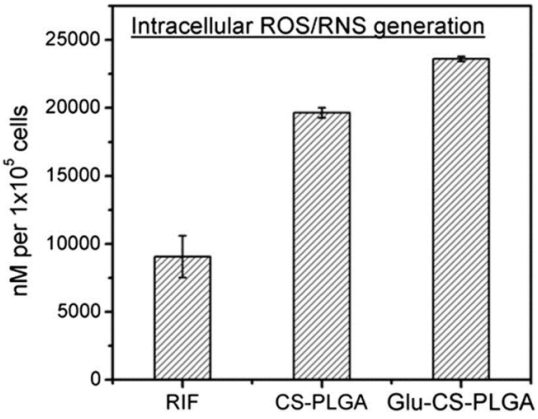

Figure 2.6: Results from Dube et al., 2014 showing total ROS/RNS generated after six hours of incubation of ALM with free drug solution (RIF), CS-PLGA, and Glu-CS-PLGA nanoparticles (Reprinted from Dube et al., 2014, with permission).

In these two separate studies (Dube et al., 2014 and D'Souza et al., 2022), the authors' designed drug delivery systems proposed to address the hard-to-treat infectious disease (TB) using NPs modified with ligands that can concurrently modulate the cellular immune response and deliver a drug. Curdlan and 1,3-β-glucan modified PLGA NPs were designed, respectively, following a well-established modified emulsion-solvent evaporation technique. In both studies, the authors showed the effectiveness of designed nanosystems intended for host-directed therapy by applying proteomic techniques such as immunoassays to quantify and analyse various cytokines, producing reliable experimental results. The results obtained in these studies are crucial for future research exploring HDT-TB based nanomaterials and adjuvants.

Sharma et al. investigated the possibility of using PLGA nanoparticles encapsulated with a synthetic Magainin-I analogue peptide (MIAP) as host-directed therapy against TB (Sharma et al., 2018). Porous Nanoparticle Aggregates Particles (PNAP), a micron-sized inhalable platform with nano-scale physiognomies, was created to increase MIAP-peptide delivery and stability. The pathogenic H37Rv TB bacteria was used in antimicrobial and mechanistic research of MIAP-PNAP. The MIAP-PNAP nano-assemblies showed dose and time-dependent antibacterial activity against pathogenic Mtb, considerably lowering the percentage of viable bacteria compared to the non-treated group during 48-96 hours in the Mtb infected macrophages shown in Table 3 in detail (Sharma et al., 2018). Furthermore, MIAP nano-formulation improved host defence mechanisms by preventing bacteria-induced inhibition of phagosomal-lysosome fusion and apoptosis, indicating that MIAP-PNAP nanoparticles can be

used as an adjunctive host-directed TB therapy to boost the efficacy of standard anti-TB drugs (Sharma et al., 2018).

Table 2.3: Detailed results from Sharma et al., 2018 showing the total number of Mtb CFU recovered after dose- and time-dependent treatment with bare and encapsulated MIAP and INH in a Colony Forming Assay (Reprinted from Sharma et al., 2018, with permission).

Treatment groups	**Log10 CFU/ml of Cell lysate**			
		24 h	**48 h**	**96 h**
Placebo	Untreated	6.14 ± 1.15	6.09 ± 1.04	6.21 ± 0.89
	Blank-PNAP	6.09 ± 0.78	6.08 ± 0.57	5.98 ± 0.51
Isoniazid Solution	INH (3 µg/ml)	2.08 ± 0.31	2.05 ± 0.88	1.25 ± 0.24
MIAP-PNAP group	MIAP-PNAP (10 µM)	5.57 ± 0.57	5.15 ± 0.78	4.92 ± 0.49
	MIAP-PNAP (50 µM)	5.36 ± 1.04	4.25 ± 1.12	4.02 ± 0.48
	MIAP-PNAP (100 µM)	3.65 ± 0.41	3.64 ± 0.74	3.18 ± 0.12
MIAP Solution Group	Pure MIAP (10 µM)	5.96 ± 0.54	5.86 ± 0.65	5.53 ± 0.28
	Pure MIAP (50 µM)	5.58 ± 1.08	5.49 ± 1.18	5.41 ± 0.47
	Pure MIAP (100 µM)	5.42 ± 0.19	4.89 ± 0.41	4.64 ± 0.58
MIAP+INH- PNAP	MIAP-PNAP (100 µM) plus INH (1 µg/ml)	2.14 ± 1.26	1.85 ± 1.25	1.17 ± 0.14

Rifabutin-loaded Glucan nanoparticles [(RB-NPs)-GP] have also been reported to enhance a robust innate immune response in Mtb-infected J774 macrophage cells, including the production of ROS/RNS, Autophagy, and apoptosis (Upadhyay et al., 2019). The efficacy testing of these NPs in murine macrophages revealed that the (RB-NPs)-GP formulation increased the efficacy of the RB drug by 2.5 fold, implying that the set of innate responses conducive to killing intracellular bacteria elicited by (RB-NPs)-GP play a critical role in impeding intracellular Mtb survival (Upadhyay et al., 2019). This study found that the (RB-NPs)-GP formulation not only activates Mtb-infected, immune-suppressed macrophages for host-directed therapy but also increases the effectiveness of the loaded drug. Thus making

(RB-NPs)-GP formulation a viable strategy that should be investigated further as an alternative or complement to the current TB treatment and host-directed regime (Upadhyay et al., 2019).

N-acetyl-L-cysteine (NAC) is an FDA-approved antidote for a hepatotoxic dosage of acetaminophen that has been listed as an essential medicine by WHO (Puri et al., 2022). NAC acts as an antioxidant, mucolytic agent, anti-inflammatory, and antimycobacterial effect by enhancing interleukins and INF-γ production (Amaral et al., 2016). Puri et al. used the double emulsion method to fabricate inhalable NAC-modified PLGA mucus penetrating particles for target delivery to AMs, minimising dose-related adverse effects, efficiently encapsulating hydrophilic drug, with sustained release profile, and prolonging the retention time for the treatment of TB (Puri et al., 2022). Coated NAC-PLGA-MPPs showed favourable results in terms of emitted dose (86%), MMAD value (2.57 μm), GSD value (1.55 μm), and FPF of 62% for deposition and targeting the lungs in an in vitro lung deposition investigation. Finally, in vitro, effectiveness experiments revealed that NAC-PLGA-MPPs had more antibacterial activity than NAC alone against the Mtb H37Rv strain (Puri et al., 2022). As a result, PLGA-based particles may be a better strategy for delivering NAC to the lungs while also acting as an excellent HDT-TB agent.

2.5.2. Solid Lipid Nanoparticles-based HDT-TB Drug Delivery System

SLNs are made up of polymeric NPs and LPs, as previously stated. Compared to vesicular drug delivery systems and polymeric NPs, SLNPs have longer/higher stability, improved encapsulation efficiency, and require a small amount of organic solvents (Nasiruddin et al., 2017). Superior tolerability (owing to their genesis in physiological lipids), scaling up practicality, the capacity to integrate hydrophobic or hydrophilic drugs and enhanced drug stability are the main defining features of SLNPs (Kaur and Singh, 2014). Pereira and colleagues developed a host-directed strategy against Mtb infection by designing a biocompatible nanocarrier for phage-derived protein delivery, using M. smegmatis as a model (Pereira et al., 2015). The rationale behind the study design was that Mtb pathogenicity is strongly supported by the presence of lipids in the cell wall. Thus, its degradation induces bacterial destruction through cell wall hydrolysis (Pereira et al., 2015). The proposed Ms6 LysB-containing lipid nanocarrier (SLN LysB) investigated the known benefits of nano-based systems for selectively targeting phagocytic cells, allowing LysB intracellular accumulation and more effective Mtb infection eradication (Pereira et al., 2015). The adsorption efficiency value suggested the system's potential as a protein nanocarrier.

Furthermore, encouraging results were achieved in host-infected macrophages treated with SLN LysB. The results demonstrated that the proposed technique was more potent than free LysB in preventing the proliferation of M. smegmatis, which might be attributed to nanocarrier internalisation (Pereira et al., 2015). The protein-guided delivery in the infected phagocytic cells enabled it to exert its hydrolytic activity on the Mtb lipid layer, indicating the effectiveness of the protein nanocarriers as an alternative host-directed TB therapeutic (Pereira et al., 2015). In another work, Ma et al. created a mannose-modified macrophage-targeting SLN (MAN-IC-SLN) loaded with the pH-sensitive prodrug of INH to cure latent TB infection. To target macrophages, the surface of SLNs was modified with a synthetic 6-octadecylimino-hexane-1,2,3,4,5-pentanol (MAN-SA), and the modified SLNs demonstrated a greater cell uptake in macrophages than unmodified SLNs (Ma et al., 2021). The prodrug isonicotinic acid octylidene-hydrazide (INH-CHO) was synthesised to produce a pH-sensitive release of INH in macrophages. The pH-sensitive release profile of the INH-CHO-loaded SLNs was observed, with a higher pH medium achieving a more significant cumulative release than a lower pH medium (Ma et al., 2021). M smegmatis was used in place of Mtb. Because of the pH-sensitive degradation of INH-CHO and MAN-SA in SLNs, the MAN-IC-SLNs demonstrated a fourfold increase in intracellular antibiotic effectiveness and improved macrophage uptake (Ma et al., 2021). In the in vivo antibiotic effectiveness test, the SLNs group had a considerably more extensive reduction in colony-forming units than the free INH group. The research found that macrophage targeting and pH-sensitive SLNs might be a suitable platform for latent TB treatment (Ma et al., 2021). SLNs serve as an excellent carrier that can be further modified and employed for further development of host-directed-TB therapy in future.

Aside from the nano-formulations mentioned above, the area possesses a surplus of other nanocarriers yet to be fully explored in the HDT-TB niche. For example, a dual drug-loaded (RIF and INH) SNLPs system was designed in a more recent work by Banerjee et al., exhibiting a sustained in vitro release pattern. The developed carrier system successfully localised within the various compartments of THP-1, and in vivo tests indicated that the relative bioavailability from the SLNPs was 7.5 times more than that of the drug solution, demonstrating the efficacy provided by SLNPs (Banerjee et al., 2020). In another separate study, a single oral administration of SLNPs formulation enclosing INH resulted in a six-fold increase in plasma drug concentration and a four-fold increase in brain concentration compared to a free drug at the same dose with improved relative bioavailability (Bhandari and Kaur, 2013). Lastly, SLNPs formulations for pulmonary administration of RIF utilising stearic acid and taurocholate were also shown to be capable of delivering large drug loads to the lung's AMs, with in vitro studies on the J774 cell line indicating non-cytotoxicity on cells (Maretti et al., 2014).

2.5.3. Vesicular-based HDT-TB drug delivery systems: Liposomes and Niosomes

Vesicular-based drug delivery systems (liposomes and niosomes) are closed vesicles made up of a phospholipid bilayer that encases an aqueous region (Nasiruddin et al., 2017, Hussain et al., 2019). They have been extensively investigated as a potential drug delivery platform for bioactive molecules due to their unique ability to encapsulate hydrophilic and hydrophobic molecules (Nasiruddin et al., 2017, Hussain et al., 2019). Owing to their biocompatibility and biodegradability, vesicular systems as carriers offer immense potential for drug delivery systems; nevertheless, novel LPs systems suffer from a lack of reproducibility and poor stability during storage due to drug-carrier complex alterations (Rodrigues et al., 2003). LPs are phagocytised by macrophagic cells to meet their fate, making them a possible choice for delivering anti-TB therapeutics to the host (Nabi et al., 2020). Niosomes, on the other hand, resemble LPs except that they are made up of a surfactant bilayer with hydrophilic ends exposed to the aqueous phase on the outside and interior of the vesicle and hydrophobic chains facing each other within the bilayer (Hussain et al., 2019, Mozafari, 2007). Niosomes can be employed as orally controlled release systems; for example, orally active anti-TB hydrophilic drugs like INH and PZA demonstrated sustained drug release from the tyloxapol niosomes membrane (Mehta and Jindal, 2013). The biocompatible surfactant tyloxapol in the production of niosomes drug delivery systems encapsulating anti-TB drugs resulted in a very stable nanosystem with a considerably increased dissolution rate and high drug entrapment efficiency with no drug-carrier interaction (Mehta and Jindal, 2013).

The key pathogenetic event of Mtb and HIV coinfection is chronic immunological activation (Poerio et al., 2022). In an in vitro model of Mtb-HIV coinfection, Poerio et al. evaluated the therapeutic potential of phosphatidylserine-liposome (PS-L). PS-L inhibited nuclear factor- κB activation and the downstream generation of IL-1β, TNF-α, and IL-6 in BCG-infected macrophages, as well as TNF-α and IL-1 β in Mtb-HIV-coinfected macrophages. Notably, there was a considerable decrease in intracellular Mtb viability and HIV replication (Poerio et al., 2022). These findings suggest that PS-L might be used as a host-directed treatment for Mtb-HIV coinfection in the future.

A novel liposomal adjuvant including N, N-Dimethyltryptamine (DMT), a potent inducer of Th1-biased immune response, dimethyl-dioctadecyl-ammonium (DDA), and two pattern recognition receptor agonists, monophosphoryl lipid A and trehalose 6,6'-behenate (TDB), was developed (Tian et al., 2018). The pCMFO antigen-loaded DDA liposomes were formulated and evaluated with and without mono-phosphoryl lipid A (MPLA) and TDB. In vivo studies on experimental mice were conducted using various treatments: pCMFO,

pCMFO/DDA, or pCMFO/DMT. The immunogenicity and efficacy of BCG-vaccinated mice against Mtb were also compared and assessed. In vaccinated mice, the DDA liposome alone or combined with TDB or MPLA triggered early IL-17 and interferon responses (Tian et al., 2018). Thus, the controlled release function of the DMT liposome may be linked to the improved efficacy of DMT (adjuvant) vaccination against TB, illustrating the practical benefits afforded by liposomes (Tian et al., 2018).

Kulkarni et al. synthesised dual drug-loaded self-assembled niosomes containing ethionamide and D-Cycloserine to treat MDR-TB effectively. Box Behnken design was used to improve the niosomes, which were then evaluated for the antibacterial test, osmotic shock and in vitro haemodialysis, among other studies (Kulkarni et al., 2019). The haemodialysis tests demonstrated that dual drug-loaded niosomes may be safely administered intravenously and that dual drug-loaded niosomes had the lowest MIC compared to pure drug and single drug-loaded niosomes. The delayed release of lipophilic ethambutol and the early burst release of D-Cycloserine contributed to its efficacy (Kulkarni et al., 2019). As a result, the synergistic impact of two drugs in niosomes proved to be an efficient TB therapy (Kulkarni et al., 2019). In a separate study, Rani et al. investigated the bactericidal activities of prepared niosomes of RIF and gatifloxacin against sensitive (H37Rv) and resistant (RF 8554) Mtb strains, revealing inhibition and a reduced bacterial growth index, indicating that niosomes provided an extensive release of drugs, allowing for a lower dose, fewer days of treatment, and greater patient compliance (Rani et al., 2010). However, because most studies on NPs with potential HDT-TB applications around the world have gone unnoticed, there has been a scarcity of data on the use of liposomes and niosomes for host-directed therapy in TB. **Table 2.4** summarises some nanosystems that can be investigated further for use as host-directed TB therapies in the near future due to their favourable observed outcomes.

Table 2.4: Summary of anti-mycobacterial nanoparticle-based carriers that can be employed for HDT-TB.

Drug/s encapsulated	Nanocarrier Composition material	Outcome observed or achievements.	References
RIF	Gelatine NPs	Better biodistribution of RIF and higher blood levels in mice.	(Saraogi et al., 2010)
INH	Monnosylated Gelatine NPs	Reduced bacteria in TB-infected mice and hepatotoxicity of the drug.	(Saraogi et al., 2011)

RIF	CS-coated PLGA NPs	Enhanced intracellular trafficking and drug concentration compared to free drugs.	(Kutscher et al., 2019)
RIF	Solid-lipid NPs	Increased RIF levels in alveolar macrophages.	(Chuan et al., 2013)
RIF	Monnosylated Cationic lipid NPs	Higher uptake efficiency by alveolar macrophages was observed.	(Song et al., 2015)
RIF and ascorbic acid	CS-coated alginate tween 80 NPs	NPs significantly suppressed Mtb at the same concertation when compared to free drugs and enhanced cell viability even more.	(Scolari et al., 2019)
INH/RIF	Chitosan NPs	It improved the in vitro and in vivo efficacy of INH/RIF compared to free drugs.	(Pourshahab et al., 2011, Garg et al., 2016)
RIF	Lactose-conjugated PLGA NPs	Significantly Increased lung uptake of RIF.	(Jain et al., 2010)
Tuftsin	Pluronic F127 coated PLGA NPs	It significantly increased the internalisation of the drug within the macrophages.	(Horvati et al., 2018)
RIF	Poly (ethylene oxide) monomethyl ether-block poly(e-caprolactone) NPs	The NPs were easily taken up by the macrophages and quickly associated with the lysosomal compartment.	(Trousil et al., 2017)
INH	Mycolic acid-PLGA NPs	Increased uptake and fusion with lysosomes containing mycobacteria.	(Lemmer et al., 2015)

2.6. Delivery of NPs to the targeted host

Material modification with suitable transport mediating molecules can further assist with the preferred NPs delivery route, which could be via the gastrointestinal system, topical, urogenital tract, or pulmonary route, as shown in **Figure 2.7** (Woodrow et al., 2009, Look et al., 2010). As a result of these distinct properties, NPs can be easily loaded or coupled with immunomodulatory substances such as immune cell-specific ligands or cytokines and be

administered through various routes to improve immunity against infectious disease (Look et al., 2010). In Mtb treatment, oral, intravenous, and pulmonary delivery of nanocarriers has shown great potential, with oral administration as the most preferred delivery route (Baranyai et al., 2020). Because oral administration is less intrusive and more convenient, it may boost patients' compliance to complete the treatment (Plapied et al., 2011, Baranyai et al., 2020). However, the extreme environment present in the stomach, medium-low pH and highly proteolytic media – as well as the hepatic first-pass metabolism, restrict the possible formulations that may be used and impair bioavailability (Plapied et al., 2011). While Intravenous administration bypasses the first-pass metabolism, allowing drugs to be absorbed quickly and directly into the systemic circulation while allowing for more accurate administered dosage control (Monopoli et al., 2012).

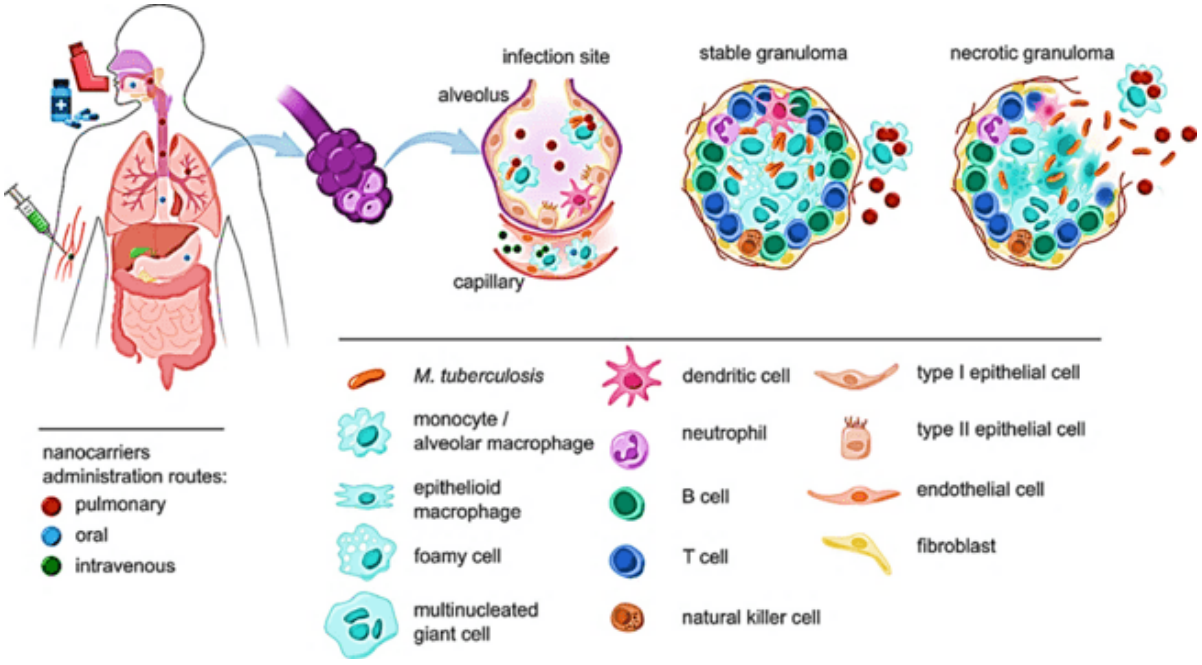

Figure 2.7: Different routes of nanoparticle administration targeting the host and granuloma (Reprinted from Baranyai et al., 2020, with permission).

In pulmonary TB, direct targeting of the Mtb with pulmonary administration is the most promising approach because it allows for far more efficient therapy with lower administration doses and lower toxicity than the oral route (Costa et al., 2016, Baranyai et al., 2020). Most anti-TB drugs have low water solubility, low biodistribution, and adverse effects when administered orally; therefore, pulmonary delivery is more efficacious and promising (Costa et al., 2016). The significantly improved bioavailability also advances the use of the pulmonary route since the activity of the drug-metabolizing enzymes is restricted compared to parental

routes of administration (Costa et al., 2016). It can also improve patient compliance because it is non-invasive and self-administrable (Momin et al., 2019). On the other hand, the respiratory system's structure and function play a role in pathogen defence; as a result, overcoming anatomical and biological obstacles in the respiratory system might be difficult (Baranyai et al., 2020).

2. 7. Conclusion and future research perspective

Several potential research and development opportunities exist in using immunomodulatory nanoparticles to improve infectious disease outcomes, particularly in the treatment of Mtb infection. Despite the tremendous work done to contain the Mtb pandemic, Mtb has developed numerous strategies to circumvent the host's protective response. The rise in Mtb resistance to a range of current anti-TB therapeutics has become a global health concern. As a result, developing novel therapeutic techniques has become the main priority. At least three new requirements necessitate extra attention in developing immunomodulatory nanoparticle-based therapies for Mtb infection: Multidrug-resistant infection, co-infection with several diseases (HIV/TB), and host-directed treatment. Nanotechnology solutions coupled with immunomodulatory agents/AICs as part of HDT therapies (HDT-TB) may assist in meeting this demand by increasing treatment regimen efficacy, minimising the development of drug-resistant strains, and possibly decreasing the frequency and expense of dosing while boosting the host's immunological response to infection. This will further enable more targeted drug delivery, reducing harmful side effects while increasing drug concentration in target cells.
Although many AICs and NPs are accessible, there is still a small amount of research on the use of AICs and therapeutic NPs to treat Mtb.

Aside from reducing treatment time and improving antibiotic effectiveness, another objective of host-directed TB therapy is to prevent irreparable lung damage caused by an ineffective inflammatory response. Immunocompetent individuals with active TB have significant pro-inflammatory immune responses that fail to control bacterial growth, resulting in tissue damage and ineffective inflammation. As a result, numerous AICs that have the potential to minimise non-productive inflammation and potentially severe tissue damage may be explored further by incorporating them into NPs for active targeting. Matrix metalloproteinase inhibitors, TNF antagonists, and corticosteroids are examples of these. Modulating individual immunosuppressive immune responses, on the other hand, may increase the immune system's innate bactericidal activity and speed up bacterial clearance. As a result, repurposing

immunosuppressive reagents such as phosphodiesterase inhibitors, Treg-depleting immunotherapies, and anti-IL-10 therapies may benefit the HDT-TB strategy.

In addition, many vitamins have been studied for their involvement in pathogenic and bactericidal activity. Further investigation into these vitamins combined with nanotechnology and traditional anti-TB therapeutics may further pave the way forward for HDT-TB therapeutics. As discussed in **Section 2.3.1**, supplementing standard anti-TB therapeutics with some vitamins decreased antigen-stimulated pro-inflammatory cytokine production and expedited inflammatory response resolution throughout therapy, improving clinical and radiological results. This, in combination with nanotechnology, may further allow for lower doses of standard anti-TB therapeutics, resulting in a shorter treatment duration and the development of treatment-resistant TB.

In conclusion, mechanical elements of the macrophage response to Mtb and its inhibition of autophagy must be explored further to enable a rational nanomedicine design for this infection. Although nanotechnology and HDT-TB appear promising, they have not provided any product in the market for this disease, and the number of patents in the sector is significantly low due to limited safety and biocompatibility profiles. To make ground-breaking progress, concerns regarding nanotechnology biocompatibility must be addressed regarding their application as immunomodulators. As a result, developing clinical effectiveness, cost, accessibility, and toxicity studies will boost the overall value of new HDT-TB therapies and nanotechnology, paving the way for commercialisation.

2. 8. Acknowledgement

This work was supported by the National Research Foundation (NRF) South Africa [grant numbers: UID 131269]. The content is solely the authors' responsibility and does not necessarily represent the official views of the National Research Foundation.

2. 9. References

Abed, N. & Couvreur, P. 2014. Nanocarriers for antibiotics: a promising solution to treat intracellular bacterial infections. *Int J Antimicrob Agents,* 43**,** 485-96.

Adikesavalu, H., Gopalaswamy, R., Kumar, A., Ranganathan, U. D. & Shanmugam, S. 2021. Autophagy Induction as a Host-Directed Therapeutic Strategy against Mycobacterium tuberculosis Infection. *Medicina (Kaunas),* 57**,** 522.

Alavi-Naini, R., Sharifi-Mood, B. & Metanat, M. 2012. Association between tuberculosis and smoking. *Int J High Risk Behav Addict,* 1**,** 71-4.

Allue-Guardia, A., Garcia, J. I. & Torrelles, J. B. 2021. Evolution of Drug-Resistant Mycobacterium tuberculosis Strains and Their Adaptation to the Human Lung Environment. *Front Microbiol,* 12**,** 612675.

Amaral, E. P., Conceicao, E. L., Costa, D. L., Rocha, M. S., Marinho, J. M., Cordeiro-Santos, M., et al. Andrade, B. B. 2016. N-acetyl-cysteine exhibits potent anti-mycobacterial activity in addition to its known anti-oxidative functions. *BMC Microbiol,* 16**,** 251.

Andrade, F., Rafael, D., Videira, M., Ferreira, D., Sosnik, A. & Sarmento, B. 2013. Nanotechnology and pulmonary delivery to overcome resistance in infectious diseases. *Adv Drug Deliv Rev,* 65**,** 1816-27.

Andrade, F., Videira, M., Ferreira, D. & Sarmento, B. 2011. Micelle-based systems for pulmonary drug delivery and targeting. *Drug Delivery Letters,* 1**,** 171-185.

Aranow, C. 2011. Vitamin D and the immune system. *J Investig Med,* 59**,** 881-6.

Atri, C., Guerfali, F. Z. & Laouini, D. 2018. Role of Human Macrophage Polarization in Inflammation during Infectious Diseases. *Int J Mol Sci,* 19**,** 1801.

Banerjee, D. & Bhattacharyya, R. 2014. Statin therapy may prevent development of tuberculosis in diabetic state. *Med Hypotheses,* 83**,** 88-91.

Banerjee, S., Roy, S., Bhaumik, K. N. & Pillai, J. 2020. Mechanisms of the effectiveness of lipid nanoparticle formulations loaded with anti-tubercular drugs combinations toward overcoming drug bioavailability in tuberculosis. *J Drug Target,* 28**,** 55-69.

Baranyai, Z., Soria-Carrera, H., Alleva, M., Millán-Placer, A. C., Lucía, A., Martín-Rapún, R., et al. De La Fuente, J. M. 2020. Nanotechnology-Based Targeted Drug Delivery: An Emerging Tool to Overcome Tuberculosis. *Advanced Therapeutics,* 4**,** 2000113.

Barberis, I., Bragazzi, N. L., Galluzzo, L. & Martini, M. 2017. The history of tuberculosis: from the first historical records to the isolation of Koch's bacillus. *J Prev Med Hyg,* 58**,** E9-E12.

Bedard, K. & Krause, K. H. 2007. The NOX family of ROS-generating NADPH oxidases: physiology and pathophysiology. *Physiol Rev,* 87**,** 245-313.

Behar, S. M., Martin, C. J., Booty, M. G., Nishimura, T., Zhao, X., Gan, H. X., et al. Remold, H. G. 2011. Apoptosis is an innate defense function of macrophages against Mycobacterium tuberculosis. *Mucosal Immunol,* 4**,** 279-87.

Bekale, R. B., Du Plessis, S. M., Hsu, N. J., Sharma, J. R., Sampson, S. L., Jacobs, M., et al. Dube, A. 2018. Mycobacterium Tuberculosis and Interactions with the Host Immune System: Opportunities for Nanoparticle Based Immunotherapeutics and Vaccines. *Pharm Res,* 36**,** 8.

Bento, C. F., Empadinhas, N. & Mendes, V. 2015. Autophagy in the fight against tuberculosis. *DNA Cell Biol,* 34**,** 228-42.

Bhandari, R. & Kaur, I. P. 2013. Pharmacokinetics, tissue distribution and relative bioavailability of isoniazid-solid lipid nanoparticles. *International journal of pharmaceutics,* 441**,** 202-12.

Bigelow, K. M., Tasneen, R., Chang, Y. S., Dooley, K. E. & Nuermberger, E. L. 2020. Preserved Efficacy and Reduced Toxicity with Intermittent Linezolid Dosing in Combination with Bedaquiline and Pretomanid in a Murine Tuberculosis Model. *Antimicrob Agents Chemother,* 64**,** e01178-20.

Booysen, L. L., Kalombo, L., Brooks, E., Hansen, R., Gilliland, J., Gruppo, V., et al. Du Plessis, L. H. 2013. In vivo/in vitro pharmacokinetic and pharmacodynamic study of spray-dried poly-(dl-lactic-co-glycolic) acid nanoparticles encapsulating rifampicin and isoniazid. *International journal of pharmaceutics,* 444**,** 10-7.

Bourigault, M. L., Vacher, R., Rose, S., Olleros, M. L., Janssens, J. P., Quesniaux, V. F. & Garcia, I. 2013. Tumor necrosis factor neutralization combined with chemotherapy enhances Mycobacterium tuberculosis clearance and reduces lung pathology. *Am J Clin Exp Immunol,* 2**,** 124-34.

Cadena, A. M., Flynn, J. L. & Fortune, S. M. 2016. The Importance of First Impressions: Early Events in Mycobacterium tuberculosis Infection Influence Outcome. *mBio,* 7**,** e00342-16.

Cambau, E. & Drancourt, M. 2014. Steps towards the discovery of Mycobacterium tuberculosis by Robert Koch, 1882. *Clin Microbiol Infect,* 20**,** 196-201.

Campbell, G. R. & Spector, S. A. 2011. Hormonally active vitamin D3 (1alpha,25-dihydroxycholecalciferol) triggers autophagy in human macrophages that inhibits HIV-1 infection. *J Biol Chem,* 286**,** 18890-902.

Chai, Q., Wang, L., Liu, C. H. & Ge, B. 2020. New insights into the evasion of host innate immunity by Mycobacterium tuberculosis. *Cell Mol Immunol,* 17**,** 901-913.

Chai, Q., Zhang, Y. & Liu, C. H. 2018. Mycobacterium tuberculosis: An Adaptable Pathogen Associated With Multiple Human Diseases. *Front Cell Infect Microbiol,* 8**,** 158.

Chuan, J., Li, Y., Yang, L., Sun, X., Zhang, Q., Gong, T. & Zhang, Z. 2013. Enhanced rifampicin delivery to alveolar macrophages by solid lipid nanoparticles. *Journal of Nanoparticle Research,* 15**,** 1-9.

Chun, R. F., Adams, J. S. & Hewison, M. 2011. Immunomodulation by vitamin D: implications for TB. *Expert Rev Clin Pharmacol,* 4**,** 583-91.

Conradie, F., Diacon, A., Everitt, D., Mendel, C., Van Niekerk, C., Howell, P., et al. Spigelman, M. The NIX-TB trial of pretomanid, bedaquiline and linezolid to treat XDR-TB. Conference on retroviruses and opportunistic infections (CROI), 2017. 13-16.

Conradie, F., Diacon, A. H., Ngubane, N., Howell, P., Everitt, D., Crook, A. M., et al. Nix, T. B. T. T. 2020. Treatment of Highly Drug-Resistant Pulmonary Tuberculosis. *N Engl J Med,* 382**,** 893-902.

Costa, A., Pinheiro, M., Magalhaes, J., Ribeiro, R., Seabra, V., Reis, S. & Sarmento, B. 2016. The formulation of nanomedicines for treating tuberculosis. *Adv Drug Deliv Rev,* 102**,** 102-15.

Coussens, A. K., Wilkinson, R. J., Hanifa, Y., Nikolayevskyy, V., Elkington, P. T., Islam, K., et al. Martineau, A. R. 2012. Vitamin D accelerates resolution of inflammatory responses during tuberculosis treatment. *Proceedings of the National Academy of Sciences of the United States of America,* 109**,** 15449-54.

Coussens, A. K., Wilkinson, R. J. & Martineau, A. R. 2015. Phenylbutyrate Is Bacteriostatic against Mycobacterium tuberculosis and Regulates the Macrophage Response to Infection, Synergistically with 25-Hydroxy-Vitamin D3. *Plos Pathog,* 11**,** e1005007.

Crowther, R. R. & Qualls, J. E. 2020. Metabolic Regulation of Immune Responses to Mycobacterium tuberculosis: A Spotlight on L-Arginine and L-Tryptophan Metabolism. *Front Immunol,* 11**,** 628432.

D'souza, S., Du Plessis, S. M., Egieyeh, S., Bekale, R. B., Maphasa, R. E., Irabin, A. F., et al. Dube, A. 2022. Physicochemical and Biological Evaluation of Curdlan-Poly(Lactic-Co-Glycolic Acid) Nanoparticles as a Host-Directed Therapy Against Mycobacterium Tuberculosis. *J Pharm Sci,* 111**,** 469-478.

Dahl, J. L., Wei, J., Moulder, J. W., Laal, S. & Friedman, R. L. 2001. Subcellular localization of the Iitracellular survival-enhancing Eis protein of Mycobacterium tuberculosis. *Infect Immun,* 69**,** 4295-302.

Dartois, V. 2014. The path of anti-tuberculosis drugs: from blood to lesions to mycobacterial cells. *Nat Rev Microbiol,* 12**,** 159-67.

Deretic, V. 2014. Autophagy in tuberculosis. *Cold Spring Harb Perspect Med,* 4**,** a018481.

Dhiman, N., Awasthi, R., Sharma, B., Kharkwal, H. & Kulkarni, G. T. 2021. Lipid Nanoparticles as Carriers for Bioactive Delivery. *Frontiers in Chemistry,* 9.

Dobrovolskaia, M. A., Shurin, M. & Shvedova, A. A. 2016. Current understanding of interactions between nanoparticles and the immune system. *Toxicol Appl Pharmacol,* 299**,** 78-89.

Dong, X. P., Shen, D., Wang, X., Dawson, T., Li, X., Zhang, Q., et al. Xu, H. 2010. PI(3,5)P(2) controls membrane trafficking by direct activation of mucolipin Ca(2+) release channels in the endolysosome. *Nat Commun,* 1**,** 38.

Dube, A., Reynolds, J. L., Law, W. C., Maponga, C. C., Prasad, P. N. & Morse, G. D. 2014. Multimodal nanoparticles that provide immunomodulation and intracellular drug delivery for infectious diseases. *Nanomedicine : nanotechnology, biology, and medicine,* 10**,** 831-8.

Efremenko, Y. V., Arjanova, O. V., Prihoda, N. D., Yurchenko, L. V., Sokolenko, N. I., Mospan, I. V., et al. Kutsyna, G. A. 2012. Clinical validation of sublingual formulations of Immunoxel (Dzherelo) as an adjuvant immunotherapy in treatment of TB patients. *Immunotherapy,* 4**,** 273-82.

Fang, F., Ge, Q., Li, R., Lv, J., Zhang, Y., Feng, A., et al. Qian, Z. 2020. LPS restores protective immunity in macrophages against Mycobacterium tuberculosis via autophagy. *Mol Immunol,* 124**,** 18-24.

Farazi, A., Shafaat, O., Sofian, M. & Kahbazi, M. 2015. Arginine adjunctive therapy in active tuberculosis. *Tuberc Res Treat,* 2015**,** 205016.

Floto, R. A., Sarkar, S., Perlstein, E. O., Kampmann, B., Schreiber, S. L. & Rubinsztein, D. C. 2007. Small molecule enhancers of rapamycin-induced TOR inhibition promote autophagy, reduce toxicity in Huntington's disease models and enhance killing of mycobacteria by macrophages. *Autophagy,* 3**,** 620-2.

Gagneux, S. 2018. Ecology and evolution of Mycobacterium tuberculosis. *Nat Rev Microbiol,* 16**,** 202-213.

Galetti, M., Rossi, S., Caffarra, C., Gerboles, A. G. & Miragoli, M. 2019. Innovation in nanomedicine and engineered nanomaterials for therapeutic purposes. *In:* MARMIROLI, N., WHITE, J. C. & SONG, J. (eds.) *Exposure to Engineered Nanomaterials in the Environment.* Elsevier.

Garcia, I., Guler, R., Vesin, D., Olleros, M. L., Vassalli, P., Chvatchko, Y., et al. Ryffel, B. 2000. Lethal Mycobacterium bovis Bacillus Calmette Guerin infection in nitric oxide synthase 2-deficient mice: cell-mediated immunity requires nitric oxide synthase 2. *Lab Invest,* 80**,** 1385-97.

Garg, T., Rath, G. & Goyal, A. K. 2016. Inhalable chitosan nanoparticles as antitubercular drug carriers for an effective treatment of tuberculosis. *Artif Cells Nanomed Biotechnol,* 44**,** 997-1001.

Ghazaei, C. 2018. Mycobacterium tuberculosis and lipids: Insights into molecular mechanisms from persistence to virulence. *J Res Med Sci,* 23**,** 63.

Gina, P., Davids, M. & Dheda, K. 2019. Manipulation of autophagy for host-directed tuberculosis therapy. *Afr J Thorac Crit Care Med,* 25**,** 10.7196/AJTCCM.2019.v25i2.014.

Goletti, D., Petruccioli, E., Romagnoli, A., Piacentini, M. & Fimia, G. M. 2013. Autophagy in Mycobacterium tuberculosis infection: a passepartout to flush the intruder out? *Cytokine Growth Factor Rev,* 24**,** 335-43.

Green, D. R. 2011. *Means to an end: apoptosis and other cell death mechanisms*, Cold Spring Harbor Laboratory Press.

Grotz, E., Tateosian, N., Amiano, N., Cagel, M., Bernabeu, E., Chiappetta, D. A. & Moretton, M. A. 2018. Nanotechnology in Tuberculosis: State of the Art and the Challenges Ahead. *Pharm Res,* 35**,** 213.

Gu, F., Zhang, L., Teply, B. A., Mann, N., Wang, A., Radovic-Moreno, A. F., et al. Farokhzad, O. C. 2008. Precise engineering of targeted nanoparticles by using self-assembled biointegrated block copolymers. *Proceedings of the National Academy of Sciences of the United States of America,* 105**,** 2586-91.

Guirado, E., Schlesinger, L. S. & Kaplan, G. 2013. Macrophages in tuberculosis: friend or foe. *Semin Immunopathol,* 35**,** 563-83.

Gutierrez, M. G., Master, S. S., Singh, S. B., Taylor, G. A., Colombo, M. I. & Deretic, V. 2004. Autophagy is a defense mechanism inhibiting BCG and Mycobacterium tuberculosis survival in infected macrophages. *Cell,* 119**,** 753-66.

Haimhoffer, Á., Rusznyák, Á., Réti-Nagy, K., Vasvári, G., Váradi, J., Vecsernyés, M., et al. Fenyvesi, F. 2019. Cyclodextrins in Drug Delivery Systems and Their Effects on Biological Barriers. *Scientia Pharmaceutica,* 87**,** 33.

Hinchey, J., Lee, S., Jeon, B. Y., Basaraba, R. J., Venkataswamy, M. M., Chen, B., et al. Porcelli, S. A. 2007. Enhanced priming of adaptive immunity by a proapoptotic mutant of Mycobacterium tuberculosis. *J Clin Invest,* 117**,** 2279-88.

Hmama, Z., Pena-Diaz, S., Joseph, S. & Av-Gay, Y. 2015. Immunoevasion and immunosuppression of the macrophage by Mycobacterium tuberculosis. *Immunol Rev,* 264**,** 220-32.

Horvati, K., Gyulai, G., Csampai, A., Rohonczy, J., Kiss, E. & Bosze, S. 2018. Surface Layer Modification of Poly(d,l-lactic- co-glycolic acid) Nanoparticles with Targeting Peptide: A Convenient Synthetic Route for Pluronic F127-Tuftsin Conjugate. *Bioconjug Chem,* 29**,** 1495-1499.

Hunter, R. L., Olsen, M., Jagannath, C. & Actor, J. K. 2006. Trehalose 6,6'-dimycolate and lipid in the pathogenesis of caseating granulomas of tuberculosis in mice. *Am J Pathol,* 168**,** 1249-61.

Hussain, A., Singh, S., Das, S. S., Anjireddy, K., Karpagam, S. & Shakeel, F. 2019. Nanomedicines as Drug Delivery Carriers of Anti-Tubercular Drugs: From Pathogenesis to Infection Control. *Curr Drug Deliv,* 16**,** 400-429.

Italiani, P., Mazza, E. M., Lucchesi, D., Cifola, I., Gemelli, C., Grande, A., et al. Boraschi, D. 2014. Transcriptomic profiling of the development of the inflammatory response in human monocytes in vitro. *PLoS One,* 9**,** e87680.

Jaguin, M., Houlbert, N., Fardel, O. & Lecureur, V. 2013. Polarization profiles of human M-CSF-generated macrophages and comparison of M1-markers in classically activated macrophages from GM-CSF and M-CSF origin. *Cell Immunol,* 281**,** 51-61.

Jain, S. K., Gupta, Y., Ramalingam, L., Jain, A., Jain, A., Khare, P. & Bhargava, D. 2010. Lactose-Conjugated PLGA Nanoparticles for Enhanced Delivery of Rifampicin to the Lung for Effective Treatment of Pulmonary Tuberculosis. *PDA J Pharm Sci Technol,* 64**,** 278-87.

Jhaveri, A. M. & Torchilin, V. P. 2014. Multifunctional polymeric micelles for delivery of drugs and siRNA. *Front Pharmacol,* 5**,** 77.

Kalscheuer, R. & Koliwer-Brandl, H. 2014. Genetics of Mycobacterial Trehalose Metabolism. *Microbiol Spectr,* 2.

Kaufmann, S. H. E., Dorhoi, A., Hotchkiss, R. S. & Bartenschlager, R. 2018. Host-directed therapies for bacterial and viral infections. *Nat Rev Drug Discov,* 17**,** 35-56.

Kaur, I. P. & Singh, H. 2014. Nanostructured drug delivery for better management of tuberculosis. *J Control Release,* 184**,** 36-50.

Khosa, A., Reddi, S. & Saha, R. N. 2018. Nanostructured lipid carriers for site-specific drug delivery. *Biomedicine & Pharmacotherapy,* 103**,** 598-613.

Kilinc, G., Saris, A., Ottenhoff, T. H. M. & Haks, M. C. 2021. Host-directed therapy to combat mycobacterial infections. *Immunol Rev,* 301**,** 62-83.

Koch, A., Cox, H. & Mizrahi, V. 2018. Drug-resistant tuberculosis: challenges and opportunities for diagnosis and treatment. *Curr Opin Pharmacol,* 42**,** 7-15.

Kolloli, A. & Subbian, S. 2017. Host-Directed Therapeutic Strategies for Tuberculosis. *Front Med (Lausanne),* 4**,** 171.

Kulkarni, P., Rawtani, D. & Barot, T. 2019. Formulation and optimization of long acting dual niosomes using Box-Behnken experimental design method for combinative delivery of Ethionamide and D-cycloserine in Tuberculosis treatment. *Colloids and Surfaces A: Physicochemical and Engineering Aspects,* 565**,** 131-142.

Kumari, P. & Meena, L. S. 2014. Factors affecting susceptibility to Mycobacterium tuberculosis: a close view of immunological defence mechanism. *Appl Biochem Biotechnol,* 174**,** 2663-73.

Kutscher, H. L., Morse, G. D., Prasad, P. N. & Reynolds, J. L. 2019. In vitro Pharmacokinetic Cell Culture System that Simulates Physiologic Drug and Nanoparticle Exposure to Macrophages. *Pharm Res,* 36**,** 44.

Lammas, D., Stober, C., Harvey, C., Kendrick, N., Panchalingam, S. & Kumararatne, D. 1997. ATP-induced killing of mycobacteria by human macrophages is mediated by purinergic P2Z (P2X7) receptors. *Immunity,* 7**,** 433-444.

Lee, C. & Bhakta, S. 2021. The Prospect of Repurposing Immunomodulatory Drugs for Adjunctive Chemotherapy against Tuberculosis: A Critical Review. *Antibiotics (Basel),* 10**,** 91.

Lee, J., Hartman, M. & Kornfeld, H. 2009. Macrophage apoptosis in tuberculosis. *Yonsei Med J,* 50**,** 1-11.

Lemmer, Y., Kalombo, L., Pietersen, R. D., Jones, A. T., Semete-Makokotlela, B., Van Wyngaardt, S., et al. De Chastellier, C. 2015. Mycolic acids, a promising mycobacterial ligand for targeting of nanoencapsulated drugs in tuberculosis. *J Control Release,* 211**,** 94-104.

Liu, C. H., Liu, H. & Ge, B. 2017. Innate immunity in tuberculosis: host defense vs pathogen evasion. *Cell Mol Immunol,* 14**,** 963-975.

Long, R., Light, B. & Talbot, J. A. 1999. Mycobacteriocidal action of exogenous nitric oxide. *Antimicrob Agents Chemother,* 43**,** 403-5.

Look, M., Bandyopadhyay, A., Blum, J. S. & Fahmy, T. M. 2010. Application of nanotechnologies for improved immune response against infectious diseases in the developing world. *Adv Drug Deliv Rev,* 62**,** 378-93.

Lu, Y. & Park, K. 2013. Polymeric micelles and alternative nanonized delivery vehicles for poorly soluble drugs. *International journal of pharmaceutics,* 453**,** 198-214.

Ma, C., Wu, M., Ye, W., Huang, Z., Ma, X., Wang, W., et al. Wu, C. 2021. Inhalable solid lipid nanoparticles for intracellular tuberculosis infection therapy: macrophage-targeting and pH-sensitive properties. *Drug Deliv Transl Res,* 11**,** 1218-1235.

Ma, J., Yang, B., Yu, S., Zhang, Y., Zhang, X., Lao, S., et al. Wu, C. 2014. Tuberculosis antigen-induced expression of IFN-alpha in tuberculosis patients inhibits production of IL-1beta. *FASEB J,* 28**,** 3238-48.

Ma, Z., Lienhardt, C., Mcilleron, H., Nunn, A. J. & Wang, X. 2010. Global tuberculosis drug development pipeline: the need and the reality. *Lancet,* 375**,** 2100-9.

Macmicking, J. D., North, R. J., Lacourse, R., Mudgett, J. S., Shah, S. K. & Nathan, C. F. 1997. Identification of nitric oxide synthase as a protective locus against tuberculosis. *Proceedings of the National Academy of Sciences of the United States of America,* 94**,** 5243-8.

Maphasa, R. E., Meyer, M. & Dube, A. 2020. The Macrophage Response to Mycobacterium tuberculosis and Opportunities for Autophagy Inducing Nanomedicines for Tuberculosis Therapy. *Front Cell Infect Microbiol,* 10**,** 618414.

Maretti, E., Costantino, L., Rustichelli, C., Leo, E., Croce, M. A., Buttini, F., et al. Iannuccelli, V. 2017. Surface engineering of Solid Lipid Nanoparticle assemblies by methyl alpha-d-mannopyranoside for the active targeting to macrophages in anti-tuberculosis inhalation therapy. *International journal of pharmaceutics,* 528**,** 440-451.

Maretti, E., Rossi, T., Bondi, M., Croce, M. A., Hanuskova, M., Leo, E., et al. Iannuccelli, V. 2014. Inhaled Solid Lipid Microparticles to target alveolar macrophages for tuberculosis. *International journal of pharmaceutics,* 462**,** 74-82.

Martin, C. J., Peters, K. N. & Behar, S. M. 2014. Macrophages clean up: efferocytosis and microbial control. *Curr Opin Microbiol,* 17**,** 17-23.

Martinez, J., Almendinger, J., Oberst, A., Ness, R., Dillon, C. P., Fitzgerald, P., et al. Green, D. R. 2011. Microtubule-associated protein 1 light chain 3 alpha (LC3)-associated phagocytosis is required for the efficient clearance of dead cells. *Proceedings of the National Academy of Sciences of the United States of America,* 108**,** 17396-401.

Martinez, J., Cunha, L. D., Park, S., Yang, M., Lu, Q., Orchard, R., et al. Guy, C. 2016. Noncanonical autophagy inhibits the autoinflammatory, lupus-like response to dying cells. *Nature,* 533**,** 115-119.

Martinez, J., Malireddi, R. K., Lu, Q., Cunha, L. D., Pelletier, S., Gingras, S., et al. Green, D. R. 2015. Molecular characterization of LC3-associated phagocytosis reveals distinct roles for Rubicon, NOX2 and autophagy proteins. *Nat Cell Biol,* 17**,** 893-906.

Mckell, M. C., Crowther, R. R., Schmidt, S. M., Robillard, M. C., Cantrell, R., Lehn, M. A., et al. Qualls, J. E. 2021. Promotion of Anti-Tuberculosis Macrophage Activity by L-Arginine in the Absence of Nitric Oxide. *Front Immunol,* 12**,** 653571.

Mehta, P., Henault, J., Kolbeck, R. & Sanjuan, M. A. 2014. Noncanonical autophagy: one small step for LC3, one giant leap for immunity. *Curr Opin Immunol,* 26**,** 69-75.

Mehta, S. K. & Jindal, N. 2013. Formulation of Tyloxapol niosomes for encapsulation, stabilization and dissolution of anti-tubercular drugs. *Colloids Surf B Biointerfaces,* 101**,** 434-41.

Mily, A., Rekha, R. S., Kamal, S. M., Akhtar, E., Sarker, P., Rahim, Z., et al. Raqib, R. 2013. Oral intake of phenylbutyrate with or without vitamin D3 upregulates the cathelicidin LL-37 in human macrophages: a dose finding study for treatment of tuberculosis. *BMC Pulm Med,* 13**,** 23.

Mily, A., Rekha, R. S., Kamal, S. M., Arifuzzaman, A. S., Rahim, Z., Khan, L., et al. Raqib, R. 2015. Significant Effects of Oral Phenylbutyrate and Vitamin D3 Adjunctive Therapy in Pulmonary Tuberculosis: A Randomized Controlled Trial. *PLoS One,* 10**,** e0138340.

Mishra, R., Krishan, S., Siddiqui, A. N., Kapur, P., Khayyam, K. U. & Sharma, M. 2020. Potential role of adjuvant drugs on efficacy of first line oral antitubercular therapy: Drug repurposing. *Tuberculosis (Edinburgh, Scotland),* 120**,** 101902.

Mohamed, F. & Van Der Walle, C. F. 2008. Engineering biodegradable polyester particles with specific drug targeting and drug release properties. *J Pharm Sci,* 97**,** 71-87.

Momin, M. a. M., Rangnekar, B., Sinha, S., Cheung, C. Y., Cook, G. M. & Das, S. C. 2019. Inhalable Dry Powder of Bedaquiline for Pulmonary Tuberculosis: In Vitro Physicochemical Characterization, Antimicrobial Activity and Safety Studies. *Pharmaceutics,* 11**,** 502.

Monopoli, M. P., Aberg, C., Salvati, A. & Dawson, K. A. 2012. Biomolecular coronas provide the biological identity of nanosized materials. *Nat Nanotechnol,* 7**,** 779-86.

Mortaz, E., Adcock, I. M., Tabarsi, P., Masjedi, M. R., Mansouri, D., Velayati, A. A., et al. Barnes, P. J. 2015. Interaction of Pattern Recognition Receptors with Mycobacterium Tuberculosis. *J Clin Immunol,* 35**,** 1-10.

Mozafari, M. R. 2007. *Nanomaterials and nanosystems for biomedical applications*, Springer Science & Business Media.

Muankaew, C. & Loftsson, T. 2018. Cyclodextrin-Based Formulations: A Non-Invasive Platform for Targeted Drug Delivery. *Basic & Clinical Pharmacology & Toxicology,* 122**,** 46-55.

Murray, P. J. 2017. Macrophage Polarization. *Annu Rev Physiol,* 79**,** 541-566.

Nabi, B., Rehman, S., Aggarwal, S., Baboota, S. & Ali, J. 2020. Nano-based anti-tubercular drug delivery: an emerging paradigm for improved therapeutic intervention. *Drug Deliv Transl Res,* 10**,** 1111-1121.

Narita, M. & Spitters, C. 2017. Tuberculosis in Travelers and Immigrants. *In:* SANFORD, C. A., POTTINGER, P. S. & JONG, E. C. (eds.) *The Travel and Tropical Medicine Manual.* Elsevier.

Nasiruddin, M., Neyaz, M. K. & Das, S. 2017. Nanotechnology-Based Approach in Tuberculosis Treatment. *Tuberc Res Treat,* 2017**,** 4920209.

Niemi, M., Backman, J. T., Fromm, M. F., Neuvonen, P. J. & Kivisto, K. T. 2003. Pharmacokinetic interactions with rifampicin : clinical relevance. *Clin Pharmacokinet,* 42**,** 819-50.

Olugbosi, M., Everitt, D., Conradie, F., Crook, A., Wills, G. & Sun, E. 2020. Efficacy and safety outcomes (HIV subgroup analysis) in the Nix-TB Trial - bedaquiline, pretomanid and linezolid for treatment of extensively resistant, intolerant or non-responsive pulmonary multidrug-resistant tuberculosis. *J Int Aids Soc,* 23**,** 20-20.

Organization, W. H. 2017. Guidelines for treatment of drug-susceptible tuberculosis and patient care.

Organization, W. H. 2019. *Global tuberculosis report 2019,* Geneva, World Health Organization.

Organization, W. H. 2020. Global Tuberculosis Report. 2020.

Organization, W. H. 2021. Global tuberculosis report 2021.

Ouyang, Q., Zhang, K., Lin, D., Feng, C. G., Cai, Y. & Chen, X. 2020. Bazedoxifene Suppresses Intracellular Mycobacterium tuberculosis Growth by Enhancing Autophagy. *mSphere,* 5**,** e00124-20.

Pai, M., Kasaeva, T. & Swaminathan, S. 2022. Covid-19's Devastating Effect on Tuberculosis Care - A Path to Recovery. *N Engl J Med,* 386**,** 1490-1493.

Paik, S., Kim, J. K., Chung, C. & Jo, E. K. 2019. Autophagy: A new strategy for host-directed therapy of tuberculosis. *Virulence,* 10**,** 448-459.

Pandey, R. & Khuller, G. K. 2005. Antitubercular inhaled therapy: opportunities, progress and challenges. *The Journal of antimicrobial chemotherapy,* 55**,** 430-5.

Pauwels, A. M., Trost, M., Beyaert, R. & Hoffmann, E. 2017. Patterns, Receptors, and Signals: Regulation of Phagosome Maturation. *Trends Immunol,* 38**,** 407-422.

Pereira, L., Diogo, J., Mateus, R., Pimentel, M. & Videira, M. 2015. Host-directed strategies using lipid nanoparticles to reduce mycobacteria survival. *Journal of Nanoparticle Research,* 17.

Periyasamy, K. M., Ranganathan, U. D., Tripathy, S. P. & Bethunaickan, R. 2020. Vitamin D - A host directed autophagy mediated therapy for tuberculosis. *Mol Immunol,* 127**,** 238-244.

Pieters, J. 2008. Mycobacterium tuberculosis and the macrophage: maintaining a balance. *Cell Host Microbe,* 3**,** 399-407.

Plapied, L., Duhem, N., Des Rieux, A. & Préat, V. 2011. Fate of polymeric nanocarriers for oral drug delivery. *Current Opinion in Colloid & Interface Science,* 16**,** 228-237.

Poerio, N., Caccamo, N. R., La Manna, M. P., Olimpieri, T., De Angelis, L. H., D'andrea, M. M., et al. Fraziano, M. 2022. Phosphatidylserine Liposomes Reduce Inflammatory Response, Mycobacterial Viability, and HIV Replication in Coinfected Human Macrophages. *J Infect Dis,* 225**,** 1675-1679.

Poirier, V., Bach, H. & Av-Gay, Y. 2014. Mycobacterium tuberculosis promotes anti-apoptotic activity of the macrophage by PtpA protein-dependent dephosphorylation of host GSK3α. *J Biol Chem,* 289**,** 29376-29385.

Pourshahab, P. S., Gilani, K., Moazeni, E., Eslahi, H., Fazeli, M. R. & Jamalifar, H. 2011. Preparation and characterization of spray dried inhalable powders containing chitosan nanoparticles for pulmonary delivery of isoniazid. *J Microencapsul,* 28**,** 605-13.

Praphakar, R. A., Munusamy, M. A. & Rajan, M. 2017. Development of extended-voyaging anti-oxidant Linked Amphiphilic Polymeric Nanomicelles for Anti-Tuberculosis Drug Delivery. *International journal of pharmaceutics,* 524**,** 168-177.

Prashar, A., Schnettger, L., Bernard, E. M. & Gutierrez, M. G. 2017. Rab GTPases in Immunity and Inflammation. *Front Cell Infect Microbiol,* 7**,** 435.

Puri, V., Chaudhary, K. R., Singh, A. & Singh, C. 2022. Inhalation potential of N-Acetylcysteine loaded PLGA nanoparticles for the management of tuberculosis: In vitro lung deposition and efficacy studies. *Curr Res Pharmacol Drug Discov,* 3**,** 100084.

Queval, C. J., Brosch, R. & Simeone, R. 2017. The Macrophage: A Disputed Fortress in the Battle against Mycobacterium tuberculosis. *Front Microbiol,* 8**,** 2284.

Ralph, A. P., Waramori, G., Pontororing, G. J., Kenangalem, E., Wiguna, A., Tjitra, E., et al. Anstey, N. M. 2013a. L-arginine and vitamin D adjunctive therapies in pulmonary tuberculosis: a randomised, double-blind, placebo-controlled trial. *PLoS One,* 8**,** e70032.

Ralph, A. P., Yeo, T. W., Salome, C. M., Waramori, G., Pontororing, G. J., Kenangalem, E., et al. Anstey, N. M. 2013b. Impaired pulmonary nitric oxide bioavailability in pulmonary tuberculosis: association with disease severity and delayed mycobacterial clearance with treatment. *J Infect Dis,* 208**,** 616-26.

Rani, N. P., Suriyaprakash, T. & Senthamarai, R. 2010. Formulation and evaluation of rifampicin and gatifloxacin niosomes on logarithmic-phase cultures of Mycobacterium tuberculosis. *International Journal of Pharma and Bio Sciences,* 1**,** 379-387.

Rao, M., Ippolito, G., Mfinanga, S., Ntoumi, F., Yeboah-Manu, D., Vilaplana, C., et al. Maeurer, M. 2019. Improving treatment outcomes for MDR-TB - Novel host-directed therapies and personalised medicine of the future. *Int J Infect Dis,* 80S**,** S62-S67.

Rivas-Santiago, B., Rivas Santiago, C. E., Castaneda-Delgado, J. E., Leon-Contreras, J. C., Hancock, R. E. & Hernandez-Pando, R. 2013. Activity of LL-37, CRAMP and antimicrobial peptide-derived compounds E2, E6 and CP26 against Mycobacterium tuberculosis. *Int J Antimicrob Agents,* 41**,** 143-8.

Rodrigues, C., Gameiro, P., Prieto, M. & De Castro, B. 2003. Interaction of rifampicin and isoniazid with large unilamellar liposomes: spectroscopic location studies. *Biochimica et biophysica acta,* 1620**,** 151-9.

Roszer, T. 2015. Understanding the Mysterious M2 Macrophage through Activation Markers and Effector Mechanisms. *Mediators Inflamm,* 2015**,** 816460.

Russell, D. G., Cardona, P. J., Kim, M. J., Allain, S. & Altare, F. 2009. Foamy macrophages and the progression of the human tuberculosis granuloma. *Nat Immunol,* 10**,** 943-8.

Salahuddin, N., Ali, F., Hasan, Z., Rao, N., Aqeel, M. & Mahmood, F. 2013. Vitamin D accelerates clinical recovery from tuberculosis: results of the SUCCINCT Study [Supplementary Cholecalciferol in recovery from tuberculosis]. A randomized, placebo-

controlled, clinical trial of vitamin D supplementation in patients with pulmonary tuberculosis'. *BMC Infect Dis,* 13**,** 22.

Salamon, H., Bruiners, N., Lakehal, K., Shi, L., Ravi, J., Yamaguchi, K. D., et al. Gennaro, M. L. 2014. Cutting edge: Vitamin D regulates lipid metabolism in Mycobacterium tuberculosis infection. *Journal of immunology (Baltimore, Md. : 1950),* 193**,** 30-34.

Samuel, L. P., Song, C. H., Wei, J., Roberts, E. A., Dahl, J. L., Barry, C. E., et al. Friedman, R. L. 2007. Expression, production and release of the Eis protein by Mycobacterium tuberculosis during infection of macrophages and its effect on cytokine secretion. *Microbiology (Reading),* 153**,** 529-540.

Saraogi, G. K., Gupta, P., Gupta, U. D., Jain, N. K. & Agrawal, G. P. 2010. Gelatin nanocarriers as potential vectors for effective management of tuberculosis. *International journal of pharmaceutics,* 385**,** 143-9.

Saraogi, G. K., Sharma, B., Joshi, B., Gupta, P., Gupta, U. D., Jain, N. K. & Agrawal, G. P. 2011. Mannosylated gelatin nanoparticles bearing isoniazid for effective management of tuberculosis. *J Drug Target,* 19**,** 219-27.

Scanga, C. A., Mohan, V. P., Tanaka, K., Alland, D., Flynn, J. L. & Chan, J. 2001. The inducible nitric oxide synthase locus confers protection against aerogenic challenge of both clinical and laboratory strains of Mycobacterium tuberculosis in mice. *Infect Immun,* 69**,** 7711-7.

Schaible, U. E., Winau, F., Sieling, P. A., Fischer, K., Collins, H. L., Hagens, K., et al. Kaufmann, S. H. 2003. Apoptosis facilitates antigen presentation to T lymphocytes through MHC-I and CD1 in tuberculosis. *Nat Med,* 9**,** 1039-46.

Schiebler, M., Brown, K., Hegyi, K., Newton, S. M., Renna, M., Hepburn, L., et al. Floto, R. A. 2015. Functional drug screening reveals anticonvulsants as enhancers of mTOR-independent autophagic killing of Mycobacterium tuberculosis through inositol depletion. *EMBO Mol Med,* 7**,** 127-39.

Schon, T., Elias, D., Moges, F., Melese, E., Tessema, T., Stendahl, O., et al. Sundqvist, T. 2003. Arginine as an adjuvant to chemotherapy improves clinical outcome in active tuberculosis. *Eur Respir J,* 21**,** 483-8.

Schuller, S., Neefjes, J., Ottenhoff, T., Thole, J. & Young, D. 2001. Coronin is involved in uptake of Mycobacterium bovis BCG in human macrophages but not in phagosome maintenance. *Cell Microbiol,* 3**,** 785-93.

Scolari, I. R., Paez, P. L., Sanchez-Borzone, M. E. & Granero, G. E. 2019. Promising Chitosan-Coated Alginate-Tween 80 Nanoparticles as Rifampicin Coadministered Ascorbic Acid Delivery Carrier Against Mycobacterium tuberculosis. *AAPS PharmSciTech,* 20**,** 67.

Scriba, T. J., Netea, M. G. & Ginsberg, A. M. 2020. Key recent advances in TB vaccine development and understanding of protective immune responses against Mycobacterium tuberculosis. *Semin Immunol,* 50**,** 101431.

Sharma, A., Vaghasiya, K., Gupta, P., Gupta, U. D. & Verma, R. K. 2018. Reclaiming hijacked phagosomes: Hybrid nano-in-micro encapsulated MIAP peptide ensures host directed therapy by specifically augmenting phagosome-maturation and apoptosis in TB infected macrophage cells. *International journal of pharmaceutics,* 536**,** 50-62.

Sharma, V., Makhdoomi, M., Singh, L., Kumar, P., Khan, N., Singh, S., et al. Kumar, D. 2021. Trehalose limits opportunistic mycobacterial survival during HIV co-infection by reversing HIV-mediated autophagy block. *Autophagy,* 17**,** 476-495.

Shehzad, A., Rehman, G., Ul-Islam, M., Khattak, W. A. & Lee, Y. S. 2013. Challenges in the development of drugs for the treatment of tuberculosis. *Braz J Infect Dis,* 17**,** 74-81.

Shelley, H. & Babu, R. J. 2018. Role of Cyclodextrins in Nanoparticle-Based Drug Delivery Systems. *Journal of Pharmaceutical Sciences,* 107**,** 1741-1753.

Shin, D. M., Jeon, B. Y., Lee, H. M., Jin, H. S., Yuk, J. M., Song, C. H., et al. Jo, E. K. 2010. Mycobacterium tuberculosis eis regulates autophagy, inflammation, and cell death through redox-dependent signaling. *Plos Pathog,* 6**,** e1001230.

Sia, J. K., Georgieva, M. & Rengarajan, J. 2015. Innate Immune Defenses in Human Tuberculosis: An Overview of the Interactions between Mycobacterium tuberculosis and Innate Immune Cells. *J Immunol Res,* 2015**,** 747543.

Singh, R., Dwivedi, S. P., Gaharwar, U. S., Meena, R., Rajamani, P. & Prasad, T. 2020. Recent updates on drug resistance in Mycobacterium tuberculosis. *Journal of applied microbiology,* 128**,** 1547-1567.

Song, X., Lin, Q., Guo, L., Fu, Y., Han, J., Ke, H., et al. Zhang, Z. 2015. Rifampicin loaded mannosylated cationic nanostructured lipid carriers for alveolar macrophage-specific delivery. *Pharm Res,* 32**,** 1741-51.

Stanley, S. A., Barczak, A. K., Silvis, M. R., Luo, S. S., Sogi, K., Vokes, M., et al. Hung, D. T. 2014. Identification of host-targeted small molecules that restrict intracellular Mycobacterium tuberculosis growth. *Plos Pathog,* 10**,** e1003946.

Sturgill-Koszycki, S., Schlesinger, P. H., Chakraborty, P., Haddix, P. L., Collins, H. L., Fok, A. K., et al. Russell, D. G. 1994. Lack of acidification in Mycobacterium phagosomes produced by exclusion of the vesicular proton-ATPase. *Science,* 263**,** 678-81.

Sun-Wada, G. H., Tabata, H., Kawamura, N., Aoyama, M. & Wada, Y. 2009. Direct recruitment of H+-ATPase from lysosomes for phagosomal acidification. *J Cell Sci,* 122**,** 2504-13.

Sun, J., Singh, V., Lau, A., Stokes, R. W., Obregon-Henao, A., Orme, I. M., et al. Hmama, Z. 2013. Mycobacterium tuberculosis nucleoside diphosphate kinase inactivates small GTPases leading to evasion of innate immunity. *Plos Pathog,* 9**,** e1003499.

Sunnetcioglu, A., Sunnetcioglu, M., Binici, I., Baran, A. I., Karahocagil, M. K. & Saydan, M. R. 2015. Comparative analysis of pulmonary and extrapulmonary tuberculosis of 411 cases. *Ann Clin Microbiol Antimicrob,* 14**,** 34.

Swanson, B., Keithley, J. K., Zeller, J. M. & Sha, B. E. 2002. A pilot study of the safety and efficacy of supplemental arginine to enhance immune function in persons with HIV/AIDS. *Nutrition,* 18**,** 688-90.

Tarique, A. A., Logan, J., Thomas, E., Holt, P. G., Sly, P. D. & Fantino, E. 2015. Phenotypic, functional, and plasticity features of classical and alternatively activated human macrophages. *Am J Respir Cell Mol Biol,* 53**,** 676-88.

Tian, M., Zhou, Z., Tan, S., Fan, X., Li, L. & Ullah, N. 2018. Formulation in DDA-MPLA-TDB Liposome Enhances the Immunogenicity and Protective Efficacy of a DNA Vaccine against Mycobacterium tuberculosis Infection. *Front Immunol,* 9**,** 310.

Tinsley-Bown, A. M., Fretwell, R., Dowsett, A. B., Davis, S. L. & Farrar, G. H. 2000. Formulation of poly(D,L-lactic-co-glycolic acid) microparticles for rapid plasmid DNA delivery. *J Control Release,* 66**,** 229-41.

Tobin, D. M. & Ramakrishnan, L. 2013. TB: the Yin and Yang of lipid mediators. *Curr Opin Pharmacol,* 13**,** 641-5.

Trousil, J., Filippov, S. K., Hruby, M., Mazel, T., Syrova, Z., Cmarko, D., et al. Stepanek, P. 2017. System with embedded drug release and nanoparticle degradation sensor showing efficient rifampicin delivery into macrophages. *Nanomedicine : nanotechnology, biology, and medicine,* 13**,** 307-315.

Upadhyay, S., Mittal, E. & Philips, J. A. 2018. Tuberculosis and the art of macrophage manipulation. *Pathog Dis,* 76.

Upadhyay, T. K., Fatima, N., Sharma, A., Sharma, D. & Sharma, R. 2019. Nano-Rifabutin entrapment within glucan microparticles enhances protection against intracellular Mycobacterium tuberculosis. *Artif Cells Nanomed Biotechnol,* 47**,** 427-435.

Vanaporn, M. & Titball, R. W. 2020. Trehalose and bacterial virulence. *Virulence,* 11**,** 1192-1202.

Velmurugan, K., Chen, B., Miller, J. L., Azogue, S., Gurses, S., Hsu, T., et al. Briken, V. 2007. Mycobacterium tuberculosis nuoG is a virulence gene that inhibits apoptosis of infected host cells. *Plos Pathog,* 3**,** e110.

Vergne, I., Chua, J. & Deretic, V. 2003. Tuberculosis toxin blocking phagosome maturation inhibits a novel Ca2+/calmodulin-PI3K hVPS34 cascade. *J Exp Med,* 198**,** 653-9.

Walburger, A., Koul, A., Ferrari, G., Nguyen, L., Prescianotto-Baschong, C., Huygen, K., et al. Pieters, J. 2004. Protein kinase G from pathogenic mycobacteria promotes survival within macrophages. *Science,* 304**,** 1800-4.

Wallis, R. S. & Hafner, R. 2015. Advancing host-directed therapy for tuberculosis. *Nat Rev Immunol,* 15**,** 255-63.

Woodrow, K. A., Cu, Y., Booth, C. J., Saucier-Sawyer, J. K., Wood, M. J. & Saltzman, W. M. 2009. Intravaginal gene silencing using biodegradable polymer nanoparticles densely loaded with small-interfering RNA. *Nat Mater,* 8**,** 526-33.

Yang, C. S., Lee, J. S., Rodgers, M., Min, C. K., Lee, J. Y., Kim, H. J., et al. Jung, J. U. 2012. Autophagy protein Rubicon mediates phagocytic NADPH oxidase activation in response to microbial infection or TLR stimulation. *Cell Host Microbe,* 11**,** 264-76.

Yao, Y., Xu, X. H. & Jin, L. 2019. Macrophage Polarization in Physiological and Pathological Pregnancy. *Front Immunol,* 10**,** 792.

Young, C., Walzl, G. & Du Plessis, N. 2020. Therapeutic host-directed strategies to improve outcome in tuberculosis. *Mucosal Immunol,* 13**,** 190-204.

Zazo, H., Colino, C. I. & Lanao, J. M. 2016. Current applications of nanoparticles in infectious diseases. *J Control Release,* 224**,** 86-102.

Zhai, W., Wu, F., Zhang, Y., Fu, Y. & Liu, Z. 2019. The Immune Escape Mechanisms of Mycobacterium Tuberculosis. *Int J Mol Sci,* 20**,** 340.

Zumla, A., Maeurer, M., Host-Directed Therapies, N., Chakaya, J., Hoelscher, M., Ntoumi, F., et al. Wallis, R. S. 2015a. Towards host-directed therapies for tuberculosis. *Nat Rev Drug Discov,* 14**,** 511-2.

Zumla, A., Rao, M., Dodoo, E. & Maeurer, M. 2016. Potential of immunomodulatory agents as adjunct host-directed therapies for multidrug-resistant tuberculosis. *BMC Med,* 14**,** 89.

Zumla, A., Rao, M., Parida, S. K., Keshavjee, S., Cassell, G., Wallis, R., et al. Maeurer, M. 2015b. Inflammation and tuberculosis: host-directed therapies. *J Intern Med,* 277**,** 373-87.

CHAPTER 3

SYNTHESIS AND CHARACTERIZATION OF 1,3-B-GLUCAN-MODIFIED NANOPARTICLES ENCAPSULATING RIFAMPICIN AND VITAMIN D3 FOR POTENTIALDELIVERY IN TUBERCULOSIS THERAPY

3.1. Introduction

With an estimated 10.4 million new cases and 1.7 million deaths annually, tuberculosis (TB) remains a significant global health concern, especially in developing countries (Kolloli and Subbian, 2017, Khoza et al., 2022). Before the SARS-CoV-2 pandemic, it was the leading cause of mortality from a single infectious agent, with nearly one-third of the world's population infected with latent mycobacterium tuberculosis (LTBI) (Khoza et al., 2022, Kolloli and Subbian, 2017, Mphaphuli et al., 2023). HIV coinfection, the emergence of drug-resistant Mtb strains, and the coexistence of other chronic conditions like diabetes all contribute to an acceleration of the morbidity and mortality rate caused by TB (Kolloli and Subbian, 2017). In 2020 alone, about 10 million people were estimated to have contracted TB, with only about 5.8 million cases being diagnosed and recorded due to substantial SARS-CoV-2 outbreaks and disruption in healthcare services (Organization, 2021, Khoza et al., 2022, Pai et al., 2022). As a result, TB mortality increased significantly, with around 1.5 million fatalities worldwide, the first upsurge in TB mortalities since 2005 (Organization, 2021). After inhaling, Mtb enters the alveolar space, where it is bathed in alveolar lining fluid (ALF) and directly touches the soluble lung mucosa components before interacting with the cellular compartment, mainly alveolar macrophages (AM) and other immune cells (Allue-Guardia et al., 2021). The current TB treatment regimen consists of a six-month regimen that includes a two-month intensive phase in which patients receive four first-line antibiotics [isoniazid (INH), ethambutol hydrochloride (EMB), and pyrazinamide (PZA)], followed by a four-month continuous phase in which patients receive RIF and INH (Maphasa et al., 2020, Allue-Guardia et al., 2021).

Despite all the current chemotherapeutics, the global TB epidemic has worsened due to HIV co-infection, the absence of a viable vaccination, the length of treatment, drug toxicity, and the rise of multidrug-resistant (MDR) bacteria (Mayer-Barber et al., 2014, Paik et al., 2019). In addition, the expensive, time-consuming anti-TB medication for cases requiring multiple drugs has adverse side effects that make it difficult for patients to adhere to their treatment regimen (Kolloli and Subbian, 2017). These dire limits highlight the urgent need for innovative drug-sensitive and drug-resistant TB therapy and management techniques. Much effort has

recently been expended to create novel/improved therapeutics by regulating host responses to TB (i.e., host-directed therapy and autophagy) (Paik et al., 2019, Khoza et al., 2022, Kolloli and Subbian, 2017). In contrast to traditional treatment, host-directed therapy (HDT) targets pathways disturbed by the Mtb pathogen without interfering with the pathogen to boost host defence systems against Mtb (Kilinc et al., 2021). Autophagy is an intracellular catabolic process that aids in maintaining homeostasis or removing invading pathogens such as Mtb through a lysosomal degradation process (Goletti et al., 2013). The activation of autophagy by various drugs or agents may represent a promising treatment strategy against Mtb infection, even for drug-resistant strains, when combined with traditional treatment therapeutics (Paik et al., 2019). Vitamin D3 (VITD3) is one of the most researched autophagy mediators/activators against TB due to the link between VITD3 insufficiency, TB susceptibility, and its ability to promote autophagy and the synthesis of antimicrobial peptides (Lee and Bhakta, 2021). Through its active form, the 1,25-dihydroxy vitamin D3 (1,25D) pathway, VITD3 exerts an immunomodulatory effect on macrophages by upregulating their response and inflammatory response, respectively (Chun et al., 2011). Additionally, VITD3 further stimulates macrophage production of RONS, antimicrobial peptides like beta-defensin-4 (DEFB4) and cathelicidin antimicrobial peptide (CAMP/LL-37), which increases bactericidal activity (Sia et al., 2015). Furthermore, 1,25D regulates the synthesis of ATGs, such as ATG5 and Beclin-1, to facilitate the onset of autophagosomes and their fusion with lysosomes, which promotes the prevention of Mtb development (Khoza et al., 2022).

Active targeting of therapeutics for TB is a highly sought-after field due to the complex nature of the disease and the challenges associated with its treatment. While passive targeting relies on the enhanced permeability and retention (EPR) effect, it lacks cellular specificity, making active targeting strategies more desirable for diseases like TB that affect specific immune cells. One promising approach involves using β-glucans, which have potent immunomodulatory effects on innate and adaptive immune responses (Tae et al., 2019, Soto et al., 2016). β-glucans bind to dectin-1 receptors on innate immune cells such as macrophages, neutrophils, and dendritic cells, triggering a robust immune response that includes phagocytosis and pro-inflammatory cytokine production, aiding in eliminating infectious agents (Cognigni et al., 2021, Mata-Martinez et al., 2022). By functionalising biopolymeric nanoparticles with β-glucan, active targeting of macrophages can be achieved, significantly enhancing the efficacy of anti-TB bioactives (Zhao et al., 2020, Mata-Martinez et al., 2022). This strategy allows for the direct delivery of the therapeutic agents to the site of infection, alveolar macrophages, while protecting the drugs from premature elimination and improving their absorption across biological barriers (Zhao et al., 2020, Mata-Martinez et al.,

2022). Such targeted therapies improve drug concentration at the infection site and help overcome barriers such as drug resistance, bioavailability issues, and the prolonged treatment duration required for TB (Nair et al., 2023). As a result, β-glucan-functionalized nanoparticles represent a promising avenue in developing more effective TB treatments, potentially transforming the management and outcome of the disease. To investigate this, 1,3- β glucan surface-functionalized biopolymeric nanoparticles were fabricated, encapsulating RIF or VITD3. These nanoparticles were tested for physicochemical properties, including stability over time and their release profile at different pH levels. Additionally, their cytotoxicity was evaluated against RAW 264.7 cell lines. The cytotoxicity was further assessed to ascertain the cytocompatibility of the nanoparticles with macrophages.

3.2. Materials and Methods

3.2.1. Materials

Polycaprolactone (M_n 80,000), chitosan oligosaccharide lactate (CS, M_n 5,000 Da), Cholecalciferol (Vitamin D3, MW; 384.64), Rifampicin (RFP, MW;822.94), β-1,3-Glucan from Euglena gracilis, poly (vinyl alcohol, 87-90% hydrolysed, MW; 30 000-70 000), and phosphate-buffered saline (PBS) were all purchased from Sigma-Aldrich (St. Louise, MO, USA). Dichloromethane (DCM) and methanol were procured from Merck (Pty Ltd., South Africa). RAW 264.7 cell line was procured from Separation Scientific Pty Ltd (Johannesburg, SA). 3-(4,5-dimethylthiazole-2-yl)-2,5-diphenyl tetrazolium bromide (MTT) assay Kit (MTT Cell Proliferation Kit I, Roche, Basel, Switzerland) was purchased from Sigma-Aldrich (St. Louise, MO, USA). All chemicals were of analytical reagent grade and were used without prior modification. Double deionised water (DDW) was used for all the preparations.

3.2.2. Synthesis/formulation of functionalised and non-functionalized Nanoparticles

Cholecalciferol (VITD3) and RIF-loaded nanoparticles were prepared following a modified single-emulsion method (Tripathi et al., 2010). Briefly, 20 mg/mL of polycaprolactone (PCL, Mn 80,000 Da) solution in dichloromethane containing 2.5 mg/mL of the drug *(either VITD3 or RIF)* was added dropwise to a 0.1% w/v polyvinyl alcohol (Mn 31,000 Da) solution in double-distilled water (DDW) containing 2 mg/mL of chitosan oligosaccharide lactate (CS, Mn 5, 000 Da) under stirring at 1100 rpm at room temperature. The resulting solution was then probe sonicated for 20 min (in a pulsed manner, 40% intensity) over an ice bath. The solution was left stirring (1100 rpm) overnight at room temperature to evaporate excessive DCM.

Nanoparticles were then collected through centrifugation at 12000 rpm for 20 min, followed by washing with DDW and lyophilised for 20 hours at temperatures between -30°C and 25°C under a vacuum collector pressure of 1.030 mBar. For functionalisation, a modified method by Dube et al. 2014 was followed (Dube et al., 2014). Briefly, 40 mL of nanoparticle solution was incubated with 250 µg/mL of 1,3-β-glucan solution in DDW for 24 hours to make a final concentration of 25 µg/mL of 1,3-β-glucan. Unattached 1,3-β-glucan was removed by centrifugation (5000 rpm for 5 minutes), followed by washing with DDW and lyophilisation.

3.2.3. Analysis of hydrodynamic particle size distribution, zeta potential, and polydispersity index (PDI)

The average hydrodynamic particle size, zeta potential (ZP), and polydispersity index (PDI) of loaded, unloaded, functionalised, and non-functionalized nanoparticles were measured using Malvern ZetaSizer NanoZS (Malvern Panalytical, Malvern, UK) at 25°C. Briefly, each sample was concentrated (1:9) with DDW, vortexed briefly for dispersion, and 1 ml of each sample was placed in a disposable cuvette for size and PDI measurements. The same samples were then transferred into zeta potential cuvettes (DTS 1070) for zeta potential measurement. All measurements were performed in triplicate.

3.2.4. Evaluation of Drug Entrapment Efficiency and Loading Capacity of the Nanoparticles

The entrapment efficiency of VITD3 and RIF encapsulated within CS-PCL-VITD3/RIF and Glu-CS-PCL-VITD3/RIF nanoparticles was determined by allowing each drug-loaded nanoparticle formulation to dissolve completely. Briefly, lyophilised nanoparticle formulation of known mass was dissolved in adequate PBS at pH 4.6 and left in an orbital shaker (25 rpm) incubator at 37 ºC for 3 days to allow for complete dissolution. The resulting suspension was centrifuged at 5000 rpm for 5 minutes. The concentration of VITD3 and RIF in the clear supernatant was determined using an Implen Nanophotometer (IMPLEN Nanophotometer™, Implen GmbH, Munich Germany) set at λmax = 265 nm and 335 nm, respectively, following generation of calibration curves for each drug (R^2 > 0.99). The percentage value of drug entrapment efficacy (%EE) and loading capacity (%LC) were determined using equations (3.1) and (3.2). The measurements were carried out in triplicates and presented as mean ± STD.

$$\%\mathrm{EE} = \frac{\mathrm{Aq}}{\mathrm{Tq}} \times 100 \ldots\ldots\ldots\ldots\ldots\ldots \text{(Equation 3.1)}$$

A_q represents the amount of drug measured by the Implen Nanophotometer (IMPLEN Nanophotometer™, Implen GmbH, Munchen Germany), and Tq represents the amount of the drug employed in the formulation.

$$\%\mathrm{LC} = \frac{\mathrm{Aq}}{\mathrm{W}} \times 100 \ldots\ldots\ldots\ldots\ldots\ldots \text{ (Equation 3.2)}$$

A_q is the amount of drug measured by the Implen Nanophotometer, and W represents the weight of the nanoparticle formulation.

3.2.5. Quantification of β-1,3-Glucan content on β-1,3-Glucan Functionalized Nanoparticles

The density of β-1,3-Glucan on Glu-CS-PCL-VITD3/RIF nanoparticles was quantified using the modified phenol-sulfuric method (Granum and Myklestad, 2002, Nielsen, 2010, Taylor, 1995). Briefly, 100 µL of Glu-CS-PCL nanoparticles (5mg/mL) solution were dispensed into a 96-well plate. Concentrated sulfuric acid (150 µL) was ejected into the dispensed nanoparticles solution. The plate was shaken gently on a shaker to allow for homogeneous mixing of the solution before adding 5% (w/v) phenol solution (50 µL). The reaction was allowed to proceed for 1 hour on a shaker, permitting adequate reduction of β-1,3-Glucan. Non-functionalized CS-PCL nanoparticles were used as a control to account for polymer interference with the assay. The absorbance of standards and unknown samples were measured at a wavelength of 490 nm using a Multimodal microplate reader (Perkin Elmer VICTOR X3 2030 MultiLabel Plate Reader). The surface coverage of β-1,3-Glucan molecules on the functionalised nanoparticles was computed relative to the generated standard curve.

3.2.6. Morphological analysis

The morphological surface of the nanosystem was determined by employing Scanning electron Microscopy (SEM) analysis (Carl Zeiss Microscopy Ltd., Cambridge, UK) and High-Resolution Transmission Electron Microscopy (HRTEM) version TECNAIF3OST-TEM. Dispersions of the nanoparticles were concentrated to approximately 1:9 with DDW and sonicated for 30 seconds in a water bath. A drop of the nanosystem suspension from each sample was placed on a metallic sample stub and left to air dry overnight under a fume hood before being sputter-coated twice with gold-palladium (AuPd). The samples were then observed under different magnifications at an accelerated voltage of 20 kV using SEM.

Similarly, TEM was employed to ascertain the morphology of the nanoparticles. A drop of the concentrated sample was mounted on a carbon-coated copper grid and air-dried under a fume hood before being visualised under the electron microscope.

3.2.7. Evaluation of Functional Transformation and Chemical Transitions of Nanoparticles Using Fourier transform infrared spectroscopy (FTIR)

The FTIR spectra of various powdered nanoparticle samples were analysed to identify specific interactions between pristine polymers, the drug, and the fabricated nanoparticles. This analysis was performed using a Spectrum 100 spectrophotometer (PerkinElmer Inc., Waltham, MA, USA) to ascertain functional transformations resulting from surface functionalisation and to confirm drug encapsulation. The spectra were obtained to evaluate how surface modifications affect the chemical environment of the nanoparticles and their interaction with the encapsulated drug. The spectrometer operated within a wavelength range of 4000–550 cm^{-1} with a resolution of 4 cm^{-1}.

3.2.8. Analysis of the crystallographic structure of the nanoparticles

The degree of crystallinity of the starting materials, bioactives, and fabricated nanoparticle samples was evaluated using a benchtop X-ray powder diffractometer (XRPD) (Rigaku MiniFlex 600, Tokyo, Japan) equipped with CuKα radiation at 15 mA and 40 kV. Powdered samples were mounted on an aluminium sample holder and analysed to obtain diffractograms. The 2θ scan range was set between 10° and 90°, with a scan rate of 10°/minute. This diffraction analysis allowed for assessing the degree of crystallinity of the fabricated nanoparticles.

3.2.9. Evaluation of the thermal behaviour/properties of the optimised Nanoparticle samples

The formulated nanoparticles' thermal stability and decomposition temperatures were assessed using a Thermogravimetric Analyzer (TGA 4000, PerkinElmer Inc., Waltham, MA, USA). Samples weighing ≥ 10 mg were placed in the TGA furnace and analysed under a nitrogen atmosphere, with a heating rate of 10°C/min from 30°C to 900°C. The weight changes of the samples were recorded and analysed as a function of temperature. Additionally, the thermophysical properties of the nanoparticles and all starting materials were evaluated using

a Differential Scanning Calorimeter (DSC, Mettler Toledo, STARe System, Schwerzenbach, ZH, Switzerland). Samples weighing 5-10 mg were sealed in aluminium crucibles and heated from 20°C to 400°C at 10°C/min under continuous nitrogen flow. The DSC curves were plotted to show heat flow as a function of temperature.

3.2.10. *In vitro release* of VITD3 and RIF in formulated nanoparticles

The drug release profile of VITD3/RIF in the nanoparticles was evaluated using a dialysis membrane approach at three different pH values (4.6, 6.8, and 7.4). Briefly, the lyophilised nanoparticle sample was weighted and dissolved in an appropriate volume of PBS at three different pHs. The dissolved samples were then loaded into a dialysis tubing membrane (SnakeSkin™, 3500 MWCO) and submerged into the relevant drug release media buffer of the corresponding pH and incubated (37 ºC) in an orbital shaker (25 rmp) (YIHDER LM-530, YIHDER Co., Ltd., Taipei, Taiwan) until completion of release study. The dialysis membrane was used to facilitate only free VITD3/RIF diffusion into the release medium for assay. Sampling (2 mL) was undertaken at different time intervals (t = 1, 2, 4, 8, 12, 24, and 48 h). An equivalent amount of pre-warmed fresh media was replaced into the sample release media to sustain sink conditions. A nanophotometer was employed to quantify VITD3 and RIF at 265 and 335 nm, respectively, with each experiment carried out in triplicate.

3.2.11. *In vitro* cytotoxicity assay of formulated nanoparticles

The effects of different formulated nanoparticles on the metabolic activity and cytotoxicity of the RAW 264.7 macrophage cell line were assessed using an MTT Cell Proliferation Kit I (Roche, Basel, Switzerland). Briefly, the cells were cultured in DMEM supplemented with 1% penicillin-streptomycin and 10% fetal bovine serum at 37°C in a humidified incubator with 5% CO_2. The growth medium was replenished with fresh medium every 48-72 hours until the cells reached confluence. Cells were seeded at a density of $1x10^5$ per well in 96-well plates, with triplicate wells for each condition. After 24 hours, the adhered cells were treated with different nanoparticle solutions at varying concentrations and incubated for 48 hours under the same conditions. Following the incubation period, each well was treated with 10 µL of 5 mg/mL MTT solution and incubated for 4 hours. Afterwards, 100 µL of a solubilising agent (acid-isopropanol; 0.04 N HCl in isopropanol) was added to dissolve the formed formazan crystals, and the plates were incubated overnight under the same conditions. The absorbance of cell activity was then measured using a multimodal microplate reader (Victor X3, PerkinElmer,

Waltham, MA, USA) at 570 nm, with a reference wavelength of 620 nm. A parallel assay included positive controls (cells treated with culture medium only), negative controls (cells treated with 4% v/v DMSO), and blank wells containing only the solubilising agent and growth medium. The absorbance measurements were calculated (mean ± SD) and used to determine the percentage of cell viability using Eq. (3.3).

$$\% \text{ Cell viability} = \frac{\text{Atest}-\text{Ablank}}{\text{Acontrol}-\text{Ablank}} \times 100 \quad \text{..... (Equation 3.3)}$$

A_{test} is test absorbance, A_{blank} is blank, and $A_{control}$ is a control absorbance in nm.

3.3. Results and Discussion

This section covers key aspects of the formulated nanoparticles, including particle size distribution, zeta potential, PDI, stability, morphology, and drug entrapment efficiency. We will evaluate the functional transformation of the nanoparticles before and after drug encapsulation and functionalisation, followed by an analysis of their crystallographic structure. The optimised nanoparticles' thermal behaviour and storage stability will also be assessed. An *in vitro* release study of VITD3 and RIF will also be conducted. Finally, the cytotoxicity and metabolic activity of the nanoparticles will be evaluated using the RAW 264.7 cell line to determine their safety and therapeutic potential.

3.3.1. Particle size distribution, zeta potential, PDI, stability, morphology, and drug entrapment efficiency

The average hydrodynamic particle size, zeta potential, PDI and drug entrapment efficiency for the formulated nanoparticles were measured and summarised in **Table 3.1** and **Figure 3.1** and **3.2**. The nanoparticles displayed an average hydrodynamic particle size within the range of 122.63 ± 5.11 nm to 182.90 ± 4.70 nm and a positive average zeta potential ranging from +19.5 ± 0.21 to +26.3 ± 0.45 mV, with narrow size distribution for all formulations (PdI < 0.30) as shown in **Table 3.1**. β-1,3-Glucan functionalisation of the CS-PCL-VITD3/RIF nanoparticles had minor changes to the average size, ZP and PDI as they remained in the same range as non-functionalized CS-PCL-VITD3/RIF nanoparticles as seen in **Figure 3.1** and **3.2** and **Table 3.1**. The generated average particle size distribution, ZP, for the formulated nanoparticles showed the formulations' uniformity in size and zeta potential, supported by SEM results as displayed in **Figure 3.3**. The average dynamic particle size and surface charge have been

shown to play a significant role in the uptake or internalisation of nanoparticles by phagocytic cells, including macrophages (Foroozandeh and Aziz, 2018). Following this, the formulated average nanoparticle size range can be internalised via clathrin- or caveolin-mediated or clathrin- or caveolin-independent endocytosis, which follows pinocytosis mechanisms (Foroozandeh and Aziz, 2018), supporting the hypothesis that the formulated nanoparticles with average particle sizes ranging from 122.63 ± 5.11 nm to 182.90 ± 4.70 nm can potentially improve the delivery of VITD3/RIF payload to the macrophages.

Table 3.1: DLS properties of CS-PCL unloaded, loaded, functionalised and non-functionalized nanoparticles, and the drug loading capacity and entrapment efficiency.

Formulation	Particle size (nm)	ZP (mV)	PDI (a.u)	% LC	% EE
CS-PCL	175.60 ± 2.51	+20.5 ± 0.40	0.28 ± 0.010	-	-
CS-PCL-VITD3	182.13 ± 4.70	+26.3 ± 0.45	0.24 ± 0.004	2.98 ± 0.35	62 ± 0.97
Glu-CS-PCL-VITD3	182.90 ± 1.15	+24.8 ± 0.73	0.15 ± 0.006	2.60 ± 0.22	54 ± 0.88
CS-PCL-RIF	156.13 ± 1.12	+20.6 ± 1.05	0.14 ± 0.027	4.60 ± 0.64	96 ± 1.03
Glu-CS-PCL-RIF	122.63 ± 5.11	+19.5 ± 0.21	0.27 ± 0.009	3.00 ± 1.01	62 ± 1.44

Another crucial factor influencing the cellular uptake of nanoparticles is their surface charge. Over the past decade, nano surface modification has been used to engineer the surface charge of nanoparticles to be either cationic or anionic (Zhu et al., 2013). The formulated nanoparticles displayed positive average surface charge, as shown in **Figure 3.1-3.2** and **Table 3.1**, due to cationic surface coating by chitosan, which will enhance internalisation as previous studies have shown that positively charged nanoparticles have enhanced internalisation by cells via micropinocytosis compared to neutral and negatively charged nanoparticles (Marano et al., 2011, Dausend et al., 2008, Foroozandeh and Aziz, 2018, Makvandi et al., 2021). Further, macrophage cells display a negatively charged surface sialic acid; the positive surface charge of the formulated nanoparticles may further encourage macrophage-particulate electrostatic interaction, thereby enhancing nanoparticle uptake as shown by previous studies (Puigdellivol et al., 2020, Jeon et al., 2018, Shannahan et al., 2013). In addition, the average surface charge (**Figure 3.1** and **3.2**) and PdI, as displayed in **Table 3.1** of the formulated nanoparticles, indicated the stability and homogeneity of the nanoparticles in terms of aggregation, flocculation, sedimentation, coagulation and creaming as charged nanoparticles are kept apart by robust electrostatic repulsion between them (Jain et al., 2018, Huang et al., 2023).

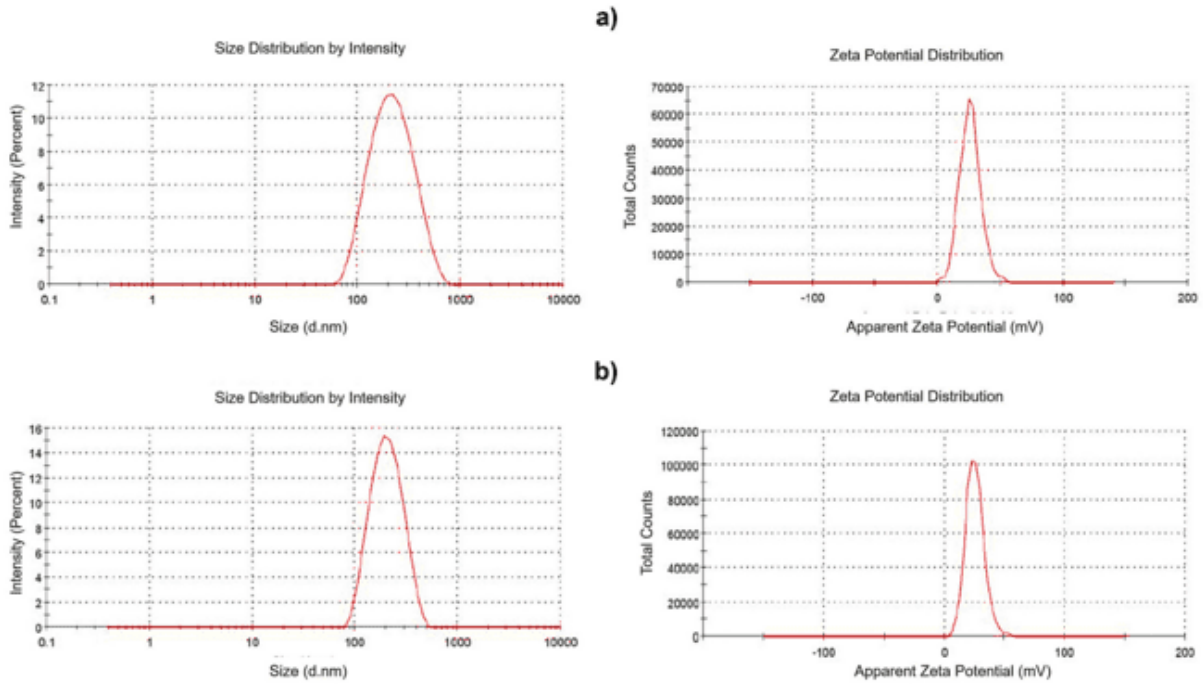

Figure 3.1: Particle Size Distribution and Zeta Potential of **(a)** CS-PCL-VITD3 and **(b)** Glu-CS-PCL-VITD3 Nanoparticles, Indicating Favorable Characteristics for Macrophage Internalization.

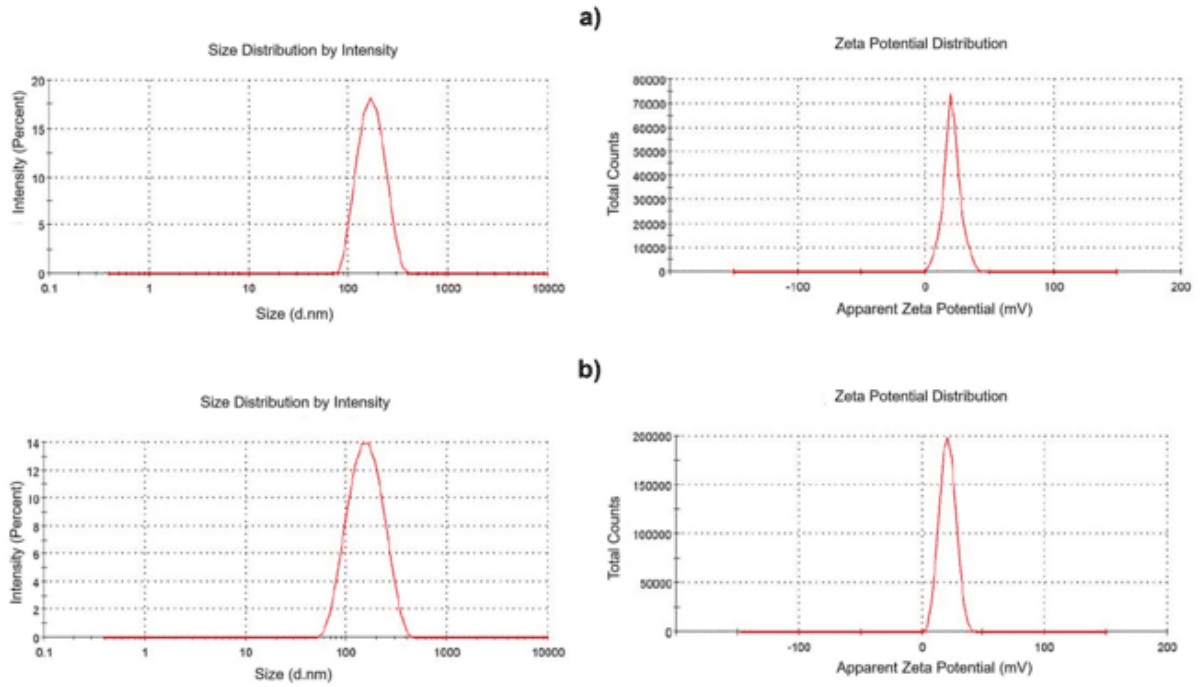

Figure 3.2: Particle Size Distribution and Zeta Potential of **(a)** CS-PCL-RIF and **(b)** Glu-CS-PCL-RIF Nanoparticles, Indicating Favorable Characteristics for Macrophage Internalisation.

In addition to size, the shape of the nanoparticles also plays a pivotal role in the uptake pathway and trafficking of nanoparticles (Foroozandeh and Aziz, 2018). Therefore, SEM and TEM were employed to evaluate the formulated nanoparticles' surface morphology and shape. The SEM and TEM images revealed that the prepared nanoparticles had spherical, smooth, uniform shapes with intact structures, **Figure 3.3**. Observation in **Figure 3.3b** shows non-functionalized nanoparticles with a smooth, spherical surface morphology, which remains consistent in **Figure 3.3c**, where β-1,3-Glucan functionalised nanoparticles display a similarly smooth and uniform spherical morphology. The morphology profile showed slight aggregation of the nanoparticles after the entrapment of bioactives (**Figure 3.3b**) compared to CS-PCL nanoparticles (**Figure 3.3a**). The spherical shape of the formulated nanoparticles may enhance their internalisation by macrophages, as multiple studies have demonstrated that spherical nanoparticles exhibit higher uptake than rod-shaped nanoparticles (Chithrani and Chan, 2007, Foroozandeh and Aziz, 2018, Chithrani et al., 2006, Behzadi et al., 2017, Zhao et al., 2017). For example, the study by Chithrani et al. revealed that spherical nanoparticles had a five-fold higher uptake than rod-shaped nanoparticles (Chithrani et al., 2006). In another work, researchers investigated spherical and rod-shaped transferrin-coated AuNP uptake on three cell lines. They observed that all the cell lines internalised spherical AuNPs at a higher rate than rod-shaped AuNPs (Chithrani and Chan, 2007). Furthermore, the particle size distribution for all the nanoparticles was within the nanoscale, which correlated with the data obtained from the DLS, as shown in **Table 3.1**.

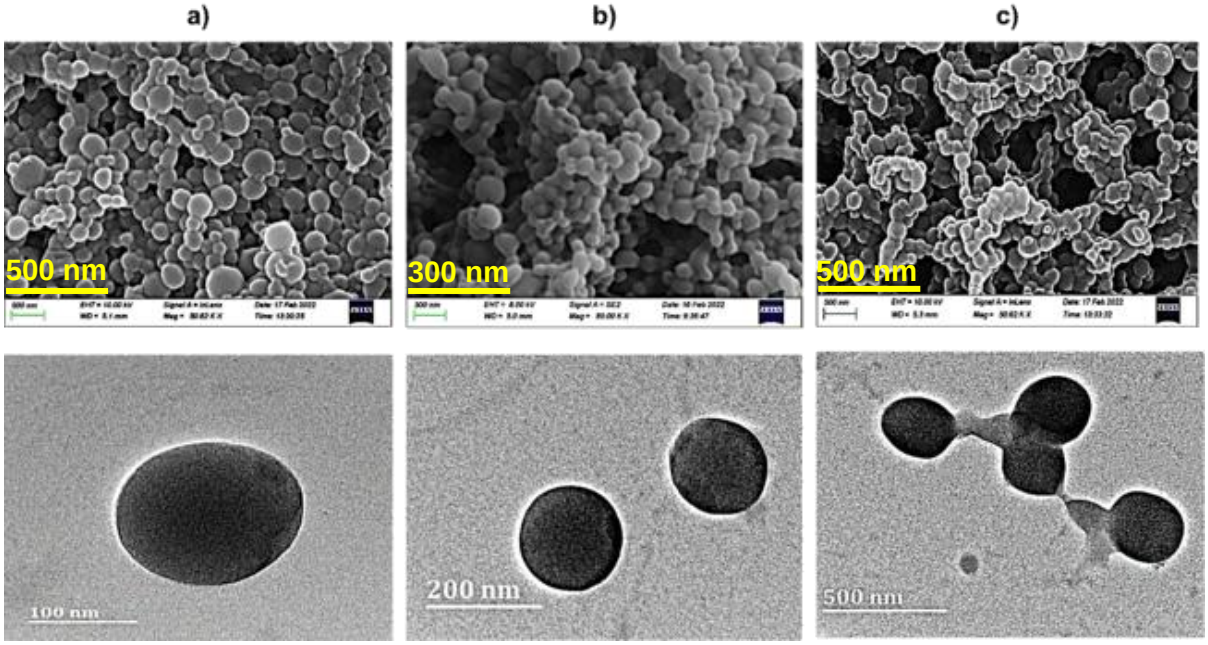

Figure 3.3: SEM and TEM images, respectively, showcasing the morphological characteristics of **(a)** unloaded CS-PCL nanoparticles, **(b)** drug-loaded CS-PCL nanoparticles, and **(c)** β-1,3-Glucan surface-functionalized CS-PCL nanoparticles. The images illustrate

smooth, spherical, and well-segregated nanoparticles at varying magnifications. The observed particle sizes correspond closely with those obtained from DLS analyses, as presented in **Figure 3.1** and **3.2**, confirming the consistency in size distribution and morphology across different characterisation techniques.

Determination of VITD3/RIF %LC and %EE of the fabricated nanoparticles was undertaken, as shown in **Table 3.1**. CS-PCL NPs exhibited a high % encapsulation efficiency of 96% for RIF compared to VITD3. However, when these nanoparticles were modified with glucan, the encapsulation efficiency decreased to 62% and 54% for RIF and VITD3, respectively, as seen in **Table 3.1**. This reduction in encapsulation efficiency may be attributed to potential drug leaching through the incubation period during functionalisation. Furthermore, prior research has demonstrated that VITD3 and its derivatives often exhibit reduced encapsulation efficiency when incorporated into polymeric nanoparticles due to their pronounced hydrophobic nature and inherent stability, which might explain the low encapsulation efficiency observed for VITD3 (Almouazen et al., 2013). In addition, VITD3 possess significant lipophilic characteristics, indicating a propensity to associate with or dissolve in lipid-rich environments; consequently, effectively encapsulating them within polymeric nanoparticles becomes a challenging endeavour (Almouazen et al., 2013). However, the observed encapsulation is suitable as the functionalisation aims to enhance the effectiveness of drug delivery at lower doses by improving target specificity and reducing any potential toxicity associated with high drug dosage (Oak and Khare, 2022).

Furthermore, the degree of glucan functionalisation as a function of time was investigated. Results showed that the highest degree of functionalisation (41.8%) was achieved at 24 hours of stirring time, while stirring further than 24 hours had no significant effect on the degree of functionalisation, as observed in **Figure 3.4**. This phenomenon might be attributable to the glucan functionalisation reaction reaching a saturation point after 24 hours of continuous stirring. This implies that no additional functional groups can be affixed to the glucan surface or that the glucan may no longer bind effectively to the nanoparticle's surface (Kaur et al., 2020). This limitation could arise from the restricted availability of reactive sites or due to the reversible or competitive nature of the functionalisation reaction. In such a scenario, some functional groups on the glucan may detach from the nanoparticle surface or be substituted by other molecules, resulting in a plateau in the degree of functionalisation after 24 hours of stirring (Kaur et al., 2020).

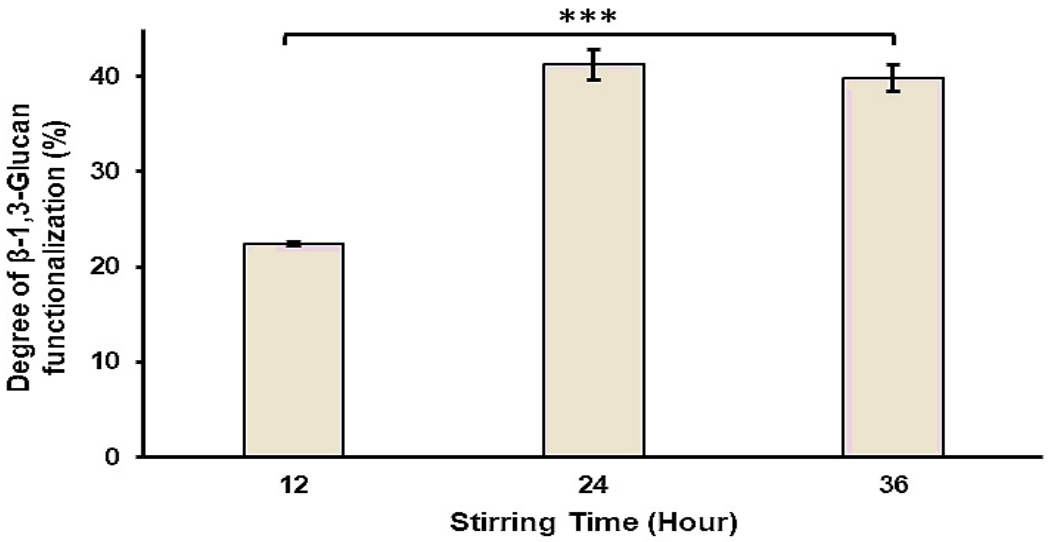

Figure 3.4: Percentage degree of β-1,3-Glucan functionalisation of CS-PCL nanoparticles as a function of time (n = 3, mean ± SD). Statistical significance between 12 hours and other groups is indicated as *** (very significant, $p < 0.001$).

3.3.2. Evaluation of Functional Transformation of Nanoparticles Before and After Drug Encapsulation and Functionalization

FTIR is usually used to study and characterise the nature of functional groups occurring at molecular surfaces. FTIR analysis was carried out for all excipient materials, non-functionalised and functionalised nanoparticles, and presented in **Figure 3.5** and **3.6**. The pure PVA main peaks were assigned as follows, with the main prominent absorption peaks at 3297 cm^{-1} (-OH stretching), 2910 cm^{-1} (-CH stretching), 1731 cm^{-1} (C=O stretching and -CH bending) and 1028 cm^{-1} (-C-O- stretching) corresponding to literature (Abureesh et al., 2016, Suflet et al., 2021). In the FTIR spectrum of CS, the following prominent peaks were also assigned; 3297 cm^{-1} (-OH and -NH symmetric vibration), 2878 cm^{-1} (-CH stretching), 1615-1515 cm^{-1} (Amide I and Amide II stretching), 1424-1326 (-CH stretching), 1059-1027 cm^{-1} (-C-O-stretching) and 895 cm^{-1} (saccharine structure) as previously reported in the literature (Abureesh et al., 2016, Fernandes Queiroz et al., 2015, Suflet et al., 2021). The PCL prominent peaks were also characterised as follows: 2944 cm^{-1} and 2863 cm^{-1} (Asymmetric and symmetric -CH stretching), 1721 cm^{-1} (C=O stretch),1237 cm^{-1} (asymmetric COC stretch) and 1161 cm^{-1} (COC symmetric stretch and OC-O stretching) (Gorodzha et al., 2015). The resulting nanoparticles (CS-PCL) exhibited major absorption peaks corresponding to the starting materials, with some, such as the 1721 cm^{-1} (C=O stretch) of PCL, showing reduced intensity. Each component was dispersed throughout the matrix without any chemical

transformation, as illustrated in **Figure 3.5a**. The reduced intensity suggests that PCL is well-integrated into the CS matrix, possibly with some level of interaction with the CS and PVA, resulting in less pronounced or weaker interactions between adjacent PCL chains, reducing the intensity of the C=O stretching vibration observed in the FTIR spectrum (**Figure 3.5a**) (Abureesh et al., 2016). In addition, the resulting CS-PCL nanoparticles showed the characteristic peaks of PVA and CS. The broadband at 3194 cm^{-1} corresponded to the stretching vibrations of hydrogen-bonded -OH and -NH, which slightly shifted to lower wavenumbers, while the -CH stretching peak at 2935 cm^{-1} was retained (**Figure 3.5a**). Furthermore, the PCL's fingerprint region in the 1161-1000 cm-1 ranger was present on the CS-PCL spectrum, showing the presence of PCL and evidence of composition formation.

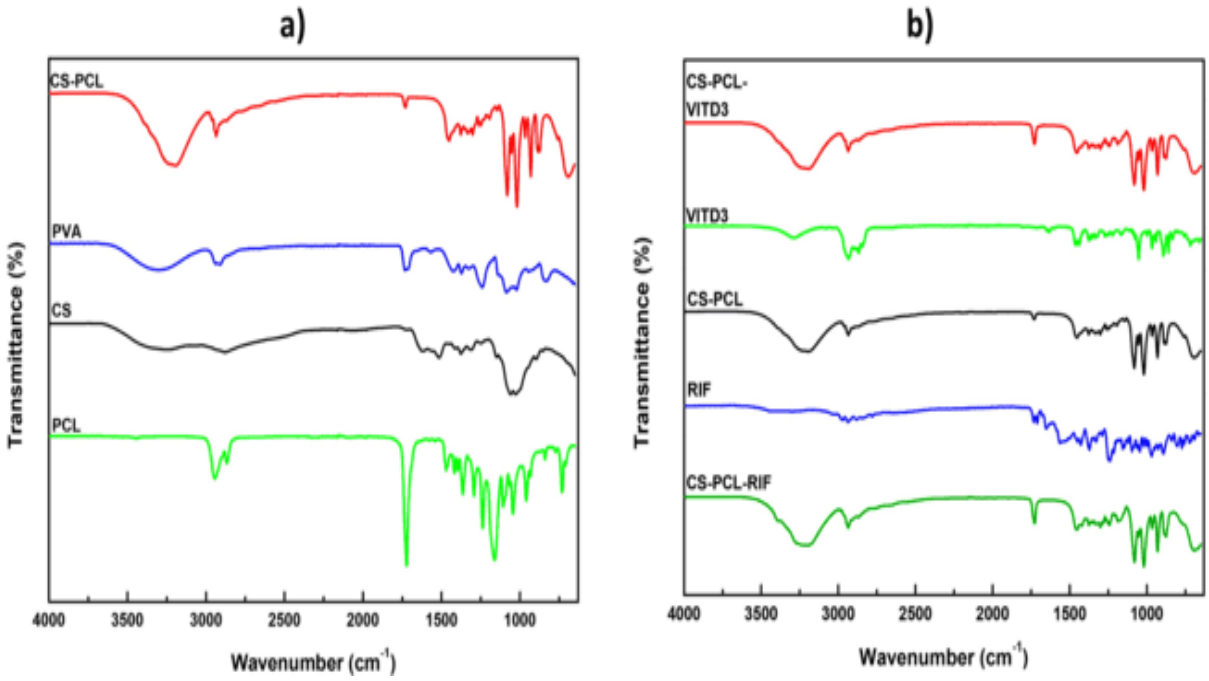

Figure 3.5: FTIR spectra analysis illustrating the molecular composition and transitions. **(a)** Comparison between excipient pristine polymers and the formulated CS-PCL nanoparticles, highlighting the characteristic peaks and indicative of polymer hybridisation. **(b)** Spectra of the formulated CS-PCL nanoparticles, excipient drugs, and the drug-loaded nanoparticles (CS-PCL-VITD3/RIF) demonstrating the incorporation of active ingredients and the resulting molecular interactions. The spectra reveal shifts and intensity changes that confirm the integration of the bioactive agents into the polymer matrix.

When VITD3/RIF was incorporated within the CS-PCL nanoparticles, no bands or absorption peaks of either VITD3/RIF were detected, signifying encapsulation of VITD3/RIF within CS-PCL nanoparticles in the PCL matrix via hydrophobic interaction without the formation of new

bonds as seen in **Figure 3.5b** (El Yousfi et al., 2023). Upon surface functionalisation of the CP-PCL NPs with β-1,3-Glucan, significant distinctions were observed in the spectra of Glu-CS-PCL NPs, as highlighted in **Figure 3.6**. The absorption spectrum of CS-PCL displayed an initial band at 1727 cm^{-1}, which was notably intensified in Glu-CS-PCL (**Figure 3.6**). This enhancement can be attributed to the chemisorption or physisorption of β-1,3-Glucan, resulting from interactions with hydroxyl groups and the C=O stretching vibration of the ester group (Trombino et al., 2022); additionally, the presence of β-1,3-Glucan was evident in Glu-CS-PCL NPs spectrum within the spectral range of 1500-950 cm^{-1}, as a new broader peak formed as highlighted in **Figure 3.6**. This spectrum shows the successful surface functionalisation of the NPs with β-1,3-Glucan.

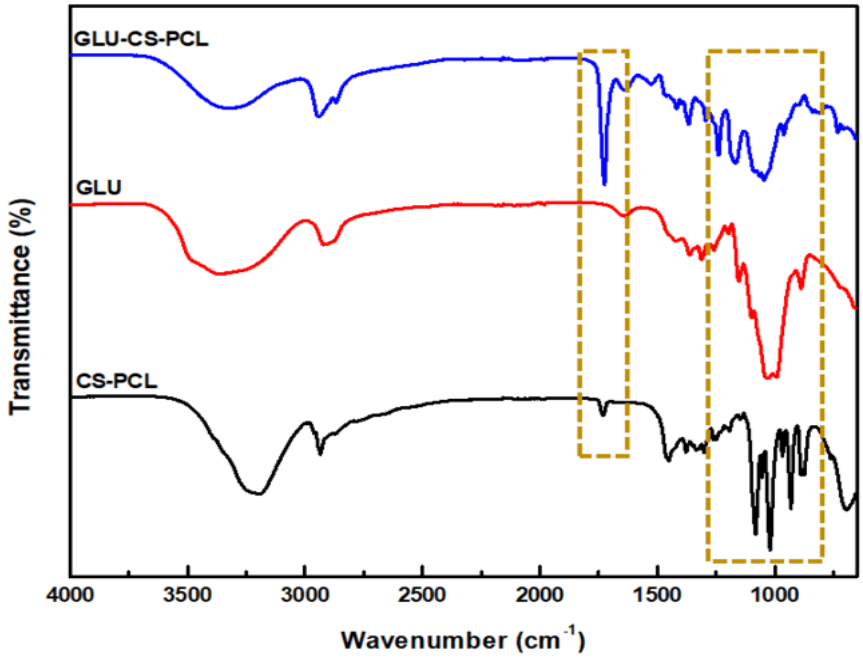

Figure 3.6: FTIR Spectra of Pristine β-1,3-Glucan (Glu), Functionalized (Glu-CS-PCL), and Non-Functionalized (CS-PCL) Nanoparticles: Demonstrating Molecular Composition and Transitions upon Surface Functionalization.

3.3.3. Analysis of the crystallographic structure of the nanoparticles

The degree of crystallinity of the host polymer matrix is an essential parameter in the drug release study profile, with a higher drug release rate observed in polymers with a low degree of crystallinity, whilst delayed sustained drug release being observed in polymers with a higher degree of crystallinity (Jeong et al., 2003, Karavelidis et al., 2011, Kamaly et al., 2016). The

crystallinity degree of the formulated nanoparticle and all the excipients' materials using the XRD technique was carried out and presented in **Figure 3.7**. The XRD pattern of pure chitosan, which is relatively amorphous, exhibited broad peaks at 2θ ~ 10° and 20°, as depicted in the pattern obtained for pristine CS in **Figure 3.7a**. Similarly, semi-crystalline PCL displays two major peaks at 2θ ~ 21° and 23°, corresponding to the pattern obtained for pristine PCL in **Figure 3.7a**. Furthermore, the strong semi-crystalline diffraction peaks of PVA at 2θ ~ 19° and 20° were also observed in the same region, consistent with prior literature reports, respectively (Siafaka et al., 2016, Suganthi et al., 2020, Castilla-Cortazar et al., 2019). Formulated nanoparticle (CS-PCL) depicted a high major crystalline diffraction peak at 9.6º, which might be attributed to polymer hybridisation to form crystalline nanoparticles (Abureesh et al., 2016, Jana et al., 2014).

The peak intensity of PCL (~18.8 - 23.36º) was significantly lowered, as observed in **Figure 3.7a** and **3.7b**. It is possible that the coordination properties of PCL polymer molecules were altered due to the presence or being incorporated within the CS/PVA shell, leading to the reduction of PCL peak intensities as observed with the FTIR spectrum in **Figure 3.5a** (Abureesh et al., 2016, Jana et al., 2014). This phenomenon may signify good miscibility of component materials in the CS/PCL blend (Jana et al., 2014). Two semi-crystalline peaks were further observed for CS-PCL from 18.8 - 23.36º and 23.5 - 25.34º. Other crystalline peaks with low intensities were further observed at 35.65º and 40.36 - 45º, confirming the crystallinity of the formulated nanoparticles. The crystallinity of CS-PCL observed may contribute to sustained drug release as previously reported that polymers/drug delivery systems with a higher degree of crystallinity, with particular emphasis on PCL, have been shown to have sustained drug release (Jeong et al., 2003, Miyajima et al., 1997, Bhadran et al., 2023, El Yousfi et al., 2023).

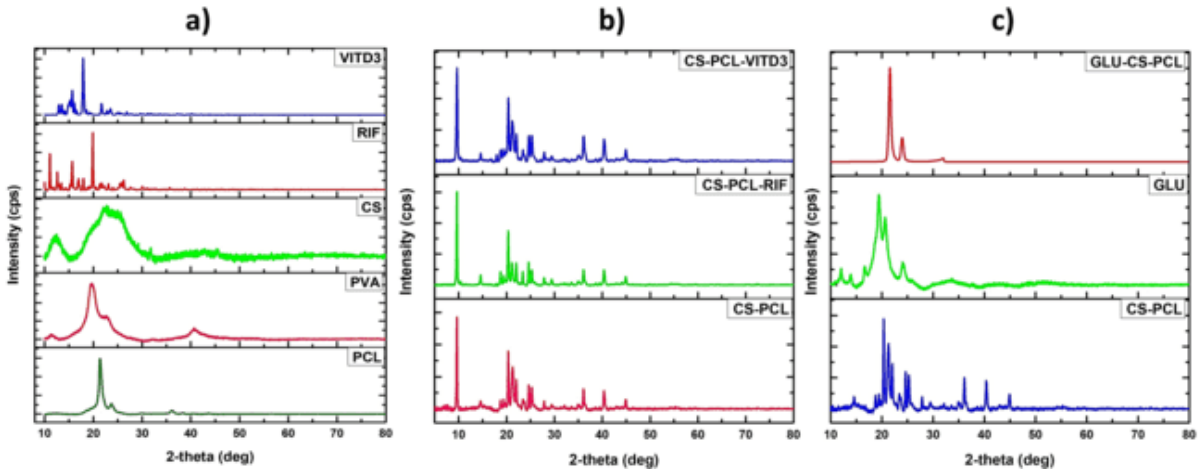

Figure 3.7: XRD Diffractograms of **(a)** Excipient Materials, **(b)** Formulated Nanoparticles with and without Drug Encapsulation, and **(c)** Pristine β-1,3-Glucan, Functionalized, and Non-Functionalized Nanoparticles: Illustrating the Crystallinity of Formulated Nanoparticles.

The XRD pattern of pure VITD3/RIF corresponded to the previously reported strong crystalline diffraction peaks, as displayed in **Figure 3.7a** (Sharma et al., 2021, Vora et al., 2018). After encapsulating either VITD3 or RIF, the diffraction patterns of nanoparticles loaded with these drugs resembled those of the unloaded nanoparticles (CS-PCL), as shown in **Figure 3.7b**. These patterns did not exhibit any peaks corresponding to drug crystals. This observation indicates that VITD3 or RIF was either in an amorphous state within the polymer matrix or dispersed within the amorphous regions of the matrix rather than being present in a crystalline form, further confirming the successful incorporation of the drugs within the nanoparticles (Jeong et al., 2003, Bodmeier and McGinity, 1987, Mazumder et al., 2017, Rodriguez et al., 2020). Following the surface functionalisation of CS-PCL nanoparticles with β-1,3-Glucan, a noticeable change in the diffraction pattern of CS-PCL occurred (**Figure 3.7c**). This change was attributed to the presence of β-1,3-Glucan and manifested as two distinct crystalline peaks at approximately 21.5º and 23.5º, as illustrated in **Figure 3.7c**. This observation confirms the presence of β-1,3-Glucan on the surface of the modified nanoparticles.

3.3.4. Evaluation of the thermal behaviour and storage stability of the optimised Nanoparticles

TGA was performed to evaluate the thermal stability of the formulated nanoparticles by analysing weight loss as a function of temperature. The thermal degradation temperature is defined as the temperature at which the initial weight loss of the material is observed (Anju et

al., 2020). The degradation temperatures of the excipient materials, including β-1,3-Glucan, were consistent with those reported in the literature, confirming the accuracy of the thermal analysis as seen in **Figure 3.8** (Hori et al., 2020, Abraham et al., 2016, Longo et al., 2022, Jannasari et al., 2019). The thermal degradation of all nanoparticle formulations started at temperatures higher than those of the starting materials, beginning around 250°C, showing the thermal stability of the nanoparticles as seen in **Figure 3.8**. Interestingly, PCL as a starting material exhibited higher degradation temperatures than the formulated nanosystems. Several factors could explain this discrepancy. The formulation process involving CS and PVA likely introduces a complex matrix that can alter the thermal properties of PCL (Reyna-Urrutia et al., 2022). Interactions between PCL and these components may disrupt PCL's crystalline structure, resulting in a lower degradation temperature as lower crystallinity is often associated with decreased thermal stability, which may contribute to the observed reduction in degradation temperature of the nanoparticles compared to PCL (Fernández-Tena et al., 2023).

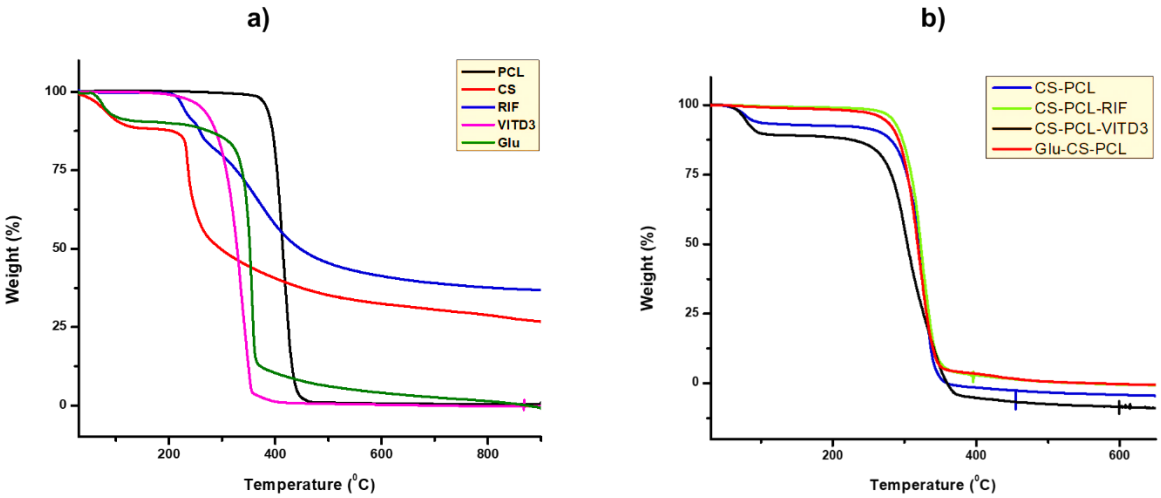

Figure 3.8: Thermogravimetric Analysis of **a)** Excipient Materials and **b)** Nanoparticles: Degradation Temperatures of Formulated Nanoparticles.

DSC was further employed to assess the formulated nanoparticles' thermal characteristics, stability, and drug encapsulation behaviour by analysing thermal phase transitions from controlled temperature changes driven by heat flow (Bakonyi et al., 2017, Bannov et al., 2020). Thermal transitions for all excipient materials were consistent with those previously reported in the literature (Branton and Jana, 2017, Ignjatovic et al., 2018, Jana et al., 2014, Kerman et al., 2005, Mwila and Walker, 2020, Tipa et al., 2021), as shown in **Figure 3.9**, alongside the transitions of the formulated nanoparticles. A notable endothermic melting peak in CS-PCL nanoparticles was observed at approximately 166.31°C, higher than the melting temperatures

of the individual starting polymers, CS and PCL, as shown in **Figure 3.9a**. This new peak can be attributed to the interaction between the blended polymers, suggesting a significant degree of miscibility and resulting in a single-phase transition peak (She et al., 2007). Upon loading the nanoparticles with VITD3 or RIF, the endothermic melting peaks of the CS-PCL nanoparticles remained unchanged. Additionally, the peaks corresponding to pristine VITD3, or RIF, were absent, as shown in **Figure 3.9b**. This observation indicates that the encapsulation of VITD3 or RIF did not significantly affect the stability or thermal behaviour of the nanoparticles. It suggests that the drug molecules either remained isolated within the nanoparticle matrix or were effectively dispersed, preventing them from undergoing distinct bulk transition phases (Jia et al., 2020, Adekiya et al., 2022). This assertion supports the data presented in **Figure 3.7** (XRD) and **Figure 3.5** (FTIR), further corroborating the notion of drug isolation and dispersion within the nanoparticles' matrix.

Upon functionalising CS-PCL nanoparticles with β-1,3-Glucan, a discernible enhancement in the PCL peak at 53.42°C was observed (**Figure 3.9c)**, and a similar observation was made in the FTIR spectrum in **Figure 3.6**. This enhancement can be attributed to the chemisorption or physisorption of 1,3-beta-glucan onto the nanoparticle's surface, arising from interactions with hydroxyl groups and the ester groups (Trombino et al., 2022). The thermogram for Glu-CS-PCL nanoparticles shows distinct thermal transitions, with prominent peaks corresponding to either β-1,3-Glucan or the CS-PCL nanoparticles; notably, these peaks are shifted to lower or upper temperatures than the 1,3-beta-glucan or CS-PCL sample (**Figure 3.9c**). For the β-1,3-Glucan (Glu), sharp and broad endothermic melting peaks are observed at approximately 84°C and 328°C, indicating its thermal transition. However, these peaks are shifted to higher and lower temperatures in the Glu-CS-PCL nanoparticles, around 94°C and 225°C, respectively (**Figure 3.9c).** Similarly, the CS-PCL nanoparticles alone show a notable peak at around 166°C, associated with the polymer blend's melting transition.

The presence of 1,3-beta-glucan in the Glu-CS-PCL formulation does not eliminate this peak but instead adds additional transitions, as seen with the β-1,3-Glucan peak, which has shifted from 328°C to around 225°C (**Figure 3.9c**). This down and upward shift suggests that the functionalisation process has introduced significant interactions between glucan and the CS-PCL matrix. These shifts further indicate a change in the thermal stability of CS-PCL nanoparticles when β-1,3-Glucan is incorporated into its surface or vice versa, likely due to the intermolecular interactions between the components. These findings confirm that β-1,3-Glucan has been successfully incorporated into the CS-PCL nanoparticles and suggest that

the β-1,3-Glucan is not simply attached but interacts at a molecular level with the polymer matrix. In addition, the formulated nanoparticles, whether they were functionalised or not, demonstrated favourable thermal stability characteristics that are well-suited for polymeric nanoparticles and align with their intended applications, as evident from their consistently elevated melting points and degradation temperature (Mansfield and Banash, 2023, Mansour, 2012).

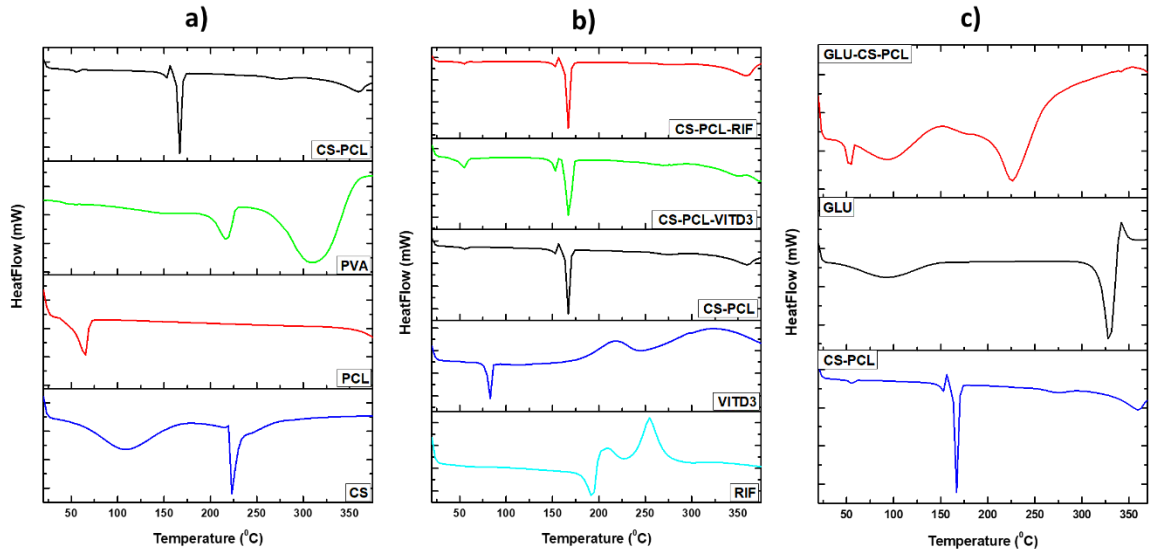

Figure 3.9: DSC Thermograms of **(a)** Formulated CS-PCL Nanoparticles and Excipient Polymers, **(b)** Formulated Nanoparticles with Excipient Drugs/Bioactives, and **(c)** β-1,3-Glucan and Glucan-Functionalized CS-PCL Nanoparticles. Illustrating the Good Miscibility of Pristine Drugs and Their Interaction with the Nanoparticle's Matrix.

Various factors, including particle size, surface charge, and PDI influence nanoparticles' stability. Stability is often indicated by minimal changes in particle size, zeta potential, and PDI over time, reflecting resistance to aggregation or agglomeration (Phan and Haes, 2019, Jain et al., 2018). A higher zeta potential enhances stability by increasing electrostatic repulsion between particles, while a lower PDI signifies a more uniform size distribution, contributing to overall stability (Phan and Haes, 2019, Jain et al., 2018). The storage stability of the formulated nanoparticles was carried out using DLS after 3 months by measuring any changes in particle size, zeta potentials and PDI, as presented in **Table 3.2**. Particle size for all the formulations increased in the range of 10-25 nm, with only Glu-CS-PCL-RIF having a 48 nm increase, whilst the zeta potential for all formulations exhibited slight changes, including PDI (**Table 3.2**). The observed increase in particle size, ranging from 20 to 50 nm across all formulations, indicates a notable yet relatively modest change over a period of 3 months. The

increase, which does not exceed 50 nm, can be considered insignificant, as the nanoparticles remain within an acceptable size range for phagocytosis or endocytosis by macrophages (Lazzari et al., 2012, Kiio and Park, 2020). This increase in particle size can be attributed to various factors, including potential aggregation or minor structural adjustments. The slight changes in zeta potential, as well as the persistence of consistent PDI values across all formulations, are indicative of the nanoparticles' ability to maintain their electrostatic stability and size distribution over the observed time frame, which thus effectively resist agglomeration or aggregation (Hu et al., 2011, Hernandez-Giottonini et al., 2020). The sustained stability of these nanoparticles over 3 months is a promising indication of their potential utility as drug delivery systems. Such stability is vital to ensure the reliability and effectiveness of nanoparticle-based formulations, as it suggests that the nanoparticles can retain their desired characteristics and functionality over extended periods.

Table 3.2: Stability profile of formulated nanoparticles as a function of time using DLS at room storage temperature.

Time	**0 month**			**After 3 months**		
Formulation	**Particle size (nm)**	**ZP (mV)**	**PDI (a.u)**	**Particle size (nm)**	**ZP (mV)**	**PDI (a.u)**
CS-PCL	175.60 ± 2.51	+20.5 ± 0.40	0.28 ± 0.010	187.51 ± 1.31	+18.8 ± 0.51	0.23 ± 0.110
CS-PCL-VITD3	182.13 ± 4.70	+26.3 ± 0.45	0.24 ± 0.004	201.36 ± 1.30	+25.8 ± 0.50	0.28 ± 1.031
Glu-CS-PCL VITD3	182.90 ± 1.15	+24.8 ± 0.73	0.15 ± 0.006	200.23 ± 2.28	+21.6 ± 1.40	0.26 ± 0.012
CS-PCL-RIF	156.13 ± 1.12	+20.6 ± 1.05	0.14 ± 0.027	179.39 ± 0.09	+21.3 ± 1.05	0.19 ± 0.160
Glu-CS-PCL-RIF	122.63 ± 5.11	+19.5 ± 0.21	0.27 ± 0.009	170.23 ± 0.83	+22.1 ± 0.59	0.21 ± 0.016

3.3.5. *In vitro release* of VITD3 and RIF in formulated nanoparticles

The rate and quantity of drug release significantly impact dosing frequency. Extended-release formulations reduce the need for frequent administration, which is crucial for ensuring patient compliance with infectious diseases like TB (Sumaila et al., 2023). This study examined *in vitro* release profiles of two drugs, VITD3 and RIF, from nanoparticles. These nanoparticles were either functionalised with β-1,3-Glucan or non-functionalized. The experiments were conducted under various pH conditions (4.6, 6.8, and 7.4) using appropriate release media solutions, and the results are presented in **Figure 3.10** (for VITD3) and **Figure 3.11** (for RIF).

The analysis of drug release kinetics, depicted in both **Figure 3.10** and **3.11**, revealed a similar pattern between functionalised and non-functionalized nanoparticles.

Specifically, for VITD3, an initial burst release was observed at the 1-hour mark, accounting for approximately 20%, 26%, and 30% of the total release at pH 7.4, 6.8, and 4.6, respectively, in both functionalised and non-functionalized nanoparticles (**Figure 3.10**). Subsequently, between 4 to 48 hours, a sustained release phase occurred, as indicated by the plateau in the release curve. This phase resulted in cumulative releases of approximately 46%, 55%, and 78% at pH 7.4, 6.8, and 4.6, respectively, at the 6-hour mark. Notably, the highest drug release, reaching approximately 86%, was observed at pH 4.6, compared to 37% and 85% at pH 7.4 and 6.8 after 48 hours. The release continues gradually, approaching a plateau close to 90% after 48 hours. Similarly, for RIF, an initial burst release of 11%, 18%, and 14% at the 1-hour mark was observed at pH 7.4, 6.8, and 4.6 for both functionalised and non-functionalized nanoparticles (**Figure 3.11**). The release continues gradually, eventually approaching a plateau similar to what was observed for VITD3 in **Figure 3.10**. RIF exhibited its maximum cumulative release at pH 4.6, with approximately 96%, followed by pH 6.8 and 7.4, with 85% and 37%, respectively, after 48 hours of drug release (**Figure 3.11**).

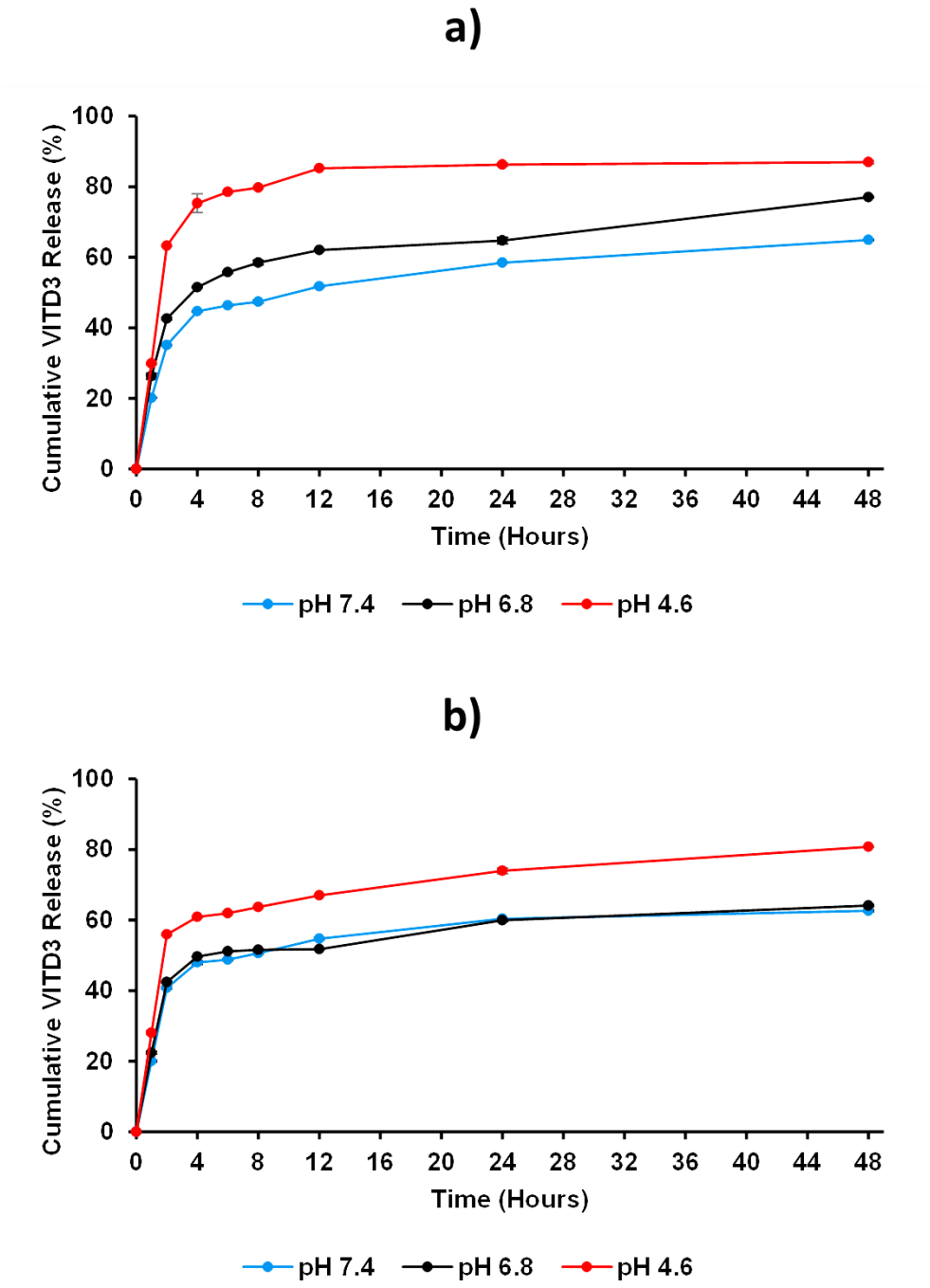

Figure 3.10: Cumulative release of VITD3 from **(a)** CT-PCL-VITD3 and **(b)** Glu-CS-PCL-VITD3 nanoparticles over 48 hours at different pH levels (pH 4.6, 6.8, and 7.4) at 37°C, highlighting sustained and pH-dependent release profiles (n = 3, mean ± SD).

This observed release behaviour in **Figure 3.10** and **Figure 3.11** can be attributed to the interplay of factors such as pH-dependent nanoparticle degradation and the nanoparticle's structural properties (Pandey et al., 2022). The initial burst release observed at the 1-hour

mark may be attributed to the rapid dissolution of the drug molecules that are readily accessible on the nanoparticles' surface (Ramalho et al., 2017). This phenomenon is a common occurrence in nanoparticle-based drug delivery systems; following the initial burst release, the drug encapsulated within the nanoparticles is subsequently released at a slower rate, often resulting in a biphasic release profile characterised by an initial rapid release phase followed by a more controlled and gradual release phase as observed in **Figure 3.10** and **Figure 3.11** (Sung et al., 2009, Ramalho et al., 2017). Subsequently, as the release medium's pH influences the degradation of nanoparticles, variations in pH conditions can result in differential release rates (Chen et al., 2020, Chu et al., 2022). The elevated release rate of both VITD3 and RIF observed at pH 4.6 can be attributed to enhanced degradation of the nanoparticles in acidic environments.

This behaviour aligns with prior research indicating that chitosan and polycaprolactone nanoparticles exhibit greater drug release at lower pH levels, as these polymers demonstrate pH-responsive characteristics (Nair et al., 2019, Lu et al., 2019). In acidic conditions, chitosan exhibits enhanced solubility and swelling of its nanoparticles due to the protonation of its amino groups, particularly pronounced at lower pH values such as 4.6, which facilitates the release of encapsulated drugs; likewise, the degradation of PCL nanoparticles primarily occurs through ester linkage hydrolysis in aqueous environments, and at lower pH values, this hydrolysis rate accelerates, resulting in faster PCL nanoparticle degradation and consequently higher drug release rates (Lu et al., 2019, Nair et al., 2019). Whilst at neutral pH (7.4), the nanoparticles exhibit greater stability, resulting in a slower drug release, as observed across all release profiles (**Figure 3.10** and **3.11**) (Chen et al., 2023).

The plateau in drug release after reaching 86% (VITD3) and 96% (RIF) indicates that a significant portion of the drug payload has been released, and the system has reached equilibrium (Heredia et al., 2022). These results explain the drug release characteristics of the nanoparticles under varying pH conditions, offering valuable insights into their potential applications in drug delivery. The pH within macrophages infected with Mtb rapidly shifts from neutral to acidic (pH 4.5-5) during phagolysosome acidification, facilitating bacterial killing. However, Mtb can survive within these macrophages by inhibiting the biogenesis and acidification of the phagolysosome, thereby stabilising the pH between 6.2-6.5 within the phagosome, allowing Mtb to persist within the intracellular environment (Queval et al., 2017, Khoza et al., 2022). As a result, the fabricated nanosystem is strategically positioned to enhance the delivery of drug payloads to macrophages infected by Mtb. The nanosystem has

demonstrated a high drug release rate at pH levels of 4.6 and 6.8. These pH levels are critical for the survival and degradation of Mtb within the macrophages, indicating that the nanosystem is effectively tuned to the intracellular environment of the infected macrophages. This could lead to improved treatment outcomes by ensuring that drugs are released where they are most needed and in a manner that aligns with the survival mechanisms of Mtb.

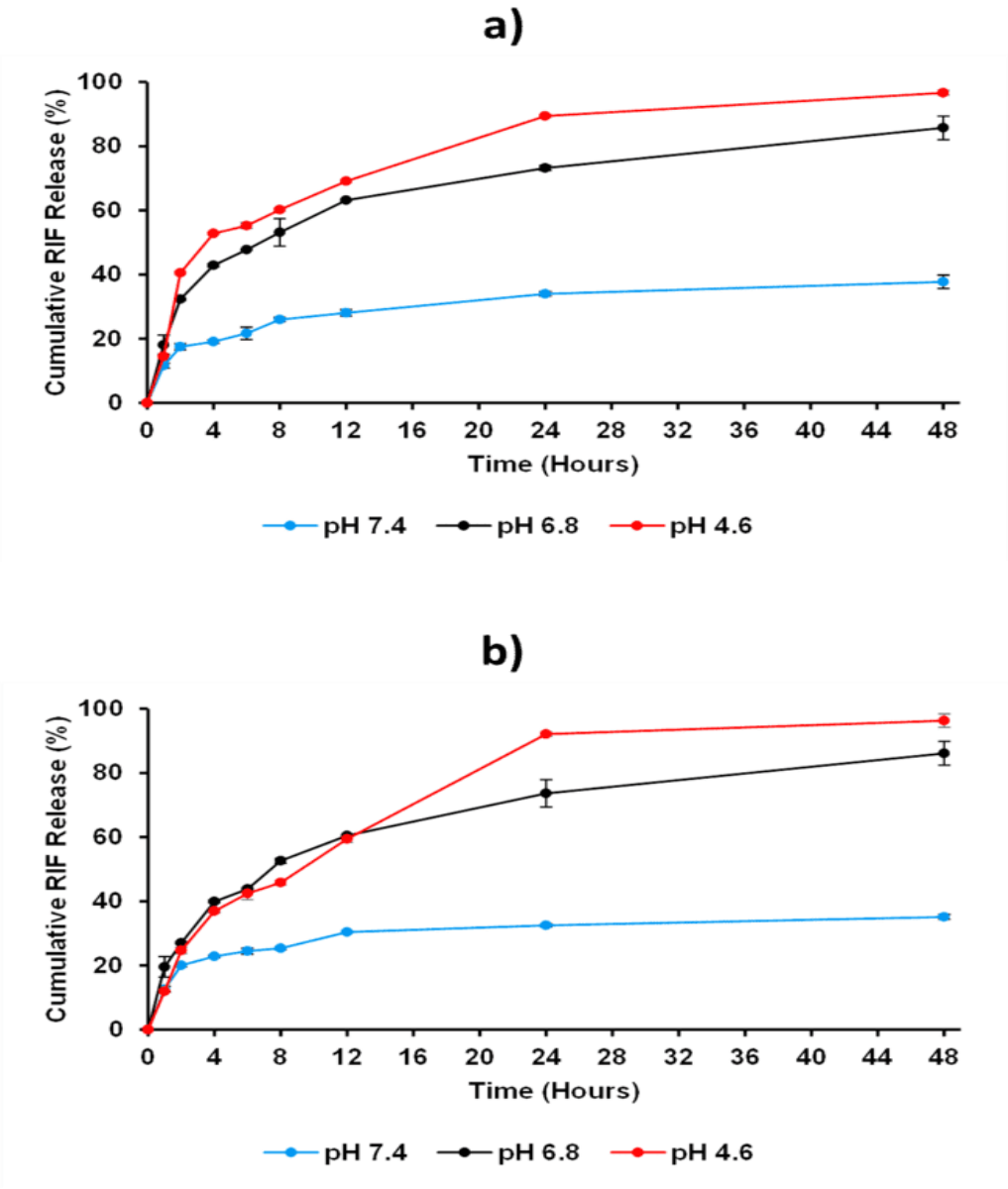

Figure 3.11: Cumulative release of RIF from **(a)** CT-PCL-RIF and **(b)** Glu-CS-PCL-RIF nanoparticles over 48 hours at different pH levels (pH 4.6, 6.8, and 7.4) at 37°C, highlighting sustained and pH-dependent release profiles (n = 3, mean ± SD).

3.3.6. *In Vitro* Cytotoxicity Assay and Metabolic Activity of Formulated Nanoparticles in RAW 264.7 Cell Line

The effect of the formulated nanoparticles and the pristine bioactive substance on cellular metabolic activity in the RAW 264.7 macrophage cell line, as well as their cytotoxicity, were evaluated over 48 hours using a 3-(4,5-dimethylthiazole-2-yl)-2,5-diphenyl tetrazolium bromide (MTT) assay (MTT Cell Proliferation Kit I, Roche, Basel, Switzerland). This assessment provides valuable insights into the cytocompatibility of the synthesised nanoparticles. Specifically, cell viability percentages below 40% indicate potent cytotoxicity, percentages ranging from 40%-60% suggest moderate cytotoxicity, percentages within the 60%-80% range indicate weak cytotoxicity and percentages exceeding 80% are indicative of a non-toxic response (Iso, 2009, Lopez-Garcia et al., 2014). As shown in **Figure 3.12**, treatment with CS-PCL nanoparticles and free RIF solution had no significant effect on the cellular metabolic activity of the RAW 264.6 cell line when compared to the untreated control with cell viability of ~100% at all treatment concentration ranges showing cytocompatibility of formulated nanoparticles with RAW 264.6 cell line.

Treatment with VITD3 resulted in significant cytotoxicity at the highest concentrations, with cell viability percentages of 2% at 300 µg/mL and 38% at 145 µg/mL, as shown in **Figure 3.12**. In contrast, there was no observed cell cytotoxicity at moderate to low concentrations of VITD3 (75 and 38 µg/mL) as the percentage of cell viability was above 100%, respectively. When cells were treated with CS-PCL encapsulating VITD3 (CS-PCL-VITD3), there was no observed cell cytotoxicity at all concentration ranges (300-38 µg/mL) as percentage cell viability was above 80%, signifying non-toxic effect and cytocompatibility of CS-PCL-VITD3 nanoparticles with RAW 264.6 cell line. Similarly, no cell toxicity was observed with RIF-encapsulated nanoparticles (CS-PCL-RIF), as shown in **Figure 3.12**. These experimental results show that encapsulating VITD3 into CS-PCL nanoparticles could help reduce the *in vitro* cytotoxicity of VITD3 at higher concentrations.

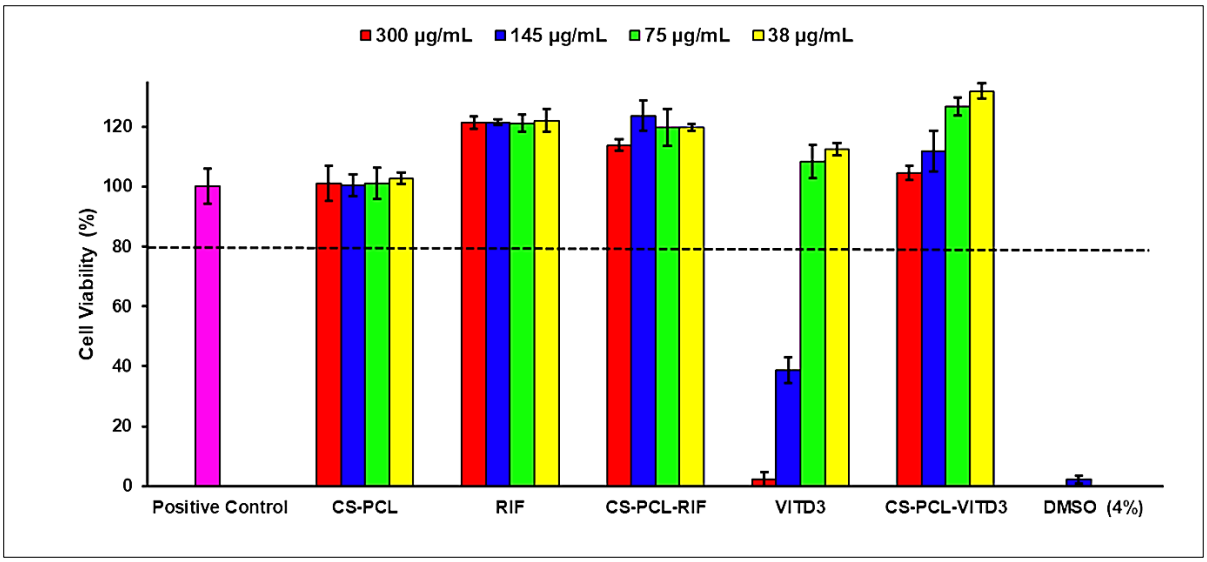

Figure 3.12: MTT assay measurement of the viability of RAW 264.7 murine macrophage cells after 48-hour treatment with free RIF, VITD3, CS-PCL and VITD3/RIF CS-PCL nanoparticles at different concentrations (n = 3, mean ± SD). The horizontal line at 80% represents the threshold for non-toxic effects.

Similarly, the cytotoxicity and cytocompatibility of the nanoparticles formulated after functionalisation with β-1,3-Glucan Euglena gracilis was assessed. The concentrations ranged from 6.25-25 µg/mL for β-1,3-Glucan Euglena gracilis and 300, 145, and 75 µg/mL forβ-1,3-Glucan functionalised nanoparticles. As illustrated in **Figure 3.13**, β-1,3-Glucan exhibited non to weak toxic effects on RAW 264.7 cells, with a concentration-dependent response. Functionalising the nanoparticles with β-1,3-Glucan showed no toxic effects on the cells, and the percentage of cell viability exceeded 80% at all concentrations (**3.13)**, indicating that β-1,3-Glucan can be safely used to target macrophage cells actively. In summary, the formulated nanoparticles hold promise for application in formulation science as an effective delivery system capable of safely encapsulating high concentrations of VITD3 and RIF. This system can facilitate the sustained release of bioactive contents over an extended duration while maintaining therapeutic concentrations at non-toxic levels, thereby reducing dosing frequency and enhancing overall therapeutic efficacy.

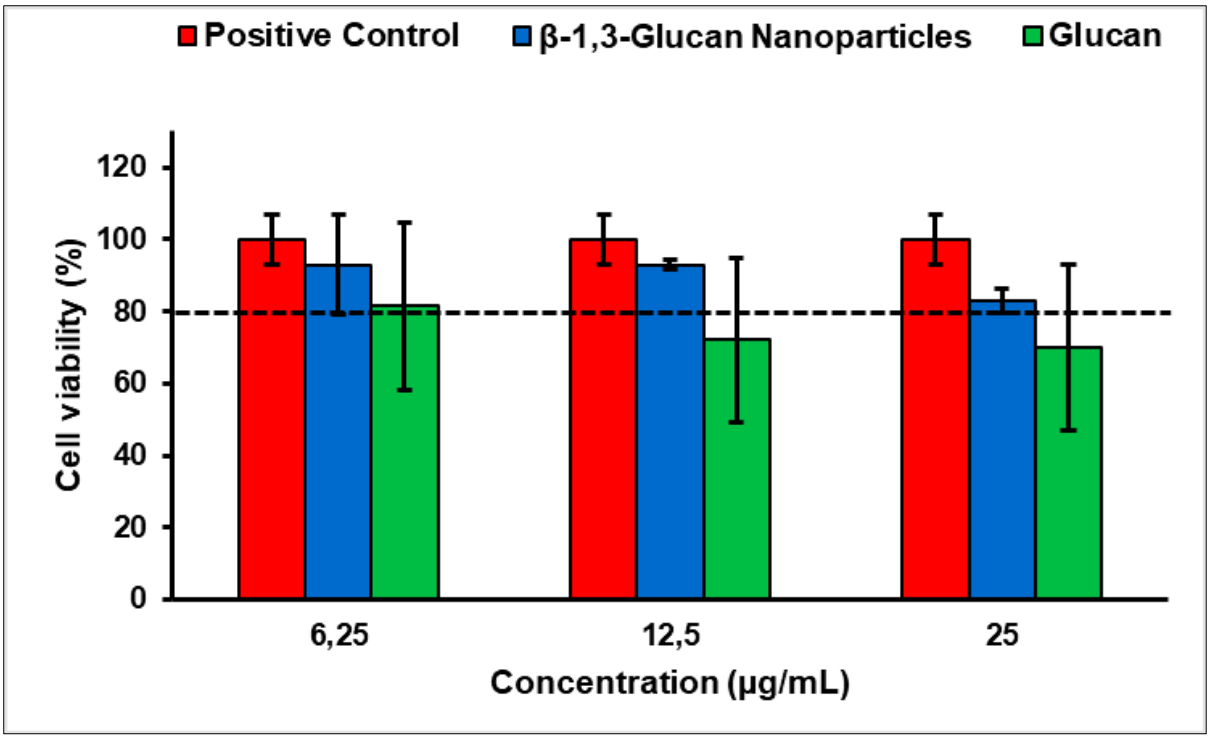

Figure 3.13: MTT assay measurement of RAW 264.7 cell viability after 48-hour treatment with pristine β-1,3-Glucan and β-1,3-Glucan functionalised nanoparticles at different concentrations (n = 3, mean ± SD). The horizontal line at 80% represents the threshold for non-toxic effects.

3.4. Concluding Remarks

In conclusion, this section provides valuable insights into the potential of formulated nanoparticles with an average particle size ranging from 122.63 ± 5.11 nm to 182.90 ± 4.70 nm as a promising approach to improve the delivery of VITD3/RIF payloads to macrophages. The findings suggest that these nanoparticles can be internalised through various endocytosis mechanisms, including clathrin- or caveolin-mediated and clathrin- or caveolin-independent pathways, which follow pinocytosis mechanisms. Furthermore, the nanoparticles exhibited good stability, homogeneity, and thermal resilience, making them suitable for various applications, including drug delivery systems. The sustained stability over 3 months is particularly promising, as it indicates the potential for long-term reliability and effectiveness. One of the significant advantages of this nanosystem is its ability to release drugs at pH levels relevant to the intracellular environment of macrophages infected by Mtb. This tailored drug release mechanism can lead to improved treatment outcomes by ensuring that drugs are delivered precisely where they are needed and in a manner aligned with Mtb's survival mechanisms.

This section also highlights the potential of the formulated nanoparticles being functionalised with β-1,3-Glucan as a safe targeting mechanism for macrophage cells, underscoring its non-toxic attributes and compatibility with RAW macrophages. A study focusing on macrophage polarisation is recommended further to explore the potential immunomodulatory effects of formulated nanoparticles. This study should include quantifying reactive oxygen species and cytokines such as TNF and IL-10. Additionally, investigating the synergistic effects of VITD3 as an immunomodulator and RIF as an antibacterial agent could yield valuable insights into developing more effective TB treatments. These studies would further contribute to our understanding of the capabilities and applications of the formulated nanoparticles and their potential to improve TB treatment strategies.

3.5. References

Abraham, A., Soloman, P. A. & Rejini, V. O. 2016. Preparation of Chitosan-Polyvinyl Alcohol Blends and Studies on Thermal and Mechanical Properties. *Procedia Technology,* 24**,** 741-748.

Abureesh, M. A., Oladipo, A. A. & Gazi, M. 2016. Facile synthesis of glucose-sensitive chitosan–poly (vinyl alcohol) hydrogel: Drug release optimisation and swelling properties. *International journal of biological macromolecules,* 90**,** 75-80.

Adekiya, T. A., Kumar, P., Kondiah, P. P. D., Ubanako, P. & Choonara, Y. E. 2022. In Vivo Evaluation of Praziquantel-Loaded Solid Lipid Nanoparticles against S. mansoni Infection in Preclinical Murine Models. *Int J Mol Sci,* 23.

Allue-Guardia, A., Garcia, J. I. & Torrelles, J. B. 2021. Evolution of Drug-Resistant Mycobacterium tuberculosis Strains and Their Adaptation to the Human Lung Environment. *Front Microbiol,* 12**,** 612675.

Almouazen, E., Bourgeois, S., Jordheim, L. P., Fessi, H. & Briancon, S. 2013. Nano-encapsulation of vitamin D3 active metabolites for application in chemotherapy: formulation study and in vitro evaluation. *Pharm Res,* 30**,** 1137-46.

Anju, S., Prajitha, N., Sukanya, V. S. & Mohanan, P. V. 2020. Complicity of degradable polymers in health-care applications. *Materials Today Chemistry,* 16**,** 100236.

Bakonyi, M., Berkó, S., Budai-Szűcs, M., Kovács, A. & Csányi, E. 2017. DSC for evaluating the encapsulation efficiency of lidocaine-loaded liposomes compared to the ultracentrifugation method. *Journal of Thermal Analysis and Calorimetry,* 130**,** 1619-1625.

Bannov, A. G., Popov, M. V. & Kurmashov, P. B. 2020. Thermal analysis of carbon nanomaterials: advantages and problems of interpretation. *Journal of Thermal Analysis and Calorimetry,* 142**,** 349-370.

Behzadi, S., Serpooshan, V., Tao, W., Hamaly, M. A., Alkawareek, M. Y., Dreaden, E. C., et al. Mahmoudi, M. 2017. Cellular uptake of nanoparticles: journey inside the cell. *Chemical Society reviews,* 46**,** 4218-4244.

Bhadran, A., Shah, T., Babanyinah, G. K., Polara, H., Taslimy, S., Biewer, M. C. & Stefan, M. C. 2023. Recent Advances in Polycaprolactones for Anticancer Drug Delivery. *Pharmaceutics,* 15.

Bodmeier, R. & Mcginity, J. W. 1987. The preparation and evaluation of drug-containing poly(dl-lactide) microspheres formed by the solvent evaporation method. *Pharm Res,* 4**,** 465-71.

Branton, A. & Jana, S. 2017. A Study on the Effect of the Energy of Consciousness Healing Treatment on Physicochemical and Thermal Properties of Vitamin D 3 (Cholecalciferol). *Science Journal of Analytical Chemistry,* 5.

Castilla-Cortazar, I., Vidaurre, A., Mari, B. & Campillo-Fernandez, A. J. 2019. Morphology, Crystallinity, and Molecular Weight of Poly(epsilon-caprolactone)/Graphene Oxide Hybrids. *Polymers,* 11.

Chen, W., Xie, W., Zhao, G. & Shuai, Q. 2023. Efficient pH-Responsive Nano-Drug Delivery System Based on Dynamic Boronic Acid/Ester Transformation. *Molecules,* 28**,** 4461.

Chen, X., Yang, W., Zhang, J., Zhang, L., Shen, H. & Shi, D. 2020. Alkalinity triggered the degradation of polydopamine nanoparticles. *Polymer Bulletin,* 78**,** 4439-4452.

Chithrani, B. D. & Chan, W. C. 2007. Elucidating the mechanism of cellular uptake and removal of protein-coated gold nanoparticles of different sizes and shapes. *Nano letters,* 7**,** 1542-50.

Chithrani, B. D., Ghazani, A. A. & Chan, W. C. 2006. Determining the size and shape dependence of gold nanoparticle uptake into mammalian cells. *Nano letters,* 6**,** 662-8.

Chu, S., Shi, X., Tian, Y. & Gao, F. 2022. pH-Responsive Polymer Nanomaterials for Tumor Therapy. *Front Oncol,* 12**,** 855019.

Chun, R. F., Adams, J. S. & Hewison, M. 2011. Immunomodulation by vitamin D: implications for TB. *Expert Rev Clin Pharmacol,* 4**,** 583-91.

Cognigni, V., Ranallo, N., Tronconi, F., Morgese, F. & Berardi, R. 2021. Potential benefit of beta-glucans as adjuvant therapy in immuno-oncology: a review. *Exploration of targeted anti-tumor therapy,* 2**,** 122-138.

Dausend, J., Musyanovych, A., Dass, M., Walther, P., Schrezenmeier, H., Landfester, K. & Mailander, V. 2008. Uptake mechanism of oppositely charged fluorescent nanoparticles in HeLa cells. *Macromol Biosci,* 8**,** 1135-43.

Dube, A., Reynolds, J. L., Law, W. C., Maponga, C. C., Prasad, P. N. & Morse, G. D. 2014. Multimodal nanoparticles that provide immunomodulation and intracellular drug delivery for infectious diseases. *Nanomedicine : nanotechnology, biology, and medicine,* 10**,** 831-8.

El Yousfi, R., Brahmi, M., Dalli, M., Achalhi, N., Azougagh, O., Tahani, A., et al. El Idrissi, A. 2023. Recent Advances in Nanoparticle Development for Drug Delivery: A Comprehensive Review of Polycaprolactone-Based Multi-Arm Architectures. *Polymers,* 15**,** 1835.

Fernandes Queiroz, M., Melo, K. R. T., Sabry, D. A., Sassaki, G. L. & Rocha, H. a. O. 2015. Does the Use of Chitosan Contribute to Oxalate Kidney Stone Formation? *Marine Drugs,* 13**,** 141-158.

Fernández-Tena, A., Pérez-Camargo, R. A., Coulembier, O., Sangroniz, L., Aranburu, N., Guerrica-Echevarria, G., et al. Müller, A. J. 2023. Effect of Molecular Weight on the Crystallization and Melt Memory of Poly(ε-caprolactone) (PCL). *Macromolecules,* 56**,** 4602-4620.

Foroozandeh, P. & Aziz, A. A. 2018. Insight into Cellular Uptake and Intracellular Trafficking of Nanoparticles. *Nanoscale research letters,* 13**,** 339.

Goletti, D., Petruccioli, E., Romagnoli, A., Piacentini, M. & Fimia, G. M. 2013. Autophagy in Mycobacterium tuberculosis infection: a passepartout to flush the intruder out? *Cytokine Growth Factor Rev,* 24**,** 335-43.

Gorodzha, S., Surmeneva, M. & Surmenev, R. Fabrication and characterization of polycaprolactone cross-linked and highly-aligned 3-D artificial scaffolds for bone tissue regeneration via electrospinning technology. IOP Conference Series: Materials Science and Engineering, 2015. IOP Publishing, 012024.

Granum, E. & Myklestad, S. M. 2002. A simple combined method for determination of β-1,3-glucan and cell wall polysaccharides in diatoms. *Hydrobiologia,* 477**,** 155-161.

Heredia, N. S., Vizuete, K., Flores-Calero, M., Pazmino, V. K., Pilaquinga, F., Kumar, B. & Debut, A. 2022. Comparative statistical analysis of the release kinetics models for nanoprecipitated drug delivery systems based on poly(lactic-co-glycolic acid). *PLoS One,* 17**,** e0264825.

Hernandez-Giottonini, K. Y., Rodriguez-Cordova, R. J., Gutierrez-Valenzuela, C. A., Penunuri-Miranda, O., Zavala-Rivera, P., Guerrero-German, P. & Lucero-Acuna, A. 2020. PLGA nanoparticle preparations by emulsification and nanoprecipitation techniques: effects of formulation parameters. *RSC advances,* 10**,** 4218-4231.

Hori, Y., Enomoto, Y., Kimura, S. & Iwata, T. 2020. Synthesis of α-1,3- and β-1,3-glucan esters with carbon–carbon double bonds and their surface modification. *Polymer International,* 70**,** 573-581.

Hu, C. M., Zhang, L., Aryal, S., Cheung, C., Fang, R. H. & Zhang, L. 2011. Erythrocyte membrane-camouflaged polymeric nanoparticles as a biomimetic delivery platform. *Proceedings of the National Academy of Sciences of the United States of America,* 108**,** 10980-5.

Huang, J., Buratto, D. & Zhou, R. 2023. Probing the electrostatic aggregation of nanoparticles with oppositely charged molecular ions. *Aggregate,* 4.

Ignjatovic, N. L., Sakac, M., Kuzminac, I., Kojic, V., Markovic, S., Vasiljevic-Radovic, D., et al. Uskokovic, D. P. 2018. Chitosan Oligosaccharide Lactate Coated Hydroxyapatite Nanoparticles as a Vehicle for the Delivery of Steroid Drugs and the Targeting of Breast Cancer Cells. *Journal of materials chemistry. B,* 6**,** 6957-6968.

Iso, I. 2009. 10993–5: 2009 Biological evaluation of medical devices—part 5: tests for in vitro cytotoxicity. *International Organization for Standardization, Geneva*.

Jain, S., Reddy, C. S. K., Swami, R. & Kushwah, V. 2018. Amphotericin B Loaded Chitosan Nanoparticles: Implication of Bile Salt Stabilization on Gastrointestinal Stability, Permeability and Oral Bioavailability. *AAPS PharmSciTech,* 19**,** 3152-3164.

Jana, S., Leung, M., Chang, J. & Zhang, M. 2014. Effect of nano- and micro-scale topological features on alignment of muscle cells and commitment of myogenic differentiation. *Biofabrication,* 6**,** 035012.

Jannasari, N., Fathi, M., Moshtaghian, S. J. & Abbaspourrad, A. 2019. Microencapsulation of vitamin D using gelatin and cress seed mucilage: Production, characterization and in vivo study. *Int J Biol Macromol,* 129**,** 972-979.

Jeon, S., Clavadetscher, J., Lee, D. K., Chankeshwara, S. V., Bradley, M. & Cho, W. S. 2018. Surface Charge-Dependent Cellular Uptake of Polystyrene Nanoparticles. *Nanomaterials (Basel),* 8**,** 1028.

Jeong, J. C., Lee, J. & Cho, K. 2003. Effects of crystalline microstructure on drug release behavior of poly(epsilon-caprolactone) microspheres. *J Control Release,* 92**,** 249-58.

Jia, L., Wang, R. & Fan, Y. 2020. Encapsulation and release of drug nanoparticles in functional polymeric vesicles. *Soft Matter,* 16**,** 3088-3095.

Kamaly, N., Yameen, B., Wu, J. & Farokhzad, O. C. 2016. Degradable Controlled-Release Polymers and Polymeric Nanoparticles: Mechanisms of Controlling Drug Release. *Chem Rev,* 116**,** 2602-63.

Karavelidis, V., Karavas, E., Giliopoulos, D., Papadimitriou, S. & Bikiaris, D. 2011. Evaluating the effects of crystallinity in new biocompatible polyester nanocarriers on drug release behavior. *International journal of nanomedicine,* 6**,** 3021-32.

Kaur, R., Sharma, M., Ji, D., Xu, M. & Agyei, D. 2020. Structural Features, Modification, and Functionalities of Beta-Glucan. *Fibers,* 8**,** 1.

Kerman, I., Toppare, L., Yilmaz, F. & Yagci, Y. 2005. Thiophene Endedϵ-Caprolactone Conducting Copolymers and their Electrochromic Properties. *Journal of Macromolecular Science, Part A,* 42**,** 509-520.

Khoza, L. J., Kumar, P., Dube, A., Demana, P. H. & Choonara, Y. E. 2022. Insights into innovative therapeutics for drug-resistant tuberculosis: Host-directed therapy and autophagy inducing modified nanoparticles. *International journal of pharmaceutics,* 622**,** 121893.

Kiio, T. M. & Park, S. 2020. Physical properties of nanoparticles do matter. *Journal of Pharmaceutical Investigation,* 51**,** 35-51.

Kilinc, G., Saris, A., Ottenhoff, T. H. M. & Haks, M. C. 2021. Host-directed therapy to combat mycobacterial infections. *Immunol Rev,* 301**,** 62-83.

Kolloli, A. & Subbian, S. 2017. Host-Directed Therapeutic Strategies for Tuberculosis. *Front Med (Lausanne),* 4**,** 171.

Lazzari, S., Moscatelli, D., Codari, F., Salmona, M., Morbidelli, M. & Diomede, L. 2012. Colloidal stability of polymeric nanoparticles in biological fluids. *J Nanopart Res,* 14**,** 920.

Lee, C. & Bhakta, S. 2021. The Prospect of Repurposing Immunomodulatory Drugs for Adjunctive Chemotherapy against Tuberculosis: A Critical Review. *Antibiotics (Basel),* 10**,** 91.

Longo, R., Catauro, M., Sorrentino, A. & Guadagno, L. 2022. Thermal and mechanical characterization of complex electrospun systems based on polycaprolactone and gelatin. *Journal of Thermal Analysis and Calorimetry,* 147**,** 5391-5399.

Lopez-Garcia, J., Lehocky, M., Humpolicek, P. & Saha, P. 2014. HaCaT Keratinocytes Response on Antimicrobial Atelocollagen Substrates: Extent of Cytotoxicity, Cell Viability and Proliferation. *Journal of functional biomaterials,* 5**,** 43-57.

Lu, B., Lv, X. & Le, Y. 2019. Chitosan-Modified PLGA Nanoparticles for Control-Released Drug Delivery. *Polymers,* 11**,** 304.

Makvandi, P., Chen, M., Sartorius, R., Zarrabi, A., Ashrafizadeh, M., Dabbagh Moghaddam, F., et al. Tay, F. R. 2021. Endocytosis of abiotic nanomaterials and nanobiovectors: Inhibition of membrane trafficking. *Nano today,* 40**,** 101279.

Mansfield, E. & Banash, M. 2023. Thermal analysis of nanoparticles: Methods, kinetics, and recent advances. *Modeling, Characterization, and Production of Nanomaterials***,** 535-547.

Mansour, S. A. 2012. Study of thermal stabilization for polystyrene/carbon nanocomposites via TG/DSC techniques. *Journal of Thermal Analysis and Calorimetry,* 112**,** 579-583.

Maphasa, R. E., Meyer, M. & Dube, A. 2020. The Macrophage Response to Mycobacterium tuberculosis and Opportunities for Autophagy Inducing Nanomedicines for Tuberculosis Therapy. *Front Cell Infect Microbiol,* 10**,** 618414.

Marano, F., Hussain, S., Rodrigues-Lima, F., Baeza-Squiban, A. & Boland, S. 2011. Nanoparticles: molecular targets and cell signalling. *Arch Toxicol,* 85**,** 733-41.

Mata-Martinez, P., Bergon-Gutierrez, M. & Del Fresno, C. 2022. Dectin-1 Signaling Update: New Perspectives for Trained Immunity. *Front Immunol,* 13**,** 812148.

Mayer-Barber, K. D., Andrade, B. B., Oland, S. D., Amaral, E. P., Barber, D. L., Gonzales, J., et al. Sher, A. 2014. Host-directed therapy of tuberculosis based on interleukin-1 and type I interferon crosstalk. *Nature,* 511**,** 99-103.

Mazumder, S., Dewangan, A. K. & Pavurala, N. 2017. Enhanced dissolution of poorly soluble antiviral drugs from nanoparticles of cellulose acetate based solid dispersion matrices. *Asian J Pharm Sci,* 12**,** 532-541.

Miyajima, M., Koshika, A., Okada, J. I., Ikeda, M. & Nishimura, K. 1997. Effect of polymer crystallinity on papaverine release from poly (l-lactic acid) matrix. *Journal of Controlled Release,* 49**,** 207-215.

Mphaphuli, M. T., Sithole, M. N., Kumar, P., Kondiah, P. P. D., Mabrouk, M. & Choonara, Y. E. 2023. Multi-purpose prototypes for extrapulmonary Mycobacterium tuberculosis targeting: A regenerative medicine perspective. *Journal of Drug Delivery Science and Technology,* 89**,** 105039.

Mwila, C. & Walker, R. B. 2020. Improved Stability of Rifampicin in the Presence of Gastric-Resistant Isoniazid Microspheres in Acidic Media. *Pharmaceutics,* 12.

Nair, A., Greeny, A., Nandan, A., Sah, R. K., Jose, A., Dyawanapelly, S., et al. Sadanandan, P. 2023. Advanced drug delivery and therapeutic strategies for tuberculosis treatment. *J Nanobiotechnology,* 21**,** 414.

Nair, R. S., Morris, A., Billa, N. & Leong, C. O. 2019. An Evaluation of Curcumin-Encapsulated Chitosan Nanoparticles for Transdermal Delivery. *AAPS PharmSciTech,* 20**,** 69.

Nielsen, S. S. 2010. Phenol-Sulfuric Acid Method for Total Carbohydrates. *In:* NIELSEN, S. S. (ed.) *Food Analysis Laboratory Manual.* Boston, MA: Springer US.

Oak, U. & Khare, T. 2022. Nanoparticle Functionalization: Approaches and Applications. *In:* KUMAR, V., SHRIRAM, V., SHUKLA, R. & GOSAVI, S. (eds.) *Nano-Strategies for Addressing Antimicrobial Resistance.* Cham: Springer International Publishing.

Organization, W. H. 2021. Global tuberculosis report 2021.

Pai, M., Kasaeva, T. & Swaminathan, S. 2022. Covid-19's Devastating Effect on Tuberculosis Care - A Path to Recovery. *N Engl J Med,* 386**,** 1490-1493.

Paik, S., Kim, J. K., Chung, C. & Jo, E. K. 2019. Autophagy: A new strategy for host-directed therapy of tuberculosis. *Virulence,* 10**,** 448-459.

Pandey, P., Patel, J. K. & Kumar, S. 2022. Nanoparticle Properties Affecting the Drug Release, Absorption, and Pharmacokinetics of Nanoparticulate Drug Delivery Systems. *In:*

PATEL, J. K. & PATHAK, Y. V. (eds.) *Pharmacokinetics and Pharmacodynamics of Nanoparticulate Drug Delivery Systems.* Cham: Springer International Publishing.

Phan, H. T. & Haes, A. J. 2019. What Does Nanoparticle Stability Mean? *J Phys Chem C Nanomater Interfaces,* 123**,** 16495-16507.

Puigdellivol, M., Allendorf, D. H. & Brown, G. C. 2020. Sialylation and Galectin-3 in Microglia-Mediated Neuroinflammation and Neurodegeneration. *Front Cell Neurosci,* 14**,** 162.

Queval, C. J., Brosch, R. & Simeone, R. 2017. The Macrophage: A Disputed Fortress in the Battle against Mycobacterium tuberculosis. *Front Microbiol,* 8**,** 2284.

Ramalho, M. J., Coelho, M. a. N. & Pereira, M. C. 2017. Nanoparticles for Delivery of Vitamin D: Challenges and Opportunities. *In:* SIVAKUMAR, G. (ed.) *A Critical Evaluation of Vitamin D - Clinical Overview.* Rijeka: IntechOpen.

Reyna-Urrutia, V. A., Estevez, M., Gonzalez-Gonzalez, A. M. & Rosales-Ibanez, R. 2022. 3D scaffolds of caprolactone/chitosan/polyvinyl alcohol/hydroxyapatite stabilized by physical bonds seeded with swine dental pulp stem cell for bone tissue engineering. *Journal of materials science. Materials in medicine,* 33**,** 81.

Rodriguez, I., Gautam, R. & Tinoco, A. D. 2020. Using X-ray Diffraction Techniques for Biomimetic Drug Development, Formulation, and Polymorphic Characterization. *Biomimetics (Basel, Switzerland),* 6.

Shannahan, J. H., Lai, X., Ke, P. C., Podila, R., Brown, J. M. & Witzmann, F. A. 2013. Silver nanoparticle protein corona composition in cell culture media. *PLoS One,* 8**,** e74001.

Sharma, A., Puri, V., Kumar, P., Singh, I. & Huanbutta, K. 2021. Development and Evaluation of Rifampicin Loaded Alginate-Gelatin Biocomposite Microfibers. *Polymers,* 13.

She, H., Xiao, X. & Liu, R. 2007. Preparation and characterization of polycaprolactone-chitosan composites for tissue engineering applications. *Journal of Materials Science,* 42**,** 8113-8119.

Sia, J. K., Georgieva, M. & Rengarajan, J. 2015. Innate Immune Defenses in Human Tuberculosis: An Overview of the Interactions between Mycobacterium tuberculosis and Innate Immune Cells. *J Immunol Res,* 2015**,** 747543.

Siafaka, P. I., Zisi, A. P., Exindari, M. K., Karantas, I. D. & Bikiaris, D. N. 2016. Porous dressings of modified chitosan with poly(2-hydroxyethyl acrylate) for topical wound delivery of levofloxacin. *Carbohydr Polym,* 143**,** 90-9.

Soto, E. R., O'connell, O., Dikengil, F., Peters, P. J., Clapham, P. R. & Ostroff, G. R. 2016. Targeted Delivery of Glucan Particle Encapsulated Gallium Nanoparticles Inhibits HIV Growth in Human Macrophages. *J Drug Deliv,* 2016**,** 8520629.

Suflet, D. M., Popescu, I., Pelin, I. M., Ichim, D. L., Daraba, O. M., Constantin, M. & Fundueanu, G. 2021. Dual Cross-Linked Chitosan/PVA Hydrogels Containing Silver Nanoparticles with Antimicrobial Properties. *Pharmaceutics,* 13**,** 1461.

Suganthi, S., Vignesh, S., Kalyana Sundar, J. & Raj, V. 2020. Fabrication of PVA polymer films with improved antibacterial activity by fine-tuning via organic acids for food packaging applications. *Applied Water Science,* 10**,** 100.

Sumaila, M., Kumar, P., Ubanako, P., Adeyemi, S. A. & Choonara, Y. E. 2023. Dual Rifampicin and Isoniazid Mannose-Decorated Lipopolysaccharide Nanospheres for Macrophage-Targeted Lung Delivery. *Curr Drug Deliv,* 20**,** 1487-1503.

Sung, J. C., Padilla, D. J., Garcia-Contreras, L., Verberkmoes, J. L., Durbin, D., Peloquin, C. A., et al. Edwards, D. A. 2009. Formulation and pharmacokinetics of self-assembled rifampicin nanoparticle systems for pulmonary delivery. *Pharm Res,* 26**,** 1847-55.

Tae, H., Lee, S. & Ki, C. S. 2019. β-Glucan hybridized poly(ethylene glycol) microgels for macrophage-targeted protein delivery. *Journal of Industrial and Engineering Chemistry,* 75**,** 69-76.

Taylor, K. a. C. C. 1995. A modification of the phenol/sulfuric acid assay for total carbohydrates giving more comparable absorbances. *Applied Biochemistry and Biotechnology,* 53**,** 207-214.

Tipa, C., Cidade, M. T., Vieira, T., Silva, J. C., Soares, P. I. P. & Borges, J. P. 2021. A New Long-Term Composite Drug Delivery System Based on Thermo-Responsive Hydrogel and Nanoclay. *Nanomaterials,* 11**,** 25.

Tripathi, A., Gupta, R. & Saraf, S. 2010. PLGA Nanoparticles of Antitubercular Drug: Drug Loading and Release Studies of a Water-In-Soluble Drug. *Int. J. Pharm. Tech. Res.,* 2.

Trombino, S., Curcio, F., Di Gioia, M. L., Armentano, B., Poerio, T. & Cassano, R. 2022. Multifunctional Membranes Based on beta-Glucans and Chitosan Useful in Wound Treatment. *Membranes (Basel),* 12**,** 121.

Vora, L. K., Vavia, P. R., Larraneta, E., Bell, S. E. J. & Donnelly, R. F. 2018. Novel nanosuspension-based dissolving microneedle arrays for transdermal delivery of a hydrophobic drug. *J Interdiscip Nanomed,* 3**,** 89-101.

Zhao, Y., Wang, Y., Ran, F., Cui, Y., Liu, C., Zhao, Q., et al. Wang, S. 2017. A comparison between sphere and rod nanoparticles regarding their in vivo biological behavior and pharmacokinetics. *Sci Rep,* 7**,** 4131.

Zhao, Z., Ukidve, A., Kim, J. & Mitragotri, S. 2020. Targeting Strategies for Tissue-Specific Drug Delivery. *Cell,* 181**,** 151-167.

Zhu, M., Nie, G., Meng, H., Xia, T., Nel, A. & Zhao, Y. 2013. Physicochemical properties determine nanomaterial cellular uptake, transport, and fate. *Accounts of chemical research,* 46**,** 622-31.

CHAPTER 4

PRO-INFLAMMATORY VS. ANTI-INFLAMMATORY RAW 264.7 MACROPHAGE CELLS RESPONSES: INSIGHTS FROM INTRACELLULAR ROS AND CYTOKINE QUANTIFICATION POST-NANOPARTICLE TREATMENT

4.1. Introduction

In the previous chapter, 1,3-beta glucan functionalised nanoparticles were synthesised and characterised. These nanoparticles demonstrated excellent stability and facilitated the site-specific release of active drugs in environments with pH conditions associated with Mycobacterium tuberculosis (Mtb). Additionally, cytotoxicity tests on healthy RAW 267.4 cells revealed no or minimal toxic effects from these nanoparticles. Therefore, this chapter further explores the impact of polarising macrophages towards either pro-inflammatory or anti-inflammatory phenotypes upon treatment with the nanoparticles and how this polarisation could enhance the immune response against tuberculosis, as determined by the predominant macrophage phenotype induced.

The intricate interplay between Reactive Oxygen Species (ROS) and macrophage polarisation has garnered significant attention in the field of immunology, particularly regarding their roles in Mtb survival within macrophages (Khoza et al., 2022, Maphasa et al., 2020). Upon encountering Mtb, macrophages undergo a process known as phagocytosis, during which they engulf and attempt to neutralise the invading bacteria; this process triggers an oxidative burst, producing ROS, which is crucial for the bactericidal activity of macrophages; consequently, this inhibits the growth and survival of Mtb (Pellegrino et al., 2023, Cavinato et al., 2020).

Furthermore, macrophages exhibit remarkable plasticity as a protective measure, allowing them to adapt to various microenvironmental signals and adopt distinct functional phenotypes during different stages of Mtb infection (Khoza et al., 2022). This process, known as macrophage polarisation, typically results in two main phenotypes: classically activated (M1) macrophages and alternatively activated (M2) macrophages (Bo et al., 2023). M1 macrophages are pro-inflammatory and microbicidal, producing high levels of ROS, nitric oxide (NO) and pro-inflammatory cytokines such as tumour necrosis factor-alpha (TNF-α) to combat pathogens (Lendeckel et al., 2022). Furthermore, M1 show high antigen presentation

activity and downregulation of anti-inflammatory cytokines such as IL-10 (Gordon and Martinez, 2010). In contrast, M2 macrophages are associated with anti-inflammatory responses, tissue repair, and immunoregulation, often producing lower levels of ROS (Bo et al., 2023, Khoza et al., 2022). This phenotypic determination can be further validated through microscopic visualisation, where specific morphological features of the cells can be observed. M0 macrophages typically exhibit a small, round shape with a uniform appearance, M1 macrophages are larger with an elongated and irregular shape, and M2 macrophages often display a more oval morphology (Italiani and Boraschi, 2014).

Therefore, the dynamic relationship between ROS, macrophage polarisation, and Mtb survival has significant therapeutic implications. Enhancing the ROS production and M1 polarisation of macrophages could potentiate the antimicrobial response, leading to more effective clearance of Mtb (Covarrubias et al., 2013, Li et al., 2024). Conversely, controlling excessive ROS production and preventing the harmful effects of chronic inflammation could minimise tissue damage and improve patient outcomes (Amaral et al., 2021, Leavy, 2014, Li et al., 2024). This balance underscores the need for targeted therapies to modulate macrophage responses, aiming to maximise pathogen clearance while minimising host damage. Hence, in this chapter, RAW 264.7 cells were treated with formulated nanoparticles to quantify the levels of ROS and pro-inflammatory cytokines (TNF-α, IFN-γ) and anti-inflammatory cytokines (IL-4, IL-10). Additionally, the morphological changes in the macrophages upon treatment were analysed to elucidate further the nanoparticles' impact on the cells' phenotypic expression. The results are presented in **Figure 4.1-4.7**.

4.2. Materials and Methods

4.2.1. Materials

The RAW 264.7 cell line was procured from Separation Scientific Pty Ltd. (Johannesburg, SA). The Invitrogen Mouse TNF-α High Sensitivity ELISA Kit, Instant IL-4 ELISA Kit, and Mouse IL-10 Instant ELISA Kit were all purchased from Thermo Fisher Scientific (Waltham, MA, USA). The Fluorometric Intracellular ROS Assay Kit, IFN-gamma ELISA Kit and phosphate-buffered saline (PBS) were purchased from Sigma-Aldrich (St. Louis, MO, USA). All chemicals were of analytical reagent grade and used without prior modification. Double deionised water (DDW) was used for all the preparations.

4.2.2. Quantification of ROS and Pro-inflammatory Cytokines in RAW 264.7 Cells

4.2.2.1. Intracellular ROS (Superoxide and Hydroxy radicals) Quantification

A fluorometric Intracellular ROS Assay Kit (Sigma-Aldrich, St. Louis, MO, USA) was used to quantify the ROS levels secreted by RAW 264.7 cells post-treatment with formulated nanoparticles in a one-step fluorometric assay. RAW 264.7 cells were cultured in DMEM supplemented with 1% penicillin-streptomycin and 10% fetal bovine serum in a T-25 flask at 37°C and 5% CO_2 until confluency. Cells were then plated in a 96-well plate at a density of 40,000 cells per well in 90 µL of growth medium and allowed to adhere overnight. Intracellular ROS quantification followed the manufacturer's protocol, where 100 µL of master reaction mix was added to each well of the cultured plate and incubated at 37°C and 5% CO_2 for 1 hour. Subsequently, the cells were treated with 20 µL of various formulations: 145 µg/mL of CS-PCL, CS-PCL-RIF/VITD3, Glu-CS-PCL-RIF/VITD3, and 36 µg/mL of pristine RIF and VITD3. The plate was then incubated for 24 hours at 37°C and 5% CO_2 to induce ROS, after which fluorescence intensity was measured (λ_{ex} = 490/λ_{em} = 525 nm) using a GloMax Explorer multimode plate reader (version 4.92.0; Promega Corporation, Madison, USA).

4.2.2.2. TNF-α Quantification using ELISA Kit

TNF-α levels in RAW 264.7 cells were measured using the Mouse TNF-α High Sensitivity ELISA Kit (Invitrogen, Thermo Fisher Scientific Corporation, Waltham, MA, USA). RAW 264.7 cells were cultured in DMEM supplemented with 1% penicillin-streptomycin and 10% fetal bovine serum at 37°C with 5% CO_2 until they reached confluency. The cells were then plated in a 96-well plate at a density of 50,000 cells per well in 90 µL of growth medium and allowed to attach overnight. Subsequently, 10 µL of formulated nanoparticle formulations at 145 µg/mL and 36 µg/mL pristine VITD3 and RIF solutions were added to the wells, and the plate was incubated for 24 hours at 37°C and 5% CO_2. Following incubation, the supernatant was collected and analysed according to the manufacturer's protocol.

For the assay, 50 µL of samples' supernatant and control were added to the pre-coated 96-well plate in duplicate and incubated for 2 hours at room temperature with gentle shaking on a microplate shaker followed by washing six times with 1X Wash Buffer. Then, 100 µL of Streptavidin-HRP solution was added to each well and incubated for 1 hour on a microplate shaker. After additional washes, 100 µL of Amplification Solution 1 was added and incubated for 15 minutes, followed by another wash and the addition of 100 µL of Amplification Solution 2, which was incubated for 30 minutes at room temperature on a microplate shaker.

Subsequently, 100 µL of TMB substrate solution was added and incubated in the dark for 10-20 minutes. The reaction was stopped with 50 µL of Stop Solution, and absorbance was measured at 450 nm using a Victor X3 multimodal microplate reader (PerkinElmer, Waltham, MA, USA). The TNF-α concentration in the samples was determined by comparing their absorbance values to a standard curve.

4.2.2.3. IFN-γ Quantification using ELISA Kit

The IFN-γ levels in RAW 264.7 cells were quantified using the Mouse IFN-gamma ELISA Kit (RAB0224, Sigma-Aldrich, St. Louis, MO, USA). Cell culturing, plating, and treatment were conducted according to the protocol in ***section 4.2.2.2***. According to the manufacturer's protocol, 50 µL of samples and 100 µL of standards were prepared and added to the pre-coated wells. After a 2.5-hour incubation at room temperature on a microplate shaker, wells were washed four times with 300 µL of wash buffer, and 100 µL of biotin-conjugated anti-mouse IFN-γ detection antibody was added. Following a 1-hour incubation at room temperature on a microplate shaker, wells were washed again, and 100 µL of TMB substrate solution was added to each well. The reaction was allowed to proceed for 30 minutes before adding 100 µL of stop solution. Absorbance was measured at 450 nm using a multimodal microplate reader (Victor X3, PerkinElmer, Waltham, MA, USA). The concentrations of IFN-γ in the samples were determined by comparison to the standard curve generated from the known concentrations of IFN-γ standards.

4.2.3. Quantification of Anti-inflammatory Cytokines in RAW 264.7 Cells

4.2.3.1. IL-4 Quantification using ELISA Kit

IL-4 levels in RAW 264.7 macrophage cells were quantified using an Invitrogen Instant IL-4 ELISA kit (Thermo Fisher Scientific, Waltham, MA, USA). Cells were cultured, plated and treated following established protocols outlined in ***section 4.2.2.2***. For IL-4 quantification, samples and standards were prepared, added to the pre-coated wells according to the manufacturer's instructions, and incubated at room temperature on a microplate shaker. After incubation, wells were washed thrice with 400 µL wash buffer, and substrate solution was added to each well. The reaction was allowed to proceed for the recommended time before adding a stop solution. Absorbance was measured at 450 nm using a multi-modal microplate reader (Victor X3, PerkinElmer, Waltham, MA, USA). The concentrations of IL-4 in the samples were determined by comparison to the standard curve generated from the known concentrations of IL-4 standards.

4.2.3.2. IL-10 Quantification using ELISA Kit

The Mouse IL-10 Instant ELISA Kit (Invitrogen, Thermo Fisher Scientific, Waltham, MA, USA) was used to measure IL-10 levels in the RAW 264.7 macrophage cells. Cell culturing, plating and treatment were performed following a similar protocol outlined in ***section 4.2.2.2***. Per the manufacturer's protocol, 50 µL of samples were added to the pre-coated wells. After a 3-hour incubation at room temperature on a microplate shaker, wells were washed four times with 400 µL of wash buffer. 100 µL of TMB substrate solution was added to each well. The reaction was allowed to proceed for 10 minutes before adding 100 µL of stop solution. The absorbance was measured at 450 nm using a multimodal microplate reader (Victor X3, PerkinElmer, Waltham, MA, USA), and IL-10 concentrations were determined by comparing the absorbance values to a standard curve generated from the provided standards.

4.2.4. Morphological Analysis of RAW 264.7 Macrophages: Untreated vs. Treated Groups

Cells were cultured and treated for morphological analysis with the same concentration and conditions outlined in **Section *4.2.2.2*** and visualised under an inverted compound light microscope (Olympus CKX53, Olympus Corporation, Tokyo, Japan) at different magnifications.

4.2.5. Statistical analysis

Statistical analysis was conducted using GraphPad Prism 10 (GraphPad Software Inc., San Diego, CA, USA). Statistical significance (p) was determined using unpaired multiple t-tests with the Holm-Sidak correction method, considering $p < 0.05$ statistically significant. Each row was analysed individually without assuming a consistent standard deviation. Data is presented as mean values of biological samples ± SD.

4.3. Results

4.3.1. Intracellular ROS Quantification

No significant changes were observed in ROS generation (superoxide and hydroxyl radicals) between the free RIF solution (71.01 ± 2.66 RFU) and the CS-PCL (73.88 ± 1.95 RFU) or CS-

PCL-RIF (85.51 ± 9.06 RFU) nanoparticles. However, a very significant increase ($p < 0.001$) in ROS generation was observed when cells were treated with Glu-CS-PCL-RIF (131.74 ± 9.06 RFU), compared to both the CS-PCL-RIF and free RIF solution, as shown in **Figure 4.1**. The Glu-CS-PCL-RIF treatment stimulated a 1.5- and 1.8-fold enhancement in ROS levels compared to the CS-PCL-RIF and free RIF solutions.

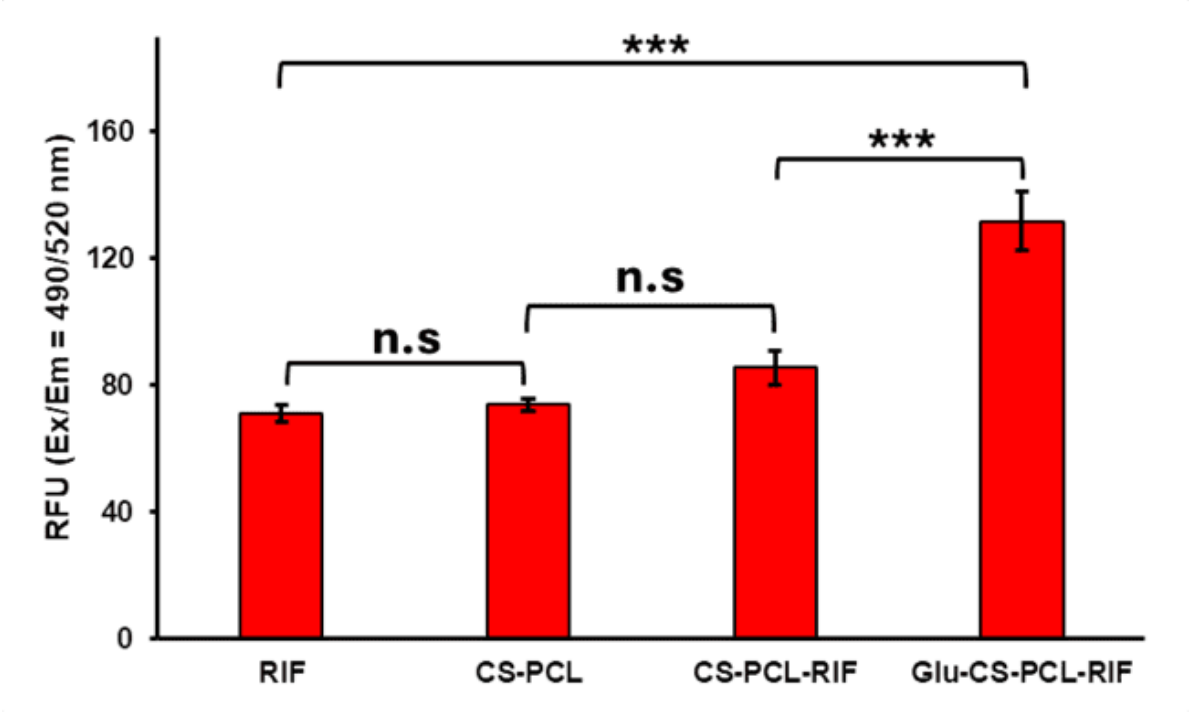

Figure 4.1: Relative Fluorescence Units (RFU) of Reactive Oxygen Species (ROS) generation in RAW 264.7 macrophage cells after 24-hour treatment with 36 µg/mL of RIF pristine drug solution and 145 µg/mL of different RIF nanoparticle solutions. Data is presented as mean ± SD. Statistical significance between groups is indicated as follows: n.s. (not significant, $p > 0.05$); and *** (very significant, $p < 0.001$).

Cells treated with VITD3 (168.57 ± 2.66 RFU) showed a very significant increase ($p < 0.001$) in ROS generation that was 2.3- and 2.0-fold higher compared to CS-PCL (72.88 ± 1.32 RFU) and CS-PCL-VITD3 (82.71 ± 6.25 RFU), respectively, as shown in **Figure 4.2**. When cells were treated with CS-PCL-VITD3, there was a non-significant increase of about 10 RFU in ROS generation compared to CS-PCL alone. Glu-CS-PCL-VITD3 (138.47 ± 5.91 RFU) showed about 1.7-fold higher ROS levels, which was significantly higher ($p < 0.001$) compared to CS-PCL-VITD3 (**Figure 4.2**).

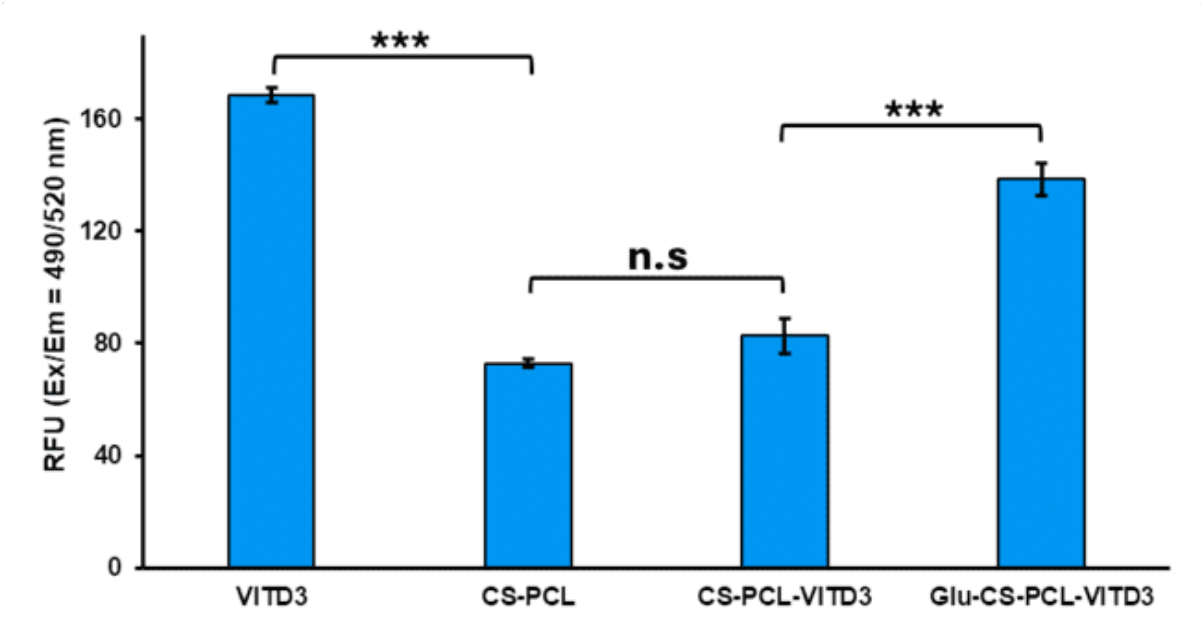

Figure 4.2: Relative Fluorescence Units (RFU) of Reactive Oxygen Species (ROS) generation in RAW 264.7 cells after 24-hour treatment with 36 µg/mL of VITD3 pristine drug solution and 145 µg/mL of different VITD3 nanoparticle solutions, respectively. Data is presented as mean ± SD. Statistical significance between groups is indicated as follows: n.s. (not significant, $p > 0.05$); and *** (very significant, $p < 0.001$).

4.3.2. Quantification of TNF-α secretion

RAW 264.7 cells were treated with free RIF, VITD3, and different nanoparticle solutions before quantifying TNF-α. The results are presented in **Figure 4.3**. The data showed a similar trend between RIF and VITD3 nanoparticles (**Figure 4.3a and Figure 4.3b**). Glu-CS-PCL-VITD3 (1377.88 ± 32.70 pg/mL) significantly ($p < 0.01$) stimulated an enhanced TNF-α secretion, showing a 1.8-fold increase compared to the control (802.25 ± 12.37 pg/mL) and a 1.7-fold increase compared to free VITD3 solution (798.50 ± 19.44 pg/mL), as observed in **Figure 4.3a**.

Additionally, Glu-CS-PCL-VITD3 (1377.88 ± 32.70 pg/mL) demonstrated a significant increase ($p < 0.01$) in TNF-α levels compared to CS-PCL-VITD3 (1102.25 ± 58.33 pg/mL), with a 1.2-fold increase (**Figure 4.3a**). CS-PCL nanoparticles (1049.75 ± 15.91 pg/mL) also significantly enhanced TNF-α production relative to the control and VITD3 alone ($p < 0.01$). In **Figure 4.3b**, RIF nanoparticles depicted a similar trend to the VITD3 nanoparticles in **Figure 4.3a**, with highly significant changes denoted in the Figure with ** ($p < 0.001$).

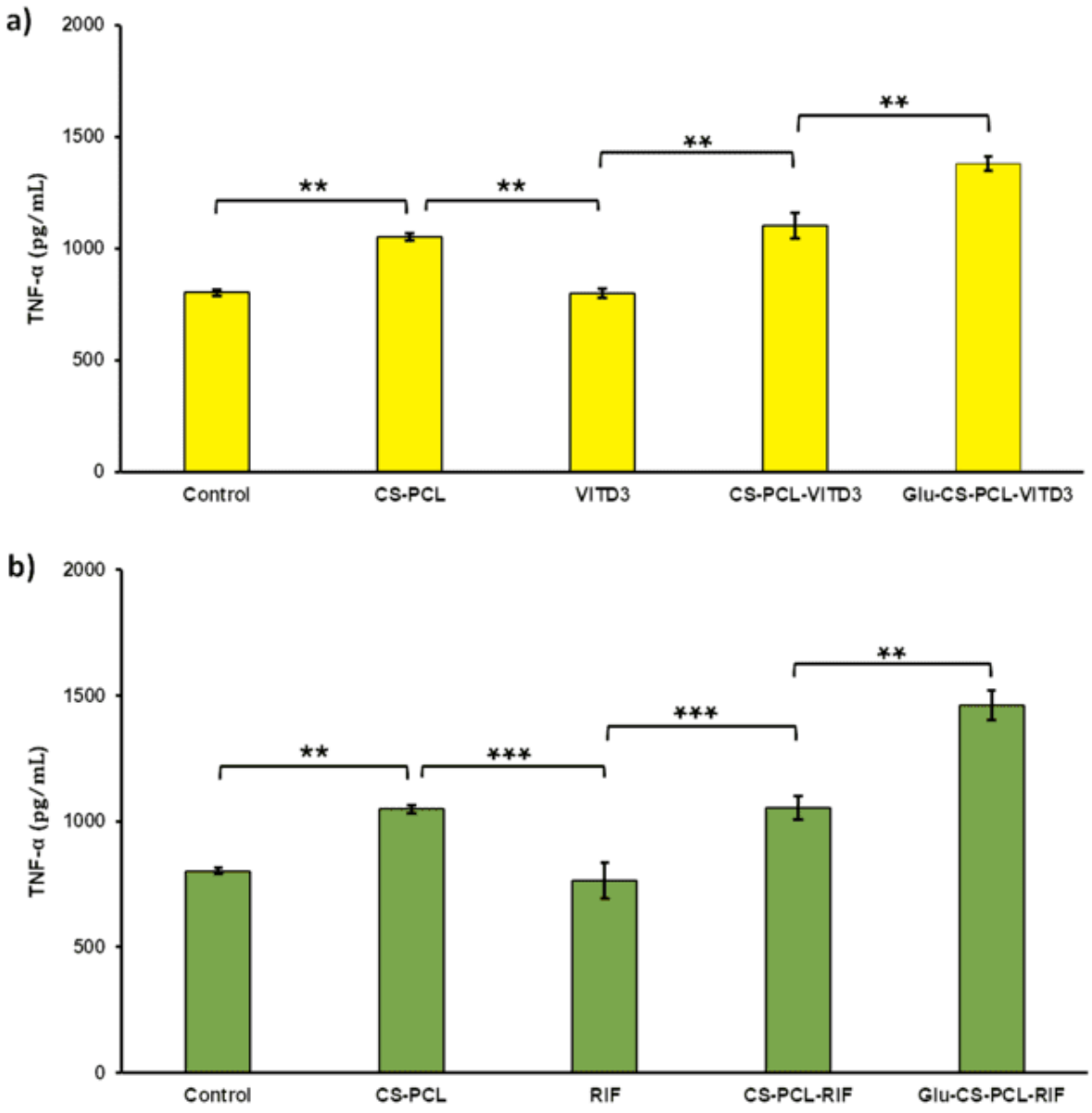

Figure 4.3: Concentration of TNF-α in RAW 264.7 macrophage cells following 24-hour treatment with 145 µg/mL and 36 µg/mL of **(a)** VITD3 nanoparticles and VITD3 pristine drug solution, and **(b)** RIF nanoparticles and RIF pristine drug solution, respectively. Data is presented as mean (n = 2) ± SD. Statistical significance compared between groups is indicated as follows: ****** (highly significant, *p < 0.01) and* *** *(*very significant, *p < 0.001).*

4.3.3. Quantification of IFN-γ secretion

Following the treatment of RAW 264.7 cells with formulated nanoparticles, the levels of IFN-gamma were quantified, and the results are shown in **Figure 4.4**. The quantification of IFN-gamma gave negative responses across all treatment groups, with values ranging between -

107.25 ± 0.044 pg/mL and -114.75 ± 0.042 pg/mL, suggesting the absence or very low non-quantifiable levels of IFN-gamma. The differences between the treatment groups and the control, as well as between each other, were deemed insignificant ($p > 0.05$).

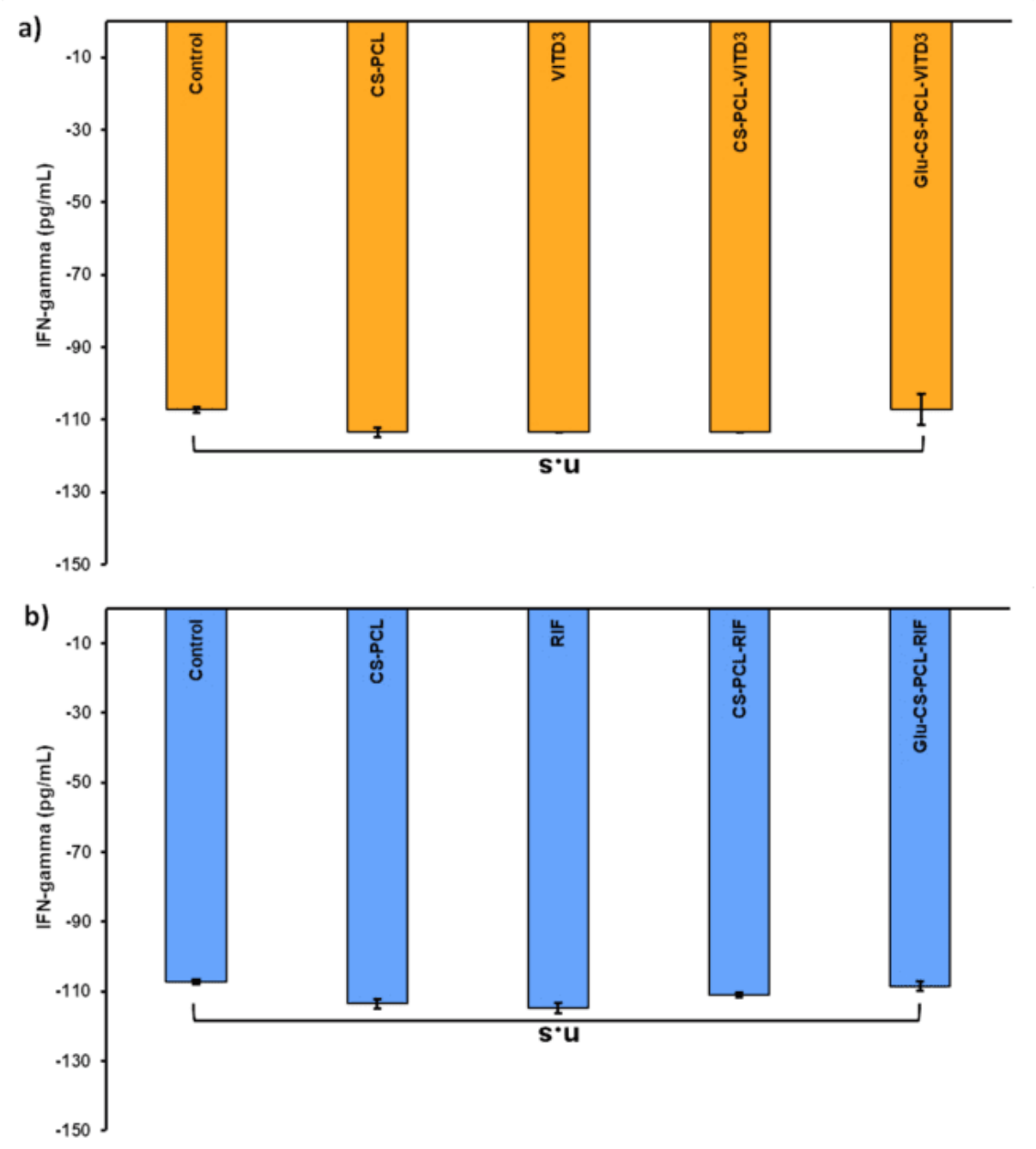

Figure 4.4: Concentration of IFN-gamma in RAW 264.7 cells following 24-hour treatment with 145 µg/mL and 36 µg/mL of **(a)** VITD3 nanoparticles and VITD3 pristine drug solution, and **(b)** RIF nanoparticles and RIF pristine drug solution, respectively. Data is presented as mean (n = 2) ± SD. Statistical significance between groups is indicated as n.s (non-significant, $p > 0.05$).

4.3.4. IL-4 Quantification in RAW 264.7 Cells

Following the treatment of RAW 264.7 cells with formulated nanoparticles, the levels of IL-4 were quantified, and the results are shown in **Figure 4.5**. The control group exhibited no or non-quantifiable levels of IL-4, as demonstrated by a negative reading in **Figure 4.5** (-12.33 ± 0.101 pg/mL). The CS-PCL nanoparticles showed a significant increase in IL-4 levels compared to the control group from non-quantifiable levels to 48,58 ± 10.16 pg/mL. Treatment with RIF (168.82 ± 18.11 pg/mL), CS-PCL-RIF (162.01 ± 6.93 pg/mL), and Glu-CS-PCL-RIF (166.76 ± 4.10 pg/mL) resulted in a significant increase in IL-4 levels compared to the control group (###, $p < 0.001$), as shown in **Figure 4.5a**. Additionally, there was a significant difference of 3.5-fold in IL-4 levels between the CS-PCL and RIF treatments ($p < 0.05$), as seen in **Figure 4.5a**.

Figure 4.5b shows the increase in IL-4 levels from non-quantifiable (control) to 58.25 ± 7.50 pg/mL when cells were treated with VITD3. There were slight, non-significant changes in IL-4 levels between VITD3 (58.25 ± 7.50 pg/mL) and CS-PCL-VITD3 (64.71 ± 4.50 pg/mL) compared to nanoparticles alone, CS-PCL (48.58 ± 10.16 pg/mL). However, CS-PCL-VITD3 showed significant changes from non-quantifiable to 64.71 ± 4.50 pg/mL compared to the control ($p < 0.05$). Treatment with Glu-CS-PCL-VITD3 resulted in a significant decrease in IL-4 levels compared to CS-PCL-VITD3, from 64.71 ± 4.50 to 34.25 ± 0.47 pg/mL, as depicted in **Figure 4.5b**

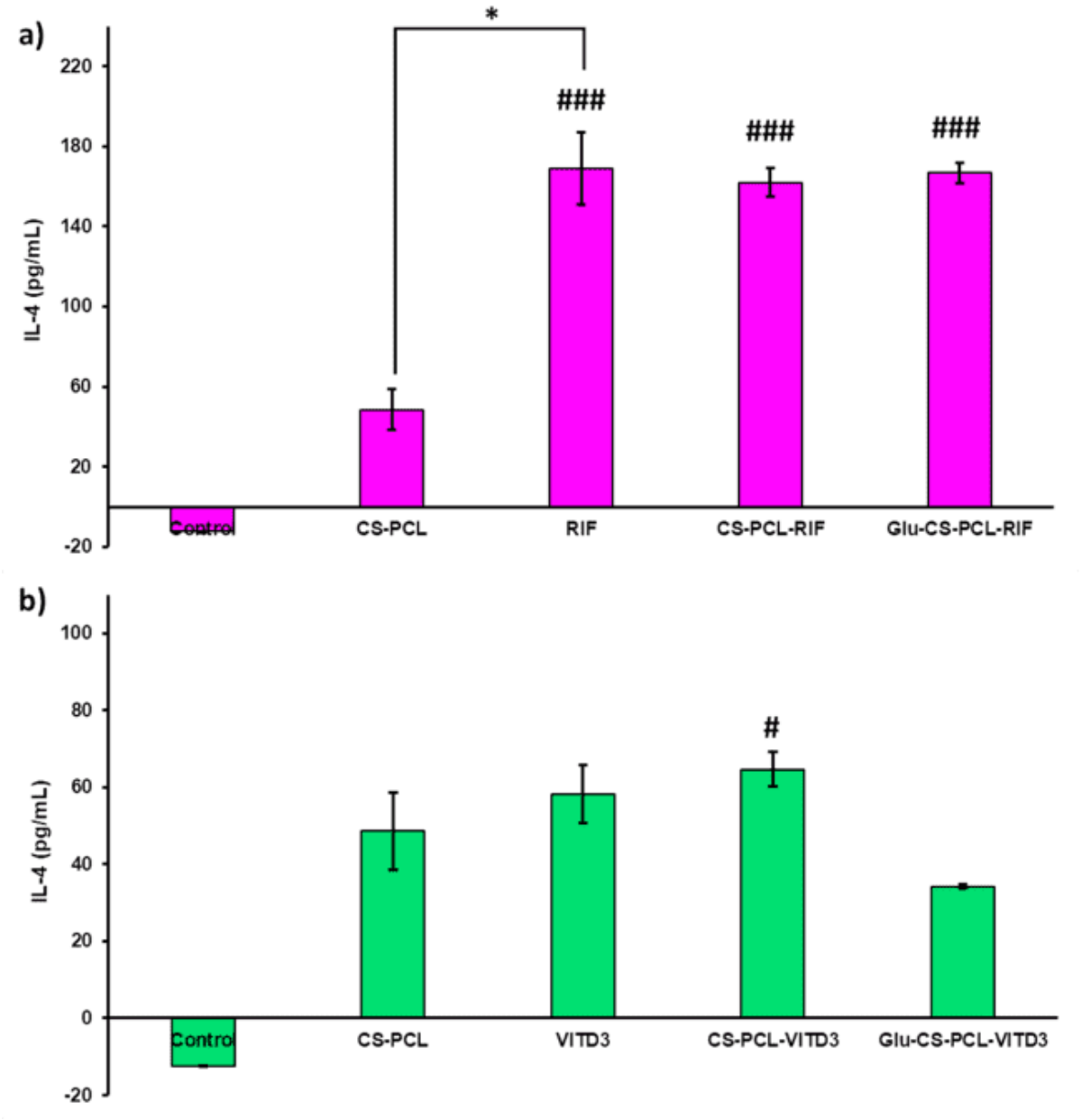

Figure 4.5: Concentration of IL-4 in RAW 264.7 cells following 24-hour treatment with 145 µg/mL and 36 µg/mL of **(a)** RIF nanoparticles and RIF pristine drug solution, and **(b)** VITD3 nanoparticles and VITD3 pristine drug solution, respectively. Data is presented as mean (n = 2) ± SD. Statistical significance compared to the control is indicated as ### (very significant, $p < 0.001$), # (significant, $p > 0.05$) and statistical significance between groups is shown as * (significant, $p < 0.05$).

4.3.5. Quantification of IL-10 secretion

Following the treatment of RAW 264.7 cells with formulated nanoparticles, the levels of IL-10 were quantified, and the results are shown in **Figure 4.6**. No significant changes were observed between the control and all other treatment groups or nanoparticle formulations. Specifically, all groups or treatments exhibited IL-10 levels below or equal to those observed in the control group, with IL-10 levels measured at 21 pg/mL for the control.

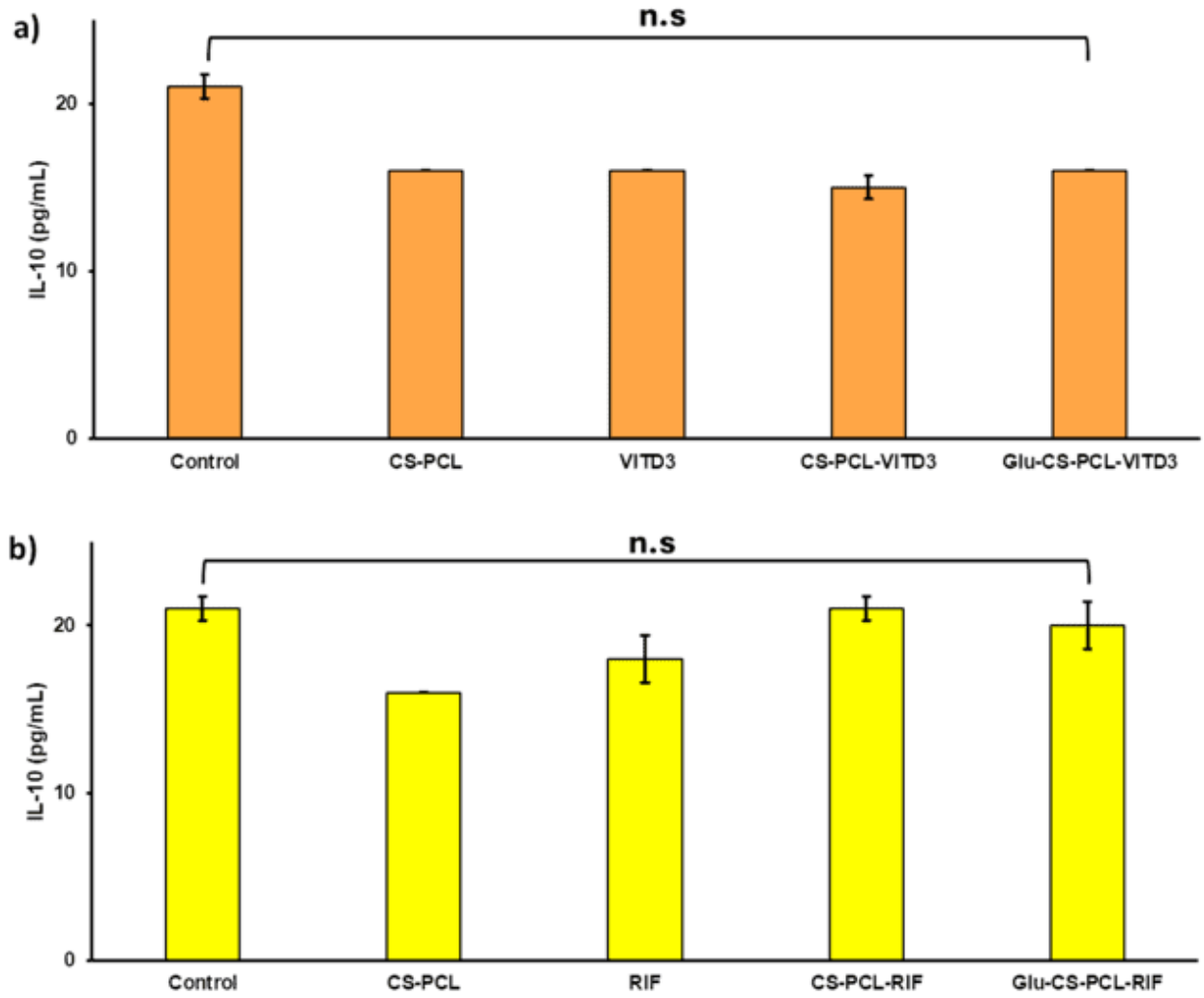

Figure 4.6: Concentration of IL-10 in RAW 264.7 cells following 24-hour treatment with 145 µg/mL and 36 µg/mL of **(a)** VITD3 nanoparticles and VITD3 pristine drug solution, and **(b)** RIF nanoparticles and RIF pristine drug solution, respectively. Data is presented as mean (n = 2) ± SD. Statistical significance between groups is indicated as n.s (non-significant, $p > 0.05$).

4.3.6. Morphological Analysis of RAW 264.7 Macrophages: Untreated vs Treated Groups

Upon morphological analysis, as shown in **Figure 4.7**, the following observations were made: The untreated group displayed small, round cells with a smooth surface and uniform appearance. The treated group exhibited larger cells with an irregular shape, elongated or spread-out morphology, and more cytoplasmic extensions with a granular look, along with some cells displaying an oval shape.

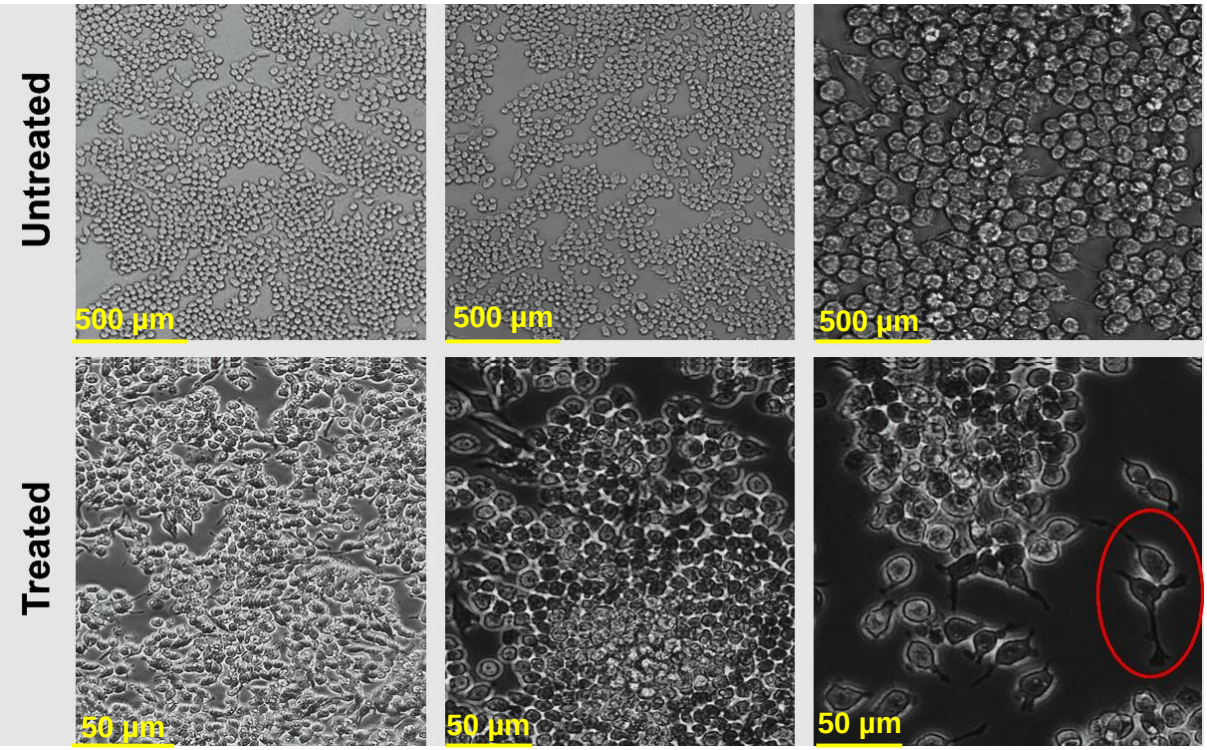

Figure 4.7: Morphological Comparison of RAW 264.7 Macrophage Cell Line in Untreated and Treated Conditions. The untreated group displays a typical round, smooth, small morphology with a uniform appearance (characteristic of the M0 phenotype). The treated group exhibits an enlarged, elongated, irregular shape with pronounced cytoplasmic extensions, typical of the M1 phenotype. Some cells in the treated group are oval-shaped, indicating partial differentiation towards the M2 phenotype at different magnifications.

4.4. Discussion

RIF, a well-known antibiotic, primarily exerts its antibacterial effects by inhibiting bacterial RNA synthesis (Mosaei and Zenkin, 2020). This mode of action does not inherently involve

oxidative stress pathways or ROS generation (Tukulula et al., 2018). Therefore, it is logical to deduce that RIF alone would not contribute to elevated ROS levels in cellular environments, as observed in both **Figure 4.1** and **Figure 4.2.** On the other hand, CS-PCL nanoparticles are composed of chitosan, a natural polysaccharide, and polycaprolactone, a biodegradable polyester; both materials are recognised for their biocompatibility and low cytotoxicity (Korniienko et al., 2024, Osanloo et al., 2024). Combining these polymers into nanoparticles is designed to enhance the delivery and efficacy of therapeutic agents, such as RIF, without inducing significant oxidative stress. Therefore, the structure and degradation products of CS-PCL nanoparticles are unlikely to interact with cellular components in a manner that would stimulate ROS production, as seen in **Figures 4.1 and 4.2**, where there were no significant changes between RIF, CS-PCL and CS-PCL-RIF treatments, suggesting that the chemical nature and the mechanism of action of both RIF and CS-PCL nanoparticles are not conducive to ROS production.

However, when nanoparticles encapsulating RIF/VITD3 were functionalised with β-1,3-glucan, ROS generation was significantly increased, approximately 2-fold, compared to non-functionalized RIF/VITD3-containing nanoparticles (**Figure 4.1 and 4.2**). The observed changes are attributed to the presence of β-1,3-glucan as this was consistent with a previous study conducted by Dube and colleagues, where it was also observed that β-1,3-glucan functionalised nanoparticles increased ROS production by 2.6-fold compared to RIF solution and by 1.2-fold compared to chitosan-poly(lactic-co-glycolic acid) (CS-PLGA) nanoparticles only (Dube et al., 2014).

These findings were consistent with the literature, as β-1,3-Glucan has been shown to stimulate the production of ROS/RNS in macrophages by targeting dectin-1 receptors (Goodridge et al., 2011). These receptors are pattern recognition receptors predominantly expressed on macrophages; when β-1,3-glucan binds to dectin-1 receptors, it triggers a series of intracellular signalling pathways, leading to ROS production as observed in Figure **4.1 and 4.2** (Goodridge et al., 2011, Mata-Martinez et al., 2022). The generation of ROS is crucial for bacterial killing and the induction of autophagy, which collectively enhance the overall immune response of macrophages; this enhanced immune activity inhibits the growth and survival of Mtb as ROS directly participate in the bacterial killing by destroying its components (Canton et al., 2021). The production of ROS not only contributes to the direct killing of pathogens but also influences macrophage polarisation; specifically, it aids in polarising macrophages towards the M1 phenotype, which is associated with pro-inflammatory responses such as

TNF-α, which enhances their antimicrobial activity (Covarrubias et al., 2013, Shekhova, 2020, Canton et al., 2021). This dual role of ROS underscores their importance in the immune system's direct and indirect mechanisms of pathogen elimination, which the formulated nanoparticles could achieve as they stimulate ROS production, as seen in **Figure 4.1 and Figure 4.2**.

Furthermore, functionalising nanoparticles with β-1,3-glucan not only targets dectin-1 receptors but also enhances the uptake and intracellular delivery of the nanoparticles (Tukulula et al., 2018). This improved targeting ensures that more VITD3 is delivered directly into the macrophages, potentially leading to a localised increase in ROS production. As a result, the efficacy of VITD3 and RIF is heightened even at low doses (Tukulula et al., 2018, Dube et al., 2014). In addition, it is essential to note that VITD3 had a highly significant impact on ROS production when compared to CS-PCL-VITD3 and Glu-CS-PCL-VITD3 nanoparticles, as shown in **Figure 4.2.** This effect is attributed to VITD3's ability to induce ROS production by upregulating the expression of various antimicrobial peptides and proteins that contribute to the oxidative burst (Laaksi, 2012). Furthermore, a higher concentration of VITD3 (36 µg/mL) was used compared to the 4 µg/mL encapsulated within the CS-PCL-VITD3 and Glu-CS-PCL-VITD3 nanoparticles used for the treatment of cells in this study, hence the observed difference in ROS production levels.

TNF-α is a crucial pro-inflammatory cytokine with a significant role in the immune response (Mohd Zawawi et al., 2023); Its production is a hallmark of M1 macrophage activation, a state characterised by enhanced microbicidal activity and inflammatory responses (Roszer, 2015, Atri et al., 2018). One of the most critical functions of TNF-α is its bactericidal action against intracellular Mtb, which is a highly adaptive pathogen capable of surviving within macrophages by evading the host's immune response (Chai et al., 2020, Vu et al., 2024). However, TNF-α enhances the macrophage's ability to control and eliminate Mtb through several mechanisms, such as activation of nitric oxide synthase, enhancement of phagosome maturation, and autophagy induction (Maphasa et al., 2020, Liu et al., 2017a, Roca and Ramakrishnan, 2013, Vu et al., 2024). Hence, quantifying TNF-α levels in macrophage cultures can provide valuable insights into the state of immune activation and the efficacy of anti-microbial responses, where high levels of TNF-α indicate a robust pro-inflammatory response and active engagement of macrophages in pathogen clearance (Viola et al., 2019, Mezouar et al., 2019).

Our data in **Figure 4.3** demonstrate that CS-PCL nanoparticles alone enhanced TNF-α levels compared to RIF, VITD3, and control treatments. This enhancement is attributed to the chitosan oligosaccharides lactate used to synthesise the nanoparticles. Previous studies have shown that chitosan can indeed influence TNF-α levels in macrophages, with specific outcomes depending on various factors, such as the properties of the chitosan, including its molecular weight, degree of deacetylation, and structural form (Kaval et al., 2022, Ravindranathan et al., 2016, Dube et al., 2014). It is also important to note that upon surface functionalisation of the nanoparticles with β-1,3-glucan, the levels of TNF-α production were further significantly increased, as seen in **Figure 4.3**. Previous studies have also evidenced that the immunostimulatory properties of β-1,3-glucan can enhance macrophage activation and TNF-α production (Dube et al., 2014).

In addition, the enhanced TNF-α produced in **Figure 4.3** after treatment with functionalised nanoparticles is directly linked to the increased levels of ROS produced by macrophages following treatment with the formulated nanoparticles, as observed in **Figures 4.1 and 4.2**. This occurs via the activation of various transcription factors, such as NF-κB (nuclear factor kappa-light-chain-enhancer of activated B cells), which are critical for the transcription of pro-inflammatory genes (Liu et al., 2017b). When ROS levels rise, they activate these transcription factors, leading to increased gene expression of TNF-α and, hence, increased levels of TNF-α, as observed in **Figure 4.3** (Liu et al., 2017b, Morgan and Liu, 2011). As mentioned previously, this contributes to the inflammatory response and the enhanced antimicrobial activity of M1 macrophages; thus, ROS not only have a direct antimicrobial effect but also amplifies the immune response by boosting the production of key inflammatory cytokines like TNF-α as seen in **Figure 4.3** (Covarrubias et al., 2013, Shekhova, 2020, Canton et al., 2021, Morgan and Liu, 2011).

IFN-γ is a pro-inflammatory cytokine primarily produced by T cells and Natural killer (NK) cells; It activates macrophages, enhancing their microbicidal and tumoricidal activities and promoting the production of pro-inflammatory cytokines, ROS and NOS, aiding in pathogen clearance (Gajanayaka et al., 2021, Wu et al., 2014). Interestingly, when IFN-γ was quantified, a negative response was observed, suggesting the absence or very low non-quantifiable levels, as seen in **Figure 4.4**. These results were the opposite of previous studies, where Dube and colleagues discovered that 1,3 β-glucan-functionalized nanoparticles increased IFN-γ by 23-fold compared to the control (Dube et al., 2014). This could be due to various reasons, with the apparent one being that macrophages do not typically produce IFN-γ

themselves; instead, they are one of the primary targets of IFN-γ, which is mainly produced by NK cells and T cells (Tao et al., 2023, Wu et al., 2014).

Other possible reasons could be that chronic or excessive production of TNF-α and ROS can lead to a negative feedback loop, reducing the secretion of IFN-γ or suppressing pathways that would usually enhance its secretion (Nunes et al., 2021). This is because prolonged inflammation and high levels of pro-inflammatory cytokines can lead to immune cell exhaustion and regulatory mechanisms that suppress further immune activation to prevent tissue damage (Li et al., 2023, Nunes et al., 2021). This balance is crucial for preventing excessive inflammation and tissue damage.

Analysing IL-4 levels in the control and various treatment groups reveals noteworthy differences in immune response modulation of the nanoparticles. In the control group, IL-4 levels were negligible or non-quantifiable, indicating a lack of anti-inflammatory response under normal conditions (**Figure 4.5**). Upon treatment with CS-PCL nanoparticles, there was a significant induction of IL-4, demonstrating that these nanoparticles can stimulate an anti-inflammatory response compared to the control group, as seen in **Figure 4.5**. This effect is primarily due to chitosan's immunomodulatory properties. It has been reported that it can activate macrophages and induce a shift towards a type 2 macrophage phenotype (M2), which is associated with the enhanced production of anti-inflammatory cytokines such as IL-4, as observed in **Figure 4.5** (Xu et al., 2022, Kumar and Kumar, 2020, Mohite et al., 2023).

M2 macrophages induced by IL-4 play a crucial role in modulating and reducing inflammation; they help resolve tissue damage, prevent excessive inflammation, and regulate the immune response, contributing to tissue repair and immune homeostasis (Chen et al., 2023, Viola et al., 2019). A substantial increase in IL-4 levels was observed between the control, CS-PCL and RIF treatments, with RIF demonstrating a more potent effect. However, when RIF was encapsulated within the nanoparticles (CS-PCL-RIF and Glu-CS-PCL-RIF), there were no significant changes in IL-4 levels, as seen in **Figure 4.5a.** This suggests that RIF, whether alone or combined with nanoparticles, has a strong capacity to induce IL-4 production, indicating its potent anti-inflammatory effect.

RIF has been associated with anti-inflammatory responses in macrophages via the activation of peroxisome proliferator-activated receptor γ (PPARγ), which can lead to anti-inflammatory impacts in macrophages during sepsis, potentially alleviating damaging inflammation (Rosette et al., 2013, Croasdell et al., 2015, Leopold Wager et al., 2019). Furthermore, RIF has been studied for its impact on macrophages, and studies suggest that RIF inhibits the secretion of pro-inflammatory cytokines (such as IL-1β and TNF-α) in various cell lines, including macrophages; hence, this may contribute to its anti-inflammatory effect as observed in **Figure 4.5a** (Haferland et al., 2022)**.** The enhanced IL-4 response with RIF treatments underscores the role of RIF in immune modulation and suggests that its incorporation into nanoparticle formulations could potentiate its therapeutic effects.

The nanoparticles had no significant effect on the production of the anti-inflammatory cytokines IL-10 (**Figure 4.6**), a prominent hallmark of the M2 phenotype (Strizova et al., 2023). As anticipated, phagocytosis of the nanoparticles via activation of Dectin-1 by 1,3 β-glucan was unlikely to induce an anti-inflammatory response, particularly the secretion of IL-10. (Dube et al., 2014, Kankkunen et al., 2010). This outcome is attributed to the high secretion of ROS and TNF-α, which favour macrophage polarisation towards the M1 phenotype, responsible for pro-inflammatory responses and microbial action. (Canton et al., 2021, Shekhova, 2020).

In addition, the untreated group displayed small, round cells with a smooth surface and uniform appearance, indicative of the M0 phenotype, which represents a baseline, non-activated state (**Figure 4.7**) (Italiani and Boraschi, 2014). In contrast, the treated group exhibited larger cells with an irregular shape, elongated or spread-out morphology, and more cytoplasmic extensions, characteristics of the M1 phenotype associated with pro-inflammatory activation. (Italiani and Boraschi, 2014). Additionally, some cells in the treated group displayed an oval shape, suggesting partial differentiation towards the M2 phenotype, which is associated with anti-inflammatory responses and tissue repair (Gordon and Martinez, 2010, Italiani and Boraschi, 2014). The observations depicted in **Figure 4.7** further indicate that the nanoparticles favour the M1 phenotype, as evidenced by the larger, irregularly shaped cells with elongated morphology and increased cytoplasmic extensions (Gordon and Martinez, 2010). This is supported by the high levels of ROS and TNF-α observed, which are characteristic of M1 macrophage activation. These pro-inflammatory markers reinforce the conclusion that the nanoparticles promote an M1 phenotype in the RAW 264.7 cells more than the M2 phenotype.

4.5. Concluding Remarks

In conclusion, the formulated nanoparticles demonstrated several promising attributes contributing to their potential as effective therapeutic agents. Notably, these nanoparticles exhibited increased production levels of ROS. ROS are crucial for bacterial killing as they help to disrupt bacterial cell walls and induce oxidative stress in bacterial cells. The elevated ROS levels also contributed to the polarisation of macrophages to the M1 phenotype. M1 macrophages are known for their role in pro-inflammatory responses and are vital for efficiently eradicating bacterial infections. Furthermore, the nanoparticles showed increased levels of TNF-α. This increase is attributed to the surface functionalisation with 1,3 β-glucan, which has been shown to enhance immune responses, and the elevated ROS levels directly influencing TNF-α production. TNF-α is a pro-inflammatory cytokine critical in mediating the body's response to infections, thereby providing a dual action mechanism: enhancing bacterial killing while stimulating a robust immune response.

Interestingly, the nanoparticles also induced partial increases in IL-4 levels. IL-4 is a cytokine associated with the M2 phenotype of macrophages, which are involved in tissue repair and anti-inflammatory responses. This induction suggests that the nanoparticles can promote tissue healing and modulate inflammation by downregulating IFN-γ, a cytokine associated with pro-inflammatory responses. However, it is essential to note that IL-10, a key feature of M2 macrophages, is typically downregulated by excess ROS and TNF-α production. This indicates that while the nanoparticles promote some aspects of the M2 phenotype, such as tissue healing, high ROS and TNF-α levels may limit the full transition to an anti-inflammatory state by suppressing IL-10. M1 and partial M2 characteristics indicate a balanced immune response where inflammation necessary for bacterial killing is present. However, it is not excessive, thanks to the anti-inflammatory effects that facilitate healing, which might be negligible considering the low levels.

This balanced response is crucial because it ensures that while the immune system aggressively targets and kills bacteria, it promotes tissue repair and prevents chronic inflammation, which can cause tissue damage. The negative feedback mechanism involving IFN-γ helps regulate the inflammatory response, ensuring it remains effective for bacterial killing without causing excessive tissue damage. It is essential to test these nanoparticles on infected cells to evaluate their efficacy against Mtb. Such studies will provide insights into their

practical applicability and effectiveness in a real-world scenario, potentially leading to new therapeutic strategies for combating bacterial infections, primarily tuberculosis.

4.6. References

Amaral, E. P., Vinhaes, C. L., Oliveira-De-Souza, D., Nogueira, B., Akrami, K. M. & Andrade, B. B. 2021. The Interplay Between Systemic Inflammation, Oxidative Stress, and Tissue Remodeling in Tuberculosis. *Antioxidants & redox signaling,* 34**,** 471-485.

Atri, C., Guerfali, F. Z. & Laouini, D. 2018. Role of Human Macrophage Polarization in Inflammation during Infectious Diseases. *Int J Mol Sci,* 19**,** 1801.

Bo, H., Moure, U. a. E., Yang, Y., Pan, J., Li, L., Wang, M., et al. Cui, H. 2023. Mycobacterium tuberculosis-macrophage interaction: Molecular updates. *Front Cell Infect Microbiol,* 13**,** 1062963.

Canton, M., Sanchez-Rodriguez, R., Spera, I., Venegas, F. C., Favia, M., Viola, A. & Castegna, A. 2021. Reactive Oxygen Species in Macrophages: Sources and Targets. *Front Immunol,* 12**,** 734229.

Cavinato, L., Genise, E., Luly, F. R., Di Domenico, E. G., Del Porto, P. & Ascenzioni, F. 2020. Escaping the Phagocytic Oxidative Burst: The Role of SODB in the Survival of Pseudomonas aeruginosa Within Macrophages. *Front Microbiol,* 11**,** 326.

Chai, Q., Wang, L., Liu, C. H. & Ge, B. 2020. New insights into the evasion of host innate immunity by Mycobacterium tuberculosis. *Cell Mol Immunol,* 17**,** 901-913.

Chen, S., Saeed, A., Liu, Q., Jiang, Q., Xu, H., Xiao, G. G., et al. Duo, Y. 2023. Macrophages in immunoregulation and therapeutics. *Signal Transduct Target Ther,* 8**,** 207.

Covarrubias, A., Byles, V. & Horng, T. 2013. ROS sets the stage for macrophage differentiation. *Cell research,* 23**,** 984-5.

Croasdell, A., Duffney, P. F., Kim, N., Lacy, S. H., Sime, P. J. & Phipps, R. P. 2015. PPARgamma and the Innate Immune System Mediate the Resolution of Inflammation. *PPAR research,* 2015**,** 549691.

Dube, A., Reynolds, J. L., Law, W. C., Maponga, C. C., Prasad, P. N. & Morse, G. D. 2014. Multimodal nanoparticles that provide immunomodulation and intracellular drug delivery for infectious diseases. *Nanomedicine : nanotechnology, biology, and medicine,* 10**,** 831-8.

Gajanayaka, N., Dong, S. X. M., Ali, H., Iqbal, S., Mookerjee, A., Lawton, D. A., et al. Kumar, A. 2021. TLR-4 Agonist Induces IFN-gamma Production Selectively in Proinflammatory Human M1 Macrophages through the PI3K-mTOR- and JNK-MAPK-Activated p70S6K Pathway. *Journal of immunology (Baltimore, Md. : 1950),* 207**,** 2310-2324.

Goodridge, H. S., Reyes, C. N., Becker, C. A., Katsumoto, T. R., Ma, J., Wolf, A. J., et al. Underhill, D. M. 2011. Activation of the innate immune receptor Dectin-1 upon formation of a 'phagocytic synapse'. *Nature,* 472**,** 471-5.

Gordon, S. & Martinez, F. O. 2010. Alternative activation of macrophages: mechanism and functions. *Immunity,* 32**,** 593-604.

Haferland, I., Wallenwein, C. M., Ickelsheimer, T., Diehl, S., Wacker, M. G., Schiffmann, S., et al. Pinter, A. 2022. Mechanism of anti-inflammatory effects of rifampicin in an ex vivo culture system of hidradenitis suppurativa. *Experimental dermatology,* 31**,** 1005-1013.

Italiani, P. & Boraschi, D. 2014. From Monocytes to M1/M2 Macrophages: Phenotypical vs. Functional Differentiation. *Front Immunol,* 5**,** 514.

Kankkunen, P., Teirila, L., Rintahaka, J., Alenius, H., Wolff, H. & Matikainen, S. 2010. (1,3)-beta-glucans activate both dectin-1 and NLRP3 inflammasome in human macrophages. *Journal of immunology (Baltimore, Md. : 1950),* 184**,** 6335-42.

Kaval, M. E., Cakir, B., Polatli, E., Rencber, S., Karavana, S. Y., Nalbantsoy, A. & Guneri, P. 2022. IL-1ss, IL-6 and TNF-alpha expression levels of macrophage cells induced by benzydamine hydrochloride, benzydamine hydrochloride with chitosan, calcium hydroxide and chlorhexidine medicaments: An ELISA study. *Dental materials journal,* 41**,** 545-551.

Khoza, L. J., Kumar, P., Dube, A., Demana, P. H. & Choonara, Y. E. 2022. Insights into innovative therapeutics for drug-resistant tuberculosis: Host-directed therapy and autophagy inducing modified nanoparticles. *International journal of pharmaceutics,* 622**,** 121893.

Korniienko, V., Husak, Y., Diedkova, K., Varava, Y., Grebnevs, V., Pogorielova, O., et al. Pogorielov, M. 2024. Antibacterial Potential and Biocompatibility of Chitosan/Polycaprolactone Nanofibrous Membranes Incorporated with Silver Nanoparticles. *Polymers,* 16**,** 1729.

Kumar, A. & Kumar, A. 2020. The virtuous potential of chitosan oligosaccharide for promising biomedical applications. *Journal of Materials Research,* 35**,** 1123-1134.

Laaksi, I. 2012. Vitamin D and respiratory infection in adults. *Proc Nutr Soc,* 71**,** 90-7.

Leavy, O. 2014. Inflammation: Regulating ROS. *Nat Rev Immunol,* 14**,** 357.

Lendeckel, U., Venz, S. & Wolke, C. 2022. Macrophages: shapes and functions. *Chemtexts,* 8**,** 12.

Leopold Wager, C. M., Arnett, E. & Schlesinger, L. S. 2019. Macrophage nuclear receptors: Emerging key players in infectious diseases. *Plos Pathog,* 15**,** e1007585.

Li, C., Deng, C., Wang, S., Dong, X., Dai, B., Guo, W., et al. Cao, L. 2024. A novel role for the ROS-ATM-Chk2 axis mediated metabolic and cell cycle reprogramming in the M1 macrophage polarization. *Redox Biol,* 70**,** 103059.

Li, W., Liu, Q., Shi, J., Xu, X. & Xu, J. 2023. The role of TNF-alpha in the fate regulation and functional reprogramming of mesenchymal stem cells in an inflammatory microenvironment. *Front Immunol,* 14**,** 1074863.

Liu, C. H., Liu, H. & Ge, B. 2017a. Innate immunity in tuberculosis: host defense vs pathogen evasion. *Cell Mol Immunol,* 14**,** 963-975.

Liu, T., Zhang, L., Joo, D. & Sun, S. C. 2017b. NF-kappaB signaling in inflammation. *Signal Transduct Target Ther,* 2**,** 17023-.

Maphasa, R. E., Meyer, M. & Dube, A. 2020. The Macrophage Response to Mycobacterium tuberculosis and Opportunities for Autophagy Inducing Nanomedicines for Tuberculosis Therapy. *Front Cell Infect Microbiol,* 10**,** 618414.

Mata-Martinez, P., Bergon-Gutierrez, M. & Del Fresno, C. 2022. Dectin-1 Signaling Update: New Perspectives for Trained Immunity. *Front Immunol,* 13**,** 812148.

Mezouar, S., Diarra, I., Roudier, J., Desnues, B. & Mege, J. L. 2019. Tumor Necrosis Factor-Alpha Antagonist Interferes With the Formation of Granulomatous Multinucleated Giant Cells: New Insights Into Mycobacterium tuberculosis Infection. *Front Immunol,* 10**,** 1947.

Mohd Zawawi, Z., Kalyanasundram, J., Mohd Zain, R., Thayan, R., Basri, D. F. & Yap, W. B. 2023. Prospective Roles of Tumor Necrosis Factor-Alpha (TNF-alpha) in COVID-19: Prognosis, Therapeutic and Management. *Int J Mol Sci,* 24**,** 6142.

Mohite, P., Shah, S. R., Singh, S., Rajput, T., Munde, S., Ade, N., et al. Dudhrejiya, A. V. 2023. Chitosan and chito-oligosaccharide: a versatile biopolymer with endless grafting possibilities for multifarious applications. *Front Bioeng Biotechnol,* 11**,** 1190879.

Morgan, M. J. & Liu, Z. G. 2011. Crosstalk of reactive oxygen species and NF-kappaB signaling. *Cell research,* 21**,** 103-15.

Mosaei, H. & Zenkin, N. 2020. Inhibition of RNA Polymerase by Rifampicin and Rifamycin-Like Molecules. *EcoSal Plus,* 9**,** 10.1128/ecosalplus.ESP-0017-2019.

Nunes, J. P. S., Andrieux, P., Brochet, P., Almeida, R. R., Kitano, E., Honda, A. K., et al. Cunha-Neto, E. 2021. Co-Exposure of Cardiomyocytes to IFN-gamma and TNF-alpha Induces Mitochondrial Dysfunction and Nitro-Oxidative Stress: Implications for the Pathogenesis of Chronic Chagas Disease Cardiomyopathy. *Front Immunol,* 12**,** 755862.

Osanloo, M., Noori, F., Varaa, N., Tavassoli, A., Goodarzi, A., Moghaddam, M. T., et al. Goodarzi, A. 2024. The wound healing effect of polycaprolactone-chitosan scaffold coated with a gel containing Zataria multiflora Boiss. volatile oil nanoemulsions. *BMC Complement Med Ther,* 24**,** 56.

Pellegrino, E., Aylan, B., Bussi, C., Fearns, A., Bernard, E. M., Athanasiadi, N., et al. Gutierrez, M. G. 2023. Peroxisomal ROS control cytosolic Mycobacterium tuberculosis replication in human macrophages. *J Cell Biol,* 222.

Ravindranathan, S., Koppolu, B. P., Smith, S. G. & Zaharoff, D. A. 2016. Effect of Chitosan Properties on Immunoreactivity. *Mar Drugs,* 14**,** 91.

Roca, F. J. & Ramakrishnan, L. 2013. TNF dually mediates resistance and susceptibility to mycobacteria via mitochondrial reactive oxygen species. *Cell,* 153**,** 521-34.

Rosette, C., Buendia-Laysa, F., Jr., Patkar, S., Moro, L., Celasco, G., Bozzella, R., et al. Gerloni, M. 2013. Anti-inflammatory and immunomodulatory activities of rifamycin SV. *Int J Antimicrob Agents,* 42**,** 182-6.

Roszer, T. 2015. Understanding the Mysterious M2 Macrophage through Activation Markers and Effector Mechanisms. *Mediators Inflamm,* 2015**,** 816460.

Shekhova, E. 2020. Mitochondrial reactive oxygen species as major effectors of antimicrobial immunity. *Plos Pathog,* 16**,** e1008470.

Strizova, Z., Benesova, I., Bartolini, R., Novysedlak, R., Cecrdlova, E., Foley, L. K. & Striz, I. 2023. M1/M2 macrophages and their overlaps - myth or reality? *Clinical science (London, England : 1979),* 137**,** 1067-1093.

Tao, H., Xu, Y. & Zhang, S. 2023. The Role of Macrophages and Alveolar Epithelial Cells in the Development of ARDS. *Inflammation,* 46**,** 47-55.

Tukulula, M., Gouveia, L., Paixao, P., Hayeshi, R., Naicker, B. & Dube, A. 2018. Functionalization of PLGA Nanoparticles with 1,3-β-glucan Enhances the Intracellular Pharmacokinetics of Rifampicin in Macrophages. *Pharm Res* [Online], 35. Available: https://doi.org/10.1007/s11095-018-2391-8 [Accessed 2018/03//].

Viola, A., Munari, F., Sanchez-Rodriguez, R., Scolaro, T. & Castegna, A. 2019. The Metabolic Signature of Macrophage Responses. *Front Immunol,* 10**,** 1462.

Vu, A., Glassman, I., Campbell, G., Yeganyan, S., Nguyen, J., Shin, A. & Venketaraman, V. 2024. Host Cell Death and Modulation of Immune Response against Mycobacterium tuberculosis Infection. *Int J Mol Sci,* 25**,** 6255.

Wu, C., Xue, Y., Wang, P., Lin, L., Liu, Q., Li, N., et al. Cao, X. 2014. IFN-gamma primes macrophage activation by increasing phosphatase and tensin homolog via downregulation of miR-3473b. *Journal of immunology (Baltimore, Md. : 1950),* 193**,** 3036-44.

Xu, J., Guan, W., Kong, Y., Liu, F., Zhao, Y., Li, G. & Yang, Y. 2022. Regulation of Macrophage Behavior by Chitosan Scaffolds with Different Elastic Modulus. *Coatings,* 12**,** 1742.

CHAPTER 5

ASSESSMENT OF ANTI-TUBERCULAR EFFICACY OF FORMULATED NANOPARTICLES AGAINST MYCOBACTERIUM TUBERCULOSIS STRAINS AND INTRACELLULAR KILLING IN ACTIVATED THP-1 MACROPHAGES

5.1. Introduction

In the previous sections, nanoparticles were synthesised and tested for their physical properties (**Chapter 3**). Further, their ability to induce immunomodulation was assessed by quantifying different cytokines and ROS released upon treatment with these nanoparticles (**Chapter 4**). These studies revealed that the nanoparticles induced polarisation towards the M1 phenotype and, to a partial extent, the M2 phenotype, both of which are crucial for bactericidal activity (Strizova et al., 2023). Building on these findings, it is now essential to further evaluate these nanoparticles by determining their Minimum Inhibitory Concentration (MIC) against different Mtb strains. Additionally, to test their efficacy in infected macrophages to provide a comprehensive understanding of their therapeutic potential.

MIC is a critical parameter in pharmacology, representing the lowest concentration of an antimicrobial agent that hinders the noticeable growth of a bacteria after the desired period of incubation (Kowalska-Krochmal and Dudek-Wicher, 2021). Determining the MIC is essential for evaluating the efficacy of antimicrobial agents (Kowalska-Krochmal and Dudek-Wicher, 2021), especially in the context of nanoparticles and new drug delivery systems. These innovative systems often exhibit unique properties and interactions with biological targets, necessitating precise MIC assessments to ensure optimal dosing, minimise resistance development, and enhance therapeutic outcomes (Ramon-Luing et al., 2022, O'Neill and Chopra, 2004). Accurate MIC determination is critical when working with TB-infected cells or macrophages, as it aids in establishing the correct starting concentration for intracellular killing assays of Mtb; this ensures that the antimicrobial agent can effectively penetrate and act within infected cells, leading to more reliable and effective treatment strategies against TB (Patankar et al., 2020).

The H37Rv and MDR11 strains of Mtb are central in TB research, particularly in determining the MIC for nanoparticles and new drug delivery systems (Arega et al., 2022, Chitale et al., 2022). H37Rv, a laboratory strain first isolated in 1905, is widely used due to its well-

characterized genome and consistent virulence in experimental models (Chitale et al., 2022). This strain is a benchmark for studying the basic biology of Mtb and assessing the efficacy of new antimicrobial agents (Chitale et al., 2022). On the other hand, the MDR11 strain represents multi-drug-resistant tuberculosis, a significant global health challenge. MDR11 is invaluable in evaluating the effectiveness of new treatments against resistant forms of TB (Arega et al., 2022). Using these strains in MIC determination offers several advantages. H37Rv provides a reliable and reproducible model for initial testing of antimicrobial activity, while MDR11 allows researchers to assess the potential of new treatments to combat drug-resistant TB (Arega et al., 2022, Chitale et al., 2022). Their use ensures that findings are robust and relevant, facilitating the development of effective therapies and advancing our understanding of TB pathogenesis and treatment.

While MIC is essential, it is equally important to assess the efficacy of antimicrobial agents in infected macrophages, such as activated THP-1 cells, derived from the MIC value. Activated THP-1 cells, a human monocytic cell line, can be differentiated into macrophage-like cells, which are then infected with Mtb to test the intracellular killing efficacy of new treatments (Theus et al., 2004). Using infected macrophages provides vital insights into the intracellular activity of antimicrobial agents, which is not captured by MIC values alone (Kowalska-Krochmal and Dudek-Wicher, 2021) Testing drugs or nanoparticles on infected macrophages help to understand how effectively the treatment reaches and eliminates intracellular bacteria, mimicking the actual conditions in a human infection (Kowalska-Krochmal and Dudek-Wicher, 2021).

Researchers comprehensively understand an antimicrobial agent's potential by combining MIC determination with intracellular efficacy studies using infected macrophages. This holistic approach is vital for developing treatments that are not only potent in vitro but also effective in the complex environment of the human body, ultimately leading to more effective and targeted therapies for tuberculosis (Belanger and Hancock, 2021, Day et al., 2024). Therefore, in this chapter, MIC of the nanoparticles developed in **Chapter 2** and tested for their immunomodulatory abilities or polarisation effects in **Chapter 3**, which favoured the M1 phenotype, are now being evaluated. The MIC was determined for both H37Rv and MDR11 strains to establish the baseline efficacy of these nanoparticles against Mtb. The nanoparticles were then tested on activated THP-1 macrophages infected with Mtb H37Rv to determine their intracellular efficacy. By conducting these comprehensive assessments, we aimed to

understand the full potential of the nanoparticles in targeting and eliminating intracellular Mtb, thereby providing a robust evaluation of their therapeutic potential.

5.2. Materials and Methods

5.2.1. Materials

THP-1 monocytes were obtained from Merck (Pty Ltd., South Africa), and 48- and 96-well microtiter plates were purchased from LTC Tech (South Africa). All chemicals used were of analytical reagent grade and applied without further modification.

5.2.2. Evaluation of Formulated Nanoparticles Against M. Tuberculosis using the Broth Microdilution Method

All methods related to mycobacterial experimentation were conducted per the regulations related to handling human specimens and guidelines for the growth of *M. tuberculosis* and handling of human specimens. All procedures were performed in a Biosafety Level III laboratory, registered with the South African Department of Agriculture Forestry and Fisheries (registration number: 39.2/NHLS-20/010) and approved by the Institutional Biosafety Committee of the University of the Witwatersrand (approval number: 20200502Lab).

The antimycobacterial activity of the seven nanoparticle formulations together with VITD3 and RIF against a drug susceptible Mtb strain (H37Rv) and a drug-resistant strain (MDR11) was investigated using the broth microdilution minimum inhibitory concentration method as previously described by Kana et al., 2010 with modifications (Kana et al., 2010). To each well of a sterile round-bottom 96-well plate, except in the first row, 100 µL of Middlebrook 7H9 media (Difco) containing 10% Middlebrook oleic acid-albumin-dextrose-catalase (OADC), 0.2 % glycerol and 0.5 % Tween 80 was added. The formulated nanoparticles and VITD3 were prepared in double distilled water to 1 mg/mL stock concentration. Stocks were diluted to a final concentration of 100 µg/ml in 7H9 media, and 100 µL of each was added in duplicate to wells in the first row of the plate. Using a multichannel pipette, 50 µl of the mixture was removed from the first row and added to the second row containing 50 µl of media. It was mixed several times before removing 50 µl and adding it to the next row. The dilution series was continued to the end of the plate, and 50 µl was discarded from the last row. The positive drug controls, rifampicin, isoniazid and streptomycin, were prepared to final concentrations to

provide a range from 3,2 µg/mL to 0.002 µg/mL, 6.4 µg/mL to 0.004 µg/mL, and 100 µg/mL to 0.04 µg/mL, respectively during the 2-fold serial dilution across the 96 well plates. An equivalent amount of DMSO was used to dissolve the nanoparticle formulations, and the anti-tuberculosis drugs were included together with wells containing cells only (uninfected) as controls. Mtb strains were grown in Middlebrook 7H9 broth at 37 ºC for 3-4 days to an OD_{600nm} = 0.5 – 0.8. The bacterial cultures were diluted 1:500 in 7H9 medium, and 50 µl was added to each well. The plates were incubated for 14 days in a CO_2 incubator at 37 ºC. and scored visually using an inverted mirror for growth as pellets at the bottom of the well at 7 days and 14 days. The last row, where no growth was observed, represented the MIC for the nanoparticle formulation. For Wells in which growth could not be visually confirmed, 10 l of Alamar Blue (Invitrogen) was added on day 14, and the plates incubated overnight before visually scoring for change in colour from blue (no growth) to pink (viable growth) using an inverted mirror.

5.2.3. Intracellular killing of Susceptible Mtb, H37Rv in THP-1 activated Macrophages

THP-1 monocytes (Merck) were grown and maintained in RPMI-1640 media (Gibco) supplemented with 10% FBS, Sigma at 37˚C, and 5% CO2 for 7–10 days, after which viability was assessed by trypan blue exclusion staining. 1 ml of cells with a density of 2 x 10^5 cells/ml were seeded in each well of a 48-well plate. THP-1 monocytes were differentiated into adherent, activated macrophages with 100 nM phorbol myristate acetate (PMA) (Sigma), 150 U of recombinant human gamma interferon (IFN-γ) for 3 days at 37˚C, 5% CO_2. A culture of Mtb, H37Rv was grown in 7H9 media supplemented with 0.2% glycerol, 10 % OADC, and 0.05% Tween 80 to exponential phase (OD_{600nm} 0.4–0.6). The culture was diluted in RPMI-1640 media supplemented with 10% FBS to a cell density of ~2 x 10^6 cells/ml (OD_{600nm} = 0.05). The media in the wells containing adherent macrophages was removed, and 1 ml of the diluted mycobacterial inoculum (10 bacteria: 1 THP1 cell) was added to all wells and incubated for 4 hours at 37˚C, 5% CO_2 to promote phagocytosis. The wells were then washed once with warmed RPMI-1640 media supplemented with 10% FBS media, and duplicate wells were treated with 7 different formulations (S1-S7; 25,108, 70, 124, 107, 180, 230 µg/ml respectively) as well as VitaminD3 (VITD3, 100 µg/ml). Rifampicin (RIF) at 100X MIC (0,05 µg/ml) was included as the control together with untreated infected macrophages. Survival was monitored by enumerating colony-forming units (CFU/ml) after 5 days of incubation. Ten microliters of 10% SDS were immediately added to wells containing untreated infected macrophages to lyse the macrophages, serving as time zero. After 5 days, the treated and untreated macrophages were lysed with 10% SDS and appropriate dilutions of the supernatant was spread in duplicate

on Middlebrook 7H11 solid media (Difco) supplemented with 10% OADC and 0,2% glycerol. The plates were incubated at 37˚C for 4 weeks before the enumeration of mycobacterial growth and analysis of CFU/ml. Two biological replicate experiments were conducted.

5.3. Results and Discussion

5.3.1. MIC Evaluation of Formulated Nanoparticles Against H37Rv and MDR11 Strains

To assess the potential of the nanoparticles as antimicrobial agents, particularly those containing RIF, since nanoparticles containing VITD3 were not expected to exhibit any direct antimicrobial activity. Each nanoparticle's minimal inhibitory concentration was tested against drug-susceptible Mtb (H37Rv) and drug-resistant Mtb (MDR11) strains. The standard anti-tubercular drugs RIF, Isoniazid, and Streptomycin were included as controls. S1, consisting of nanoparticles (CS-PCL) composed solely of chitosan and polycaprolactone, showed a MIC of 25 µg/mL against both strains of Mtb (**Tables 5.1** and **5.2)**. The antimicrobial efficacy of S1 can be attributed to the inherent antimicrobial properties of chitosan. Chitosan's polycationic nature allows it to interact with bacterial cell membranes, disrupting membrane integrity and leading to bacterial cell death (Yan et al., 2021, Ke et al., 2021). Although polycaprolactone lacks inherent antimicrobial properties, its incorporation into chitosan-based materials can enhance the mechanical properties, flexibility, and overall performance of the composite material, making it more effective for biomedical applications (Baharlou Houreh et al., 2021, Shirzaei Sani et al., 2021).

When nanoparticles were encapsulated with VITD3 (S2) and tested against the H37Rv strain, the MIC remained consistent with CS-PCL nanoparticle (S1) at 25 µg/mL. However, for the MDR11 strain, the MIC increased to 50 µg/mL on both day 7 and day 14. It is important to note that VITD3 does not exhibit direct antibacterial activity. Instead, its role lies in modulating the body's immune response to infections by regulating the functional activities of both innate and adaptive immune cells, which may account for the observed differences in MIC (Hewison, 2012, Khoza et al., 2022). The MIC of S3 (CS-PCL-RIF) nanoparticles was evaluated on both day 7 and day 14. Notably, the effectiveness of S3 decreased from 0.1 µg/ml on day 7 to 0.2 µg/ml on day 14 when compared to the RIF standard, which exhibited MICs of 0.003 µg/ml on day 7 and 0.0125 µg/ml on day 14. Despite the differences observed in the MIC values of CS-PCL-RIF and RIF standard, it is important to highlight that the drug equivalent concentration of RIF within the CS-PCL-RIF nanoparticles was calculated to be 0.0045 µg/mL at day 7 and 0.0092 µg/mL at day 14. The dug equivalent concentration at day 14 was lower than the MIC

of the RIF standard, underscoring the enhanced potency of the nanoparticle formulation. These results are particularly significant as they suggest that the CS-PCL-RIF nanoparticles exhibit a synergistic effect with RIF compared to RIF alone over time, likely due to the intrinsic antibacterial properties of chitosan.

Chitosan's ability to disrupt bacterial membranes may enhance the overall antimicrobial activity of RIF encapsulated within CS-PCL-RIF nanoparticles, thus lowering the MIC of RIF. Previous studies by Prabhu et al. (2021), Dube et al. (2014), and Gu et al. (2021) have demonstrated similar synergistic effects, where the combination of chitosan with conventional antibiotics resulted in enhanced antibacterial efficacy (Prabhu et al., 2021, Dube et al., 2014, Gu et al., 2021). The observed decline in CS-PCL-RIF potency from day 7 to day 14 can be attributed to the gradual degradation of both the nanoparticles and RIF over time, resulting in an overall reduction in the system's efficacy against the H37Rv strain. However, despite this degradation, the nanoparticles still exhibited a lower MIC on day 14 when considering the drug-equivalent concentration of RIF (0.0092 µg/mL). This suggests that even as the nanoparticles degrade, they retain a degree of antimicrobial activity, potentially offering sustained therapeutic effects over time. The bactericidal activity of CS-PCL-RIF against the MDR11 strain was similar to that of CS-PCL alone (**Table 5.1** and **5.2**). This similarity is due to the MDR11 strain's resistance to RIF, indicating that the antimicrobial efficacy of CS-PCL-RIF is driven by both the nanoparticles and RIF, not RIF alone. These findings underscore the role of nanoparticle systems in enhancing drug delivery and efficacy, even in resistant strains, and highlight the potential of CS-PCL nanoparticles to improve the therapeutic effect of RIF in cases of drug resistance.

Table 5.1: Minimum Inhibitory Concentration of Nanoparticle Formulations Against Susceptible *Mycobacterium tuberculosis*, H37Rv.

Formulation	MIC – Day 7 (µg/ml)	Drug Equiv. Conc. (µg/ml)	MIC – Day 14 (µg/ml)	Drug Equiv. Conc. (µg/ml)
S1: CS-PCL	25,0	-	25,0	-
S2: CS-PCL-VITD3	25,0	0,7450	25,0	0,7450
S3: CS-PCL-RIF	0,10	0,0046	0,20	0,0092
S4: Glu-CS-PCL-VITD3	50,00	1,30	50,0	1,30
S5: Glu-CS-PCL-RIF	0,050	0,0015	0,10	0,0030

S6: S2 + S3	0,20	0,0092	0,40	0,40
S7: S4 + S5	0,0250	0,0008	0,10	0,0030
RIF Std	0,0030	0,0030	0,0125	0,0125
ISN Std	0,050	0,050	0,050	0,050
Strep Std	0,80	0,80	0,80	0,80
VITD3 Std	50,0	50,0	50,0	50,0

The 1,3-β-glucan-functionalized nanoparticles, Glu-CS-PCL-RIF (S5), exhibited increased bactericidal effectiveness compared to the non-functionalized nanoparticles (CS-PCL-RIF) when tested against the H37Rv strain (**Table 5.1**). This enhanced potency was evident on both day 7 and day 14, with MICs of 0.05 µg/mL and 0.1 µg/mL, respectively. The increased efficacy of Glu-CS-PCL-RIF is attributed to the presence of 1,3-β-glucan. Mtb contains specific molecules known as pathogen-associated molecular patterns (PAMPs), which include components of its cell wall, such as lipopolysaccharides, mycolic acids, and glucans like arabinogalactan and peptidoglycan (Jankute et al., 2015, Kalscheuer et al., 2019, Liu et al., 2017). The complex structure of the Mtb cell wall is formed by the interaction of the peptidoglycan layer with arabinogalactan, which is further linked to mycolic acids; additionally, the peptidoglycan-arabinogalactan complex can interact with other glucans through glycosidic linkages, including 1,3-β-glucan (Kalscheuer et al., 2019); Therefore, 1,3-β-glucan Glu-CS-PCL-RIF facilitated the interaction with the peptidoglycan-arabinogalactan complex in Mtb through glycosidic linkages, as the literature suggests. This interaction likely enhanced the delivery of the nanoparticle payload directly to the bacterial cell, resulting in the increased potency of Glu-CS-PCL-RIF compared to CS-PCL-RIF against the H37Rv strain, as shown in **Table 5.1**.

Additionally, the drug equivalence MIC of Glu-CS-PCL-RIF for RIF was found to be remarkably low at 0.00149 µg/ml on day 7, which is 2 times lower than the MIC of the standard RIF drug, 0.003 µg/ml. This underscores the significant advantages of functionalised nanoparticles with 1,3-β-glucan, as it enhances the interaction between the nanoparticles and Mtb, allowing for greater drug efficacy at a much lower concentration than the standard drug. This also suggests a synergistic effect between the drug and the functionalised nanoparticles, contributing to their bactericidal action, as supported by previous studies (Dube et al., 2014, Gu et al., 2021, Kalscheuer et al., 2019, Liu et al., 2017, Prabhu et al., 2021). A similar observation was made for S7, a treatment consisting of both S5 (Glu-CS-PCL-VITD3) and S4 (Glu-CS-PCL-RIF) formulations. S7 exhibited greater potency than all other formulations despite containing a

significantly far lower concentration of RIF (<0.000754 µg/ml on day 7). This enhanced efficacy observed with S7 is due to the combined functionalised nanoparticles, which improved the interaction with Mtb bacillus, leading to a lower MIC (0.025 µg/mL) compared to Glu-CS-PCL-RIF alone (0.05 µg/mL). These findings highlight the potential of using functionalised nanoparticles to significantly boost the effectiveness of anti-TB therapies, particularly in reducing the required drug dosage while maintaining or even enhancing therapeutic outcomes.

Table 5.2: Minimum Inhibitory Concentration of Nanoparticle Formulations Against Drug-Resistant *Mycobacterium tuberculosis* MDR11 Strain.

Formulation	MIC – Day 7 (µg/ml)	Drug Equiv. Conc. (µg/ml)	MIC – Day 14 (µg/ml)	Drug Equiv. Conc. (µg/ml)
S1: CS-PCL	25,0	-	25,0	-
S2: CS-PCL-VITD3	50,0	1,490	50,0	1,250
S3: CS-PCL-RIF	25,0	1,50	25,0	1,50
S4: Glu-CS-PCL-VITD3	25,0	0,650	25,0	0,650
S5: Glu-CS-PCL-RIF	25,0	0,7450	25,0	0,7450
S6: S2 + S3	25,0	1,1500	25,0	1,150
S7: S4 + S5	6,30	0,1870	12,50	0,3725
RIF Std	>3,20	3,20	>3,20	3,20
ISN Std	>6,40	6,40	>6,40	6,40
Strep Std	3,20	3,20	3,20	3,20
VITD3 Std	50,0	50,0	>50,0	50,0

Interestingly, S7 demonstrated significant potency against the resistant MDR11 strain of Mtb despite the strain's known resistance to RIF, as per **Table 5.2**. While the standard RIF treatment had a MIC greater than 3.2 µg/ml on both days 7 and 14, the nanoparticles contained 0.745 µg/ml of RIF, which is 4 times lower. This suggests that 1,3-β-glucan-functionalized nanoparticles could enhance the bactericidal activity of RIF against drug-resistant strains while using lower drug concentrations. This aligns with existing literature, which has shown that nanoparticles containing chitosan and 1,3-β-glucan can potentially enhance the effectiveness of RIF in treating drug-resistant tuberculosis (Prabhu et al., 2021,

Rajput et al., 2021). Furthermore, the increased potency observed in S6 and S7, despite containing lower drug concentrations than standard RIF, is due to 1,3-β-glucan functionalisation.

This was observed for both H37Rv (**Table 5.1**) and MDR11 (**Table 5.2**) strains, similar to formulation S5. Comparisons can also be drawn between S4 and S3 in the MDR11 strain, although not in the H37Rv strain. In conclusion, functionalising nanoparticles with 1,3-β-glucan enhances their interaction with Mtb, thereby increasing their bactericidal action while using significantly lower RIF concentrations than the standard MIC concentration. This shows that the nanoparticles can be further applied for extracellular Mtb as the 1,3-β-glucan enables or increases interaction between the nanoparticles and Mtb. This was observed in the susceptible strain (H37Rv) and the drug-resistant strain (MDR11), as detailed in **Tables 5.1** and **5.2**. These obtained MIC values can be used to determine their safety in biomedical applications, marking a significant step in developing and evaluating new antimicrobial agents.

5.3.2. Intracellular killing of Susceptible Mtb, H37Rv in THP-1 activated Macrophages

The efficacy of formulated nanoparticles was investigated using THP-1-activated macrophage cells infected with the H37Rv Mtb strain. The formulations consisted of encapsulated nanoparticles containing either RIF or VITD3, with each formulation standardised to contain 3.2 µg/ml of the respective drug (RIF/VITD3), as shown in **Table 5.3**. Additionally, the response of the infected cells was evaluated when treated with formulated nanoparticles against standard RIF treatment at a concentration of 50 µg/ml, approximately ten times higher than the MIC determined in **Tables 5.1** and **5.2** of RIF standard at 7 days from **Section 5.3.1**. The intracellular survival of M. tuberculosis H37Rv in infected cells was monitored by enumerating colony-forming units (CFU/ml) after 5 days of incubation, with results shown in **Figure 5.1** and **Table 5.4.**

Table 5.3: Concentration of nanoparticles and drug equivalent concentration used to treat H37Rv-infected THP-1 cells.

Formulation	Treatment Conc. (µg/ml)	Drug Equiv. Conc. (µg/ml)

RIF Std	50	-
VITD3 Std	100	-
S1: CS-PCL	25	-
S2: CS-PCL-VITD3	108	3.2
S3: CS-PCL-RIF	70	3.2
S4: Glu-CS-PCL-VITD3	124	3.2
S5: Glu-CS-PCL-RIF	107	3.2
S6: S2 + S3	180	3.2
S7: S4 + S5	230	3.2

Treatment of activated THP-1 macrophages infected with Mtb H37Rv with the different formulated nanoparticles showed that formulations S3-S7 displayed significant bactericidal activity compared to the untreated groups after five incubation days (**Figure 5.1)**. CS-PCL (S1) (2.15E+05 CFU/mL) nanoparticles exhibited comparable CFU counts to the untreated group (2.15E+05 CFU/mL), indicating that the nanoparticles alone lack significant antibacterial efficacy against Mtb H37Rv-infected THP-1 cells. CS-PCL-VITD3 (7.85E+04 CFU/mL) displayed a notable divergence from the antibacterial activity of CS-PCL (**Figure 5.1** and **Table 5.4)**. While RIF (3.27E+03 CFU/mL) showed higher potency against the bacterial load in CS-PCL-VITD3 treated cells, CS-CPC-VITD3 exhibited a significant ($p < 0.005$) reduction in CFUs compared to the untreated group (Day 5) and CS-PCL, suggesting that the presence of VITD3 in CS-PCL-VITD3 contributes to the antibacterial activity compared to CS-PCL and untreated group.

Although VITD3 displayed a higher MIC (50 µg/mL) compared to RIF (0.003 µg/mL), it showed almost comparable bactericidal activity as RIF in infected THP-1 cells, with CFU counts of 4.60E+03 CFU/mL and 3.27E+03 CFU/mL, respectively (**Figure 5.1)**. This indicates that VITD3 can potentiate bactericidal mechanisms within macrophages (Khoza et al., 2022, Nouari et al., 2016, Cervantes et al., 2019), which was further confirmed with CS-PCL-VITD3, which contained a far lower concentration of VITD3 (3.2 µg/mL) but still showed a significant reduction in CFU compared to the untreated group (**Figure 5.1**). The underlying mechanisms are likely multifaceted, involving the induction of antimicrobial peptides, RONS production, autophagy, and modulation of cytokine responses, which collectively enhance bactericidal activity and promote programmed cell death in infected macrophages as observed in **Section**

4.3, where VITD3 showed a significant increase in ROS production and other cytokine compared to CS-PCL in RAW 264.7 Cells (Lee and Bhakta, 2021, Khoza et al., 2022, Wu et al., 2022). This was supported by a previous study that showed that VITD3 significantly enhanced the macrophage phagocytosis of live Mtb in normal subjects with low phagocytic potential, which can subsequently lead to bacterial clearance (Chandra et al., 2004).

Addressing potential cytotoxicity concerns, the concentration of VITD3 within CS-PCL-VITD3 nanoparticles was 3.2 µg/mL. This concentration is significantly lower than levels previously shown to be non-toxic, as demonstrated by MTT assays done in this study where macrophage survival exceeded 100% when treated with 145 µg/ml of VITD3 (**Section 3.2.11**), approximately 45 times higher than the concentration within the CS-PCL-VITD3 nanoparticles. Therefore, the observed antibacterial activity of CS-PCL-VITD3, relative to CS-PCL and the untreated group, can be solely attributed to the presence of VITD3 rather than any cytotoxic effects of VITD3. These findings support the hypothesis that VITD3 enhances the bactericidal activity of cells in THP-1 macrophages infected with Mtb H37Rv. The data suggest that the formulation's efficacy is driven by VITD3's ability to enhance innate immune responses within macrophages, offering a promising avenue for adjunctive therapy in tuberculosis treatment (Khoza et al., 2022, Chun et al., 2011, Cervantes et al., 2019).

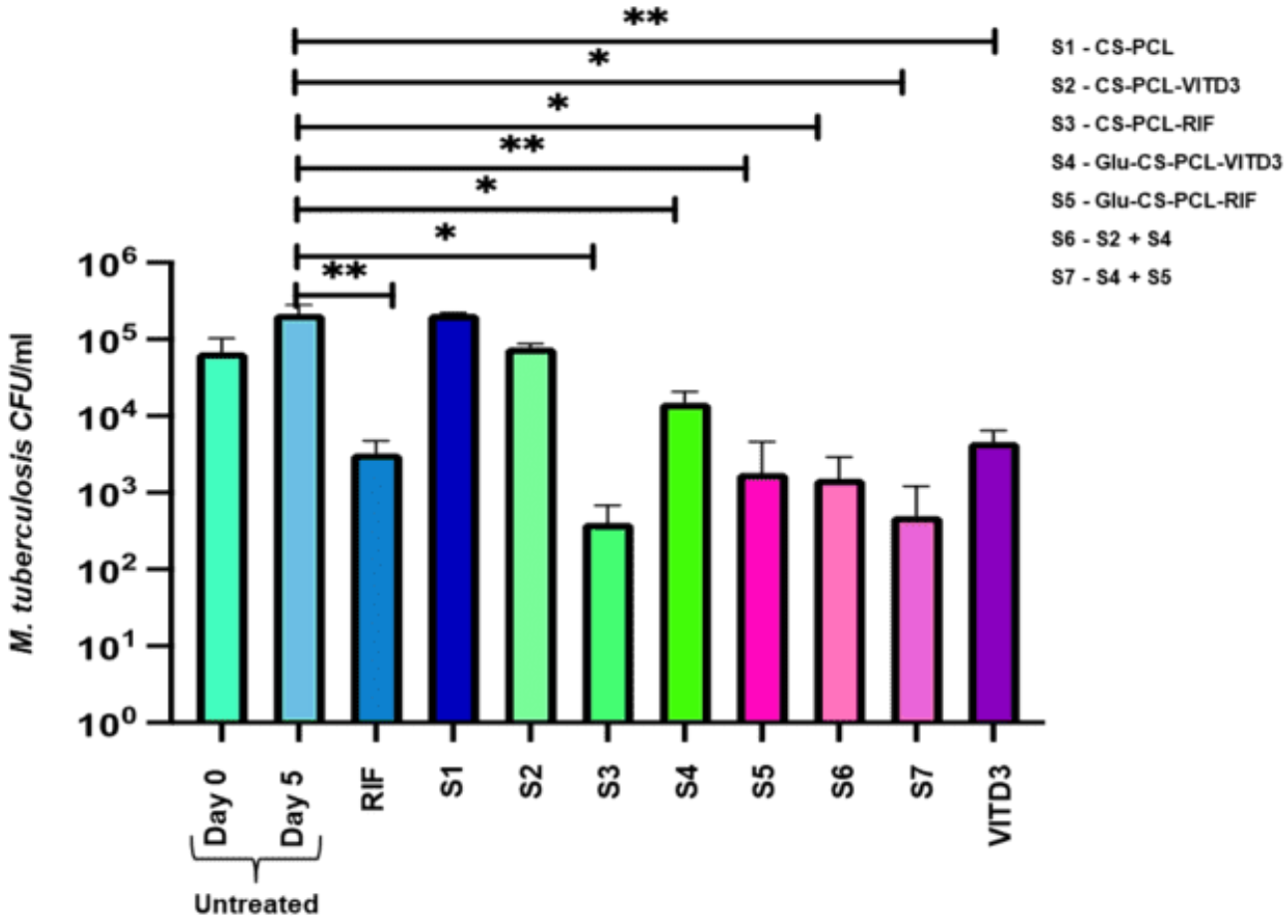

Figure 5.1: Intracellular survival of *M. tuberculosis* H37Rv in macrophages. Activated THP1 cells were infected with H37Rv bacterial cells and treated with 7 different formulations. Rifampicin was included as the control. Survival was monitored by enumerating colony-forming units (CFU/ml) after 5 days of incubation. Data is presented as mean ± SD. Statistical significance compared to the control is indicated as ** (Highly significant, $p < 0.05$), * (significant, $p > 0.05$).

CS-PCL-RIF exhibited significantly higher bactericidal activity than the standard RIF treatment, as evidenced by the Mtb CFU counts in **Figure 5.1** and **Table 5.4**, showing values of 4.05E+02 and 3.27E+03 CFU/mL, respectively. This enhanced activity is primarily due to RIF, a well-known bactericidal agent. However, it is crucial to highlight that the standard RIF concentration used to treat the cells was 50 µg/mL, approximately 15 times higher than the RIF concentration encapsulated within the CS-PCL-RIF nanoparticles (**Table 5.3**). The superior efficacy of CS-PCL-RIF, despite its lower RIF concentration, can be attributed to the presence of chitosan in the nanoparticle formulation. As previously discussed in **Section 5.3.1**, Chitosan enhances the antimicrobial efficacy of CS-PCL-RIF through its inherent antimicrobial

properties. This polycationic polymer interacts with bacterial cell membranes, disrupting their integrity and resulting in cell death (Yan et al., 2021, Ke et al., 2021). This interaction is facilitated by the electrostatic attraction between the positively charged chitosan and the negatively charged bacterial cell walls, which enhances the permeability of the bacterial membrane and allows the RIF to be more effective at lower concentrations (Meng et al., 2021). Furthermore, nanoparticles provide several advantages that can contribute to the observed synergistic effect, leading to increased RIF bioavailability within the cells. The nano-carrier or nanoparticles ensure better delivery and sustained drug release, enhancing its interaction with the bacterial cells and macrophages; this may further minimise drug degradation, resulting in more efficient bacterial killing (Patra et al., 2018, Rajendran et al., 2024).

A similar observation was made with Glu-CS-PCL-RIF nanoparticles, which showed CFU counts of 1.81E+03 CFU/mL. Compared to the standard RIF treatment, the reduced bacterial load in samples treated with CS-PCL-RIF and Glu-CS-PCL-RIF nanoparticles underscores the potential of nanoparticle-based drug delivery systems in enhancing the efficacy of conventional antibiotics. Using chitosan-based nanoparticles as a delivery vehicle not only improves the stability and bioavailability of RIF but also enhances its intrinsic antimicrobial properties, providing a dual mechanism of action. This dual action involves both the direct antibacterial effects of chitosan and the improved delivery and effectiveness of the encapsulated RIF. Consequently, these synergistic effects compensate for the lower dosage of RIF within the nanoparticles, leading to enhanced bactericidal activity, as observed in **Figure 5.1**. This approach offers a promising strategy to improve TB treatment outcomes by optimising drug delivery and reducing the required dosage of antibiotics, potentially mitigating side effects and combating antibiotic resistance.

Table 5.4: Intracellular Survival of M. tuberculosis H37Rv in THP-1 Macrophages like cells Treated with Various Nanoparticle Formulations.

Treatment	***Mtb* CFU/ml**	**Standard Error of the Mean (SME)**	**Standard Deviation (SD)**
Untreated (Day 0)	6,80E+04	5,00E+04	3,54E+04
	2,15E+05	9,00E+04	6,36E+04

Untreated (Day 5)			
Rifampicin (RIF)	3,27E+03	2,61E+03	1,50E+03
VITD3	4,60E+03	3,16E+03	1,82E+03
S1: CS-PCL	2,15E+05	1,00E+04	7,07E+03
S2: CS-PCL-VITD3	7,85E+04	1,30E+04	9,19E+03
S3: CS-PCL-RIF	4,05E+02	3,90E+02	2,76E+02
S4: Glu-CS-PCL-VITD3	1,08E+04	8,00E+03	5,66E+03
S5: Glu-CS-PCL-RIF	1,81E+03	4,80E+03	2,77E+03
S6: S2 + S3	1,53E+03	1,95E+03	1,38E+03
S7: S4 + 5	1,00E+03	1,00E+03	7,07E+02

When infected cells were treated with functionalised nanoparticles (Glu-CS-PCL-VITD3), higher bactericidal activity was observed compared to the treatment with non-functionalized CS-PCL-VITD3 nanoparticles containing VITD3, as observed in **Figure 5.1** and **Table 5.4**. This was demonstrated by Mtb CFU counts of 1.08E+04 for Glu-CS-PCL-VITD3 and 7.85E+04 for CS-PCL-VITD3. The superior bactericidal activity observed with Glu-CS-PCL-VITD3 can be attributed to the successful functionalisation of the nanoparticles with 1,3-β-glucan. 1,3-β-glucan is a polysaccharide found in the cell walls of various pathogens, including Mtb, and is recognised by Dectin receptors, such as Dectin-1, on macrophages (Wright et al., 2011, Kalscheuer et al., 2019, Khoza et al., 2022). These receptors play a crucial role in the immune response by recognising β-glucans and triggering phagocytosis (Atri et al., 2018, Liu et al., 2017); thereby, functionalising nanoparticles with 1,3-β-glucan, this mechanism is exploited to enhance the uptake of nanoparticles by macrophages, allowing the nanoparticles to mimic the structure of pathogens, facilitating their recognition and internalisation by macrophages (Dube et al., 2014). This leads to a more efficient delivery of the nanoparticles into the macrophages, where they can release VITD3 directly into the infected cells, as shown by previous studies (Dube et al., 2014).

This targeted delivery enhances antibacterial killing within the infected macrophages' intracellular and extracellular spaces by allowing functionalised nanoparticles to interact

significantly with the bacterial peptidoglycan-arabinogalactan complex, enabling direct interaction with the extracellular and intracellular Mtb as discussed in ***Section 5.3.1*** (Kalscheuer et al., 2019). Therefore, the functionalisation of nanoparticles with 1,3-β-glucan enhances their recognition and macrophage uptake, resulting in superior bactericidal activity compared to non-functionalized nanoparticles (Glu-CS-PCL-VITD3 vs CS-PCL-VITD3) as seen in **Figure 5.1**. Furthermore, as seen in ***Section 4.4***, functionalising the nanoparticles with 1,3-β-glucan increases the production of ROS and other pro-inflammatory cytokines, which polarises the macrophages towards the M1 phenotype, responsible for bacterial killing. This enhancement is reflected in the lower CFU observed with Glu-CS-PCL-VITD3 compared to CS-PCL-VITD3. The multimodal action of the functionalised nanoparticles facilitating macrophage uptake, directly interacting with extracellular bacteria and macrophage polarisation provides a robust strategy for combating Mtb infections. This approach highlights the potential of functionalised nanoparticles in enhancing the efficacy of TB treatments by optimising drug delivery.

Formulations S6 (1.53E+03 CFU/mL) and S7 (1.00E+03 CFU/mL) exhibited comparable antibacterial activity to standard RIF treatment (3.27E+03 CFU/mL), despite the nanoparticles containing only 3.2 µg/ml of each therapeutic agent compared to 50 µg/ml in the standard RIF treatment. This underscores the advantages and superiority provided by nanoparticle delivery systems, as mentioned above. A comparison between S6 and S7 showed that S7 has a significantly higher bactericidal activity than S6, as shown in **Figure 5.1**. The notable distinction between these formulations is that S6 is a combination of non-functionalized nanoparticles, while S7 is a combination of functionalised nanoparticles with 1,3-β-glucan. This functionalisation provides significant advantages over non-functionalized nanoparticles, as described in this section. Briefly, the functionalisation with 1,3-β-glucan enhances the internalisation of nanoparticles by macrophages, leading to a higher drug payload within the cells. Moreover, the observed difference in bactericidal activity could be attributed to the synergistic effects of combining VITD3 and RIF within the treatment. VITD3 promotes autophagy within cells, leading to the enhanced bactericidal killing (Hewison, 2012), while RIF directly targets the bacteria. This dual activity enhances the overall efficacy of the nanoparticles, making the functionalised formulation (S7) particularly effective and a powerful strategy to combat Mtb infection.

5.4. Concluding remarks

The results presented in this chapter show the significant impact of the fabricated nanoparticles. The nanoparticles fabricated demonstrated impressive MIC values against both susceptible H37Rv and resistant MDR11 strains, even when encapsulating a significantly lower drug concentration than the standard RIF treatment. This highlights the advantages provided by nanoparticle formulations, particularly in enhancing drug efficacy with reduced dosages. Specifically, including 1,3-β-glucan in Glu-CS-PCL-RIF nanoparticles demonstrated enhanced bactericidal activity against the H37Rv strain of M. tuberculosis, with a remarkably low MIC compared to non-functionalized nanoparticles and the standard RIF drug. This improvement is attributed to the interaction between 1,3-β-glucan and the M. tuberculosis cell wall, allowing for more efficient drug delivery and potentiated antimicrobial action.

The MIC findings served as a baseline for determining the effective concentration to use in subsequent experiments involving THP-1-infected macrophages. In these experiments, host-directed therapies using VITD3 boosted the cells' ability to kill Mtb, as evidenced by reduced colony-forming units. This suggests that VITD3 encapsulated within the nanoparticles enhances the macrophages' immune response, leading to better bacterial clearance. Additionally, experiments using THP-1 macrophage cells revealed that 1,3-β-glucan functionalisation polarises macrophages towards the M1 phenotype, boosting their bactericidal capabilities through increased ROS production and pro-inflammatory cytokine expression (**Chapter 4**). This finding was further validated by the lower CFU counts observed in Glu-CS-PCL-VITD3 treated cells (**Current Chapter**), highlighting the dual benefit of targeted drug delivery and enhanced immune response.

These findings underscore the potential of using functionalised nanoparticles to enhance the delivery and efficacy of anti-TB therapeutics and facilitate host-directed therapy. The ability of these nanoparticles to encapsulate and effectively deliver lower concentrations of drugs like RIF and VITD3 points to a promising future in TB treatment. Furthermore, treatments that combined these nanoparticles, one encapsulating RIF and another encapsulating VITD3, showed significant promise. This suggests that developing a dual-carrier system, such as a hydrogel, could be an exciting area for future research. This dual-carrier system could optimise the delivery of two different nanoparticles and enhance the therapeutic effectiveness of both drugs, offering a more comprehensive approach to TB therapy

5.5. References

Arega, A. M., Dhal, A. K., Nayak, S. & Mahapatra, R. K. 2022. In silico and in vitro study of Mycobacterium tuberculosis H37Rv uncharacterised protein (RipD): an insight on tuberculosis therapeutics. *J Mol Model,* 28**,** 171.

Atri, C., Guerfali, F. Z. & Laouini, D. 2018. Role of Human Macrophage Polarization in Inflammation during Infectious Diseases. *Int J Mol Sci,* 19**,** 1801.

Baharlou Houreh, A., Masaeli, E. & Nasr-Esfahani, M. H. 2021. Chitosan/polycaprolactone multilayer hydrogel: A sustained Kartogenin delivery model for cartilage regeneration. *Int J Biol Macromol,* 177**,** 589-600.

Belanger, C. R. & Hancock, R. E. W. 2021. Testing physiologically relevant conditions in minimal inhibitory concentration assays. *Nat Protoc,* 16**,** 3761-3774.

Cervantes, J. L., Oak, E., Garcia, J., Liu, H., Lorenzini, P. A., Batra, D., et al. Roca, X. 2019. Vitamin D modulates human macrophage response to Mycobacterium tuberculosis DNA. *Tuberculosis (Edinburgh, Scotland),* 116S**,** S131-S137.

Chandra, G., Selvaraj, P., Jawahar, M. S., Banurekha, V. V. & Narayanan, P. R. 2004. Effect of vitamin D3 on phagocytic potential of macrophages with live Mycobacterium tuberculosis and lymphoproliferative response in pulmonary tuberculosis. *J Clin Immunol,* 24**,** 249-57.

Chitale, P., Lemenze, A. D., Fogarty, E. C., Shah, A., Grady, C., Odom-Mabey, A. R., et al. Alland, D. 2022. A comprehensive update to the Mycobacterium tuberculosis H37Rv reference genome. *Nat Commun,* 13**,** 7068.

Chun, R. F., Adams, J. S. & Hewison, M. 2011. Immunomodulation by vitamin D: implications for TB. *Expert Rev Clin Pharmacol,* 4**,** 583-91.

Day, N. J., Santucci, P. & Gutierrez, M. G. 2024. Host cell environments and antibiotic efficacy in tuberculosis. *Trends Microbiol,* 32**,** 270-279.

Dube, A., Reynolds, J. L., Law, W. C., Maponga, C. C., Prasad, P. N. & Morse, G. D. 2014. Multimodal nanoparticles that provide immunomodulation and intracellular drug delivery for infectious diseases. *Nanomedicine : nanotechnology, biology, and medicine,* 10**,** 831-8.

Gu, X., Cheng, Q., He, P., Zhang, Y., Jiang, Z. & Zeng, Y. 2021. Dihydroartemisinin-Loaded Chitosan Nanoparticles Inhibit the Rifampicin-Resistant Mycobacterium Tuberculosis by Disrupting the Cell Wall. *Front Microbiol,* 12**,** 735166.

Hewison, M. 2012. Vitamin D and immune function: an overview. *Proc Nutr Soc,* 71**,** 50-61.

Jankute, M., Cox, J. A., Harrison, J. & Besra, G. S. 2015. Assembly of the Mycobacterial Cell Wall. *Annu Rev Microbiol,* 69**,** 405-23.

Kalscheuer, R., Palacios, A., Anso, I., Cifuente, J., Anguita, J., Jacobs, W. R., Jr., et al. Prados-Rosales, R. 2019. The Mycobacterium tuberculosis capsule: a cell structure with key implications in pathogenesis. *Biochem J,* 476**,** 1995-2016.

Kana, B. D., Mizrahi, V. & Gordhan, B. G. 2010. Depletion of resuscitation-promoting factors has a limited impact on the drug susceptibility of Mycobacterium tuberculosis. *The Journal of antimicrobial chemotherapy,* 65**,** 1583-5.

Ke, C. L., Deng, F. S., Chuang, C. Y. & Lin, C. H. 2021. Antimicrobial Actions and Applications of Chitosan. *Polymers,* 13**,** 904.

Khoza, L. J., Kumar, P., Dube, A., Demana, P. H. & Choonara, Y. E. 2022. Insights into innovative therapeutics for drug-resistant tuberculosis: Host-directed therapy and autophagy inducing modified nanoparticles. *International journal of pharmaceutics,* 622**,** 121893.

Kowalska-Krochmal, B. & Dudek-Wicher, R. 2021. The Minimum Inhibitory Concentration of Antibiotics: Methods, Interpretation, Clinical Relevance. *Pathogens (Basel, Switzerland),* 10.

Lee, C. & Bhakta, S. 2021. The Prospect of Repurposing Immunomodulatory Drugs for Adjunctive Chemotherapy against Tuberculosis: A Critical Review. *Antibiotics (Basel),* 10**,** 91.

Liu, C. H., Liu, H. & Ge, B. 2017. Innate immunity in tuberculosis: host defense vs pathogen evasion. *Cell Mol Immunol,* 14**,** 963-975.

Meng, Q., Sun, Y., Cong, H., Hu, H. & Xu, F. J. 2021. An overview of chitosan and its application in infectious diseases. *Drug Deliv Transl Res,* 11**,** 1340-1351.

Nouari, W., Ysmail-Dahlouk, L. & Aribi, M. 2016. Vitamin D3 enhances bactericidal activity of macrophage against Pseudomonas aeruginosa. *Int Immunopharmacol,* 30**,** 94-101.

O'neill, A. J. & Chopra, I. 2004. Preclinical evaluation of novel antibacterial agents by microbiological and molecular techniques. *Expert Opin Investig Drugs,* 13**,** 1045-63.

Patankar, Y. R., Sutiwisesak, R., Boyce, S., Lai, R., Lindestam Arlehamn, C. S., Sette, A. & Behar, S. M. 2020. Limited recognition of Mycobacterium tuberculosis-infected macrophages by polyclonal CD4 and CD8 T cells from the lungs of infected mice. *Mucosal Immunol,* 13**,** 140-148.

Patra, J. K., Das, G., Fraceto, L. F., Campos, E. V. R., Rodriguez-Torres, M. D. P., Acosta-Torres, L. S., et al. Shin, H. S. 2018. Nano based drug delivery systems: recent developments and future prospects. *J Nanobiotechnology,* 16**,** 71.

Prabhu, P., Fernandes, T., Chaubey, P., Kaur, P., Narayanan, S., Vk, R. & Sawarkar, S. P. 2021. Mannose-conjugated chitosan nanoparticles for delivery of Rifampicin to Osteoarticular tuberculosis. *Drug Deliv Transl Res,* 11**,** 1509-1519.

Rajendran, S., Ravi, S. N., Nair, V. M., Sree, R. P., Packirisamy, A. S. B. & Palanivelu, J. 2024. Recent Development and Future Aspects: Nano-Based Drug Delivery System in Cancer Therapy. *Topics in Catalysis,* 67**,** 203-217.

Rajput, A., Mandlik, S. & Pokharkar, V. 2021. Nanocarrier-Based Approaches for the Efficient Delivery of Anti-Tubercular Drugs and Vaccines for Management of Tuberculosis. *Front Pharmacol,* 12**,** 749945.

Ramon-Luing, L. A., Carranza, C., Téllez-Navarrete, N. A., Medina-Quero, K., Gonzalez, Y., Torres, M. & Chavez-Galan, L. 2022. Mycobacterium tuberculosis H37Rv Strain Increases the Frequency of CD3+TCR+ Macrophages and Affects Their Phenotype, but Not Their Migration Ability. *International Journal of Molecular Sciences,* 23**,** 329.

Shirzaei Sani, I., Rezaei, M., Baradar Khoshfetrat, A. & Razzaghi, D. 2021. Preparation and characterization of polycaprolactone/chitosan-g-polycaprolactone/hydroxyapatite electrospun nanocomposite scaffolds for bone tissue engineering. *Int J Biol Macromol,* 182**,** 1638-1649.

Strizova, Z., Benesova, I., Bartolini, R., Novysedlak, R., Cecrdlova, E., Foley, L. K. & Striz, I. 2023. M1/M2 macrophages and their overlaps - myth or reality? *Clinical science (London, England : 1979),* 137**,** 1067-1093.

Theus, S. A., Cave, M. D. & Eisenach, K. D. 2004. Activated THP-1 cells: an attractive model for the assessment of intracellular growth rates of Mycobacterium tuberculosis isolates. *Infect Immun,* 72**,** 1169-73.

Wright, W. F., Overman, S. B. & Ribes, J. A. 2011. (1–3)-β-D-Glucan Assay: A Review of its Laboratory and Clinical Application. *Laboratory Medicine,* 42**,** 679-685.

Wu, Y., Lin, X., Song, F., Xue, D. & Wang, Y. 2022. Vitamin D3 promotes autophagy in THP-1 cells infected with Mycobacterium tuberculosis. *Exp Ther Med,* 23**,** 240.

Yan, D., Li, Y., Liu, Y., Li, N., Zhang, X. & Yan, C. 2021. Antimicrobial Properties of Chitosan and Chitosan Derivatives in the Treatment of Enteric Infections. *Molecules,* 26**,** 7136.

CHAPTER 6

INTEGRATION OF NANOPARTICLES WITH A MODEL THERMOGEL: A DUAL-THERMORESPONSIVE NANOCOMPOSITE DELIVERY SYSTEM

6.1. Introduction

In the previous chapter (**5**), different nanoparticles containing RIF or VITD3 were tested for their antibacterial effects. The findings demonstrated that these nanoparticles are highly effective when used together or when cells are treated with both simultaneously. This synergistic effect suggests that developing a dual carrier to deliver both nanoparticles, those encapsulating RIF and those containing VITD3, would be beneficial. Such a dual carrier could allow for a prolonged and sustained release of these nanoparticles and their bioactives, like a thermogel. Each nanoparticle offers a distinct mechanism: VITD3 nanoparticles contribute to host-directed therapy through immunomodulation, while RIF nanoparticles provide targeted killing of the Mtb bacteria.

Hydrogels, three-dimensional networks of hydrophilic polymers, have emerged as a revolutionary material in the biomedical field and as drug-delivery systems (Liu and Chen, 2024). Their unique ability to absorb and retain substantial amounts of water while maintaining their structure makes them highly versatile (Kesharwani et al., 2021). Hydrogels' inherent biodegradability and non-toxicity make them attractive for medical applications, ensuring compatibility with biological tissues and minimising adverse effects (Kesharwani et al., 2021). These properties enable hydrogels to serve as effective carriers for therapeutic agents, providing a prolonged and sustained release of drugs compared to nanoparticles alone (Liu and Chen, 2024, Ahmad et al., 2024). When combined with nanoparticles, hydrogels create an advanced delivery platform that synergises the benefits of both materials (Ahmad et al., 2024). This combination enhances nanoparticles' stability and targeting capabilities while leveraging the extended-release profile of hydrogels (Ahmad et al., 2024). As a result, these hybrid systems offer improved therapeutic efficacy, reduced frequency of drug administration, and better patient compliance (Ezike et al., 2023).

One of the highly sought-after advantages of hydrogels is their remarkable thermoresponsive ability, representing a significant advancement in drug delivery due to their unique ability to transition from a solution at room temperature to a gel at body temperature (Shen et al., 2021).

This property is advantageous for minimally invasive drug administration, as the hydrogel can be easily injected in its liquid form and then solidify upon reaching the target site, forming a stable depot for sustained drug release (Sun et al., 2020, Liu and Chen, 2024). By forming a gel at body temperature, these hydrogels can effectively encapsulate and protect both the drugs and the nanoparticles from premature degradation, thereby maintaining their efficacy over an extended period (Nunes et al., 2022, Ahmad et al., 2024). Moreover, the gel matrix provides a sustained release profile, reducing the need for frequent dosing and improving patient compliance, as previously stated (Ezike et al., 2023). The thermoresponsive nature of these hydrogels also offers the potential for on-demand drug release, where temperature changes can trigger the release of the drug, allowing for dynamic and responsive treatment options (Askari et al., 2020). Overall, thermoresponsive hydrogels offer a versatile and efficient platform for enhancing the delivery and efficacy of various therapeutic agents.

Therefore, in this chapter, the nanoparticles synthesised and tested in previous **chapters (3-5)** are now integrated into a Model Thermogel made of Pluronic, a widely known polymer. Pluronic, also known as poloxamer, is renowned for its thermoresponsive properties, biocompatibility, and ease of use in biomedical applications (Russo and Villa, 2019). Pluronic polymer remains liquid at room temperature, facilitating easy mixing and injection, and transitions into a hydrogel upon exposure to body temperature, providing a stable matrix for sustained and controlled drug release (Russo and Villa, 2019). Integrating nanoparticles into this Pluronic-based hydrogel leverages the combined advantages of both systems and both RIF and VITD3 Nanoparticles: the targeted delivery, host-directed therapy, and enhanced stability of nanoparticles, along with the prolonged and controlled release properties of the thermogel. This chapter will explore integrating and characterising these nanoparticle-hydrogel composites, their potential applications, and their performance as a drug delivery system, emphasising their improved efficacy, stability, and compatibility.

6.2. Materials and Methods

6.2.1. Materials

Polycaprolactone (Mn 80,000), chitosan oligosaccharide lactate (CS, Mn 5, 000 Da), Cholecalciferol (Vitamin D3, MW; 384.64), Rifampicin (RFP, MW;822.94), β-1,3-Glucan from Euglena gracilis, poly(vinyl alcohol, 87-90% hydrolysed, MW; 30 000-70 000), Pluronic® (F-127 and F-68), and phosphate-buffered saline (PBS) were all purchased from Sigma-Aldrich

(St. Louise, MO, USA). Dichloromethane (DCM) and methanol were procured from Merck (Pty Ltd., South Africa). RAW 264.7 cell line was procured from Separation Scientific Pty Ltd (Johannesburg, SA). 3-(4,5-dimethylthiazole-2-yl)-2,5-diphenyl tetrazolium bromide (MTT) assay Kit (MTT Cell Proliferation Kit I, Roche, Basel, Switzerland) was purchased from Sigma-Aldrich (St. Louise, MO, USA). All chemicals were of analytical reagent grade and were used without prior modification. Double deionised water (DDW) was used for all the preparations.

6.2.2. Preparation of pure and Pluronic nanocomposite Thermogel

The Pluronic Thermogel blend was synthesised following a modified cold method (Cidade et al., 2019). F127 (30%) and F68 (10%) were mixed in the required amount of DDW while stirring gently. The mixture was then kept in the refrigerator for about 24-48 hours to dissolve until a homogeneous solution was formed fully. For nanoparticles (*See **Chapter 3** for nanoparticle synthesis)* incorporation into the hydrogel, 10% and 20% of the nanoparticle solution was slowly dispensed into the hydrogel solution dropwise while stirring gently under an ice bath for approximately 1 hour. The mixture was then left in the refrigerator for 24-48 hours before further analysis and freeze-drying where required.

6.2.3. Morphological analysis

The morphological surface of the pure thermogel and nanocomposite was determined by employing Scanning electron Microscopy (SEM) analysis (SIGMA VP, Zeiss Electron Microscopy, Carl Zeiss Microscopy Ltd; Cambridge, UK). A pure hydrogel and nanocomposite suspension drop was placed on a metallic sample stub and left to completely air dry before sputter-coating (x2) with gold-palladium (AuPd). Each sample was observed under different magnifications at an accelerated voltage of 20 kV for SEM.

6.2.4. Evaluation of Fourier transform infrared spectroscopy of the Nanocomposite

The Fourier Transform Infrared (FTIR) spectra of different powdered samples were analysed for specific interactions between pristine polymers (F-127 and F-68), nanoparticles, pure thermogel and nanocomposite using a 2000 ATR-FTIR (PerkinElmer Inc., Spectrum 100, Waltham, MA, USA) spectrophotometer fitted with a single-reflection diamond MIRTGS detector with the wavelength ranging between 4000-650 cm^{-1} and a 4 cm^{-1} resolution.

6.2.5. X-ray powder diffraction (XRPD) analysis

The degree of crystallinity of the starting materials, nanoparticles, pure thermogel and nanocomposite samples were evaluated by benchtop XRPD (Rigaku Mini Flex 600, Tokyo, Japan) diffractometer fortified with *CuKα* radiation at 15 mA and 40 kV. The 2θ scan range was selected between 10–90 degrees at a scan rate of 10 degrees/minute.

6.2.6. Evaluation of the thermal behaviour of the optimised samples

The thermogel and nanocomposite's thermal stability and decomposition temperature were evaluated using a Thermogravimetric analyser (TGA) (TGA 4000, PerkinElmer Inc., Waltham, MA, USA). Samples of ≥ 10 mg were placed in the TGA furnace, and the measurements were carried out under a nitrogen atmosphere with a heating rate of 10 °C/min from 30-600°C. The changes in sample weight were recorded and evaluated as a function of temperature. The thermophysical properties of the thermogel, nanocomposite and all other starting materials were determined using a differential scanning calorimeter (DSC) (Mettler Toledo, DSC, STARe System, Swchwerzenbach, ZH, Switzerland). The samples with a mass range between 5-10 mg were sealed in aluminium crucibles and heated over 20 to 400°C at a heating rate of 10°C/min under continuous nitrogen purging. DSC curves were plotted as heat flow against temperature.

6.2.7. Gelation Temperature and Dynamic Viscosity Analysis of Thermogel Formulations

The sol-gel transition temperature was measured using two methods adapted from Akilo and colleagues (Akilo et al., 2019). The first method was an evaluation by rheological analysis, which studied the dynamic viscosity of the hydrogel formulation. This was undertaken by carrying out temperature ramp experiments, employing a thermostatically controlled (UTC-MARS II) Modular Advanced Rheometer System (Thermo Scientific HAAKE MARS, Thermo Fischer Scientific, Karlsruhe, Germany) fitted with a cone and plate geometry with a diameter of 3.5 cm and cone angle of 1° (sensor C35/1°) Ti at a temperature range of 5-40°C. The elastic modulus (G') and viscous modulus (G'') were calculated using Rheology Advantage Data Analysis software. The second method visually examined the solution and hydrogel appearances (transparency and opacity), gelation occurrences, and gelation time using the test tube inversion method. About 2~3 mL of the sample was placed in a transparent vial. The vial was then placed in a water bath heated from 15°C, with the bath temperature increasing

by 1°C/minute. The gelation temperature was measured when the formulation no longer flowed when the vial was inverted at any angle. Each formulation was repeated or tested multiple times.

6.2.8. Porosity Profile Analysis of Nanocomposite Thermogel

The lyophilised samples' pore size, volume, and surface area were analysed using a porositometric analyser. (Micrometrics ASAP 2020, Norcross, GA, USA). Each sample was introduced to the sample tube and degassed to remove any residual moisture. The samples were then analysed for surface area, pore size and pore volume following the BET and BJH models with the following experimental conditions: evacuation rate of 50mm Hg/s with a temperature ramp rate of 10°C/min, the target temperature of 115°C and held temperature at 30°C for 900 min before completing the analysis.

6.2.9. *In vitro release* of VITD3 and RIF from the Thermogel nanocomposite

The drug release profile of VITD3/RIF in the nanocomposite was evaluated using a dialysis membrane approach at three different pH values (4.6, 6.8, and 7.4). Briefly, the appropriate amount of nanocomposite solution was loaded into a dialysis tubing membrane (SnakeSkin™, 3500 MWCO) and submerged into the relevant drug release media buffer of the corresponding pH and incubated (37 ºC) in an orbital shaker (25 rpm) (YIHDER LM-530, YIHDER Co., Ltd., Taipei, Taiwan) until completion of release study. The dialysis membrane was used to facilitate only free VITD3/RIF diffusion into the release medium for assay. Sampling (2 mL) was undertaken at different time intervals. An equivalent amount of pre-warmed fresh media was replaced into the sample release media to sustain sink conditions. A nanophotometer was employed to quantify VITD3 and RIF at 265 and 335 nm, respectively, with each experiment carried out in triplicate.

6.2.10. *In vitro* cytotoxicity assay of the Thermogel nanocomposite

The effects of the pure hydrogel and nanocomposite on RAW 264.7 cell line metabolic activity and cytotoxicity were carried out using an MTT cell proliferation Kit I (MTT Cell Proliferation Kit I, Roche, Basel, Switzerland). Briefly, DMEM supplemented with 1% penicillin-streptomycin and 10% fetal bovine serum was used to culture the cells at 37°C and 5% CO_2 (in a humidified incubator). After every 48-72 hours, the spent growth medium was replenished with fresh

growth medium until the cells reached confluence. The cells at a density of $1x10^5$ per well were seeded in 96-well plates in triplicates. After 24 h, the adhered cells were treated with pure hydrogel and nanocomposite solution at different concentrations. Subsequently, the cells were incubated for 48 hours in a humidified incubator at 37°C and 5% CO_2. Following the incubation period, each well plate was then treated with 10 µL; 5 mg/mL of MTT solution and further incubated for 4 hours before being treated with 100 µL of solubilising agent (acid-isopropanol; 0.04 N HCl in isopropanol) to dissolve formed formazan crystals and subjected to further incubation overnight at same conditions as mentioned above. The absorbance of cell activity was then measured with a multimodal microplate reader (Victor X3, PerkinElmer, Waltham, MA, USA) at 570 nm with a reference wavelength of 620 nm. A parallel assay experiment comprised positive (cells treated with culture medium only), negative (cells treated with 4% v/v DMSO) control, and blank wells only containing solubilising agent and growth medium. The absorbance measurements were computed (mean ±SD) and used to calculate % cell viability using Eq. (6.1):

$$\% \text{ Cell viability} = \frac{\text{Atest} - \text{Ablank}}{\text{Acontrol} - \text{Ablank}} \times 100 \quad \text{..... (Equation 6.1)}$$

A_{test} is test absorbance, A_{blank} is blank, and $A_{control}$ is a control absorbance in nm.

6.3. Results and Discussion

6.3.1. Integrated Analysis of the Thermogel and nanocomposite: Spectroscopy, Diffraction, and Thermal properties

The functional transformation, degree of crystallinity, thermal stability, and phase transition of the formulated hydrogel and nanocomposites were analysed and presented in **Figures 6.1-6.2**. F-127 and F-68 are both types of poloxamers that contain similar functional groups but differ in molecular weights and proportions of hydrophilic polyoxyethylene (PEO) to hydrophobic polyoxypropylene (PPO) (İspir et al., 2023, Shoukat et al., 2022). Consequently, their FTIR spectra display similarities, as observed in **Figure 6.1a**. When F127 and F68 were blended to form a hydrogel, no apparent change was observed in their absorption peaks. This indicates no physical or chemical transformation between the two polymers in the blend, as shown in **Figure 6.1a**. Upon incorporating the nanoparticles synthesised and characterised in **Chapter 3** into the hydrogel, only the peaks of the hydrogel were observed in the final nanocomposite product. The absence of nanoparticle absorption peaks in the nanocomposite's spectrum suggested that the nanoparticles were distributed within the hydrogel's pores or matrix without undergoing functional or physical transformation. The peaks

for the hydrogel blend, F127, F68, and the nanocomposite were assigned as follows: 2879 cm^{-1} (CH stretching), 1342 cm^{-1} (OH in-plane bending), and 1096 cm^{-1} (C-O stretching), respectively (**Figure 6.1a**).

The crystallinity of the nanocomposite, hydrogel, and excipient materials is depicted in **Figure 6.1b.** The XRPD pattern demonstrated that the hydrogel and nanocomposites were semi-crystalline, with significant peaks at 19.07º and 23.31º. These peaks were similar to those of the excipient materials (F127 and F68), indicating the retained physical phase of the starting materials and their degree of crystallinity (Sharma et al., 2021, Li et al., 2018). The formulated nanocomposite is expected to enable sustained drug release as the literature suggests that polymers with a low degree of crystallinity have a higher drug release rate, while those with a higher degree of crystallinity exhibit a delayed, sustained drug release (Kamaly et al., 2016). Furthermore, this characteristic is advantageous because hydrogels or nanocomposites with a higher degree of crystallinity tend to provide additional mechanical strength and stability, making the hydrogel more resilient and less prone to deformation (Kaliaraj et al., 2023).

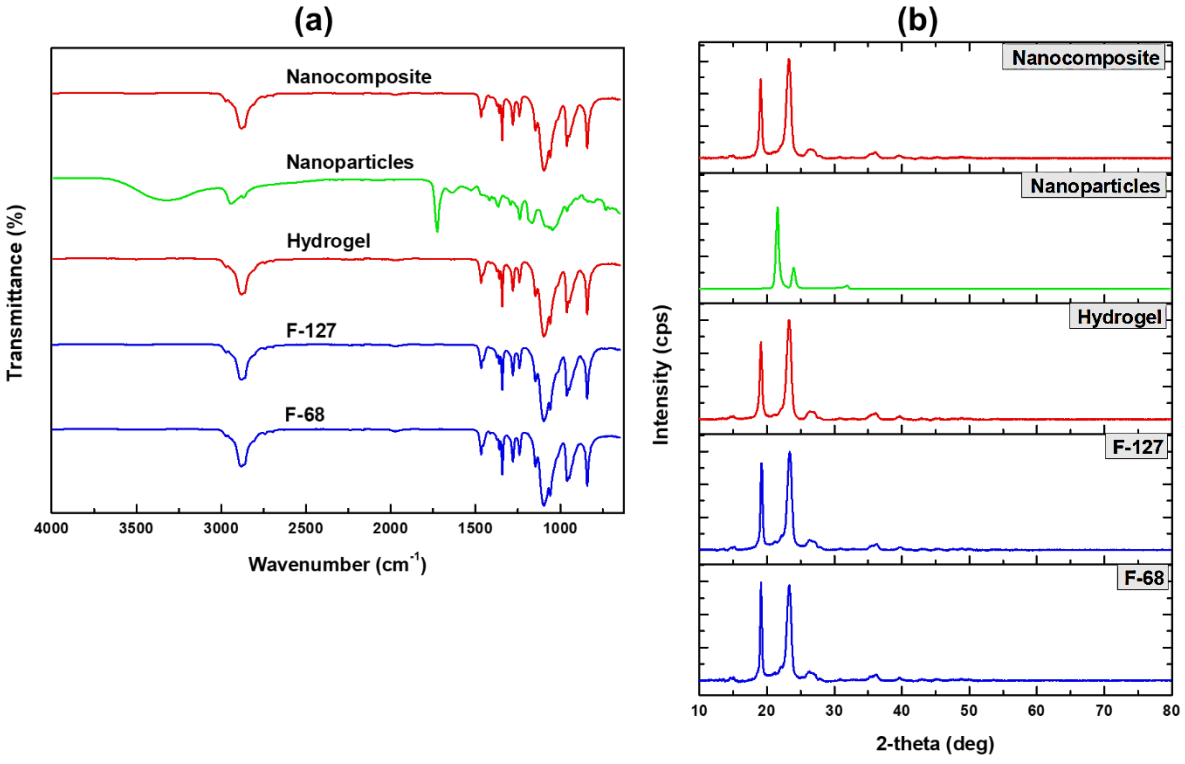

Figure 6.1: Spectroscopic and Crystallographic Analysis of the Hydrogel and Nanocomposite. **(a)** FTIR spectra of the hydrogel blend and the nanocomposite, showing similar absorption peaks at 2879, 1342, and 1096 cm^{-1} and **(b)** XRPD patterns of the nanocomposite, hydrogel and excipient materials, demonstrating semi-crystalline structures with major peaks at 19.07º

and 23.31º, indicative of retained physical phases and degree of crystallinity similar of the starting materials.

The thermal stability of the hydrogel and nanocomposite was evaluated by performing TGA. The thermal degradation temperature refers to the temperature at which the first weight loss occurs (Anju et al., 2020). **Figure 6.2a** shows the thermogravimetric curves for the different starting materials, hydrogel, nanoparticles, and nanocomposite. These curves indicated that the hydrogel and nanocomposite began to lose weight at 220-340°C, demonstrating their relatively high thermal stability compared to the nanoparticles alone, which started degrading at 60°C due to the evaporation of absorbed water or moisture content in the chitosan (Georgieva et al., 2012). DSC is typically used to ascertain changes in physical properties between the starting material and the final product. The DSC thermograms in **Figure 6.2a** showed endothermic melting peaks for the nanocomposite and hydrogel at 55.18°C and 55.14°C, respectively. These peaks are usually associated with the melting of the crystalline regions within the Pluronic polymers, indicating a transition from a semi-crystalline to an amorphous state as the crystalline domains melt (Karolewicz et al., 2017, Khaliq et al., 2023). The observed peaks for the hydrogel and nanocomposite were in the same range as those of the starting polymers, suggesting a dispersion or complete dissolution of the nanoparticles within the hydrogel's pores. This dispersion masks the thermal transitions of the nanoparticles, making them less detectable in the DSC thermogram.

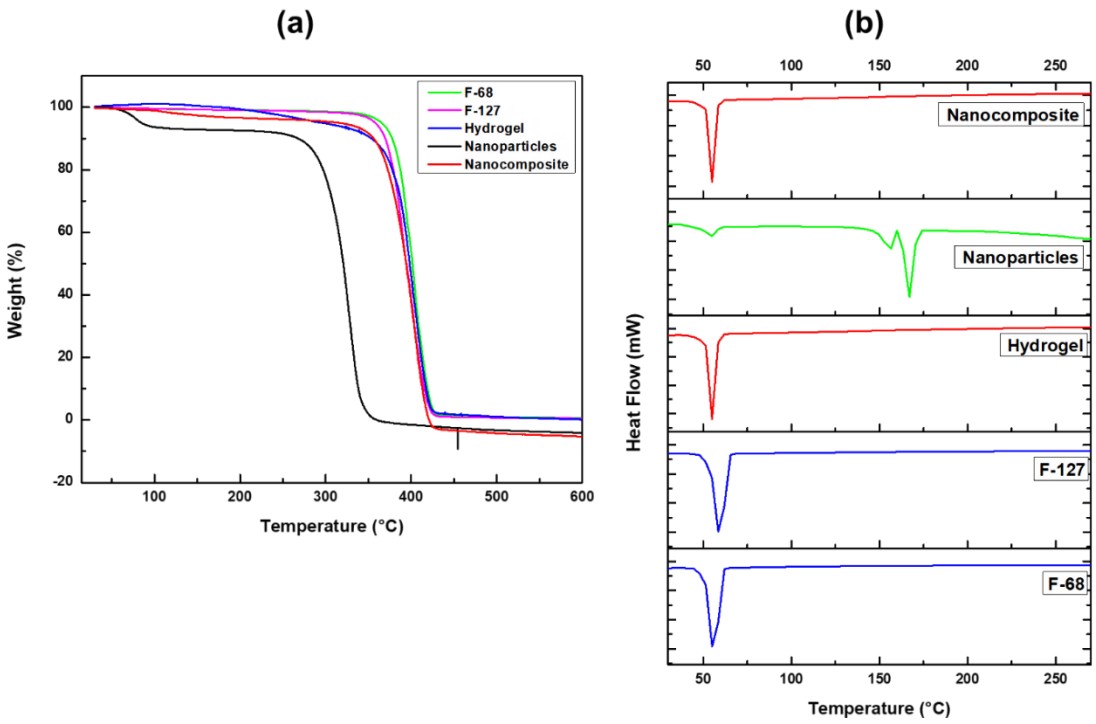

Figure 6.2: Thermal Analysis of Hydrogel and Nanocomposite. **(a)** TGA curves showing the thermal stability of the hydrogel and nanocomposite and **(b)** DSC thermograms showing the melting peaks of the hydrogel and nanocomposite at 55.18°C and 55.14°C, respectively.

6.3.2. Assessment of the Surface Morphology and Porosity of the Thermogel Nanocomposite

SEM was employed to study the surface morphology of the pure hydrogel and nanocomposite hydrogel. The SEM image of the pure hydrogel (**Figure 6.3a**) displayed an interconnected porous structure and irregular pore size. The pore walls of the pure hydrogel were thin, and the pore size was inconsistent. In contrast, the nanocomposite hydrogel (**Figure 6.3b**) exhibited significantly thicker walls with a smooth, dense, and complete surface. Furthermore, the nanocomposite surface had no visible pores due to the accumulation of nanoparticles within the segregated interior spaces of the pure hydrogel pores. This observation was corroborated by the results of the porositometric analysis, as presented in **Table 6.1** and **Figure 6.3c-d**.

The isotherm linear plots demonstrated changes in surface area, pore volume, and pore size between the pure hydrogel and the nanocomposite hydrogel (**Table 6.1**). The linear plots were classified as type IV isotherm with H1 hysteresis loop following classifications outlined by K

Sing and others (Sing, 1985, Cychosz and Thommes, 2018). Pore size, volume and surface area were determined using the Brunauer–Emmett–Teller (BET) and Barrett-Joyner-Halenda (BJH) adsorption and desorption profiles, employing the technique of relative adsorption of N_2 gas. The isotherms provided important information regarding pore size distribution in terms of pore width, categorised as micropores (< 2 nm), mesopores (2–50 nm), and macropores (> 50 nm) ranges (Sing, 1985, Groen et al., 2003). Based on this classification, the pore size distribution of the pure hydrogel lies within the macropore range, while that of the nanocomposite hydrogel lies within the mesoporous range. These results supported the observations of the SEM analysis, showing the decrease in pores available. However, it should be noted that the classical BJH model significantly underestimates the actual pore size. However, it remains widely used to characterise porous materials (Groen et al., 2003, Cychosz and Thommes, 2018, Horvat et al., 2022).

Table 6.1: Porositometric analysis summarised the pure thermogel blend and thermogel nanocomposite results.

Formulation	**Surface Area**	**Pore volume**	**Pore size**		
	Single point surface area at P/Po = 0.200169078	Single point adsorption total pore volume of pores less than 783.135 Å diameter at P/Po = 0.974645588	Adsorption average pore width (4V/A by BET): (nm)	BJH adsorption average pore diameter (4V/A): (nm)	BHJ desorption average pore diameter (4V/A): (nm)
Pure Hydrogel	0.5284 m^2/g	0.003611 cm^3/g	50.3717	26.8947	23.0159
Nanocomposite	1.8106 m^2/g	0.004086 cm^3/g	6.06605	19.0655	13.1365

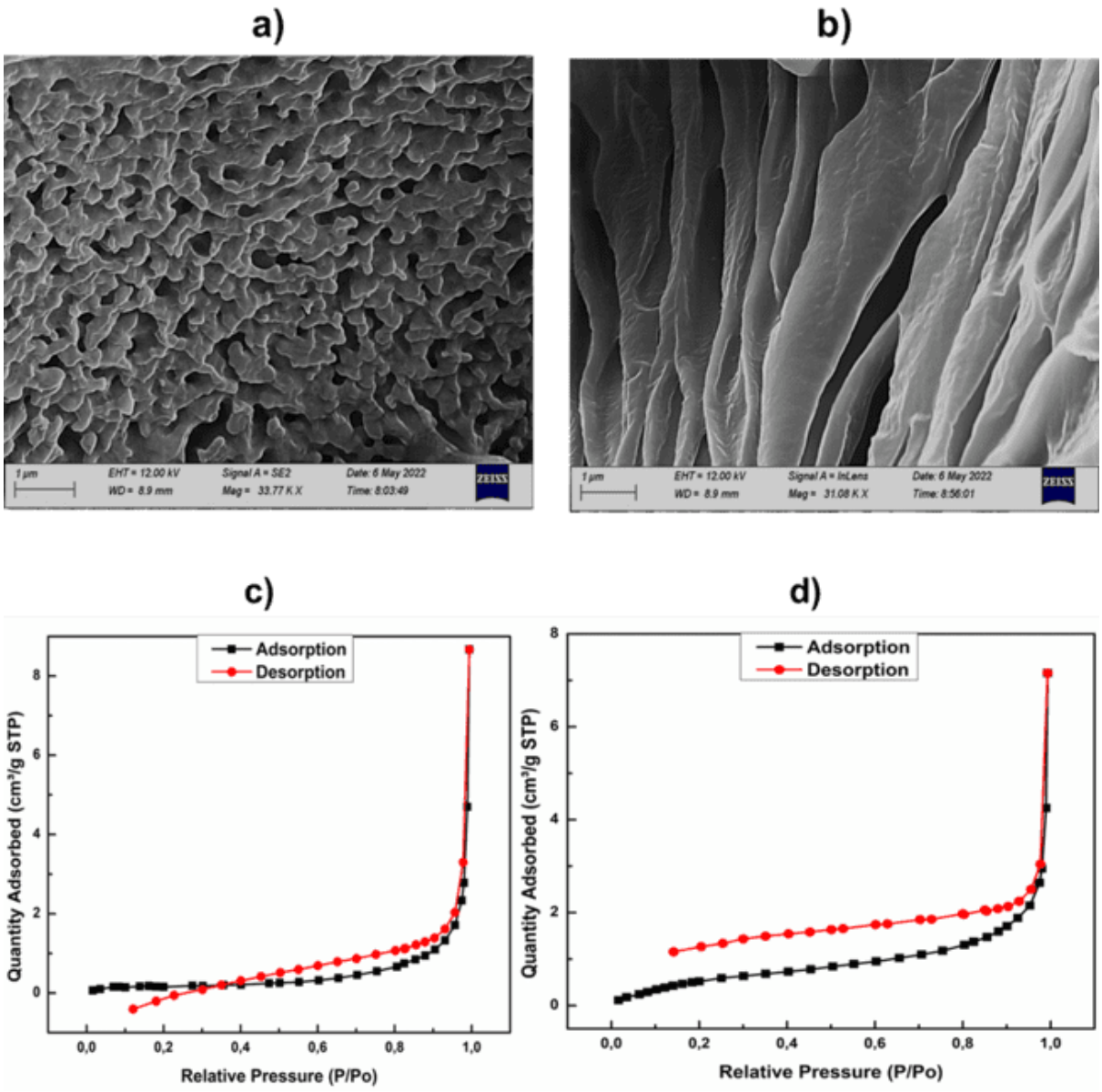

Figure 6.3: Surface Morphology and Isotherm Analysis of Hydrogel and Nanocomposite. SEM images showing the surface morphology of **(a)** pure hydrogel and **(b)** nanocomposite hydrogel; Isotherm linear plots of **(c)** pure hydrogel before incorporation with nanoparticles and **(d)** nanocomposite hydrogel, indicating changes in adsorption and Desorption due to nanoparticle incorporation.

6.3.3. Gelation Temperature and Dynamic Viscosity Analysis

The gelation temperature is the temperature at which a material transitions from a liquid phase to a solid phase (sol-gel phase transition). The sol-gel transition for the hydrogel and nanocomposite was measured by rheological temperature run analysis (**Figure 6.4**) and the

test-tube inversion technique (**Figure 6.5a**). This method determines the gelation temperature by observing the temperature at which there is a significant change or transition in the sol-gel properties of the materials (Stojkov et al., 2021). **Figure 6.4** shows a rheogram plot of storage modulus (G') and loss modulus (G'') viscosity against temperature on the same plot. The temperature at the crossover point, where the curve of G' crosses the curve of G'', is the gelling temperature (Stojkov et al., 2021). This point, illustrated in **Figure 6.4**, represents the significant phase transition from the sol to the gel state. The gelling temperature determined from the rheogram was 25°C for the pure hydrogel and 30°C for the nanocomposite containing 10% of the nanoparticles.

The gelling temperature increased with the incorporation of more nanoparticles, as seen in **Figure 6.5b**. A new crossover point was observed at 34°C when the nanoparticle concentration was increased to 20%. The observed increase in gelling temperature with the addition of nanoparticles indicates that the presence of nanoparticles affects the thermal and mechanical properties of the hydrogel. The nanoparticles likely interact with the polymer network, enhancing the structural integrity and cross-linking (Yeh et al., 2017). More cross-linking points mean a more stable gel structure, as the increased G' observed in **Figure 6.4** indicates. This enhanced stability requires a higher temperature to achieve the sol-gel transition, as seen by a shift in gelling temperature in **Figure 6.4** (Yeh et al., 2017). In addition, the incorporation of nanoparticles increases the overall viscosity of the hydrogel. This higher viscosity implies that the hydrogel matrix becomes more resistant to flow and deformation; as a result, more energy in the form of heat is required to overcome this resistance and induce the transition from a liquid to a gel state (Unal et al., 2023).

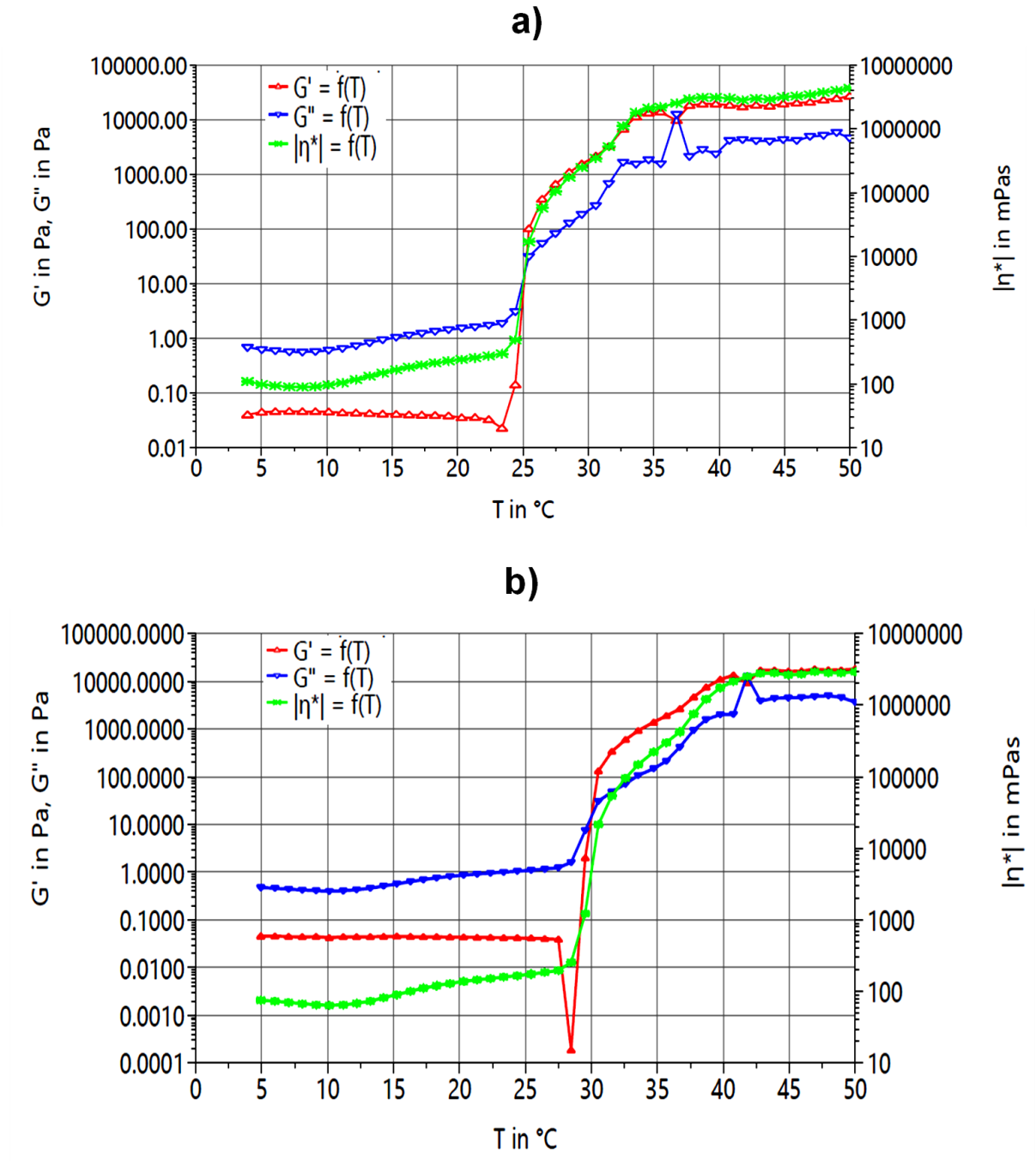

Figure 6.4: Shows elastic modulus rheogram as a function of temperature and gelation temperature for **(a)** Pure Pluronic hydrogel and **(b)** nanocomposite hydrogel containing 10% of nanoparticles.

The increased viscosity of the hydrogel due to nanoparticle incorporation was further confirmed by graphically determining the temperature at which the apparent viscosity curve begins to plateau when plotted against temperature (**Figure 6.4**). This plateau indicates the point at which the hydrogel transitions into a gel state, requiring more energy (heat) to

overcome the increased resistance due to the higher viscosity (Unal et al., 2023). Following the rheological gelation temperature measurement, the gelling ability and sol-gel transition temperature of the hydrogel and nanocomposite were further confirmed using the test tube inversion method. In this method, the gelation temperature was recorded as the temperature at which the hydrogel and nanocomposite solution stopped flowing when the vial was inverted at any angle (**Figure 6.5a-b**). The test tube inversion method results correlated well with the rheological data, as reported in **Figure 6.4**.

This behaviour suggests that the nanocomposite hydrogel has a tuneable gelation temperature, which can be adjusted by varying the concentration of nanoparticles, as seen in **Figure 6.4** and **Figure 6.5**. This property is beneficial for applications requiring specific gelation temperatures. Controlling the gelation temperature through nanoparticle incorporation opens possibilities for designing hydrogels with tailored properties for specific applications. For instance, a higher gelling temperature could enhance the stability of the hydrogel at body temperature, making it more suitable for sustained-release applications (Bellotti et al., 2021). Conversely, a lower gelling temperature might benefit applications requiring quick gelation upon administration.

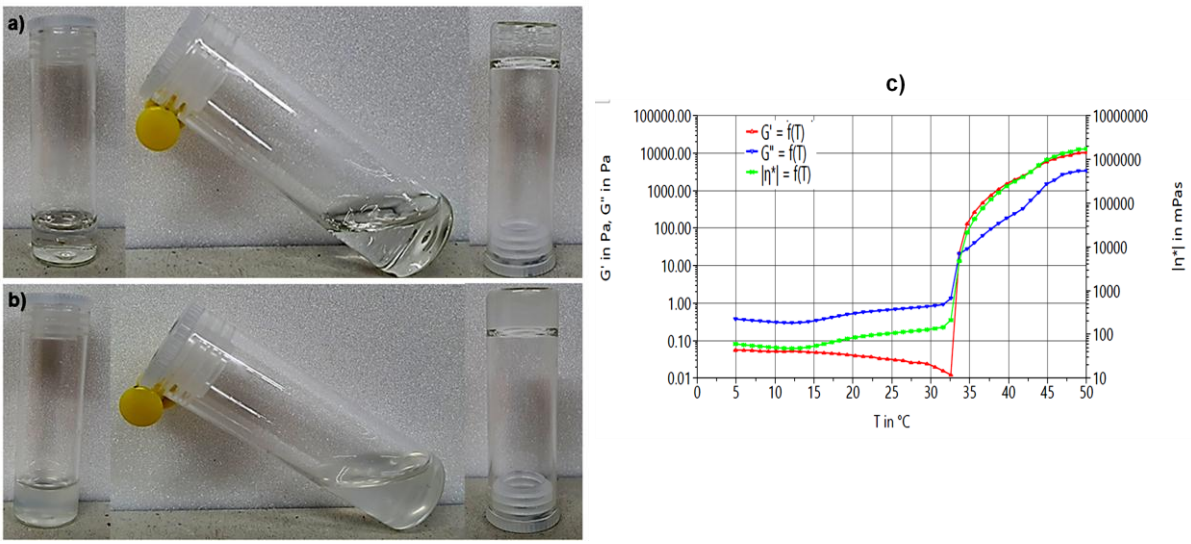

Figure 6.5: Test Tube Inversion and Rheological Analysis of Sol-Gel Transition: **(a)** Test tube inversion method showing the sol-gel transition of the pure hydrogel. **(b)** Test tube inversion method showing the sol-gel transition of the nanocomposite hydrogel. **(c)** Elastic modulus rheogram as a function of temperature, depicting the gelation temperature for the nanocomposite hydrogel with 20% nanoparticles, illustrating an increase in gelation temperature from **Figure 6.5b** with the further addition of nanoparticles.

6.3.4. pH-Dependent Release Profiles of VITD3 and RIF from Glu-CS-PCL Nanoparticles Incorporated into Pluronic Thermogel: A Thermogel Nanocomposite Release Profile

Illustrated in **Figure 6.6a** is the cumulative release of VITD3 from the nanoparticles incorporated in the pluronic hydrogel over 12 days. The release profile was assessed at different pH levels: 4.8, 6.8, and 7.4 at 37°C. The release was pH-dependent, with the highest release occurring at pH 4.8. Specifically, at pH 4.8, the cumulative release of VITD3 reached approximately 30% by day 12. At pH 6.8, the release was about 20%; at pH 7.4, the release was the lowest, reaching just over 10%. Similarly, **Figure 6.6b** presents the cumulative release of RIF from the nanoparticles in the pluronic hydrogel (nanocomposite) over the same 12-day period, measured at pH levels of 4.8, 6.8, and 7.4 under the same conditions. Like VITD3, RIF exhibited the highest release at pH 4.8, with a cumulative release of approximately 45% by day 12. At pH 6.8, the release was around 35%; at pH 7.4, the release was the lowest, reaching around 25%.

The release profiles of both VITD3 and RIF from the nanocomposite hydrogel showed an explicit pH dependency, with the highest release observed at the lower pH level of 4.8. The slower release at higher pH levels can be attributed to the ionisation state of chitosan, which is a key component of the nanoparticles. At lower pH levels, chitosan becomes more protonated, leading to increased swelling of the nanoparticles and enhanced drug release (Shikuku et al., 2024). Conversely, chitosan is less protonated at higher pH levels, resulting in reduced swelling and a slower release of the encapsulated drugs (Shikuku et al., 2024). Similarly, polycaprolactone's ester linkages tend to hydrolysis quicker at lower acidic environments, accelerating the rate of PCL degradation and faster release compared to higher pHs, as observed in **Figure 6.6** (Dong et al., 2019).

Furthermore, the slower release is attributed to the fact that the drugs not only have to escape from the nanoparticles, but the nanoparticles themselves also have to either escape from the hydrogel matrix or diffuse through it. The hydrogel matrix acts as a secondary barrier, further regulating the release rate. Again, it has also been shown that pluronic hydrogel degrades more rapidly under acidic conditions, accelerating the release of encapsulated drugs or nanoparticles, as observed in **Figure 6.6** (Seon et al., 2024, Buwalda et al., 2017). Additionally, the mechanical properties of the hydrogel, represented by the storage modulus G' and G'', as seen in **Figure 6.4**, may have played a critical role in the drug release dynamics observed. The nanocomposite hydrogel showed higher G' than the hydrogel alone, indicating

a more stable and robust structure. This enhanced mechanical strength likely contributes to the controlled and sustained release of the drugs/nanoparticles, preventing a rapid burst release and ensuring a steady diffusion of the nanoparticles.

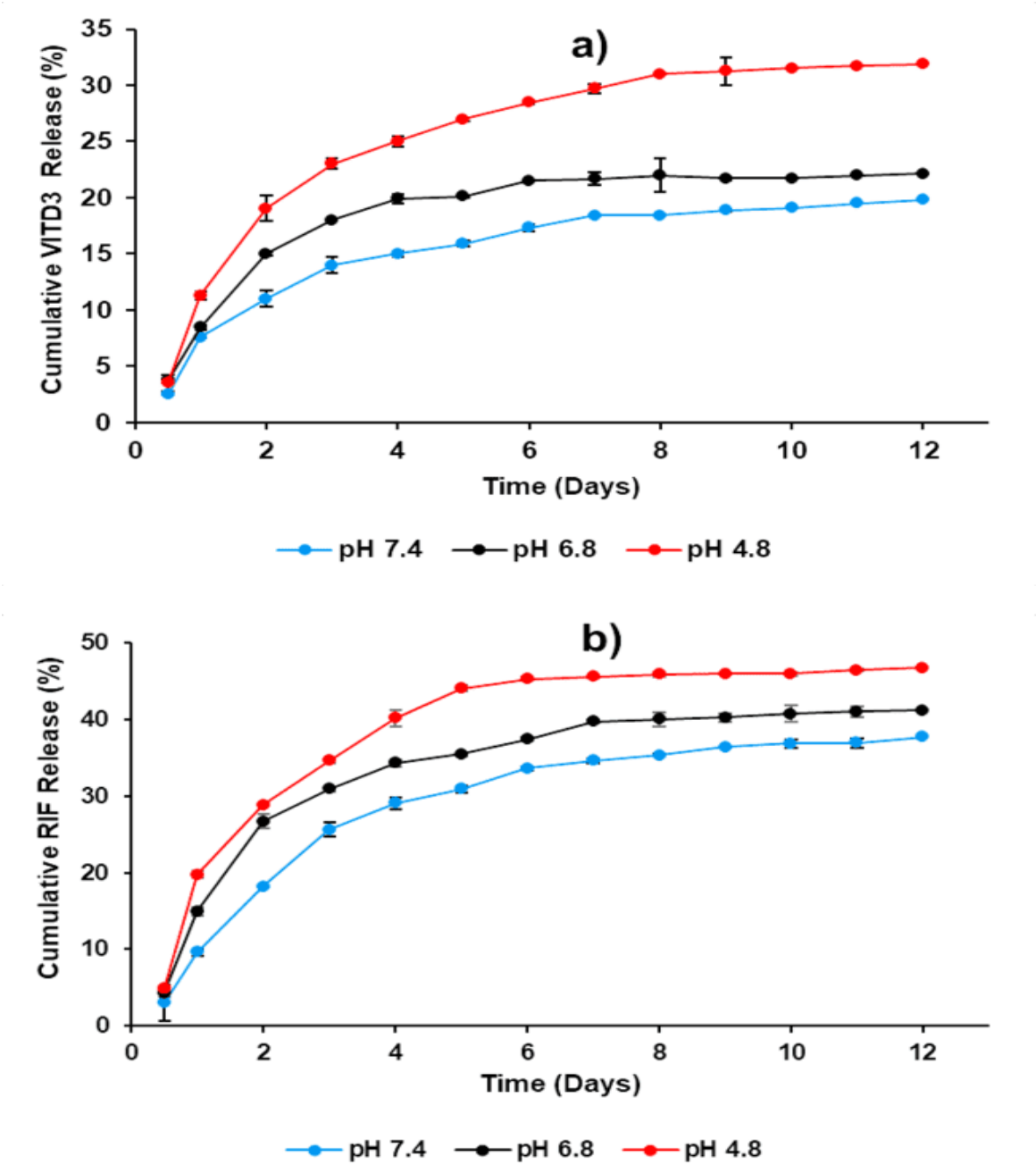

Figure 6.6: Cumulative release profiles of **(a)** VITD3 and **(b)** RIF from nanoparticles incorporated into a Pluronic hydrogel (nanocomposite) over 12 days at different pH levels (4.8, 6.8, and 7.4) at 37°C. The cumulative release of VITD3 was significantly higher at pH 4.8, reaching approximately 30% by day 12. At pH 6.8 and pH 7.4, the release was lower, reaching around 20% and just over 10%, respectively. The cumulative release of RIF was also highest at pH 4.8, reaching approximately 45% by day 12. The release at pH 6.8 was around 35%, and at pH 7.4, it was approximately 25%. The results are presented as mean ± SD (n = 3).

6.3.5. MTT Assay: Cell Viability and Cytocompatibility of the Thermogel Nanocomposite

The cytotoxicity analysis and compatibility of the hydrogel and nanocomposite at different concentrations (62.5, 125, 250, and 500 µg/mL) were evaluated using RAW 264.7 cells. The cell viability was assessed and presented in **Figure 6.7**. At 62.5 µg/mL, the hydrogel-maintained cell viability at approximately 120%, while the nanocomposite showed slightly lower viability at around 110%, and the control showed around 100% viability. At 125 µg/mL, the hydrogel still exhibited high cell viability at around 120%, whereas the nanocomposite's viability decreased to approximately 100%, and the control's viability dropped to around 90%. When the concentration was increased to 250 µg/mL, the hydrogel maintained consistent cell viability at around 120%, the nanocomposite's viability remained close to 100%, and the control's viability was about 90%. Finally, at 500 µg/mL, the hydrogel's cell viability was slightly lower but still high at around 115%, the nanocomposite's viability remained at approximately 100%, and the control's viability stayed consistent at around 90%.

The results demonstrate that the nanocomposite did not exhibit cytotoxic effects on RAW 264.7 cells. The high cell viability percentages across different concentrations indicate excellent cytocompatibility of the hydrogel and nanocomposite with RAW 264.7 cells. This suggests that the hydrogel matrix is a suitable carrier for the nanoparticles without inducing toxicity, which could be crucial for future studies involving live models and animal testing. The multidual delivery system of hydrogel and nanoparticles holds the potential for effective therapeutic applications, particularly in targeted drug delivery.

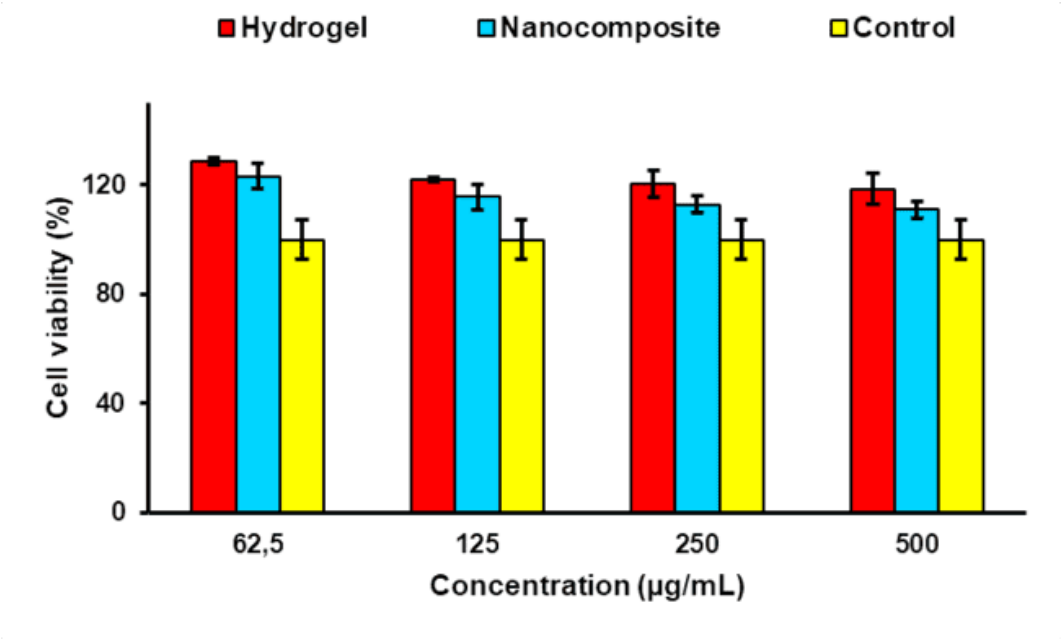

Figure 6.7: MTT assay measurement of RAW 264.7 cell viability and cytocompatibility after 48-hour treatment with different concentrations of the hydrogel and nanocomposites. The results are presented as mean ± SD (n = 3).

6.4. Concluding remarks

The study demonstrated that the nanocomposite, comprising nanoparticles incorporated within a model thermogel matrix, maintained its chemical integrity and thermal stability. The thermal stability of the nanocomposite, with degradation occurring only at higher temperatures, further supports its robustness for potential biomedical applications. A significant finding was the pH-dependent release of the nanoparticles from the thermogel. This property is particularly beneficial for targeting pathological environments such as those associated with Mtb, which typically exhibit lower pH levels. The ability to control the release rate based on pH conditions ensures that the therapeutic agents are delivered more effectively to the target site, enhancing treatment efficacy.

Moreover, the cytotoxicity assays revealed that the nanocomposite is non-toxic to RAW 264.7 cells across various concentrations. This high level of cytocompatibility indicates that the thermogel matrix does not elicit adverse cellular responses, making it a safe carrier for nanoparticles. The non-toxic nature of the nanocomposite is crucial for its application in live models and potential clinical settings. Notably, this study utilised a model thermogel, which serves as a proof of concept. For lung-targeted applications, the thermogel must be formulated

from materials such as methylcellulose, which can be easily cleared from the lung cavity, unlike Pluronic-based gels. The combination of effective drug encapsulation, controlled release, and biocompatibility underscores the potential of this nanocomposite system in advancing medical treatments, particularly for conditions requiring precise and prolonged delivery of therapeutic agents.

6.5. References

Ahmad, N., Bukhari, S. N. A., Hussain, M. A., Ejaz, H., Munir, M. U. & Amjad, M. W. 2024. Nanoparticles incorporated hydrogels for delivery of antimicrobial agents: developments and trends. *RSC advances,* 14**,** 13535-13564.

Akilo, O. D., Kumar, P., Choonara, Y. E., Du Toit, L. C., Pradeep, P., Modi, G. & Pillay, V. 2019. In situ thermo-co-electroresponsive mucogel for controlled release of bioactive agent. *International journal of pharmaceutics,* 559**,** 255-270.

Anju, S., Prajitha, N., Sukanya, V. S. & Mohanan, P. V. 2020. Complicity of degradable polymers in health-care applications. *Materials Today Chemistry,* 16**,** 100236.

Askari, E., Seyfoori, A., Amereh, M., Gharaie, S. S., Ghazali, H. S., Ghazali, Z. S., et al. Akbari, M. 2020. Stimuli-Responsive Hydrogels for Local Post-Surgical Drug Delivery. *Gels (Basel, Switzerland),* 6.

Bellotti, E., Schilling, A. L., Little, S. R. & Decuzzi, P. 2021. Injectable thermoresponsive hydrogels as drug delivery system for the treatment of central nervous system disorders: A review. *J Control Release,* 329**,** 16-35.

Buwalda, S. J., Vermonden, T. & Hennink, W. E. 2017. Hydrogels for Therapeutic Delivery: Current Developments and Future Directions. *Biomacromolecules,* 18**,** 316-330.

Cidade, M. T., Ramos, D. J., Santos, J., Carrelo, H., Calero, N. & Borges, J. P. 2019. Injectable Hydrogels Based on Pluronic/Water Systems Filled with Alginate Microparticles for Biomedical Applications. *Materials (Basel),* 12**,** 1083.

Cychosz, K. A. & Thommes, M. 2018. Progress in the Physisorption Characterization of Nanoporous Gas Storage Materials. *Engineering,* 4**,** 559-566.

Dong, H., Pang, L., Cong, H., Shen, Y. & Yu, B. 2019. Application and design of esterase-responsive nanoparticles for cancer therapy. *Drug delivery,* 26**,** 416-432.

Ezike, T. C., Okpala, U. S., Onoja, U. L., Nwike, C. P., Ezeako, E. C., Okpara, O. J., et al. Nwanguma, B. C. 2023. Advances in drug delivery systems, challenges and future directions. *Heliyon,* 9**,** e17488.

Georgieva, V., Zvezdova, D. & Vlaev, L. 2012. Non-isothermal kinetics of thermal degradation of chitosan. *Chem Cent J,* 6**,** 81.

Groen, J. C., Peffer, L. a. A. & Pérez-RamíRez, J. 2003. Pore size determination in modified micro- and mesoporous materials. Pitfalls and limitations in gas adsorption data analysis. *Microporous and Mesoporous Materials,* 60**,** 1-17.

Horvat, G., Pantic, M., Knez, Z. & Novak, Z. 2022. A Brief Evaluation of Pore Structure Determination for Bioaerogels. *Gels (Basel, Switzerland),* 8.

İspir, E., İnal, M., Gün Gök, Z. & Yiğitoğlu, M. 2023. Synthesis, characterization and in vitro release analysis of pluronic F127 copolymer micelles containing quercetin as a hydrophobic drug. *Polymer Bulletin,* 81**,** 6801-6822.

Kaliaraj, G. S., Shanmugam, D. K., Dasan, A. & Mosas, K. K. A. 2023. Hydrogels—A Promising Materials for 3D Printing Technology. *Gels (Basel, Switzerland),* 9**,** 260.

Kamaly, N., Yameen, B., Wu, J. & Farokhzad, O. C. 2016. Degradable Controlled-Release Polymers and Polymeric Nanoparticles: Mechanisms of Controlling Drug Release. *Chem Rev,* 116**,** 2602-63.

Karolewicz, B., Gajda, M., Górniak, A., Owczarek, A. & Mucha, I. 2017. Pluronic F127 as a suitable carrier for preparing the imatinib base solid dispersions and its potential in development of a modified release dosage forms. *Journal of Thermal Analysis and Calorimetry,* 130**,** 383-390.

Kesharwani, P., Bisht, A., Alexander, A., Dave, V. & Sharma, S. 2021. Biomedical applications of hydrogels in drug delivery system: An update. *Journal of Drug Delivery Science and Technology,* 66**,** 102914.

Khaliq, N. U., Lee, J., Kim, S., Sung, D. & Kim, H. 2023. Pluronic F-68 and F-127 Based Nanomedicines for Advancing Combination Cancer Therapy. *Pharmaceutics,* 15**,** 2102.

Li, W., Hu, Y., Shi, L., Zhang, X., Xiong, L., Zhang, W. & Ullah, I. 2018. Electrospinning of Polycaprolactone/Pluronic F127 dissolved in glacial acetic acid: fibrous scaffolds fabrication, characterization and in vitro evaluation. *J Biomater Sci Polym Ed,* 29**,** 1155-1167.

Liu, B. & Chen, K. 2024. Advances in Hydrogel-Based Drug Delivery Systems. *Gels (Basel, Switzerland),* 10.

Nunes, D., Andrade, S., Ramalho, M. J., Loureiro, J. A. & Pereira, M. C. 2022. Polymeric Nanoparticles-Loaded Hydrogels for Biomedical Applications: A Systematic Review on In Vivo Findings. *Polymers,* 14**,** 1010.

Russo, E. & Villa, C. 2019. Poloxamer Hydrogels for Biomedical Applications. *Pharmaceutics,* 11**,** 671.

Seon, S., Li, Y., Lee, S., Jeon, Y. S., Kang, D. S. & Ryu, D. J. 2024. Self-Assembled PLGA-Pluronic F127 Microsphere for Sustained Drug Release for Osteoarthritis. *Pharmaceuticals (Basel, Switzerland),* 17**,** 471.

Sharma, A., Puri, V., Kumar, P., Singh, I. & Huanbutta, K. 2021. Development and Evaluation of Rifampicin Loaded Alginate-Gelatin Biocomposite Microfibers. *Polymers,* 13.

Shen, J., Chang, L., Chen, D., Wang, Y., Li, W., He, Y. & Qin, J. 2021. Cross-linking induced thermo-responsive self-healing hydrogel with gel-sol–gel transition constructed on dynamic covalent bond. *Journal of Polymer Research,* 28**,** 132.

Shikuku, R., Hasnat, M. A., Mashrur, S. B. A., Haque, P., Rahman, M. M. & Khan, M. N. 2024. Chitosan-based pH-sensitive semi-interpenetrating network nanoparticles as a sustained release matrix for anticancer drug delivery. *Carbohydrate Polymer Technologies and Applications,* 7**,** 100515.

Shoukat, H., Pervaiz, F. & Rehman, S. 2022. Pluronic F127-co-poly (2 acrylamido-2-methylpropane sulphonic acid) crosslinked matrices as potential controlled release carrier for an anti-depressant drug: in vitro and in vivo attributes. *Chemical Papers,* 76**,** 2917-2933.

Sing, K. S. W. 1985. Reporting physisorption data for gas/solid systems with special reference to the determination of surface area and porosity (Recommendations 1984). *Pure and Applied Chemistry,* 57**,** 603-619.

Stojkov, G., Niyazov, Z., Picchioni, F. & Bose, R. K. 2021. Relationship between Structure and Rheology of Hydrogels for Various Applications. *Gels (Basel, Switzerland),* 7.

Sun, Y., Nan, D., Jin, H. & Qu, X. 2020. Recent advances of injectable hydrogels for drug delivery and tissue engineering applications. *Polymer Testing,* 81**,** 106283.

Unal, S., Tekeli, M., Dogan, O. & Aktas, Y. 2023. Thermosensitive Pluronic® F127-Based in situ gel formulation containing nanoparticles for the sustained delivery of paclitaxel. *Medicine Science | International Medical Journal,* 12**,** 224.

Yeh, M.-Y., Zhao, J.-Y., Hsieh, Y.-R., Lin, J.-H., Chen, F.-Y., Chakravarthy, R. D., et al. Hung, S.-C. 2017. Reverse thermo-responsive hydrogels prepared from Pluronic F127 and gelatin composite materials. *RSC advances,* 7**,** 21252-21257.

CHAPTER 7

CONCLUSIONS, LIMITATIONS AND RECOMMENDATIONS

7.1. Conclusion

Tuberculosis remains one of the most prevalent and deadly infectious diseases worldwide, with a particularly severe impact in Africa, including South Africa. Each year, millions are infected, and millions lose their lives to this persistent threat. The limitations of current TB treatments are well-documented, including lengthy treatment durations, complex medication regimens, especially for those with co-infections, and the resulting low patient compliance. This situation has been exacerbated by the emergence of multidrug-resistant TB strains, which require second and third-line drugs for treatment. These alternative drugs are not only more expensive but also come with more severe side effects compared to first-line therapies.

Given these challenges, there has been a shift in recent years towards leveraging the infected individual's immune system as a key focus for TB treatment. Mtb thrives within macrophages, a component of the innate immune system, and its persistence is often due to an insufficient immune response or Mtb's ability to evade immune mechanisms. Host-directed therapy or immunomodulation, coupled with the targeted delivery of anti-TB therapeutics using nanotechnology, represents a promising avenue of research. These approaches aim to address the limitations of current treatments by reducing the duration of therapy, enhancing the immune response to combat Mtb effectively, and ensuring the direct delivery of drugs to the infection site, thereby improving bioavailability. Harnessing both host-directed therapy and nanotechnology could be the future of combating the global TB pandemic, offering new hope for more effective and patient-friendly treatments.

The present study has explored targeted nanomedicine and host-directed therapy as viable and potential interventions for managing TB. Innovative nanosystems with active targeting capabilities were successfully formulated and evaluated by focusing on macrophage-targeted delivery of RIF to treat Mtb and VITD3 for supporting host immune responses. These systems were thoroughly assessed regarding stability, drug release, cytotoxicity, macrophage polarisation, and antibacterial activity in THP-1 infected cells. First, an in-depth review was conducted to provide insight into how Mtb survives within macrophages and the mechanisms it disrupts to evade the immune system. The review also explored alternative strategies to

overcome these challenges, including reactivating the immune response through host-directed therapy. The potential benefits of combining host-directed therapy with traditional therapeutics were also examined, emphasising how such an approach could reverse the immune suppression caused by Mtb and enhance the effectiveness of TB treatment.

Following a safety-by-design approach, 1,3-β-glucan functionalised biopolymeric nanoparticles (1,3-β Glu-CS-PCL-VITD3/RIF) were meticulously formulated and thoroughly examined for various physicochemical properties and pharmaceutical characteristics. The 1,3-β Glu-CS-PCL-VITD3/RIF nanoparticles demonstrated excellent stability over three months, with an average particle size ranging from 122.63 ± 5.11 nm (Glu-CS-PCL-RIF) to 182.90 ± 4.70 nm (Glu-CS-PCL-VITD3). These sizes are optimal for penetrating and being trapped within macrophages through various endocytosis mechanisms, including clathrin- or caveolin-mediated pathways and clathrin- or caveolin-independent pinocytosis processes. The nanoparticles further demonstrated adequate and suitable drug loading capacity and sustained drug release that was pH-responsive and specific to the Mtb environment. In addition, they exhibited excellent biocompatibility with the RAW 264.7 cell line, showing no toxic effects. Based on these findings, it was concluded that these nanoparticles are well-suited for further in-depth in vitro cell studies to evaluate their immunomodulatory effects and antibacterial activity.

Macrophage polarisation studies revealed that the developed nanoparticles favour the M1 phenotype, as evidenced by the quantification of ROS and TNF-α, both of which showed elevated levels upon treatment with the nanoparticles. These cytokines are critical in mediating the body's response to infections, thereby providing a dual-action mechanism: enhancing bacterial killing while simultaneously stimulating a robust immune response. Morphological cell studies further supported this by exhibiting the M1 phenotype with some characteristics of the M2 phenotype. This duality was highlighted by a partial increase in IL-4 cytokine levels, an anti-inflammatory cytokine associated with the M2 phenotype. These findings indicate that while the nanoparticles predominantly favour the M1 phenotype, they also maintain a partial M2 phenotype, crucial for striking a balanced immune response.

Furthermore, MIC studies of the fabricated nanoparticles demonstrated impressive MIC values against susceptible H37Rv and resistant MDR11 strains. Nanoparticles containing RIF showed killing at even lower concentrations compared to standard MIC—the functionalisation with 1,3-β-glucan significantly enhanced drug delivery and efficacy by interacting with the Mtb cell wall. The MIC findings served as a baseline for determining the effective concentration to use in subsequent experiments involving THP-1-infected macrophages. In these experiments, host-directed therapies using VITD3 and RIF boosted the cells' ability to kill Mtb, as evidenced by reduced colony-forming units. This suggests that VITD3 and RIF encapsulated within the nanoparticles enhance the macrophages' immune response, leading to better bacterial clearance. Subsequently, these separate nanoparticle systems were incorporated into a thermogel to create a dual delivery system. This system allowed for longer sustained release and demonstrated thermoresponsiveness at body temperature and pH-responsive drug release, favouring the Mtb environment. In conclusion, this study successfully developed multifunctional 1,3-β-glucan-functionalized nanoparticles with immunomodulatory capabilities (HDT) and antibacterial activity. This Nanosystem represents a promising next-generation platform for targeted TB therapy, addressing critical limitations of existing approaches through enhanced macrophage targeting, sustained dual-drug delivery, and immunomodulatory activity. As summarised in **Table 7.1**, it offers significant potential for further evaluation and development, with future *in vivo* validation essential to confirm its clinical applicability.

Table 7.1: General Comparative Summary of Reported TB Drug Delivery Systems and the Developed 1,3-β-Glu-CS-PCL Nanoparticles.

Feature	**Marketed/Reported Systems**	**Developed 1,3-β-Glu-CS-PCL-VITD3/RIF Nanoparticles**
Delivery System	Liposomes, Microparticles, Solid Lipid Nanoparticles (SLNs), Nanostructured Lipid Carriers (NLCs), Polymeric nanoparticles (non-functionalized).	Biopolymeric nanoparticles (Chitosan-PCL) functionalised with 1,3-β-glucan.
Drug(s) Delivered	Mostly Rifampicin, Isoniazid, or a combination of first-line drugs.	Rifampicin (RIF) + Vitamin D3 (VITD3) (dual delivery).
Targeting Strategy	Passive targeting (size-dependent accumulation in lungs); some active targeting (mannose, transferrin).	Active targeting via 1,3-β-glucan functionalisation (Dectin-1 receptor-mediated macrophage targeting).
Immune Modulation	Rarely addressed explicitly	Yes (Host-Directed Therapy): Enhances TNF-α, ROS production; balanced M1/M2 macrophage response.
Particle Size	100–300 nm (varies)	~123–183 nm (optimal macrophage uptake range).

Surface Charge	Variable (-5 to +20 mV)	+19.5 to +24.8 mV (favourable for cell interaction)
Drug Release Profile	Mostly sustained over 24-48 hours.	pH-responsive, sustained over 48 hours; enhanced release at acidic pH (mimicking infected sites).
Entrapment Efficiency	40-70% typical.	54% (VITD3), 62% (RIF).
Cytocompatibility	Generally good	100% cell viability confirmed (RAW 264.7 macrophages).
Bactericidal Activity (MIC)	MICs comparable or slightly improved vs free drugs	2× lower MIC for RIF vs standard in MDR Mtb; synergistic RIF+VITD3 effect.
Intracellular Killing	Some systems show enhanced uptake, limited intracellular bactericidal studies.	Significant reduction in intracellular Mtb CFUs; superior performance with less drug.
Clinical Status	Mostly preclinical; few (e.g., inhaled liposomal amikacin) approved for related pulmonary infections.	Preclinical (in vitro validated); strong basis for advancing to *in vivo* and more *In vitro* studies.

7.2. Limitations and Recommendations

One of the limitations of this study was the inability to carry out in vivo studies using TB animal models, where animals are infected with Mtb and treated with the developed nanoparticles. The primary challenges included a lack of infrastructure to house TB-infected animals safely and the inherent risks associated with conducting such studies. Despite these limitations, the study provides a strong foundation for future research. It would be essential to perform long-term toxicity and safety evaluations of the nanoparticles, both *in vitro* and *in vivo*. These studies should assess potential adverse effects on non-target cells or organs over extended periods. Ensuring the safety of these nanoparticles is crucial for their possible clinical application. Long-term studies could reveal any latent toxicity or immune responses that might arise from prolonged exposure to the nanoparticles, helping to ensure that they are safe for future applications.

In addition, future research should involve more in-depth in vitro studies where specific biomarkers and peptides are analysed in cells treated with the formulations. Furthermore, *in vivo* studies should be conducted using TB animal models, where the nanoparticles are administered both as individual entities and as part of a dual delivery system within a thermoresponsive hydrogel. Labelling the nanoparticles could provide insights into their biodistribution, allowing researchers to track their localisation and accumulation within the

animal models. Additionally, these studies could evaluate the extent of tissue damage or lesions in the lungs of TB-infected models and determine whether the nanoparticles can mitigate the progression of Mtb-induced lesions. By addressing these limitations and pursuing the recommended future studies, the full potential of these 1,3-β-glucan-functionalized nanoparticles can be realised, ultimately advancing the field of TB treatment through targeted nanomedicine and host-directed therapy.

Appendix A: Research Outputs

A1: A review on Insights into innovative therapeutics for drug-resistant tuberculosis: Host-directed therapy and autophagy inducing modified nanoparticles. Leon J. Khoza, Pradeep Kumar, Admire Dube, Patrick H. Demana, Yahya E. Choonara. *International Journal of Pharmaceutics*, 622, 12893, 2022.

International Journal of Pharmaceutics 622 (2022) 121893

Contents lists available at ScienceDirect

International Journal of Pharmaceutics

journal homepage: www.elsevier.com/locate/ijpharm



Insights into innovative therapeutics for drug-resistant tuberculosis: Host-directed therapy and autophagy inducing modified nanoparticles

Leon J. Khoza [a], Pradeep Kumar [a], Admire Dube [b], Patrick H. Demana [c], Yahya E. Choonara [a,*]

[a] Wits Advanced Drug Delivery Platform Research Unit, Department of Pharmacy and Pharmacology, School of Therapeutic Science, Faculty of Health Sciences, University of Witwatersrand, Johannesburg, Parktown 2193, South Africa
[b] School of Pharmacy, Faculty of Natural Sciences, University of the Western Cape, Cape Town, South Africa
[c] Division of Pharmaceutical Sciences, School of Pharmacy, Sefako Makgatho Health Sciences University, Pretoria 0208, South Africa

ARTICLE INFO

Keywords:
Mycobacterium tuberculosis
Innate immunity
Autophagy induction
Host-directed therapy
Nanoparticles
Alveolar macrophages

A2: Annual Young Scientists Conference 2023. University of Venda, Thohoyandou, South Africa, June 12 – 13, 2023 (**Oral Presentation**).

1A02: Functionalized immunomodulatory biopolymeric nanosystem for the targeted delivery of anti-TB bioactives

[1]Leon Khoza, [1]Pradeep Kumar, [2]Admire Dube, [1]Yahya Choonara

[1]Wits Advanced Drug Delivery Platform Research Unit, Department of Pharmacy and Pharmacology, School of Therapeutic Science, Faculty of Health Sciences,
University of Witwatersrand, Johannesburg, Parktown 2193, South Africa
[2]School of Pharmacy, Faculty of Natural Sciences,
University of the Western Cape, Cape Town, South Africa

Introduction: Tuberculosis (TB) remains a significant health concern, with 10.4 million new cases and 1.7 million annual deaths. Drug-resistant TB is a major cause of failure in clinical management and economic burden. This study aims to create a nanosystem encapsulating rifampicin and vitamin D3 to eliminate Mtb. The nanosystem will interact with macrophages to induce ROS/RNS generation and cytokine production, enhancing phagocytosis and intracellular delivery of encapsulated drugs. Vitamin D3 will activate macrophages via the IFN-γ pathway, promoting autophagy and phagolysosome fusion, producing antimicrobial peptide LL-37 for Mtb killing. Combining vitamin D3 with rifampicin may improve treatment effectiveness and reduce the development of treatment-resistant TB and treatment time.

Methods: VITD3 and RIF-loaded nanoparticles were prepared using a modified solvent evaporation method and characterized for size, zeta potential, encapsulation efficiency, drug release profile and physiochemical characteristics, including Fourier transform infrared (FTIR), Differential Scanning Calorimetry (DSC), and X-Ray diffraction (XRD), Morphological analysis (SEM & TEM) and cytotoxicity studies.

Results: The nanoparticles displayed an average hydrodynamic particle size within the range of 128.50 ± 1.15-182.10 ± 4.70 nm with encapsulation efficiency ranging between 63.10 ± 1.03-50.36 ± 1.44%. The SEM and TEM images revealed that nanoparticles had a smooth, uniform surface morphology with slight aggregation after the entrapment of bioactives, with FTIR showing successful drug entrapment. Prolonged sustained drug release was observed for 48 hours, with a total release of less than 25% and 60% of the total payload of VITD3 and RIF, respectively, for both functionalized and functionalized nanoparticles. Formulated nanoparticles had no significant effect on RAW 264.6 cell line cellular metabolic activity, while VITD3 had potent cell cytotoxicity at the highest concentrations. VITD3-loaded nanoparticles had no observed cell cytotoxicity at all concentration ranges, indicating a non-toxic effect and cytocompatibility.

Conclusions/Impact: The formulated nanoparticles successfully encapsulated the bioactive with sustained drug release. These experimental results revealed that encapsulating VITD3 into the nanoparticles could help reduce the in vitro cytotoxicity of the bioactive. This advantage may be exploited in formulation science to design a delivery system that can safely hold a high concentration of VITD3, releasing the bioactive content over a sustained period while maintaining optimum therapeutic concentrations and reducing dosing frequency. Additional and ongoing work includes macrophage polarisation by quantifying various cytokines IL6, IL-4 and IL-10.

Acknowledgements: This study is funded by the National Research Foundation of South Africa (NRF).

Presenters Bibliography: Leon Khoza is a PhD candidate in Pharmacy at the University of Witwatersrand in Johannesburg, South Africa. He conducts research in host-directed therapy, nanomaterials, and drug delivery systems as a member of the Wits Advanced Drug Delivery Platform Research Unit.

2

A3: STHS Biennial Research Day. University of the Witwatersrand, Johannesburg, South Africa, September 5, 2023 (**Poster Presentation**).

Functionalized Immunomodulatory Biopolymeric Nanosystem for the Targeted Delivery of Anti-TB Bioactives

*Leon J. Khoza[1], Pradeep Kumar[1], Admire Dube[2], and Yahya E. Choonara[1]**

[1]Wits Advanced Drug Delivery Platform Unit, Department of Pharmacy and Pharmacology, School of Therapeutic Sciences, Faculty of Health Sciences, University of Witwatersrand, Johannesburg, 7 York Road Parktown, 2193, South Africa

[2]School of Pharmacy, Faculty of Natural Sciences, University of the Western Cape, Cape Town, South Africa

*Corresponding Author: Yahya.choonara@wits.ac.za

Introduction

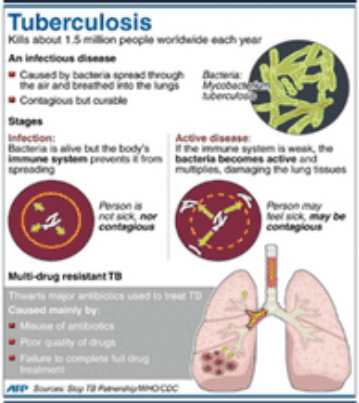

Aim

To address these pressing issues, this study proposes a pioneering innovation: an advanced drug delivery system for targeted anti-TB medication administration. This novel system involves a meticulously designed surface-functionalized biopolymeric nanosystem with versatile functions, including immunomodulation and host-directed therapy.

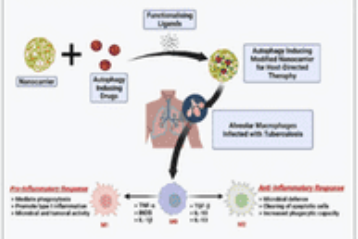

Experimental Methods

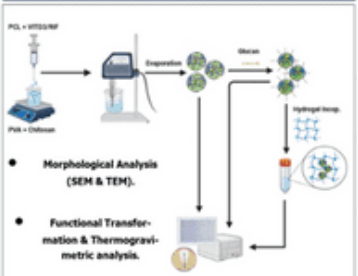

Results

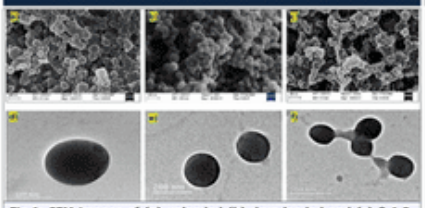

Fig.1: SEM images of (a) unloaded (b) drug-loaded and (c) β-1,3-Glucan surface functionalized nanoparticles and their TEM images, (d), (e) and (f) respectively at different scales.

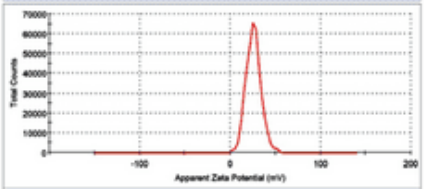

Fig.2: Zeta potential of the formulated Nanoparticles

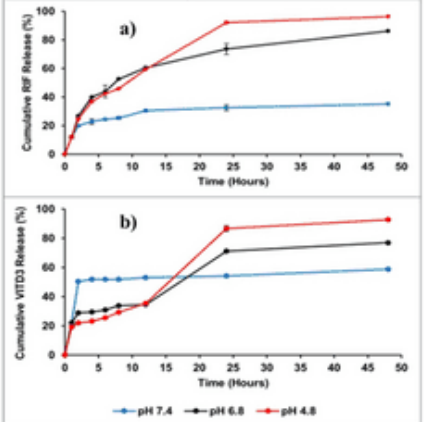

Fig.3: In vitro a) RIF and b) VITD3 release profile from CT-PCL-VITD3/RIF nanoparticles at pH 4.8, 6.8 and 7.4, and 37°C for 48-hours (n = 3, mean ± SD).

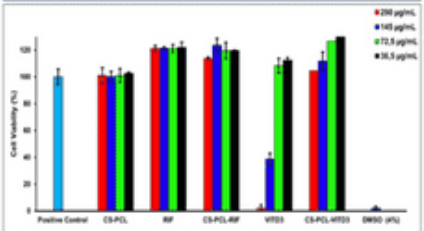

Fig. 4: MTT assay measurement of the viability of RAW 264.7 murine macrophage cell after 48-hour treatment with Free bioactives and encapsulated nanoparticles (n = 3, mean ± SD).

Discussion

Nanoparticle shape significantly affects uptake and trafficking. Surface electron microscopy (SEM) and Transmission Electron Microscope (TEM) confirmed spherical, uniform shape of nanoparticles as shown in **Fig.1**. Functionalized and non-functionalized nanoparticles exhibited similar smooth morphology. Slight aggregation occurred after bioactive entrapment (**Fig.1**). Spherical nanoparticles are preferred for enhanced macrophage internalization, as shown in various studies.

Surface charge significantly affects nanoparticle uptake. The nanoparticles' average positive charge of +25.4 mV (**Fig. 2**) could enhance interaction with negatively charged macrophage surfaces, further promoting uptake. Additionally, the nanoparticles' stability and homogeneity were indicated by their average surface charge.

In vitro drug release profiles showed that at pH 4.8, more than 80% of encapsulated RIF and VITD3 were released within 48 hours, while at pH 7.4, less than 30% and 60% of RIF and VITD3 were released, respectively (**Fig.3**). This pH-dependent release is significant, considering the acidic environment (pH 4.5 to 6.0) created within macrophages during Mtb infection, aiding in pathogen destruction. This finding suggests that the acidic pH is favorable for effective drug release.

Formulated nanoparticles' cytocompatibility was confirmed on RAW 264.7 macrophages (**Fig. 4**). VITD3 encapsulated within CS-PCL nanoparticles eliminated cytotoxicity, indicating a promising approach for safe and sustained high-concentration delivery with reduced dosing frequency.

Conclusion

Nanoparticles formulated for host-directed therapy enable sustained drug release, making them ideal for delivering anti-TB therapeutics to macrophages while reducing cytotoxicity. This opens possibilities for designing a safe, high-concentration VITD3/RIF delivery system with sustained release and reduced dosing frequency.

References

Chitkara and Chan, 2007, Forooraadeh and Aziz, 2018, Chitkara et al., 2006 Marasso et al., 2011, Dwivedi et al., 2008, Forooraadeh and Aziz, 2018

UNIVERSITY OF THE WITWATERSRAND, JOHANNESBURG 1922 2022 100 WADDP National Research Foundation NRF

Appendix B: Patent Documentation for Functionalised Nanoparticles in Antimicrobial Therapy.

COPY OF PROVISIONAL SPECIFICATION

Application No.	2024/07866
Filing Date	17 October 2024
Your Ref	
Our Ref	P99655ZP00
Name of Applicant(s)	University of the Witwatersrand, Johannesburg
Name of Inventor(s)	CHOONARA, Yahya KHOZA, Leon KUMAR, Pradeep
Title of Invention	FUNCTIONALISED NANOPARTICLES FOR ANTIMICROBIAL THERAPY
Completion Date	17 October 2025

The specification has been drafted and the patent application has been filed on the assumption that the invention is "new". The fact that we have undertaken to file this application should NOT be interpreted as an indication or guarantee that a valid patent will be obtained for the invention.

If a patent based on this application is granted then its term will be 20 years commencing with the date of filing of the complete specification, subject to payment of renewal fees.

Please keep us promptly advised of any change of contact details.

Pretoria Office
012 432 6000
Lynnwood Bridge
4 Daventry Street
Lynnwood Manor
Pretoria

Johannesburg Office
011 895 1000
2nd Floor
34 Fredman Drive
(Corner 5th Street)
Sandton

Cape Town Office
021 418 8560
28th Floor
1 Thibault Square
Corner Long Street &
Hans Strijdom Avenue
Cape Town

Durban Office
031 536 8240
Suite 2, Level 3
21 Richefond Circle
Ridgeside Office Park
Umhlanga Ridge
Durban

ATTORNEYS
Patents | Trade Marks | Copyright | Designs | Commercial | Real Estate | Dispute Resolution

ADAMS & ADAMS
Realise African Enterprise

Appendix C: Similarity Report

FUNCTIONALIZED IMMUNOMODULATORY BIOPOLYMERIC NANOSYSTEM FOR THE TARGETED DELIVERY OF ANTI-TUBERCULOSIS BIOACTIVES_Thesis 2.0_LK-44c2a5ec-f859-4958-b707-ba0f1613f996.docx

ORIGINALITY REPORT

12%	10%	13%	1%
SIMILARITY INDEX	INTERNET SOURCES	PUBLICATIONS	STUDENT PAPERS

PRIMARY SOURCES

1	wiredspace.wits.ac.za Internet Source	1%
2	www.frontiersin.org Internet Source	1%
3	doi.org Internet Source	1%
4	www.mdpi.com Internet Source	1%
5	core.ac.uk Internet Source	<1%
6	www.researchgate.net Internet Source	<1%
7	Leon J. Khoza, Pradeep Kumar, Admire Dube, Patrick H. Demana, Yahya E. Choonara. "Insights into Innovative Therapeutics for Drug-Resistant Tuberculosis: Host-Directed Therapy and Autophagy Inducing Modified	<1%